Abrasive Waterjet Contour Cutting of Thick Titanium/Graphite Laminates

Rishi Pahuja

A thesis submitted in partial fulfillment of the requirements for the degree of
Master of Science in Mechanical Engineering

University of Washington
2015

Committee:
Ramulu Mamidala
John C. Kramlich
Mohamed Hashish

Program Authorized to Offer Degree:
Mechanical Engineering

University of Washington

Abstract

Abrasive Waterjet Contour Cutting of Thick Titanium/Graphite Laminates

Rishi Pahuja

Chair of the Supervisory Committee: Professor Ramulu Mamidala
Department of Mechanical Engineering

One of the primary focus in aerospace industry is the reduction of buy-to-fly ratio. Although TiGr laminates are molded/autoclaved to a near net shape, secondary machining such as drilling, peripheral machining and contouring is often unavoidable. Machining of composites alone poses a great challenge which becomes more challenging in a three phase material system – hybrid composites, where the non-homogeneity and anisotropy of composites together with the difference in the removal mechanism for all the three different phases aggravate the machining problem.

An investigation was conducted to evaluate the feasibility and machinability of contouring thick TiGr through Abrasive Waterjet (AWJ) in terms of kerf characteristics- taper ratio and surface quality. A cutting geometry with different profile curvatures was machined with conditions according to a response surface experimental design obtained using Design Expert software. The process variables included pump pressure, jet traverse speed, load ratio (by varying abrasive flow rate) and nozzle dimensions. Material removal mechanism was studied for three different phase material systems. Kerf taper ratio was investigated to qualitatively characterize superior and inferior quality cuts. Topological characteristics of the kerf were also studied with roughness evaluation of surfaces parallel (longitudinal) and orthogonal (transverse) to jet traverse direction. Analysis of Variance (ANOVA) was used to statistically characterize the effect of operating variables on kerf taper ratio. Predictive mathematical models were developed for taper ratio and transverse roughness R_z, whereas semi-analytical model was developed to predict Average transverse roughness R_a. The AWJ process was characterized using Skewness-Kurtosis and Rq/Ra ratio of the kerf profile. Overall, machinability of thick TiGr laminates was evaluated as a function of kerf taper ratio and surface roughness and statistical optimization was done for machining with low taper and low roughness.

TABLE OF CONTENTS

LIST OF FIGURES

LIST OF TABLES

ACKNOWLEDGEMENTS

I would like to express my gratitude to my advisor, Professor Ramulu Mamidala, for his guidance in both academic and personal life. His dedication to students is an excellent example and inspiration to me. I also wish to thank author's co-advisors and colleagues in Manufacturing Science and Technology Laboratory for their enormous amount of help and valuable advice. Finally, I would like to thank my family for being a continuous support through every thick and thin.

DEDICATION

To family

NOMENCLATURE

Symbol	[Unit]	Definition	Section first used
P	[MPa]	Pump pressure	3.2
dm	[mm]	Mixing tube diameter	3.2
lm	[mm]	Mixing tube length	3.2
dn	[mm]	Orifice diameter	3.2
R	[-]	Load ratio (Ratio of mass flow rate of abrasives and water)	3.2
u	[mm/min]	Jet traverse speed (Jet feed rate)	3.2
t	[mm]	Specimen thickness	3.3.1
α_{taper}	[degree°]	Kerf taper	3.3.1
d_{entry}	[mm]	Entry kerf width	3.3.1
d_{exit}	[mm]	Exit kerf width	3.3.1
EL	[mm]	Roughness evaluation length	3.3.2
SL_i	[mm]	i_{th} Sampling length in roughness profile	3.3.2
P_i	[µm]	Distance between i_{th} peak and mean line of roughness profile	3.3.2
V_i	[µm]	Distance between i_{th} valley and mean line of roughness profile	3.3.2
R_a	[µm]	Average surface roughness	3.3.2
R_q	[µm]	Root mean square roughness	3.3.2
R_t	[µm]	SL peak to valley height	3.3.2
R_z	[µm]	EL peak to valley height	3.3.2
R_z (JIS)	[µm]	Ten point average roughness	3.3.2
RSk	[μm^3]	Skewness	3.3.2
RKu		Kurtosis	3.3.2
v_w	[m/s]	Velocity of water	4.2.2

ψ	[-]	Velocity coefficient	4.2.2
P_w	[N/m^2]	Water pressure	4.2.2
ρ_w	[kg/m^3]	Density of water	4.2.2
P_{ow}	[Nm/s]	Power of waterjet	4.2.2
$\dot{Q}_w$	[m^3/s]	Water flow rate	4.2.2
C_d	[-]	Coefficient of drag	4.2.2
v_{awj}	[m/s]	Average velocity of abrasive waterjet	4.2.2
η	[-]	Momentum transfer efficiency	4.2.2
κ	[-]	Overall power coefficient	4.2.2
U	[N/m^2]	Strain energy per unit volume	4.2.2
σ_c	[N/m^2]	Shear strength of material	4.2.2
G	[N/m^2]	Shear modulus of material	4.2.2
E_c	[N/m]	Strain energy required per unit area	4.2.2
E_o	[N/m]	Available strain energy per unit area	4.2.2
$h_{c/t}$	[m]	Composite/titanium ply thickness	4.2.2
$n_{c/t}$	[-]	Number of composite/titanium plies	4.2.2
λ	[m/m]	Jet coherency factor (ratio of mixing tube length and diameter)	4.2.2

Chapter 1. INTRODUCTION

Owing to the directional properties of composites, superior to metallic materials, Fiber Reinforced Plastics (FRP) are widely employed in aerospace and automotive industry. The composite share in recently developed Airbus A350 XWB commercial aircraft is 53% of the total material composition [1].

FRP offers several advantages over conventional metallic materials such as high specific strength and stiffness, impact strength, toughness, wear resistance, corrosion resistance, fracture toughness, damage tolerance and dimensional stability. While these advantages prove to be an undeniable value proposition for high performance in numerous applications, FRP composites have their own limitations when compared to metallic materials. These include high susceptibility to aggressive environment and moisture ingress, limited shelf life, requirement of dedicated tooling and particular conditions for repair and maintenance.

To overcome the limitations of both metals and composites, a new material system called Fiber Metal Laminate (FML) or High Temperature Composite laminate (HTCL) has been developed. It consists of alternate layers of thin metal foils and composite plies stacked together and joined using compatible adhesives. The directional properties of composites with added benefits by metal foils such as protection of composite core from heat and moisture, better distribution of point load and enhanced compression after impact (CAI) strength [2] renders high strength and stiffness to weight ratio and superior corrosion resistance, impact resistance, fracture resistance and better fatigue properties helps to outperform either of the two constituent materials, making them superior to other conventional material systems. The advantages of FMLs are discussed in detail in section 2.1.2.

Study of High temperature Fiber Metal Laminates is a key area of research owing to superior performance of structural components catered by the unique multiphase material system characteristics of FMLs. Fiber metal laminates find numerous applications, especially where high strength is required at elevated temperatures.

Over the past few years, several combinations of metals and composites have been investigated such as Aluminum/Glass-epoxy, Aluminum/Aramid, Magnesium/CFRP and Titanium/CFRP fiber metal laminates. However, only a few material systems have been able to

outperform the conventional materials owing to poor manufacturability, surface incompatibility and underdeveloped bonding technologies for metal-composite laminates.

<table>
<tr><td colspan="3">Aerospace</td></tr>
<tr><td>Boeing C-17 Globemaster-III military aircraft, Cargo door
 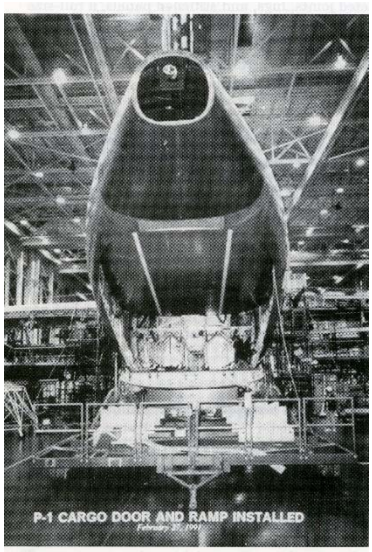

26% weight saving from conventional Aluminum [3,4]</td><td>Boeing 787 Dreamliner side and crown panel [5]
 
Crown Panel
 
Side Panel</td><td>A330/340/380 fuselage
Cargo floors of Boeing 777,
Aircraft engine cowlings, bonded GLARE patch repair,
Aircraft stiffeners, cargo containers.</td></tr>
<tr><td>Automotive</td><td>Maritime</td><td>Sporting equipment</td></tr>
<tr><td>Supercar - Zonda Cinque
 
CarboTitanium patented by Pagani Huayra [6,7]</td><td>Yacht
  </td><td>Skateboards [8]
Ski and snowboard [9]
Golf club shafts and heads [10]</td></tr>
</table>

Figure 1.1. Applications of Fiber metal laminates in several industries.

Titanium/Graphite laminate (TiGr) is one of the recent developments in FMLs and pertinent to the future needs where aircrafts could experience high skin temperatures (177 °C) due to aerofrictional heating at supersonic speeds [11–13]. TiGr is composed of alternate layers of graphite fiber reinforced composite and titanium sheets. In general, thermoset matrix PIXA and thermoplastic PEEK are two prime candidates compatible with titanium [11]. Thermoset matrix composites offer high strength at high temperature, whereas thermoplastic composites are thermally stable within a broader range of temperatures. Besides, thermoplastic based composites exhibit superior impact toughness, fire/smoke/toxicity (FST) performance and high shelf life, better fusibility and weldability. These properties of thermoplastics results in lower priced, thermally resistant components even at elevated temperatures ($9-$160/kg) when compared to typical thermosets ($92-$880/kg). Thus, Titanium graphite is a promising candidate for high temperature applications warranting the need for further development in manufacturing and processing techniques for the same.

1.1 MOTIVATION

One of the primary focus in aerospace industry is the reduction of buy-to-fly ratio. Although TiGr laminates are molded/autoclaved to a near net shape, secondary machining such as drilling, peripheral machining and contouring is often unavoidable. Machining of composites alone poses a great challenge [14], as discussed in section 2.4, which becomes more challenging in a three phase material system – hybrid composites, where the non-homogeneity and anisotropy of composites together with the difference in the removal mechanism for all the three different phases aggravate the machining problem. On one hand, the presence of hard and brittle fibers, thermally low conductive matrix material, and ductile metal foils as three different phases are advantageous, but on the other hand their machining through conventional processes leads to severe issues such as excessive tool wear and thermal distortion, fiber pull out, matrix cratering, delamination, fraying, dust and burr formation from metal foils, cropping up as limitations of conventional machining processes [15–20]. Reported composite fabrication studies claimed that around 60% of the rejected composite parts come from secondary machining defects, highlighting the need and importance of more precise and non-traditional methods in composite machining [18,19,21]

Several non-traditional methods have been studied for the machining of composites [16,17,22,23]. Electrical discharge machining (EDM) has been employed to machine electrically conductive composite materials. However, objectionable surface integrity, high delamination due to arching and low Material removal rate (MRR) reflects its inaptness for machining fiber metal laminate [24]. Laser cutting is well suited for contour trimming of carbon fiber reinforced plastics because of point-sized geometry and multidirectional cutting ability. However, uneven kerf width and decrease in static strength of components due to thermal cracking and large HAZ limits the applicability [25,26]. Abrasive Waterjet machining (AWJ) is a widely used unconventional alternative because of properties including zero thermal damage in the workpiece, high cutting speed, wide working range and environmental friendly. Several investigators have identified the feasibility of AWJ machining of FMLs mostly due to non-conductive nature of composites layers [27].

Although AWJ machining is promising for most of the material and shape feature applications, the process response variations due to continual energy loss throughout the penetration depth limits the maximum achievable thickness, which is a characteristic of almost all the beam machining processes. As established from previous investigations on AWJ machining of composites and ductile metals, process performance and associated cutting quality is significantly dependent on the properties of workpiece material being machined due to difference in jet interaction and cutting mechanisms for different materials [22,28]. It is apparent that machining of FML material system is challenging due to possible machining variations introduced by completely different and ductile metal foils interspersed in composite plies with highly brittle fibers. Besides, the jet energy variation is accountable for low control and variable quality at different profile features (size and angles) within a contour geometry [29].

Several FEM, analytical and experimental models have been developed to predict the effect of process parameters on the performance of machining ductile materials, ceramics and composites. However, the AWJ machining of fiber metal laminates is seldom studied due to the complexity of cutting process. Few research groups [23,29] have studied the material removal process and quantified the effect of operating parameters on AWJ machining of Glass fiber-Aluminum laminates (GLARE). But the work is limited to machining of thin laminates (≤ 2.5

mm). Also, there is a lack of investigation towards the effect of all major process parameters with special reference to 2-D shape contouring.

Machining of TiGr is different from Glass/Aluminum laminates due to the presence of difficult-to-cut Titanium. AWJ machining of thin TiGr laminate sheets (~1 mm) has been studied in the past but involves the effect of only two parameters on the machinability [30]. In addition, no studies on AWJ contouring and profile cutting of thick Titanium/graphite laminates (>7.5 mm) have been performed to date. An evident need exists for a systematic AWJ machining evaluation and characterization of thick TiGr laminates, especially with thermoplastic matrix composite.

1.2 OBJECTIVES

The overall goal of the current work is to study the feasibility of thick Titanium/Graphite contouring or profile cutting using Abrasive Waterjet machining in the context of industrial employability for desirable dimensional tolerances.

The objectives of this research study include:

1. Study the feasibility and AWJ machinability of ~7.5-10.5 mm thick, thermoplastic based TiGr laminates. Abrasive waterjet machinability evaluation in terms of kerf characteristics namely kerf geometry (taper) and surface characteristics, and any possible jet induced damage.
2. Assess the effect of process variables - geometric variables (mixing tube length, diameter and orifice bore size), water pressure, load ratio and traverse speed on the kerf characteristics for different sized profile features of cutting geometry.
3. Develop empirical and semi-analytical models to predict the kerf response based on the results of aforementioned findings.

Chapter 2. LITERATURE REVIEW

2.1 FIBER METAL LAMINATES

Hybrid composite laminates, also known as FML (Fiber Metal laminates) is a group of engineered materials with alternate layers of composite and monolithic metal as a material system. The laminates are specifically designed to meet the high temperature and high strength to weight requirements of modern age aircraft structures. Figure 2.1 illustrates a $(Ti/90/Ti/0)_s$ Titanium/Graphite Fiber metal laminate material system.

The directionality of composites enhances the mechanical strength to weight ratio in a given loading direction. This mechanical strength is generally in terms of hardness, fatigue and fracture characteristics. Besides, Impact damage is a relevant type of damage evaluation for aircraft structures caused by runway debris, hail, maintenance damage (i.e. dropped tools), collision between service cars or cargo and the structure, bird strikes, ice from propellers striking the fuselage, engine debris.

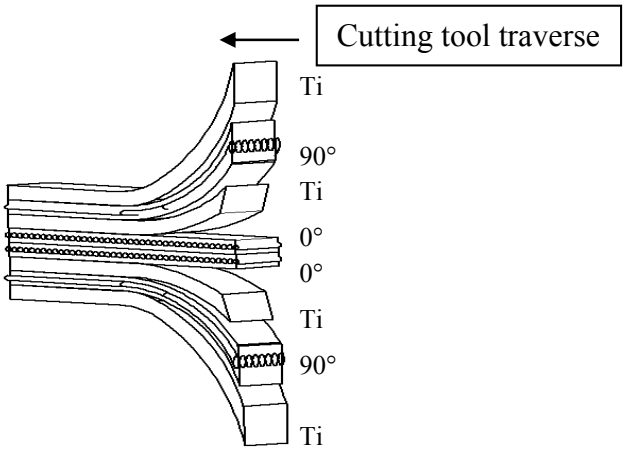

Figure 2.1. Fiber Metal Laminate – Titanium/Graphite $(Ti/90/Ti/0)_s$

Fiber Metal laminates find numerous applications, especially in aerospace industry such as lower wing panels of Fokker F-27, Boeing C-17 cargo doors (Figure 1.1). The three phase system of TiGr underscores the load bearing capacity of mechanical bolted and riveted structures [31]. Aluminum, steel and Titanium based FMLs are widely studied and employed in marine applications [32].

2.1.1 Development of Fiber Metal Laminates

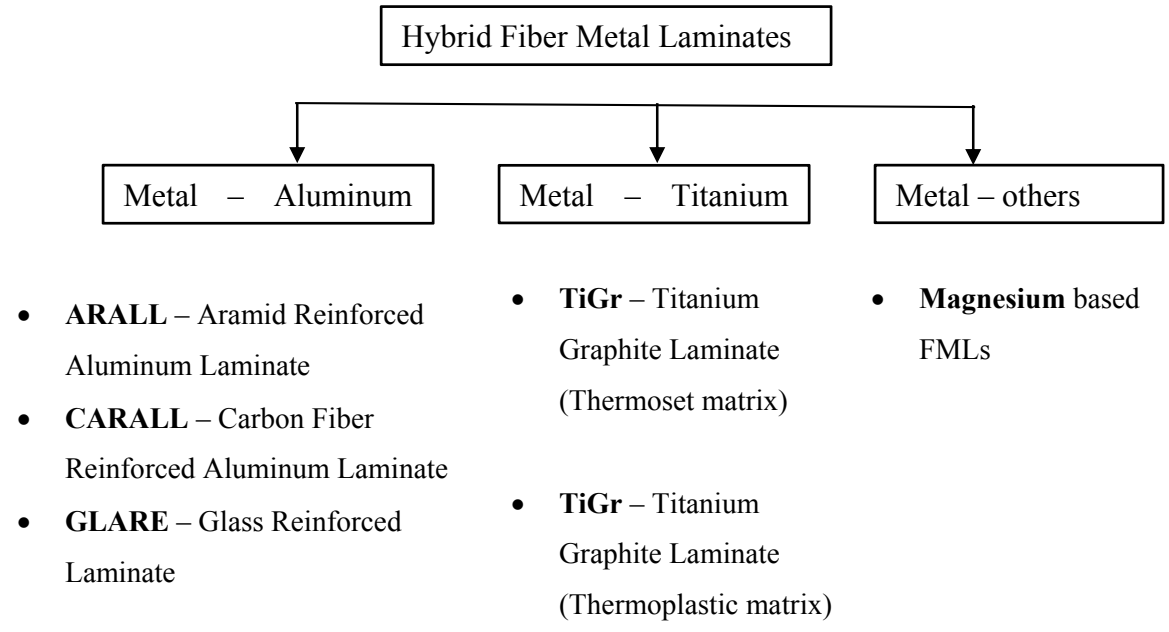

Figure 2.2. Classification of Fiber Metal Laminates

One of the rare positives of World War II was the applicatory growth of technology towards development of advanced materials for aircraft structures allowing low strength to weight ratio and enhanced integrity, especially fracture and fatigue characteristics. This stirred a domain of research in adhesively bonded aluminum panels for employability in Fokker F-27 turboprop aircraft, a 1945 post-war outcome. The bonded aluminum structures were diversified by the joint effort of Delft University of Technology and National Aerospace Laboratory, Netherlands. Figure 2.3(a) shows the bonded aluminum Fokker F-27 wing structure. Better fatigue properties were observed by replacing adhesive with composite layers.

The development of ARALL® (Aramid Aluminum Laminate) marked the era of bonded structure as a new material system. It consisted of high strength aramid fiber provided by AKZO® infused in 3M®'s thermoset epoxy matrix interleaved between thin 7075 and 2024 aluminum plies (ALCOA). ARALL® led to subsequent diversification into different grades viz, ARALL® 1-4. The use of structural Aramid fibers in laminate didn't compromise with the advantages rendered by

metals such as near isotropic stiffness, plasticity, impact strength and formability. The employability of ARALL® was widely explored as z-stiffeners in pressure cabins, fuselage and fatigue sensitive lower wings of aircrafts with design strain levels nearly 33-50% higher than those of monolithic aluminum parts [33].

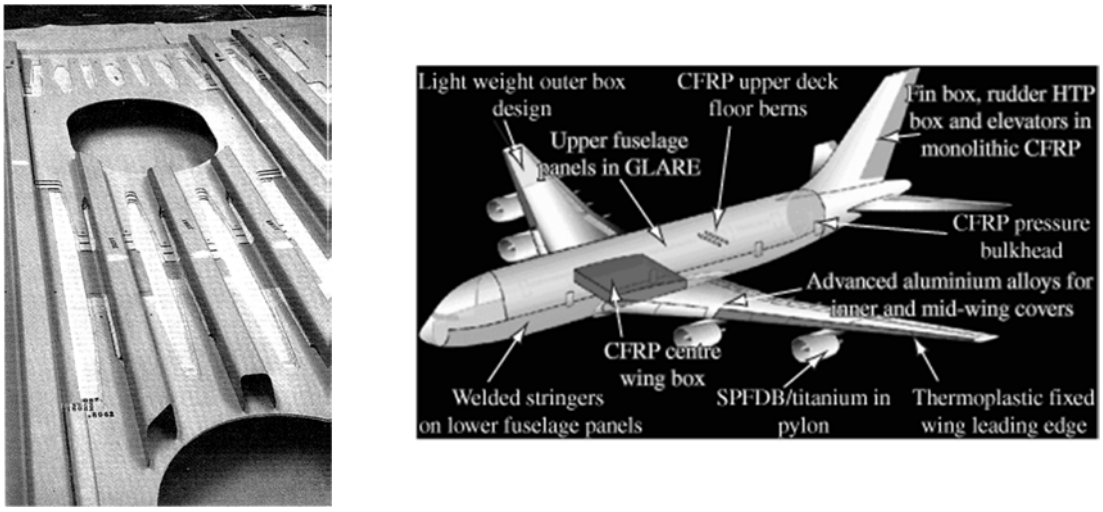

(a) (b)

Figure 2.3. (a) Bonded Metal wing structure of Fokker F-27 [34], and (b) Material application in Airbus A380 [3]

The next stage in the development of Fiber metal laminate witnessed the development of GLARE® (Glass Reinforced) Laminate or ARALL with Glass fibers. The skepticism of The Boeing Company about disbonding and possible fiber failure in using ARALL for fatigue critical structures was subsided with the much superior qualities of GLARE. GLARE offers superior adhesion between the fibers, higher compressive and tensile strength, strain to failure, residual strength, better impact behavior and enhanced compatibility among fibers to resist biaxial stress state. Glare is widely employed in Airbus A380 in the pressurized fuselage's upper and lateral shells, on the stabilizers' leading edges, leading up to 15% savings in overall operating cost just by the employment of advanced materials [1].

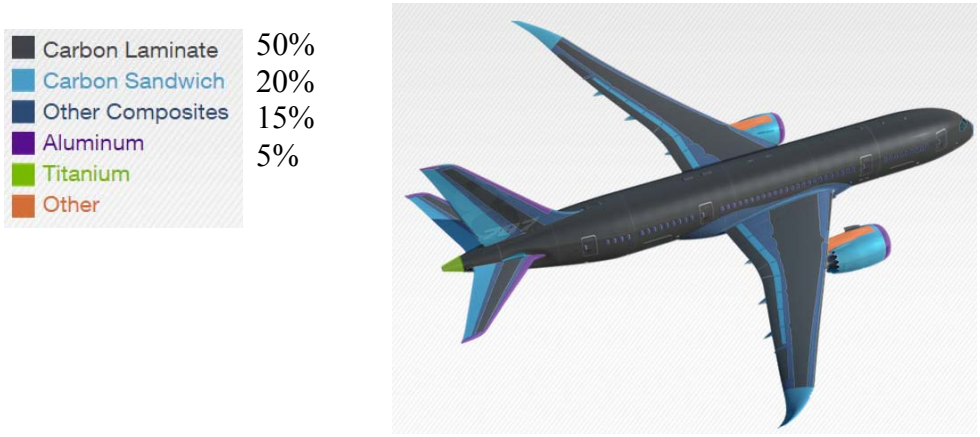

Figure 2.4. Materials application in Boeing 787 commercial aircraft [35].

Early 1970s marked the progressive development and implementation of Fracture mechanics into the real world structural components. Owing to criticality of fatigue properties, as realized through several catastrophic accidents, Federal Airworthiness Regulations became more stringent for aircraft structures. New design philosophy of damage tolerance required fatigue behavior and crack propagation as a major criteria for design evaluation of aerospace structures. In order to meet not only the damage tolerance but also high temperature requirements, TiGr (Titanium Graphite composite) was developed jointly by NASA Langley Research Center and The Boeing Company as a part of sonic cruiser development.

2.1.2 Advantages of Fiber Metal Laminates

Fiber metal laminates are found to exhibit fatigue properties superior to their monolithic counterparts, but with delamination as the dominant mode of damage, amounting to stiffness reduction [12]. The crack growth rate in hybrid composite laminates is steadier in comparison to the monolithic metals [36]. In general, monolithic metals when subjected to constant stress amplitude loading, have increased crack growth rate as the crack propagates. However, in a composite-metal material system, the crack growth rate is stable for more time due to bridging properties of composite plies as the ply-by ply failure of Titanium foils require re-initiation of crack at each Titanium-composite interface. Several studies show 10-30% increase in fatigue endurance strength when compared to properties of monolithic metals [37]. Also, furtherance of

fatigue properties of TiGr at elevated temperature (350^{o} F) has been observed due to reduction in interlaminate residual stress and increased toughness of titanium plies at elevated temperature. The fracture toughness of the laminated TiGr plate has been reported as high as 39% with 20% decrease in crack growth rate when compared to monolithic plate. A study reveals the damage tolerance life of the surface cracked TiGr laminate to be 6 to 15 times the life of a monolithic specimen [38].

Depending upon the stacking sequence, processing conditions and residual stress, FML offer high tensile strength to weight and stiffness to weight ratio [39,40]. Owing to high energy absorption characteristic of composites, FML exhibit high toughness and high velocity impact resistance when compared to monolithic metals. However, among the established Fiber Metal Laminates, although the Titanium based FMLs are superior to glass fiber based FMLs (GLARE) in terms of static strength, and fatigue properties; the high and low velocity impact strength is lower on account of low ductility of Titanium alloy [41].

TiGr offers good bearing strength and coupling stiffness which explains its high suitability for bolted joints. Besides offering high structural coupling efficiency, TiGr accounts for low sensitivity of the mechanical properties to the laminate configuration and environmental effects [31,42,43]. Fink et al. [44] studied the industrial manufacturability of TiGr spacecraft payload adaptor (Figure 2.5) and verified enhanced bearing, shear and pull-out strength capabilities using titanium reinforcement in CFRP composite laminates. Nearly 100% improvement in bolt bearing rupture load was observed with 37% titanium content.

(a) (b)

Figure 2.5. Payload adaptor (a) During fiber placement, (b) Final product after trimming [44]

The conventional use of thermosetting matrix based FMLs is being replaced by thermoplastic based FMLs to overcome the limitations of thermoset based FMLs such as inferior interlaminar fracture toughness, long processing cycles and poor reparability. Besides, thermoplastic based FMLs provide added advantages of improved chemical resistance and formability. Owing to the future potential and utility the present investigation studies the AWJ machining behavior on thermoplastic based Titanium-Graphite FML.

2.2 ABRASIVE WATERJET MACHINING PROCESS

The concept of using water as a cutting tool can be dated back to Chinese prehistoric times where the archaeological remnants suggest the use of erosive action of continuously flowing water droplets in carving the rocks. With the advance of time, more methods were developed to focus the cutting energy and thus increase the jet power. From low pressure applications (<100 MPa) such as mining coal to high pressure applications (>600 MPa) such as cutting soft industrial materials, the methods to increase water power were developed over time.

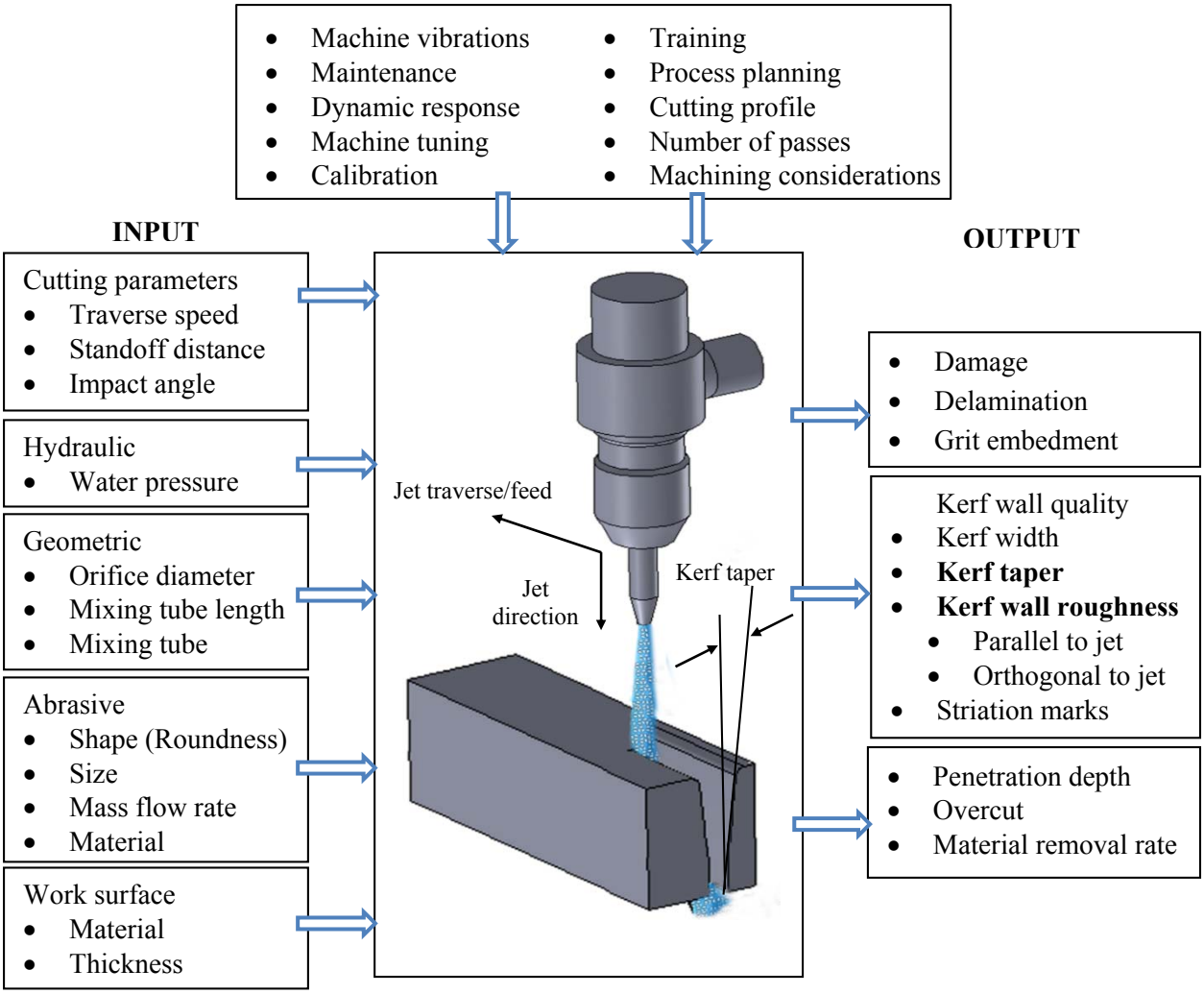

Figure 2.6. Abrasive Water Jet process parameters and typical machining response

One of the most important ways to focus the kinetic energy was developed and diversified by Dr. Hashish in 1979, when he added sharp abrasive particles to high pressure water. The process soon became an indispensable asset for machining applications.

Abrasive waterjet is a cutting technology based on collimating high energy water-abrasive slurry and using this focused beam to erode the work material either by shearing or failure due to localized stress field [28,45,46]. The layout of input and output factors of the AWJ process is depicted in Figure 2.6.

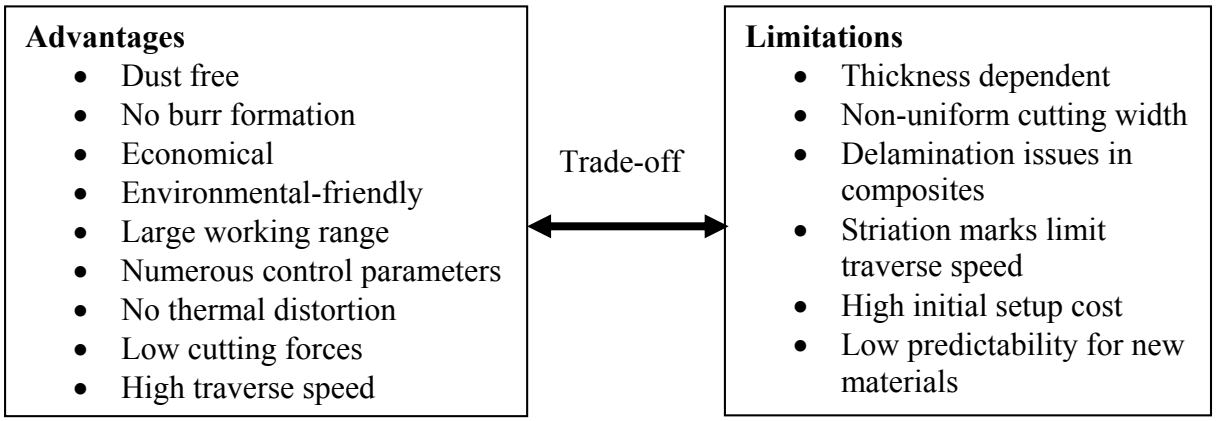

Figure 2.7. Advantages and limitations associated with Abrasive Waterjet Machining Technology

As discussed in section 1.1, Abrasive waterjet technology offers several advantages over other conventional and non-conventional machining technologies. The process is gaining popularity in several areas such as medical, aerospace, automotive, marine, oil, mining industries. Figure 2.7 tabulates the advantages and limitations of the same emphasizing the economic, social and environmental sustainability of the process [47].

The increased expanse of engineering scenarios have led to development of advanced materials whose performance is highly sensitive to the machining process, limiting the employment of unconventional processes. Heat sensitive materials such as semiconductors, high strength aerospace materials such as titanium alloys, anisotropic composites and fiber metal laminates, precision specific micro-components for medical applications, et cetera have distinct requirements pertaining to different definitions and measures of machining quality function. Although

Waterjetting is being researched and developed as a universal machining technology, the process has its own challenges and limitations.

With reference to process principles and characteristics, the high jet energy, expended in eroding the material, degenerates during the interaction process. This loss in energy is a function of available jet energy and jet-material interaction characteristics. As apparent from the physics of the process, the resisted energy affects the achievable jet penetration depth for a given material. Besides, the quality of the surface is degraded which is often assessed by kerf characteristics. The kerf taper induced during the jet penetration pass can either be convex, concave or straight. The jet trailback apparent from the striated marks is prominent at jet exit side due to insufficient cutting energy [48] and often characterized by surface roughness.

2.2.1 Machine description

Broadly, Abrasive waterjet machine consists of four major parts- (1) Pressure generation system, (2) Abrasive feed system, (3) Cutting head, (4) Catcher. Figure 3.1 depicts the components of Abrasive waterjet system.

As apparent from the name, the task of pressure generation system is to generate and continuously deliver high pressure water supply to subsequent components in the system. Higher water pressure is generally a desirable feature to improve cutting efficiency by collimating the jet energy. However, the employability of high pressures is limited by the strength and wear response of other components, and also the phase transition of water to ice at pressures above 894 MPa [49].

Pressures up to 700 MPa are achievable for industrial applications. This is generally achieved by using a crankshaft based positive displacement pumps for low pressure to mid pressure range – 100-300 MPa, and intensifiers for high and ultra-high pressure >300 MPa. Multiple cylinder intensifiers are used to maintain quasi-continuous water flow.

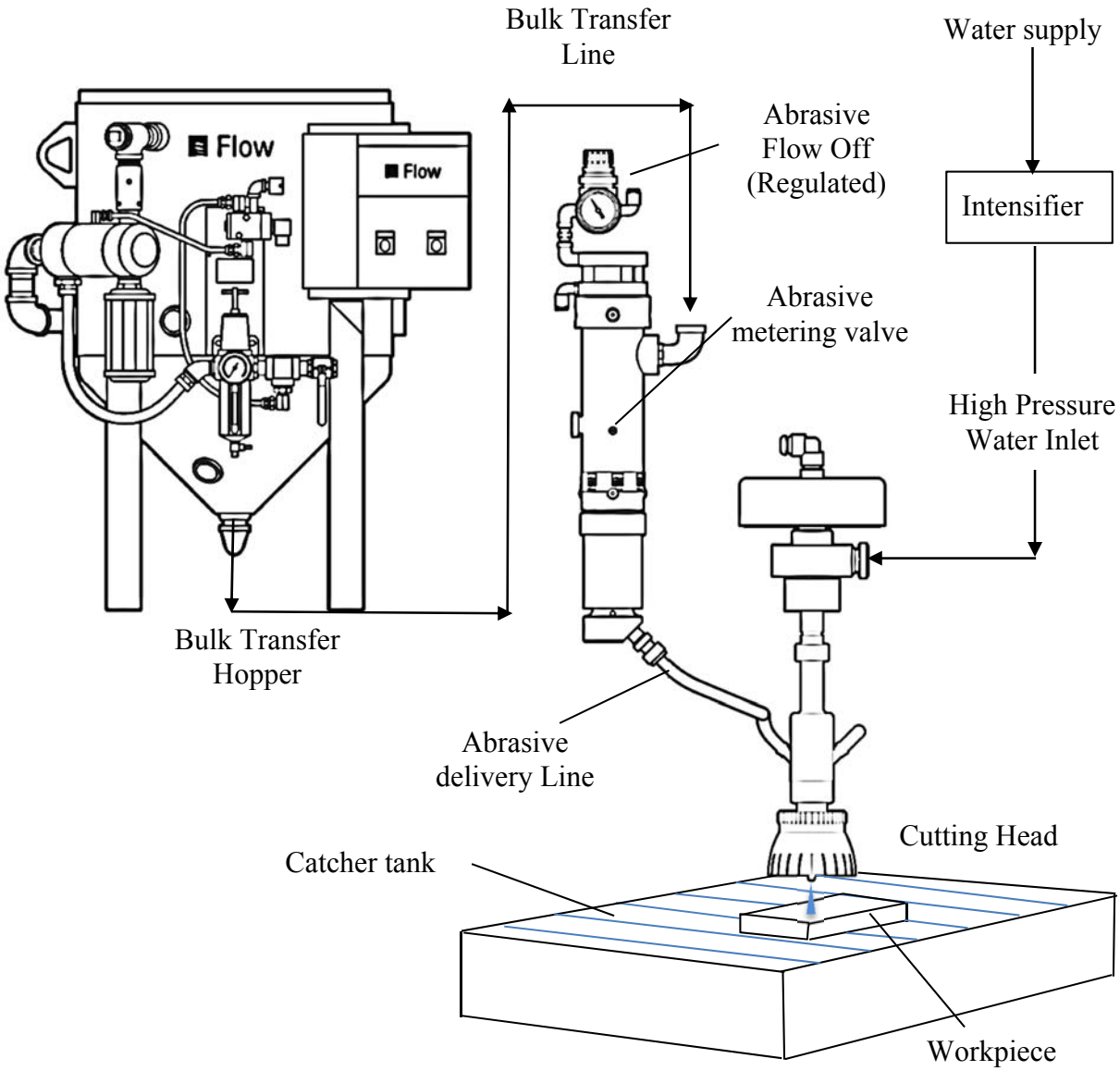

Figure 2.8. Schematic of Abrasive Waterjet machining system.

The Abrasive feed system generally consists of a bulk storage tank (abrasive hopper) and a temporary storage device to isolate dynamic instability caused due to high mass of abrasives near the cutting head. The abrasive hopper transfers the abrasives to metering section of the local storage near cutting head through an abrasion resistant hose under the action of low pressure

compressed air. The metering system is designed to isolate abrasives from air and maintain a constant (desired) abrasive flow rate at different pressures.

The cutting head receives high pressure water which enters mixing chamber through an orifice. The abrasives enter the chamber at a specified constant flow rate through a delivery line. The mixed water-abrasive slurry passes through a replaceable mixing tube or nozzle, where the momentum is transferred among the mixture phases, majorly – water and abrasives.

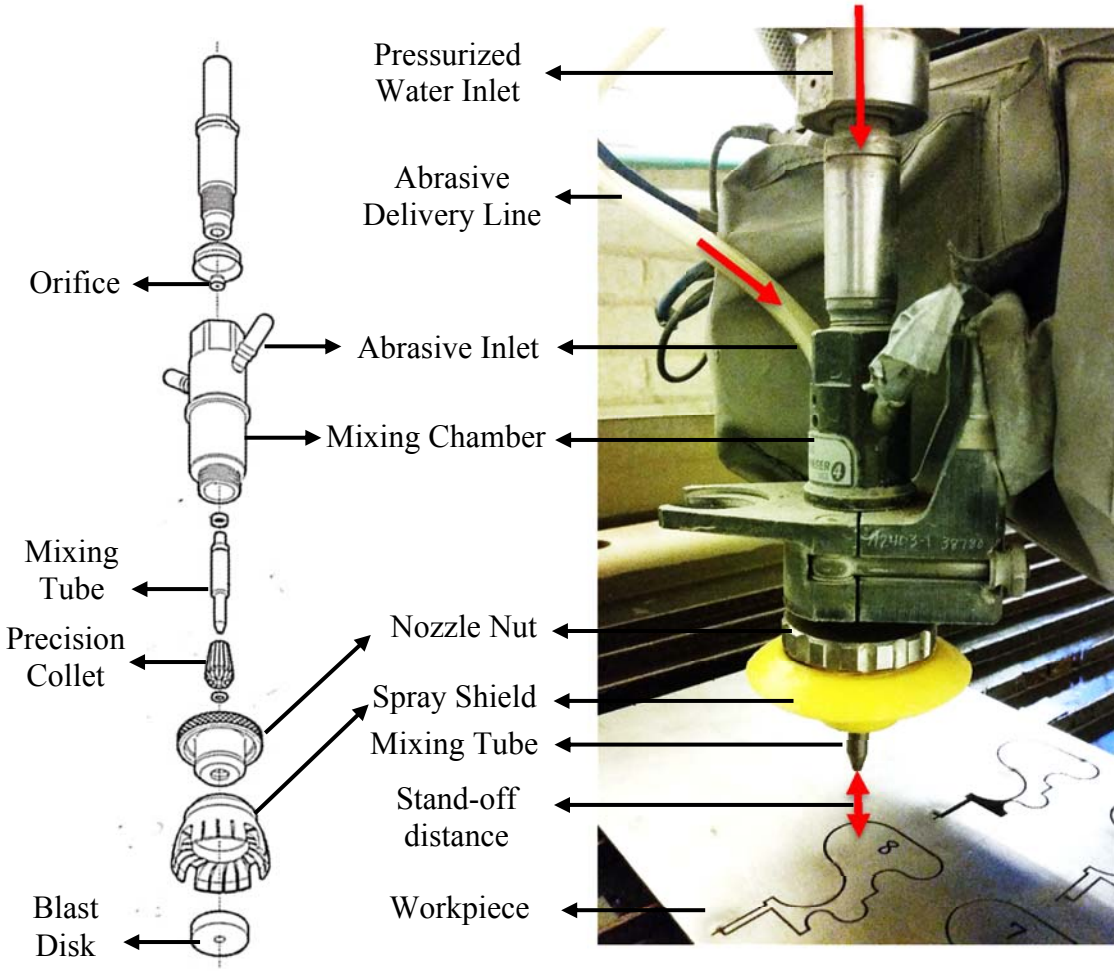

Figure 2.9. Cutting head assembly

The cutting head assembly, also known as jet former, is depicted in Figure 2.9 shows the formation process of high energy water-abrasive slurry which is obtained at the end of mixing tube. In order to form high velocity slurry jet, abrasives can either be entrained in to the high velocity water

stream or premixed and fed to a collimating tube (Abrasive suspension jet). However, for most industrial applications former technology is widely used and the same is used in this study.

The high pressure water entering the cutting head is controlled by an on/off valve. The sapphire orifice converts the available pressure energy into useful kinetic energy which enters the mixing chamber. The high velocity water stream passing through the chamber creates a partial negative pressure, which sucks the abrasives from the metering system. Sometimes, low water pressures requires an additional vacuum assist to maintain the required abrasive flow rate into the mixing chamber. Momentum is transferred between the water and abrasives at this stage. The mixture then passes through a tungsten-carbide mixing tube whose geometry is critical to mixing efficiency and energy component of the mixture constituents. In nutshell, the nozzle dimensions decide the coherency of the jet. The high energy jet impinges the work surface resting above a catcher tank which receives the residual exit jet mixture along with the debris. The catcher tank is sometimes filled with ceramic balls to dissipate the exit jet energy.

Orifice diameter

The role of orifice is to convert high pressure energy of water (hydraulic energy) to kinetic energy. It is generally composed of sapphire, ruby or diamond, and mounted on a high grade steel using a retainer ring as shown in Figure 2.10.

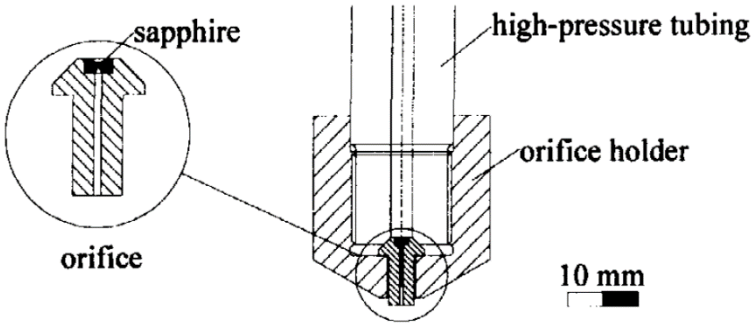

Figure 2.10. Construction of a typical orifice assembly [29]

Typically orifice diameter ranges from 0.25 for high pressure cutting to 0.4 mm for low pressure cleaning applications. Orifice diameter influences the material removal process by altering the water flow rate and jet-momentum. As depicted in Figure 2.11(a), large orifice contributes to

greater water flow rate and momentum transfer capability between water and abrasive particles, leading to enhanced cutting ability of final jet [50]. The increased energy of the jet with orifice diameter is apparent from previous investigations by Paul et al. [23] and observed by Hashish [50], as shown in Figure 2.11(b).

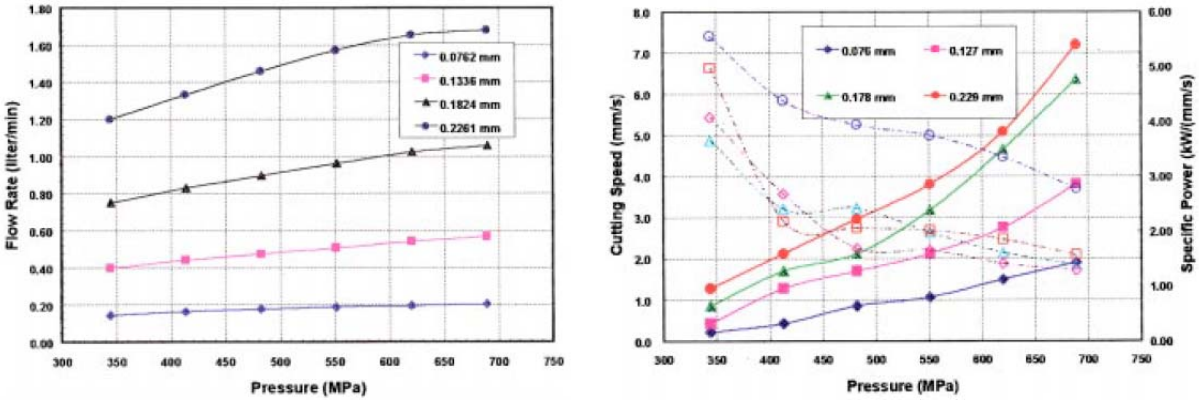

(a) (b)

Figure 2.11. (a) Effect of pressure on flow rate observed for different orifice diameter, (b) Effect of pressure on specific power of jet and cutting speed observed for different orifice diameter [50].

However, many investigators have argued that jet power and overall cutting performance decreases when large orifice diameter is used due to insufficient jet momentum to accelerate the abrasive particles [51,52] . This suggest an optimum orifice diameter (generally ~3 times mixing tube diameter) for the formation of a coherent jet with high particle velocity [53].

Mixing tube geometry

Mixing tube diameter (dm) plays a dominant role in coherency and cutting efficiency of the jet. However, contrasting results have been reported by researchers about its effect on machining quality. On one hand, small mixing tube diameter increases the slurry density and average particle velocity by more effective momentum transfer. The reasoning is backed up by large air entrainment at larger mixing tube diameter leading to high turbulence. On the other hand, small mixing tube diameter leads to high amount of collision, particle fragmentation and friction during the mixing process. It is reasonable to conclude that the discrepancies in the literature is

due to the possible interaction effect of orifice diameter with other process parameters, and the material properties and thickness.

Mixing tube length (lm) is another important aspect to determine the jet coherency. After the initial mixing of abrasives and water in mixing chamber, the momentum transfer and particle acceleration takes place over a certain distance, beyond which the drag friction and collision loss have the negative effect on abrasive velocity. This suggests an optimum length for each machining condition for a given material. Prior investigations reveal that longer mixing tube is required for large and dense abrasive particles due to increase in acceleration distance. Besides, high pump pressure requires longer mixing tube to fully exploit the high power waterjet in accelerating the particles. General trends also shows low small mixing tube requirement for high abrasive flow rate due to increased interaction during mixing process [54]. Studies suggest an optimum length (lm) to diameter (dm) ratio of 25-50 for practical use.

$$\frac{l_m}{d_m} \approx 25-50 \tag{2.1}$$

The cutting efficiency is dependent on the amount water energy being transferred to the abrasives. In ductile materials, the abrasive energy is dominant in the jet-material interaction process, whereas the significance of water energy component is higher in composite machining. It can be construed that the nozzle geometry influences the energy component and its optimization is required on the basis of jet-material interaction characteristics.

2.2.2 Analytical Models

2.2.2.1 Finnie's model

The study of solid particle interaction can be dated back to late 1950s when Finnie investigated and analytically related the behavior of single abrasive particle in predicting the erosion mechanism of ductile materials [55,56]. Figure 2.12(a) and (b) illustrates the particle striking the workpiece at an angle α. When the impact angle $\alpha \leq \alpha_c$, the abrasive particle strikes the surface in a near parallel direction. The orthogonal reaction force acting on the abrasive assists in pushing the particle outward along with the micro-chipping of the workpiece material, leaving a crater on the surface. The model assumes a constant ratio (K) between the horizontal and vertical force experienced by the particle which implies a constant average contact stress throughout the erosive action. Further, the model also assumes a constant particle width (b) and the material plastically deforms immediately after the contact (elastic stress is negligible).

Finnie determined the weight of material removed from the erosion by using the equations of motion given by equation (2.2).

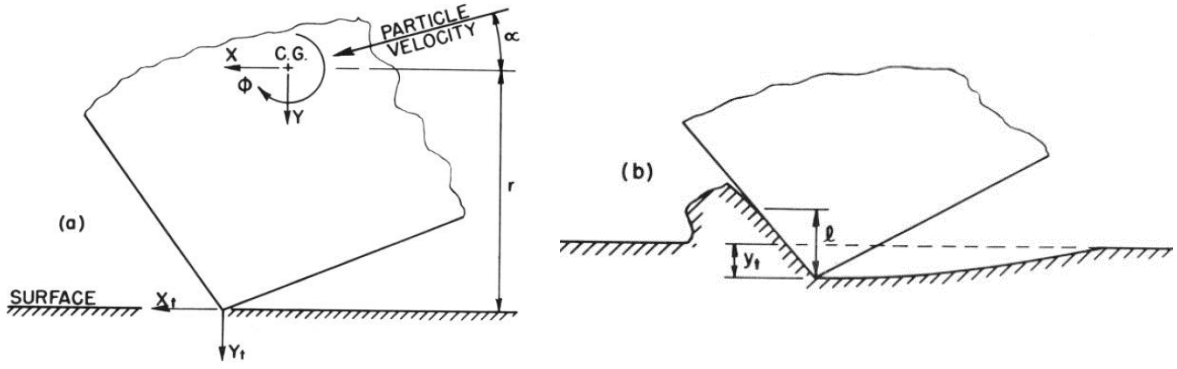

Figure 2.12. (a) Particle striking the workpiece, and (b) Particle eroding the workpiece [55]

The equations of motion can be written as

$$m\ddot{y} + pK\Psi by = 0$$
$$m\ddot{x} + pK\Psi by = 0$$
$$I\ddot{\phi} + p\Psi bry = 0$$

m = Particle mass
I = Mass moment of inertia
r = Distance from the center to the particle edge
$\Psi = l / y_t$
p = Flow stress (Horizontal component)
b = Particle width
$K = F_{Vertical} / F_{Horizontal}$

(2.2)

Using the boundary conditions and initial values given by equation, equation (2.3) can be solved for x, y and φ.

$$x(t=0) = 0$$
$$y(t=0) = 0$$
$$\dot{x}(t) = V\cos\alpha$$
$$\dot{y}(t) = V\sin\alpha$$
$$\dot{\phi}(t=0) = \phi_0$$

(2.3)

$$y = \left(\frac{V\sin\alpha}{\beta}\right)\sin\beta t$$
$$x = \left(\frac{V\sin\alpha}{\beta K}\right)\sin\beta t + (V\cos\alpha)t - \left(\frac{V\sin\alpha}{K}\right)t$$
$$\phi = \left(\frac{mrV\sin\alpha}{\beta KI}\right)(\sin\beta t - \beta t) + \dot{\phi}_0 t$$

(2.4)

Now, the weight (w) of material removed by each particle can be determined by equation (2.5).

$$w = \rho b\int_0^{t_c} y_t dx_t = \rho b\int_0^{t_c} y d(x + r\phi)$$

(2.5)

The overall weight of material removed (W) is a superposition of the contribution of material removed by each particle.

$$W = \left(\frac{\rho}{p\phi}\frac{MV^2}{K}\right)\left(\sin 2\alpha - \frac{6}{K}\sin^2\alpha\right) \quad \text{for } \tan\alpha \le K/6$$
$$W = \left(\frac{\rho}{p\phi}\frac{MV^2}{K}\right)\left(\frac{K\cos^2\alpha}{6}\right) \quad \text{for } \tan\alpha > K/6 \qquad (2.6)$$

M = Total mass of the abrasives
W = Total weight of workpiece removed by abrasives

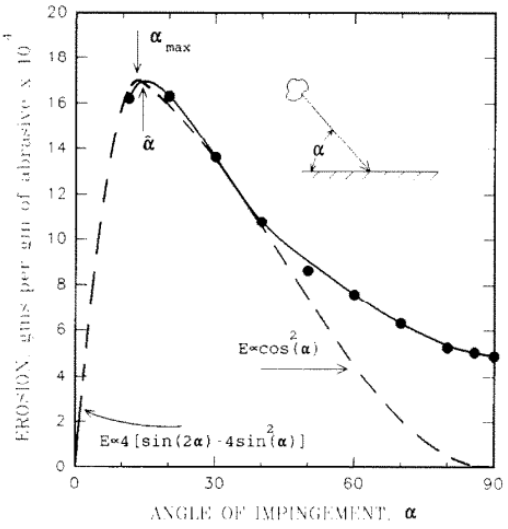

Figure 2.13. Dependence of erosion (gm/gm) on the angle of impingement of abrasive particles [56]

The model prediction was coeval with the experimentally measured data at low angle of attack, as depicted in Figure 2.13. However, at higher attack angle where the particle strikes the workpiece in near orthogonal direction (with respect to impinging flat surface), the abrasive embeds into the workpiece after plastically deforming it. This results in culmination of the erosion process with deep crater formation. The model significantly underestimates the workpiece erosion limiting the use of this model due to unaccountability of the effect of cold working and roughening by the preceding impacts of large number of abrasives, which is expected to be higher at α = 90°. In

addition the flow stress measurement is problematic and mostly an estimated value with low reproducibility at good accuracy.

2.2.2.2 Bitter model

Bitter, while working in the field of wear of pipelines and components transporting slurry, developed new relations to predict material erosion by solid impacts of abrasives entrained in fluid at high impact angles [57]. The model assumed the wear of transport lines as a combined effect of repeated deformation and cutting action of spherically idealized abrasives. Bitter illustrated that the material undergoes deformation wear at large angles of impingement and neglected the strain hardening due to deformation caused by the abrasives. An idealized elastic-plastic collision was used to determine the energy transferred by the colliding abrasive particle. The colliding particle was assumed to deform elastically while work surface was assumed to experience elastic-plastic deformation.

The elastic deformation caused by the abrasive collision introduces a reactive pullout force on the abrasive particle with a further increase in its energy. The overall plastic energy transmitted during collision is determined by equations (2.7).

$$
\begin{aligned}
&E_P = \frac{1}{2} m\ (V \sin\alpha - V_{el})^2 \\
&m = \text{mass of abrasive particle} \\
&V = \text{Abrasive velocity before collision} \\
&V_{el} = \text{Abrasive velocity just after elatic limit is reached}
\end{aligned}
\tag{2.7}
$$

The abrasive velocity at the elastic limit (critical impact velocity) is given by equation (2.8)

$$
\begin{aligned}
&V_{el} = \frac{\pi^2}{2\sqrt{10}} \sigma_y{}^{2.5} \sqrt{\frac{1}{\rho_{abr}}} \left(\frac{1-\nu_1^2}{E_1} + \frac{1-\nu_2^2}{E_2} \right)^2 \\
&\sigma_y = \text{elatic load limit} \\
&\rho_{abr} = \text{abrasive density} \\
&\nu_1, \nu_2 = \text{Poisson's ratio of spherical abrasive and impacted flat body} \\
&E_1, E_2 = \text{Young's modulus of spherical abrasive and impacted flat body}
\end{aligned}
\tag{2.8}
$$

The volume of material removed by the deformation wear is assumed to be proportional to the amount of plastic energy introduced in the material and given by equation (2.9) where ε is the specific deformation energy of the material being impacted at large attack angles.

$$W_D = \frac{\frac{1}{2}M[V\sin\alpha - V_{el}]}{\varepsilon}, \text{ if } V\sin\alpha \geq V_{el}$$
$$\varepsilon = \text{Deformation wear factor} \tag{2.9}$$

For small attack angles, the material is elastically deformed and cutting wear dominates. Bitter derived the following equations for cutting wear

$$W_{c1} = \frac{2MC(V\sin\alpha - V_{el})^2}{\sqrt{V\sin\alpha}}\left(V\cos\alpha - \frac{C(V\sin\alpha - V_{el})^2}{\sqrt{V\sin\alpha}}E_{ab}\right), \text{ if } \alpha \leq \alpha_0$$
$$W_{c2} = \frac{M}{2E_{ab}}\left(V^2\cos^2\alpha - V_1\left(V\sin\alpha - V_{el}\right)^{1.5}\right), \text{ if } \alpha > \alpha_0$$

$$M = \text{Combined mass of all abrasives impacting the surface}$$
$$E_{ab} = \text{Energy absorbed in collision process} \tag{2.10}$$
$$V_1 = 0.82\sigma_y{}^2\left(\frac{\sigma_y}{\rho_{abr}}\right)^{0.25}\left(\frac{1-\nu_1^2}{E_1} + \frac{1-\nu_2^2}{E_2}\right)^2$$
$$C = \frac{0.288}{\sigma_y}\left(\frac{\rho_{abr}}{\sigma_y}\right)^{0.25}$$

Deformation wear is prominent in brittle materials whereas cutting wear in ductile materials. However, the combined effect of deformation and cutting wear mechanism can be utilized to determine the overall material removed in any material randomly impacted by abrasives entrained in fluid medium.

$$W = \underbrace{W_D}_{\text{Deformation wear}} + \underbrace{W_{c1/c2}}_{\text{Cutting wear}} \tag{2.11}$$

Bitter model showed a good agreement with the experimentally measured results as depicted in Figure 2.14.

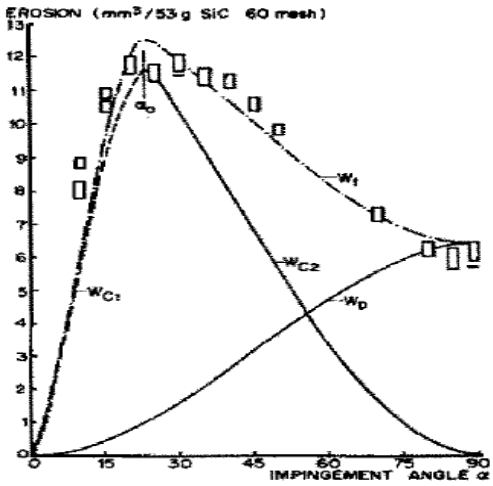

Figure 2.14. Model verification – Erosion of SAE 1055 steel with particle velocity: 107 m/s, Abrasives: silicon carbides (60 mesh) [57]

Although Bitter model addresses the shortcomings of Finnie's model in predicting erosion, it requires determination of critical impact velocity and deformation wear factor, which needs to be experimentally determined for the desired combination of abrasives and workpiece material.

2.2.2.3 Hashish's model

Hashish adopted the fundamental models developed by Bitter and Finnie to predict the maximum possible depth of cut as a function of AWJ process parameters. The developed model assumes a small, acute initial impingement angle when jet enters the work surface, resulting in cutting wear. The lower part of the work material experiences deformation wear due to high impact angle of the jet abrasives. Under assumptions of (1) negligible effect of through-the-thickness particle velocity variation, (2) negligible effect of jet spreading and hydrodynamic loading on micro-erosion process, and (3) uniform abrasive distribution over the cross-section, the maximum possible cutting depth was determined in each of the wear modes – cutting wear and deformation wear. The total predicted cutting depth can be determined using as the summation of cutting and deformation depths (equation (2.12)).

$$h_{\max} = \underbrace{h_c}_{\substack{\text{Cutting wear depth} \\ \text{(Low impact angle)}}} + \underbrace{h_d}_{\substack{\text{Deformation wear depth} \\ \text{(High impact angle)}}} \tag{2.12}$$

Cutting wear mode

Hashish assumed the material removal in cutting wear as a steady state erosion process. The model assumes that the jet impinges the work surface at a shallow impact angle $\alpha = \alpha_0$ and the cutting modes ceases to exist when impact angle reaches α_t. Local impact angle of abrasive particles is assumed to be in equilibrium with the material removal throughout the cutting depth.

The material removal rate derived by Finnie for shallow impact angles is given by equation (2.13)

.

$$\delta\dot{v} = \frac{7}{\pi}\frac{d\dot{m}}{\rho_{abr}}\left(\frac{V}{C_k}\right)^{2.5} \sin 2\alpha\sqrt{\sin\alpha}$$

$$C_k = \sqrt{\frac{3\sigma R_f^{\,3/5}}{\rho_{abr}}} \qquad (2.13)$$

C_k = Characteristic velocity
σ = Material flow stress
R_f = Particle roundness factor
$d\dot{m}$ = mass flow rate of abrasive
α = Particle impingement / jet deflection angle
ρ_{abr} = Abrasive particle density
$V = \eta\frac{v_w}{1+R}$
v_w = water velocity
R = loading ratio

Under steady state condition, the erosion rate can be related to jet kinetics (assuming a rectangular cross-section of cut) by equation (2.14).

$$\delta\dot{v} = dh\ u\ d_j \qquad (2.14)$$

The equation assumes uniform width of cut (d_j) throughout the penetration depth h. Upon using the linear dependence of jet deflection angle as a function of jet traverse position (equation (2.15)

) and assuming only a fraction C of the jet diameter contributes to the cutting wear, depth of cut can be integrated by equating equations (2.14) and (2.16).

$$\alpha = \alpha_t \left(1 - \frac{x}{Cd_j}\right)$$
$$\text{where } C = 1 - \frac{\alpha_t}{\alpha_0} \tag{2.15}$$

$$\frac{h_c}{d_j} = \frac{2}{5}\left(\frac{14\dot{m}}{\pi\rho_{abr} u d_j^{\,2}}\right)^{2/5}\left(\frac{V_0}{C_k}\right) - \frac{2}{5\alpha_0} \tag{2.16}$$

The kerf wall drag effect can be incorporated by using momentum balance across a control volume and ignoring the effective mass flow rate of the air. Besides, the effect of threshold velocity provided by Finnie's model was incorporated by Hashish with final cutting depth of cut given by equation (2.17).

$$h_c = \frac{Cd_j}{2.5}\left(\frac{14\dot{m}}{\pi\rho_{abr} u d_j^{\,2}}\right)^{2/5}\left(\frac{V_0}{C_k}\right) \tag{2.17}$$

$$h_c = \frac{\left(\frac{V_0}{C_k}\right) d_j}{\left(\frac{\pi\rho_{abr} u d_j^{\,2}}{14\dot{m}}\right)^{2/5} + \left(\frac{V_e}{C_k}\right)} \text{ (incorporating threshold velocity effect)} \tag{2.18}$$

V_e = Threshold velocity of jet to erode in cutting mode
such that $V_0 \sin\alpha_t \geq Ve$

Limitations

The model is based on several assumptions which makes it unclear while relating the local phenomenon to the global erosion process. While using momentum balance to incorporate frictional drag forces, the momentum interaction due to cutting action on the wall is not incorporated in the model. The abrasive distribution and jet velocity is assumed to be a uniform through the cross-section which is likely to be an unreasonable assumption due to possible high

velocity gradient from center to the jet boundary, as substantiated by the knowledge of kerf drag in fluid medium.

Deformation wear mode

To calculate depth of cut in deformation mode, Hashish utilized Bitter's model

$$\delta\dot{v} = \frac{\frac{1}{2}\dot{m}[V\sin\alpha - V_e]}{\sigma}, \text{ if } V\sin\alpha \geq V_e \tag{2.19}$$

Macroscopically, the material removal rate can be written as equation (2.20).

$$\delta\dot{v} = \frac{\pi}{4} d_j^{\,2} \frac{dh}{dt} \tag{2.20}$$

Equating equation (2.19) and (2.20), and assuming the fraction of jet diameter unused in cutting erosion mode (1-C) contributes towards deformation wear, depth of cut can be determined as given by equation (2.21).

$$h_d = \frac{1}{\frac{\pi d_j \sigma u}{2(1-C)\dot{m}(V_0 - V_e)^2} + \frac{C_f}{d_j}\frac{V_0}{(V_0 - V_e)}}$$

$$\text{where } C_f = \text{Coefficient of frictional drag} \tag{2.21}$$

The maximum possible depth is given as

$$h = h_c + h_d$$

$$h = \frac{Cd_j}{2.5}\left(\frac{14\dot{m}}{\pi\rho_{abr} u d_j^{\,2}}\right)^{2/5}\left(\frac{V_0}{C_k}\right) + \frac{1}{\frac{\pi d_j \sigma u}{2(1-C)\dot{m}(V_0 - V_e)^2} + \frac{C_f}{d_j}\frac{V_0}{(V_0 - V_e)}} \tag{2.22}$$

Despite several limitations, experimental factors and uncorroborated assumptions, the model provides a detailed approach with a closed-form solution in the end. Hashish also determined flow

stress experimentally as σ = Elastic modulus/14 with a strong (>90%) correlation for a variety of materials.

2.2.2.4 Raju-Ramulu model extension

Ramulu et al. developed cutting depth model as an attempt to overcome the shortcomings of Hashish's model [58]. Ramulu argued the idea of Hashish's model based on dependence of material removal mechanism on erosion depth and proposed the jet velocity as a prime factor in determination of jet curving and striation marks. Two cutting zones, smooth cutting region (SCR) and rough cutting region (RCR) were identified similar to cutting and deformation zones in Hashish's model. The model concentrates the velocity reduction as a dominant feature, which in turn is dependent on kerf wall drag forces. These drag forces were experimentally and proven to be ten times higher than those predicted by Hashish's model.

Material removal rate provided by Finnie and Bitter were related to the jet kinetic and jet-material interaction parameters. A set of differential equations were derived using empirical constant related to wavelength of the striations in both SCR and RCR, and momentum balance of the slurry. The prediction of kerf shape was possible only after experimentally determining certain factors such as coefficients of jet frictional drag in SCR and RCR, striation spacing and specific erosion energy of the work material.

Within the given range of parameters, the model appreciably predicts the kerf geometry, but heavily relies on empirical factors. Besides, the velocity reduction in the kerf was unsubstantiated.

2.2.2.5 Momber-Kovacevic model

Momber and kovacevic developed the waterjet erosion model based on the energy balance at each stage of the cutting process. Figure 2.15 illustrates the energy of waterjet being considered at each stage of waterjet process. The abrasive waterjet energy is realized during the erosion process. However, certain proportion of energy is lost during the erosion process due to friction, water-particle film damping, erosion debris formation, acceleration and particle fragmentation. This dissipated energy was assumed to account for the jet curving, which is prominent at higher penetration depth. The cutting front geometries in ideal (no energy loss) and non-ideal conditions are illustrated in Figure 2.16.

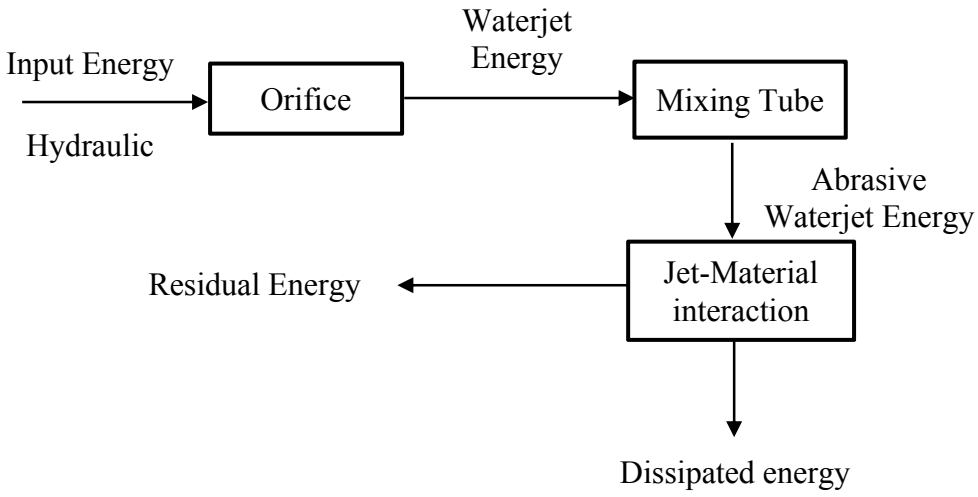

Figure 2.15. Structure of energy modelling

By energy balance, dissipated energy is the difference of the input AWJ energy and residual energy

$$E_{diss} = E_s - E_{ex}$$

E_{diss} = Dissipated energy under ideal condition
E_s = Slurry input energy
E_{ex} = Slurry exit energy

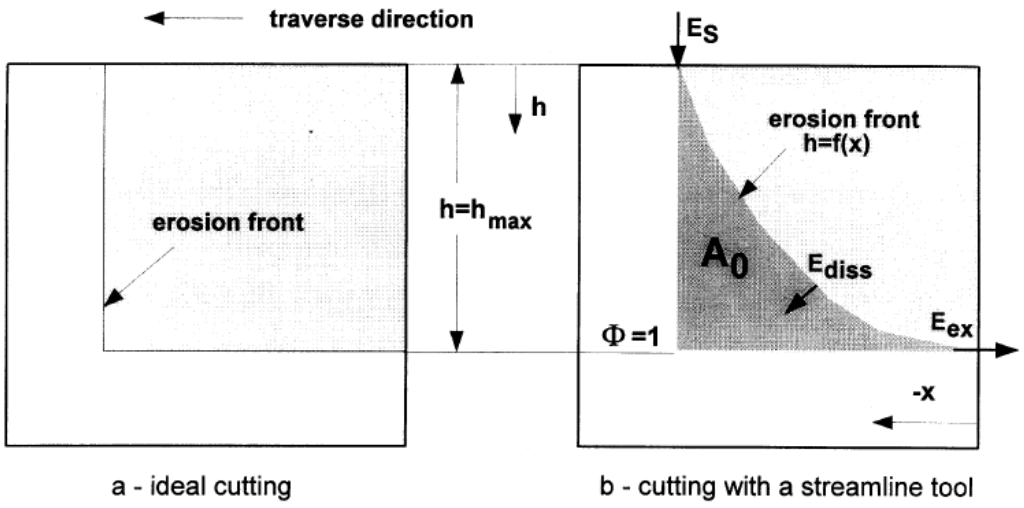

Figure 2.16. Comparison between cutting fronts at ideal (non-dissipative process) and non-ideal (dissipative process) depicting the contribution of energy towards cutting front geometry [59]

The dissipated energy as a function of penetration depth under real cutting conditions. Ratio of penetration depth to maximum possible depth is defined as follows

$$\phi = \frac{h}{h_{\max}} \tag{2.23}$$

Therefore, dissipation energy can be rewritten for real cutting condition as

$$E_{diss}(\phi) = \chi(\phi)(E_s - E_{ex})$$

$$\text{where, } \chi(\phi) = \text{dissipation constant} \tag{2.24}$$
$$\text{such that } \chi(\phi = 0) = 0,\ \chi(\phi = 1) = 1$$

A systematic technique for experimental determination of dissipation constant as a second order lumped constant was suggested by Momber and Kovacevic [60]. Although the model is much simplified in comparison to the previously developed models, the determination of dissipation factor used in the model is cumbersome and could be erroneous due to its dependence on a several phenomenon during the cutting process. This necessitates an extensive experimental study before determining the penetration depth of any new material.

2.2.2.6 TU Delft model

Paul and Hoogstrate developed a comprehensive model based on power level of the jet to predict the penetration depth and kerf taper. The model not only encompasees ductile materials but also extends to advanced fiber metal laminates.

The following equations were derived to determine the power of water jet entering the mixing tube.

By conservation of energy law,

$$v_w = \psi \sqrt{\frac{2P_w}{\rho_w}}$$

$$\begin{aligned} v_w &= \text{Velocity of water} \\ \psi &= \text{Velocity coefficient} \\ P_w &= \text{Water pressure} \\ \rho_w &= \text{Density of water} \end{aligned} \tag{2.25}$$

The power of water jet passing through orifice is given by the product of water flow rate and pressure.

$$P_{ow} = \dot{Q}_w \times P_w \tag{2.26}$$

$$\dot{Q}_w = A \times v_{water} \tag{2.27}$$

$$\begin{aligned} \dot{Q}_w &= \frac{\pi d_o^2}{4} \times C_d \sqrt{\frac{2P_w}{\rho_w}} \\ d_o &= \text{Orifice diamteter} \\ \text{C}_d &= \text{Coefficient of drag} \end{aligned} \tag{2.28}$$

The power of waterjet at the exit of orifice is given by equation (2.29).

$$P_{ow} = C_d \frac{\pi}{2\sqrt{2\rho_w}} d_o^2 P_w^{3/2} \tag{2.29}$$

The water and abrasives enter the mixing chamber alongwith small amount of air and momentum is transferred from entrained air and water to abrasive particles in the control volume. The

abrasives are initially at rest and the momentum of air can be neglected for negligible mass flow rate. Equation (2.30) is the impulse balance equation without considering any losses in the process.

$$\Sigma\left(\dot{m}v\right)_{before\ mixing} = \Sigma\left(\dot{m}v\right)_{after\ mixing} \tag{2.30}$$

$$\left(\dot{m}_w v_w\right)_{before} = \left(\dot{m}_w v_w + \dot{m}_a v_a\right)_{after} \tag{2.31}$$

The equation assumes the negligible air flow and a relation between waterjet and abrasive waterjet velocity can be found using:

$$\dot{m}_w v_w = \left(\dot{m}_w + \dot{m}_a\right) v_{awj} \tag{2.32}$$

$$v_{awj} = \frac{\dot{m}_w}{\dot{m}_w + \dot{m}_a} v_w \tag{2.33}$$

$$v_{awj} = \eta \frac{1}{1+R} v_w \tag{2.34}$$

Here R (load ratio) is defined as the ratio of mass flow rate to abrasive flow rate ($R = \dot{m}_a / \dot{m}_w$) and η is the momentum transfer efficiency.

$$\kappa = \frac{\frac{1}{2}\dot{m}_a v_{awj}^2}{\frac{1}{2}\dot{m}_w v_w^2} \tag{2.35}$$

$$\kappa = \frac{\eta^2 R}{\left(1+R\right)^2} \tag{2.36}$$

Conclusively, AWJ power can be determined as

$$P_{o(AWJ)} = \kappa P_{ow}$$

$$P_{o(AWJ)} = \frac{\eta^2 C_d R}{\left(1+R\right)^2} \frac{\pi}{2\sqrt{2\rho_w}} d_o^2 P_w^{3/2} \tag{2.37}$$

The material removal is dependent on this input power as

$$\frac{dV}{dt} \propto P_{0(AWJ)}$$

$$\frac{dV}{dt} = \xi \frac{P_{0(AWJ)}}{e_c}$$

ξ = Cutting efficiency (function of abrasive mechanical and geometric characteristics)

e_c = Specific cutting energy of work surface (2.38)

The material removal rate can be equated to jet motion parameters as:

$$\frac{dV}{dt} = \frac{1}{2}(W_{top} - W_{bottom}) h_{\max} u \tag{2.39}$$

The model provides an easy power based approach to determine the maximum depth.

2.2.3 Empirical and semi-empirical Models

Several empirical and semi-empirical models have been developed which require extensive experimental data to predict the penetration depths, kerf quality.

2.2.3.1 Wang and Guo model

Wang et al. developed a semi-empirical model to predict depth of cut in layered polymer matrix composites. The model is based on machining layered PMCs without any delamination. The predictability of composite machining is inherently poor based on the reasoning that composites involve different cutting mechanisms for different constituents. Wang argued that matrix is eroded by combined shearing and brittle cracking, whereas fibers are predominantly removed by bending, shearing and pull-out, and that the modeling based on different erosion theories is bound to be erroneous. A new model based on energy approach was developed. The model assumes material removal rate proportional to the impinging kinetic particle energy, i.e.

$$\frac{dV}{dt} \propto \frac{dK_e}{dt} \tag{2.40}$$

Also, assuming a constant kerf width, material removal rate can be related to jet motion as

$$\frac{dV}{dt} = h\ W\ u$$

V = Volume of material removed

h = Jet penetration depth

W = Kerf width

u = Jet traverse speed (2.41)

The kerf width is assumed to be a function of traverse rate, jet diameter, water pressure and abrasive mass flow rate.

$$W = k_1 \frac{d_j m_a^{\alpha_1} P_w^{\alpha_2}}{u^{\alpha_3}}$$

where, $k_1, \alpha_1, \alpha_2, \alpha_3$ are constants

d_j = Jet diameter

$\dot{m}_a$ = Abrasive mass flow rate

P_w = Water pressure (2.42)

Also, the kinetic energy can be expressed as given by equation (2.43)

$$\frac{dK_e}{dt} = \frac{1}{2}\dot{m}_a v_a^2 \tag{2.43}$$

Also, using the momentum equation during abrasive-water mixing process

$$\dot{m}_w v_{wj} = k_2(\dot{m}_w + \dot{m}_a)v_{awj}$$

$\dot{m}_w$ = Mass fow rate of water

$\dot{m}_a$ = Mass flow rate of abrasives

$v_{wj/awj}$ = Velocity of waterjet/abrasive waterjet (2.44)

The authors expressed the mass ratio as a constant and determined the velocity of abrasive waterjet given by equation (2.45).

$$\dot{m}_w v_{wj} = k_2(\dot{m}_w + \dot{m}_a)v_{awj} \tag{2.45}$$

$$v_{awj} = k_2 k_3 v_{wj}$$

where k_2, k_3 are constants (2.46)

Finally using abovementioned relations and Bernoulli's equation to relate water pressure and water velocity, the penetration depth can be determined as follows.

$$\alpha_t = k \frac{\dot{m}_a^{1-\alpha_1} P_w^{1-\alpha_2}}{d_j u^{1-\alpha_2} \rho_w} \tag{2.47}$$

A good correlation between predicted and experimental results was found using this model. The model is simple based on numerous assumptions, however, the requirement of large number of experiments to determine the constants over a different range of experimental conditions proves to be a major drawback of this model. The model overestimated the penetration depth at pressures >380 MPa. This limits the usability of model under high pressure cutting requirements (>380 MPa).

2.2.3.2 Paul and Hoogstrate kerf model

Paul and Hoogstrate [61] determined the kerf shape of ductile materials by experimentally verifying the linear dependence of minimum kerf width on nozzle diameter, and assuming linear reduction of kerf width with jet penetration depth.

$$W = W_{top} - \left(\frac{W_{top} - \lambda d_j}{h_c} \right) h$$

W = Kerf width upto cutting width
W_{top} = Jet entry kerf width
h = Penetration depth
h_c = Penetration depth in cutting wear mode
d_j = Nozzle diameter
λ = Constant

(2.48)

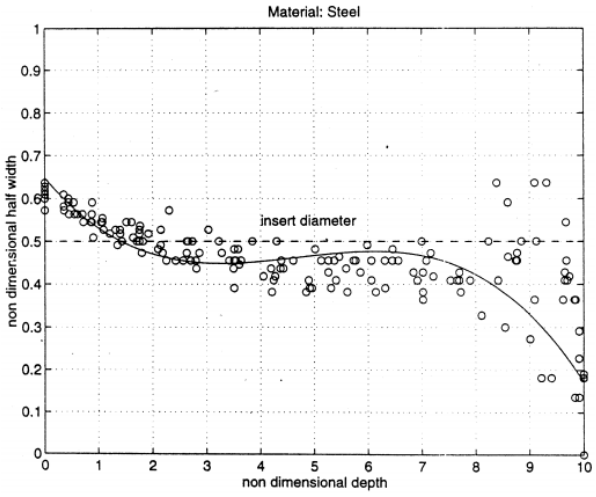

Figure 2.17. Experimental kerf width variation for steel

The investigation shows a variation of kerf width up to cutting depth (as given by Hashish's model) and a constant kerf width in deformation zone. Using this kerf width, maximum depth of cut can be determined using Hashish's model. The model is limited to the applicability on ductile materials and is purely based on linearity assumption.

2.3 MACHINING OF TITANIUM ALLOYS

The use of conventional machining methods and machine tools in machining notoriously difficult-to-cut titanium-based alloys is mainly limited by the high strength with high thermal damage due to low conductivity of titanium. Due to good deformability and weldability, build up edges and premature tool failure is often a primary concern. Besides, high strength at elevated temperature and poor conductivity results in high residual stress [62]. High chemical affinity of titanium further impairs its machinability. All these factors along with low modulus account for high cutting forces in conventional machining of titanium alloys, which adds up to chatter and accelerated tool wear [63] .

Ezugwu and Wang [64] reviewed the conventional machining of Titanium alloys. Tungsten carbides (WC/Co) were found superior in all machining processes of titanium alloys. CVD coated carbides and ceramics were reported as poor tool materials due to low fracture toughness and poor thermal conductivity of ceramics. The review also identified severe thermal and mechanical loads due to high cutting stresses and temperature, influencing the tool wear rate. Flank and crater wear, notch wear, chipping and catastrophic failure were identified as major tool failure modes. This necessitates the use of appropriate cutting fluid to increase the tool life.

Che-Haron and Jawaid [65] investigated the surface integrity of rough machining of Ti-6Al-4V with uncoated carbide tools under dry cutting conditions. Experiments were conducted for 45-100 m/min cutting speed and 0.25-0.35 mm/rev feed rate with constant depth of cut (2 mm). Surface roughness was found to decrease with cutting speed with higher roughness obtained as tool approached its wear life. Subsurface work hardening was reported. Microstructure alteration and increased hardness on the top white layer with average surface roughness < 6 μm was observed.

Ginting et al. [66] studied the surface integrity of dry machined titanium alloys using CVD-coated carbide tools. They reported poor roughness of surface generated by CVD-coated carbide tools (0.39 μm -0.72 μm) when compared to uncoated tool (0.43 μm -0.69 μm).

Tool wear problems were eliminated by using unconventional machining processes. EDM and AWJ are two viable processes for machining titanium alloys. However, machinability of Titanium alloys using only AWJ is discussed here. While employing Abrasive waterjet, titanium is removed by shear deformation as dominant mode as characterized by lip formations and ploughing marks adjacent to abrasive path. Owing to low ductility of titanium alloys (typically <15%), typical evidences of rubbing along with ploughing have been reported [28,67].

Seo et al. [68] studied the AWJ machining of Ti-6Al-4V and reported ductile shearing , abrasive scooping and scratching action of abrasives as removal mechanism. Surface roughness of 3.04 μm -10.22 μm was observed with smoother surface at high pressure, low traverse rate and intermediate abrasive size.

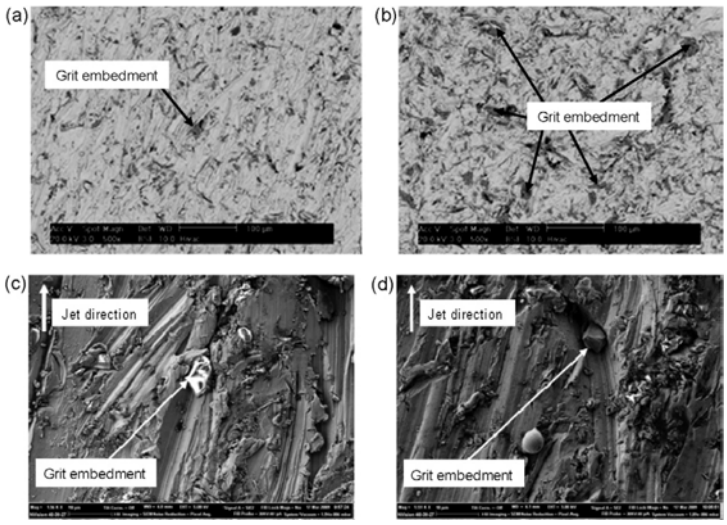

Figure 2.18. Grit embedment in AWJ machining of titanium alloys [46]

Shipway et al. [46] studied the abrasive waterjet machining of titanium alloys and identified several damages and challenges such as grit embedment and low traverse rate in comparison to aluminum.

2.4 MACHINING OF COMPOSITES

Traditional machining of ductile metals and some polymeric materials often involves deformation and failure along shear plane. This results in formation continuous or intermittent chips and burrs. However, material removal mechanism in composites is highly complex and dependent on the fiber orientation with respect to cutting direction [14,69]. Ramulu [14] reviewed the machining and surface integrity of fiber reinforced plastics, and identified cutting mechanisms in conventional machining of the same. As illustrated in Figure 2.19, composites with 0° fiber orientation were removed by mode I loading with fracture along the fiber/matrix interface. Mode II loading with tool advancement and subsequent bending and transverse fiber fracture was also observed. For composites with fiber orientation between 15° and 75°, the chip removal was found as a result of fracture from compression-induced shear across the fiber axis combined with shearing at fiber/matrix interface along the fiber direction during chip advancement. For fiber orientations >75°, compression induced fracture orthogonal to fibers and Interlaminar shear fracture along fiber/matrix interface was primarily observed.

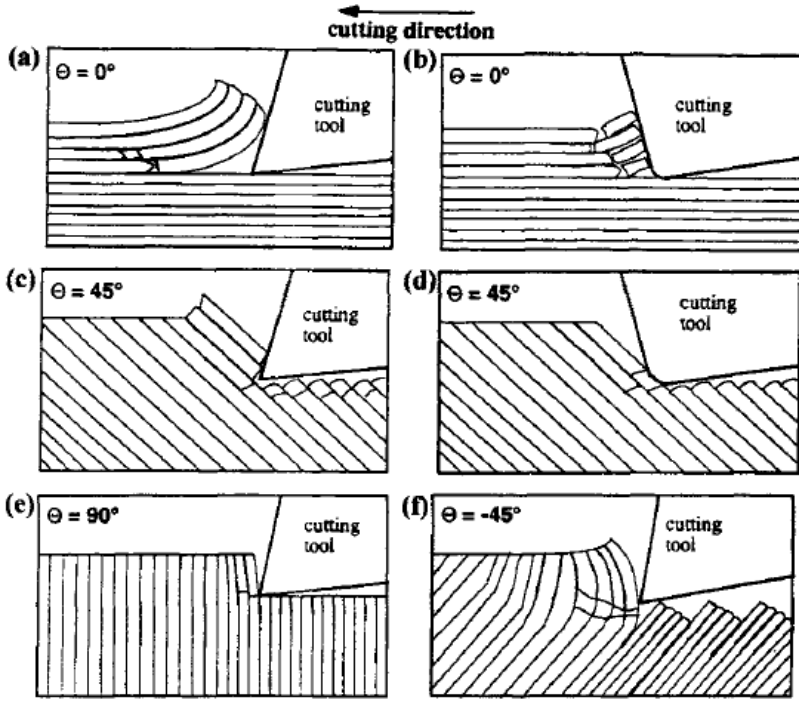

Figure 2.19. Cutting mechanisms in traditional orthogonal machining of graphite/epoxy (a) Delamination, (b) fibre buckling, (c) & (d) fibre cutting, (e) deformation, and (f) shearing.

Unlike metals, conventional machining of composite materials often generates microscopic dust particles which are fumed in air if not vacuumed properly. Recent investigations show that over-exposure to these dust particles can prove carcinogenic.

Regardless of machining tools and techniques, machining of Fiber reinforced composite is challenging due to its constitutional heterogeneity and thermal sensitivity. The soft matrix and abrasive nature of fibers often pose great challenge in optimizing the machining response.

Typical damage type in conventional machining of FRPs using polycrystalline diamond tool, depicted in Figure 2.20, include thermal distortion of matrix, fiber disbonding, delamination and interlaminate failure and often lead to high tool wear rate and machining cost [70–73].

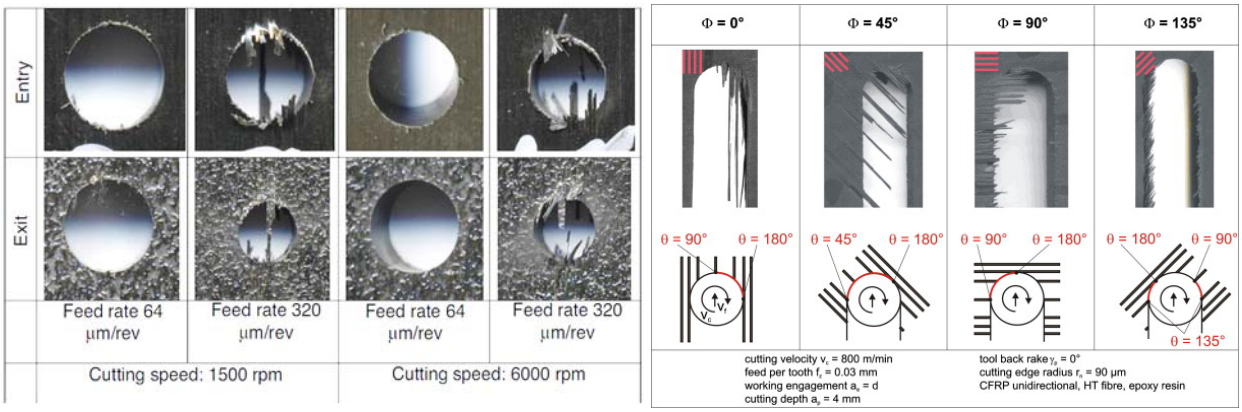

(a) (b)

Figure 2.20. Typical damage in unidirectional Carbon Fiber Reinforced Plastic composite (a) drilling, and (b) milling [71,72]

Abrate and Walton [74] reviewed the traditional composite machining processes and reported severe matrix cratering, thermal alterations, fiber pullout and fuzzing in drilling process. Along with geometric irregularities, interlaminar cracks and delamination at top (peel-up) and exit plies were identified as common defects when PCD and carbide tools were employed in drilling CFRP and GFRP. Effective negative coefficient of thermal expansion in composites and high temperature due to friction and abrasive nature of fibers was found as a major reason of drill tool squeezing and depreciation. During cutting experiments of unidirectional graphite-epoxy, 0.1-0.3 mm deep cracks were found with fracture failure and chip generation when machining direction was

perpendicular to the fiber direction. However, when machining parallel to fiber direction, a series of fractures and negligible plastic deformation was observed.

Ramulu et al. studied the surface finish and tool wear while cutting 25.4 mm thick graphite-epoxy laminates with PCD tools with 228.6 m/min cutting speed, 0.1778 mm/rev feed rate and 4.76 mm depth of cut. Average peak to valley roughness (Ry) was found between 23-37μm. Flank wear initially increased with machining time which later stabilized.

Edge trimming of Graphite/Epoxy with diamond Abrasive cutter was investigated by Colligan and Ramulu [70]. Delamination free machined edges with regular abrasive grooving marks was obtained. The surface roughness was observed between 3-4.3μm and proportional to abrasive size. They reported that surface finish is hardly affected by feed rate or cutting mode and cutter forces were found to increase with material removal rate. Boudelier et al. [75]studied the effect of diamond abrasive tool parameters (grit size, nickel level and tool diameter) and process parameters (feed rate and cutting speed) by analyzing the cutting forces and the specific cutting energy. They suggested high cutting speeds because of improved cuts due to thermal effects, but feed rate was limited by tool parameters as saturation of abrasive cutter was observed beyond a threshold value.

Unconventional machining methods are widely employed in machining composites. The high surface and structural integrity offered by Abrasive waterjet machining process while overcoming the limitations of conventional machining makes it a viable process in machining composites. However, Abrasive waterjet has its own challenges and limitations in machining composites.

Arola et al. [28] investigated the material removal mechanism in AWJ machining of unidirectional graphite/epoxy composite with 0°, 45° and 90° fiber orientation with reference to cutting direction. They observed abrasive wear tracks near top kerf and high delamination at jet exit side along with extensive fiber pull-out. Top kerf width was found greater than pure waterjet. Fibers were machined by non-repeated fractures by shearing and micro-machining action of abrasives. Microbending delamination of matrix material was observed at the jet exit side. Hackle pull-out and shear cusps were prominent in 0° fiber orientation.

The study suggested better performance of Abrasive waterjet cutting over Plain waterjet due to high degree of damage such as hydrowedging, delamination and high surface roughness

involved with pure waterjet. Maximum peak to valley height (Ry) was reported maximum (~23 μm) for 45° fiber orientation.

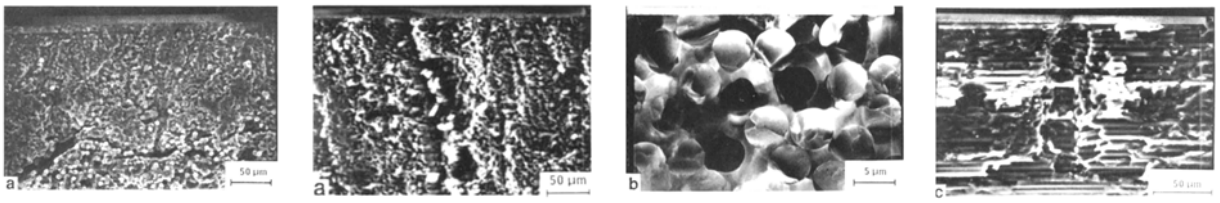

(a) (b) (c) (d)

Figure 2.21. Typical SEM micrographs of AWJ machined graphite /epoxy with different fiber orientation to cutting direction (a) 90° fiber direction – delamination at jet exit, (b) 90° fiber direction – fiber pull-out, (c) 45° fiber direction –wear pattern near jet entry side, (d) fiber roll-out near jet exit

Rahmah et al. [76] machined Kevlar/phenolic composite, Azmir et al. [77] machined Aramid fiber reinforced composite and observed an increase in taper ratio with increment in jet traverse speed, standoff distance and reduction in water pressure. Wang [78] studied the machinability of 3 mm thick polymer matrix composites in terms of kerf width and surface roughness. Increase in kerf width (top and bottom) with water pressure and stand-off distance was reported. It was found that kerf taper was increased with both water pressure and stand-off distance, with insignificant effect of traverse speed.

Wang and Guo developed semi-empirical predictive depth model based on delamination in polymer matrix composites [79]. Penetration depth was found to increase with decrease in jet traverse rate, pressure and abrasive flow rate (up to an optimum value). Conner et al. [80] studied the AWJ machining of thin aero-structural sheets of Inconel, titanium, aluminum and graphite /epoxy composite. A positive trend of average surface roughness was observed with traverse rate. Bottom kerf width was found significantly decreasing with traverse speed and slightly increasing with abrasive flow rate. The insignificance of fiber direction in machining composites was also reported. Jain et al. [81] employed genetic algorithm (GA) and found the increase in material removal rate with water pressure, nozzle diameter, traverse speed, mass flow rate of water and abrasives within a given range. Siddiqui et al. [82] employed hybrid Taguchi and response surface

method in optimization of surface roughness of kerf wall generated in AWJ machining of Kevlar-epoxy composites. High pressure, low flow rate and low traverse rate was found desirable for optimum surface roughness.

Azmir et al. [83] investigated the influence of AWJ process parameters on surface roughness (Ra) of GFRP composites. The investigation was carried out on 5 and 10 mm thick GFRP with following experimental conditions: Pressure 138-276 MPa, standoff distance 1.5-4.5 mm, abrasive mass flow rate 2.5-7.5 g/s, jet traverse speed 1.5-4.5 mm/s. Cutting orientation, abrasive mass flow rate and standoff distance was reported as an insignificant factor in controlling kerf roughness. However, pressure and traverse rate were found equally significant. Also, thickness and form of fibers were observed as important noise factors. Average roughness of 2.50-6.0 μm was reported. Azmir et al. also studied the effect of AWJ process parameters on kerf taper ratio and found a negative trend with increase in hydraulic pressure and abrasive flow rate. However, taper ratio was found to increase with stand-off distance and traverse rate. No clear trend was observed to account for the effect of cutting orientation (0°-45°). Similar effects were reported for surface roughness except for the cutting orientation. The minimum surface roughness was found at 22.5° and maximum at 0°.

Shanmugam et al. [84] developed empirical model to predict the kerf taper in AWJ machining of graphite/epoxy and glass epoxy composite laminates. The kerf taper angle is given by equation (2.49). High water pressure (280 MPa), low traverse speed (20 mm/s), and low standoff distance (2 mm) was recommended to achieve kerf taper angles blow 2° and 6° for glass/epoxy and graphite/epoxy composite respectively.

$$\alpha_{\text{kerf}} = 0.25\left(\frac{s}{d_j}\right)^{0.451}\left(\frac{Ed_j^2}{u\dot{m}_a}\right)^{-1.23}\left(\frac{P}{\rho_w}\frac{\dot{m}_a^2}{d_j^4 E^2}\right)^{-0.84}$$

s = Standoff distance (m)

d_j = Jet diameter (m)

E = Young's modulus (kg/ms^2)

$\dot{m}_a$ = Abrasive mass flow rate (Kg/s)

P = Pump pressure (MPa)

ρ_w = Water density (kg/m^3)

(2.49)

A comparative study of jetting technologies for composites machined at different angles 180°, 135°, 90°, and 45° concluded that minimum taper in AWJ machining of unidirectional aerospace composites can be achieved for straight cuts, and maximum for 45° angle due to inertial effects of nozzle traverse [85].

2.5 MACHINING OF FIBER METAL LAMINATES

Fiber metal laminates are primarily used in aerospace applications where superior edge qualities and tight tolerances are required. Due to difference in material removal mechanism in ductile materials (section 2.3) and composite materials (section 2.4), desired tolerance and part quality is often difficult to attain. Ramulu et al. reported the metal burrs migrating to resin and causing thermal distortion and damage to the same. Paul et al. [23] studied the AWJ machining of thin Glass Fiber/Aluminum laminates and reported that aluminum was removed by micro-machining, ploughing and plastic deformation. 90° fibers were removed by micro cutting and bending, while 0° were removed by bulk action of abrasives and brittle fracture. Substantial amount of secondary erosion by fibers was observed. The investigation also reported increased penetration depth and cutting ability with traverse water pressure and load ratio.

Ramulu et al. [30] studied the AWJ and EDM machining of thin TiGr sheets and reported concluded AWJ as a better alternative due to smoother and faster cuts with small damage. Isvilanonda et al. [86] investigated the effect of EDM and AWJ process parameters on flexural properties of thin TiGr sheets and found that the properties were unaffected by the AWJ process parameters, but different power settings in EDM resulted in thermal damage which influenced the flexural properties. Surface roughness between 3.1 μm and 9.7 μm was obtained for AWJ machined specimens which was 62.5-120.9 % higher than diamond cut surface [87].

2.6 SUMMARY

Titanium/Graphite is an immensely promising material for high temperature and high strength applications. Secondary trimming and contouring of TiGr is often required even after near-net shape molding. Previous investigations concluded the feasibility and appropriateness of machining thin TiGr (~ 1 mm) using AWJ machining process. However, since AWJ is a thickness dependent process, investigation into machining of thicker TiGr laminates is required. Besides, it was found that not all the major parameters were explored for machining Fiber metal laminates except for Aluminum/Glass fiber. However, studies related to Al/Glass fiber were restricted to only straight cutting and drilling. It is apparent from the review that machinability of titanium and graphite fiber matrix composite involves several challenges and more difficult than machining Al/Glass fiber FML owing to the hardness and low conductivity of titanium. No work has been reported on AWJ contouring of multi-layer thick TiGr laminate. Besides, none of the investigators studied the dependency of cutting quality on the cutting geometry.

Chapter 3. EXPERIMENTAL PROCEDURE AND ANALYSES

In order to determine the machinability of TiGr through AWJ and study the effect of profile curvature on process performance, AWJ machining was employed in a systematic manner. This Chapter discusses in detail the material specifications and experimental conditions used in this study. The profile geometry is defined and experimental design strategy is explained. Primary machining responses – kerf taper and kerf wall surface roughness evaluated in this investigation are discussed in detail along with the measuring instruments used for data acquisition. Both observational and statistical analyses strategies are discussed in detail.

3.1 WORKPIECE MATERIAL

Two 29.5 x 14.5 mm TiGr plates were obtained from The Boeing Company each with different thickness – 10.50 mm and 7.56 mm. These plates were made up of the layers of graphite reinforced thermoplastic (PEEK) matrix composite and titanium alloy foils stacked together with autoclave consolidation process under different configuration for different thickness. The specimens are depicted in Figure 3.1 and their layup configuration is shown in Table 3.2.

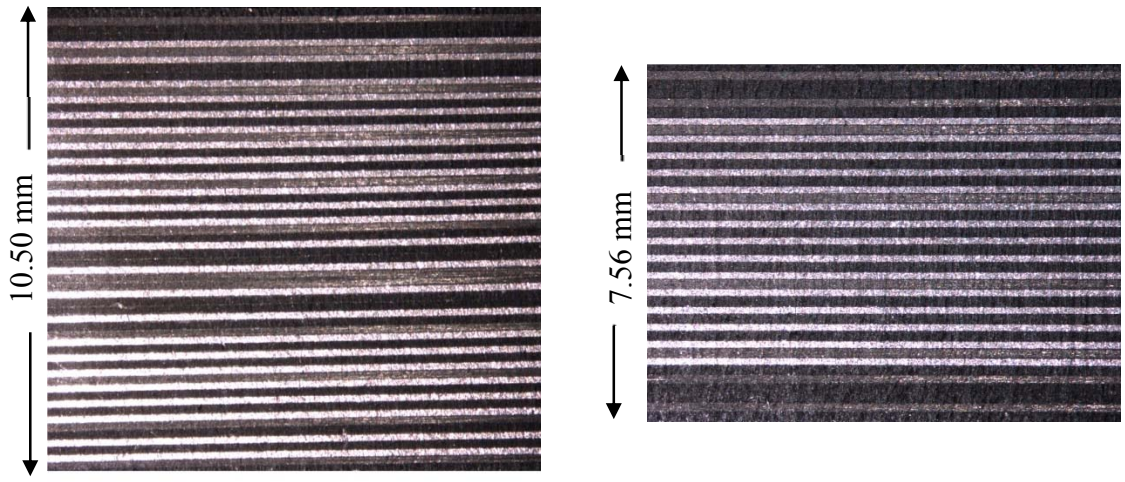

Figure 3.1. Cross section of thick TiGr specimens with thickness (a) 10.5 mm, (b) 7.56 mm

The as-obtained specimens were analyzed under Energy Dispersed Spectrometer (EDAX) to verify the composition of the material system using X-ray mapping technique. The common properties of industrial grade of these materials is mentioned in Table 3.1

Table 3.1. Properties of constituent materials [13,88]

Material	Properties
Titanium alloy (Ti-15V-3Cr-3Al-3Sn)	33.75 GPa (Shear modulus), 875 MPa (Shear strength)
PEEK (Polyetheretherketone)/Graphite	8.9 GPa (Transverse modulus), 80 MPa (Transverse strength)

The ply layup of the composite and titanium layers is different in both the thickness levels as depicted in Table 3.2. The reason for selecting different layups for different levels of thickness is to facilitate capturing of the possible variations in AWJ machining behavior caused by the ply arrangement. It can be noted from Table 3.2 and Figure 3.1 that 10.5 mm thick specimen has three composite face-plies at the top side and one composite ply at the bottom with a distinctive region of ply arrangement near the bottom where a titanium ply is alternated after every two composite plies instead of one. In 7.5 mm thick specimen, the entry and exit side has higher number of composite plies (6 composite plies). The overall volumetric percentage of composite and Titanium alloy is 72.22% and 27.77% respectively in 7.56 mm thick laminate, and 68% and 32% in 10.5 mm thick laminate. Thus, both the laminates are spatially dominated by composites.

Another reason for selecting different ply layups for this investigation is to enable the study of machining characteristics of these laminates as a global qualitative function. This would allow a statistical quality analysis from an industrial standpoint by considering more variation of ply arrangements for a given percentage composition of constitutive materials in the laminate.

Table 3.2. Ply thickness and layup of two different specimens

Specimen Thickness (mm)	Ply type and ply thickness (μm)		No. of Plies	Layup
10.75	Ti alloy	140	24	0°, -45°, 45°, Ti, 0°, Ti, -45°, 45°, Ti, 0°, Ti, -45°, Ti, 45°, Ti, 0°, Ti, -45°, Ti, 45°, Ti, 0°, Ti, -45°, Ti, 45°, Ti, 0°, -45°, Ti, 45°, -45°, Ti, 0°, 0°, Ti, -45°, 45°, Ti, -45°, 0°, Ti, 45°, Ti, -45°, Ti, 0°, Ti, 45°, Ti, -45°, Ti, 0°, 45°, Ti, -45°, Ti, 0°
	0° ply	210	12	
	45° ply	210	10	
	-45° ply	210	12	
7.56	Ti alloy	140	15	45°, 0°, -45°, 45°, 0°, -45°, Ti, 0°, Ti, 45°, Ti, -45°, Ti, 45°, Ti, 0°, Ti, -45°, Ti, 45°, Ti, 45°, Ti, -45°, Ti, 0°, Ti, 45°, Ti, -45°, Ti, 45°, Ti, 0°, Ti, -45°, 0°, 45°, -45°, 0°, 45°
	0° ply	210	8	
	45° ply	210	10	
	-45° ply	210	8	

AWJ Experiment

Table 3.3 provides the description of experimental conditions. The geometric variables include orifice diameter, mixing tube length and diameter. Besides, the pump pressure, abrasive flow rate and jet traverse speed were varied for two thickness levels according to industrial judgement and previous investigations [11,13,16,21]. Orifice diameter to mixing tube diameter ratio was varied between 0.23 and 0.50. Mixing tube aspect ratio (length/diameter) was varied between 66.7 and 150. The stand-off distance was maintained at best minimum possible for minimum energy loss before the jet interacts with workpiece and also to avoid pull-up delamination of top plies.

Table 3.3. AWJ Experimental conditions

Parameter	**Description**
Grit type	Garnet
Grit size (mesh#)	120
Impact angle	90°
Stand-off distance (mm)	0.75
Variable	**Range**
Nozzle (mm)	Length 76.2, 50.8 mm, Diameter: Ø 0.508, 0.762 mm
Orifice (mm)	Sapphire, Diameter: Ø 0.178, 0.254 mm
Specimen thickness (mm)	7.56, 10.75
Jet Pressure (MPa)	380, 600
Load ratio (%)	8.0, 9.2, 10.1
Jet traverse speed (mm/min)	50.8, 152.4

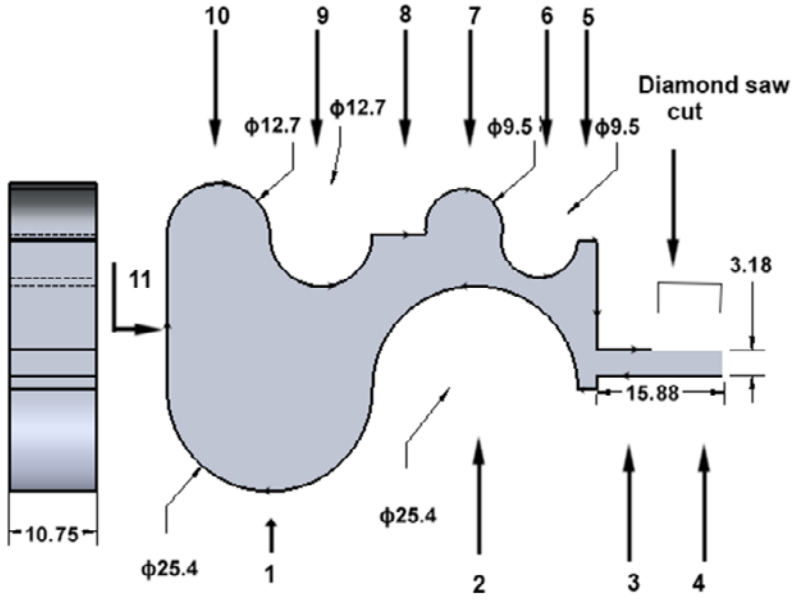

Figure 3.2. 2-D contour profile

The chosen profile of cut is illustrated in Figure 3.2. The rationale for selecting such geometry is to accommodate wide range of cutting curvatures for intricate contour cutting applications in aerospace industry and possible replacement of drilling operation with trepanning. Three levels of curved profiles, two characterized as small and one as large arc, are used in the cutting profile to study the effect of curvatures on machining responses.

The curvature size (diameter) of profile features was varied between 9.6 to 25.4 mm. However, small variance and undiscernible trend between the machining responses of small level curvatures necessitated the consideration of only the smallest arc feature. Also, both the inner and outer arcs were machined for each feature in order to investigate into the jet acceleration and deceleration effects, and profile concavity and convexity on the process performance. To further emulate the industry requirement, specificity of responses due to a particular sequence of these features, affecting the jet dynamics, was reduced by adding multiple sequences of profile curvatures including straight cuts followed by arc, arc followed by straight cuts, and arc followed by arc.

Table 3.4. Interpretation of point numbers in the cutting profile

Profile Number	Profile	Dimension (mm)	Projected Linear Length (mm)
1	Large outer arc	25.4	39.9
2	Large inner arc	25.4	39.9
(3,4),5,8	Straight cut	15.88, 1.59, 6.35	15.88, 1.59, 6.35
7,10	Small outer arc	9.6, 12.7	14.9, 19.95
6,9	Small inner arc	9.6, 12.7	14.9, 19.95

The profile features and their respective dimensions are mentioned in Table 3.4. The projected linear length indicates the actual jet traverse distance. The total jet trajectory distance in one single pass of waterjet cutting is 216.18 mm.

3.2 EXPERIMENTAL DESIGN

Experimental design was obtained using optimal response surface design in 'Design-Expert v9.0.4' software. With 7 numeric factors, 192 experimental runs were obtained which were further reduced to 32 based on practical constraints. The final Experimental design is depicted in Table 3.5. All the experiments were performed at Flow International Corporation because the chosen experimental conditions required state of the art Ultra High Pressure (600 MPa) waterjet machine.

Table 3.5. Response surface Design of Experiment

Experiment No	**Thickness**	**Test Parameters**					
		Pump Pressure (P)	Nozzle			Abrasive Load (R)	Speed u
			dm	lm	dn		
	(mm)	(MPa)	(mm)	(mm)	(mm)	%	(mm/min)
1	7.56	380	50.8	0.508	0.178	0.092	152.4
2	7.56	380	76.2	0.508	0.178	0.092	50.8
3	7.56	600	76.2	0.508	0.178	0.086	152.4
4	10.5	600	76.2	0.762	0.178	0.086	152.4
5	7.56	380	76.2	0.508	0.254	0.092	152.4
6	10.5	600	50.8	0.508	0.254	0.101	50.8
7	10.5	380	76.2	0.762	0.178	0.092	50.8
8	10.5	380	50.8	0.508	0.254	0.092	152.4

9	10.5	600	76.2	0.508	0.178	0.086	50.8
10	7.56	600	50.8	0.762	0.178	0.086	152.4
11	7.56	380	76.2	0.762	0.254	0.092	50.8
12	7.56	600	76.2	0.762	0.178	0.086	50.8
13	7.56	600	76.2	0.508	0.254	0.101	50.8
14	10.5	600	50.8	0.762	0.254	0.101	152.4
15	7.56	600	76.2	0.762	0.254	0.101	152.4
16	7.56	380	50.8	0.762	0.178	0.092	50.8
17	10.5	600	76.2	0.762	0.254	0.101	50.8
18	10.5	380	50.8	0.508	0.178	0.092	50.8
19	7.56	380	50.8	0.762	0.254	0.092	152.4
20	7.56	380	50.8	0.508	0.254	0.092	50.8
21	10.5	380	76.2	0.508	0.254	0.092	50.8
22	7.56	380	76.2	0.762	0.178	0.092	152.4
23	10.5	600	50.8	0.508	0.178	0.086	152.4
24	7.56	600	50.8	0.508	0.178	0.086	50.8
25	10.5	380	50.8	0.762	0.178	0.092	152.4
26	10.5	380	76.2	0.508	0.178	0.092	152.4
27	7.56	600	50.8	0.762	0.254	0.101	50.8
28	10.5	380	50.8	0.762	0.254	0.092	50.8
29	7.56	600	50.8	0.508	0.254	0.101	152.4
30	10.5	380	76.2	0.762	0.254	0.092	152.4
31	10.5	600	50.8	0.762	0.178	0.086	50.8
32	10.5	600	76.2	0.508	0.254	0.101	152.4

Henceforth each AWJ machining condition is denoted by the following notation: “AWJ-X” where ‘X’ refers to the condition number specified in Table 3.5. For instance, AWJ-32 refers to Abrasive waterjet specimen machined with experimental condition number 32 which corresponds to 10.5 mm thick TiGr specimen machined with 600 MPa pressure, 76.2 mm mixing tube length, 0.508 mm mixing tube diameter, 0.254 mm orifice diameter, 0.101 load ratio and 152.4 mm/min jet traverse speed.

3.3 MACHINING RESPONSES

Macrographs of AWJ machined straight cut cross-section were acquired using stereoscopic zoom Microscope SMZ 1000 attached with NI-150 high intensity fiber optic illuminator. The images were acquisitioned using a Nikon camera interfaced with digital sight DS-U1 interfaced with a computer system. NIS-Elements Basic Research© version 2.10 (Build 217) software was used at the signal receiving terminal to capture and process the image data. Following machining responses were recorded and investigations were carried forward to analyze the samples machined under different experimental conditions for five different profiles features.

3.3.1 Kerf taper and Kerf taper ratio

Kerf Taper is defined as the difference between entry and exit kerf width normalized with twice the thickness of workpiece.

$$\text{Kerf taper } (\alpha_{taper}) = \frac{(d_{entry} - d_{exit})}{2t}$$
$$d_{entry} = \text{Jet entry kerf width}$$
$$d_{exit} = \text{Jet exit kerf width} \qquad (3.1)$$
$$t = \text{Specimen thickness}$$

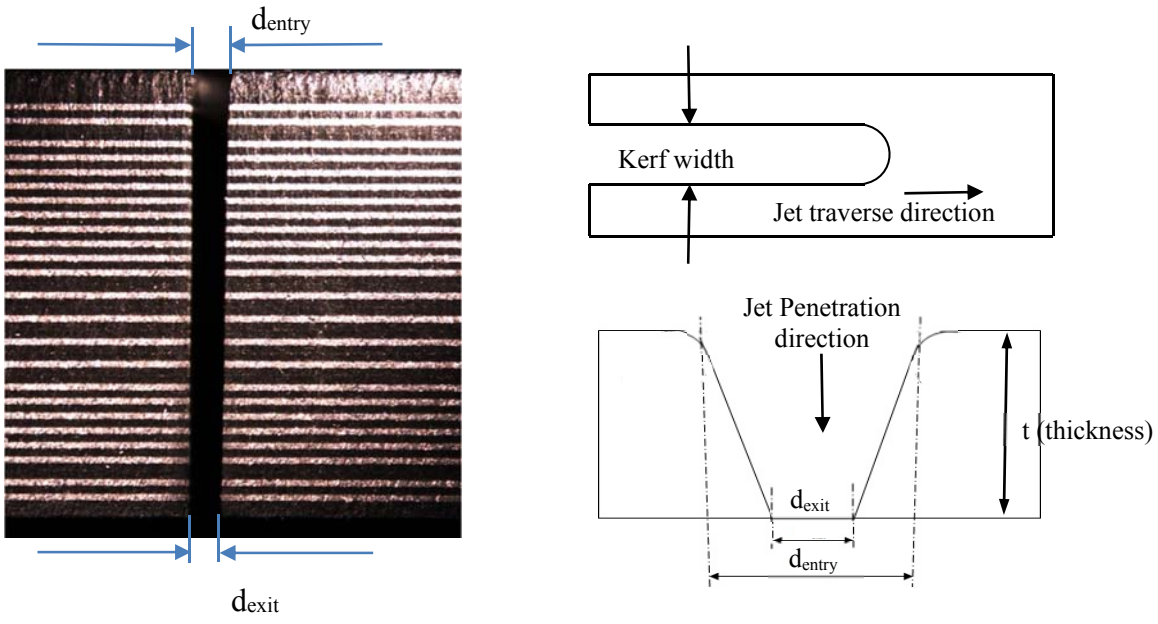

Figure 3.3. Kerf dimensions for straight cut AWJ machined profile

Kerf ratio is defined as the ratio of jet entry kerf width and jet exit kerf width.

$$\text{Kerf Taper ratio} = \frac{d_{entry}}{d_{exit}} \tag{3.2}$$

Figure 3.3 illustrates the kerf wall nomenclature of AWJ machined specimens. Top and bottom kerf width was measured using MicroVu Sol Precision measuring machine equipped with Programmable LED coax light and autofocus detection through 6.5x zoom lens. The kerf width was averaged for five different locations on each profile feature. Kerf ratio and kerf taper are alternatively used in this study in order to explore the comparability with previous investigations in the literature.

3.3.2 Kerf wall topography

The kerf surface profile was measured longitudinally and transversely with reference to the jet traverse direction. The surface roughness of the kerf wall was evaluated using MahrSurf XR 20 surface roughness measuring equipment in terms of standard roughness parameters. This XR 20 contact type profilometer was equipped with a stylus based, 2.5µm radius conical diamond tip with 5 nm resolution. Longitudinal passes, along specimen's centerline were obtained with a cutoff length of 0.8 mm and a specific traverse length. Table 3.6 depicts the roughness measurement parameters. In order to quantify the surface topology, the longitudinal Roughness Average (R_a), Maximum Roughness (R_t) and the Ten Point Height Roughness (R_z) were calculated.

Table 3.6. Roughness measurement parameters

Parameters	**Value**
Measurement instrument	Mahr Data Acquisition Board
Drive Unit	GD 25
Pick-up	MFW-250
Traversing Length (L_t)	Variable (3.75 to 10.5 mm)
Traversing Speed (V_t)	0.5 mm/s
Cutoff Wave Length (L_s)	2.5 µm
Number of Points	Variable (7500-21000)

Although longitudinal surface roughness is widely used and efficiently describe the cutting process characteristic of a machined monolithic workpiece, the employment of available resources in measuring roughness along each ply in a hybrid material involved several challenges. The large size of the specimens limited the measurement over curved features, especially smaller arced profiles. Besides, the fidelity of measuring probe along a 200 μm profile was difficult to maintain and a small deviation in the measuring probe trajectory could lead to false data due to high difference in surface roughness of titanium and composite ply. Thus, transverse surface roughness was extensively measured in comparison to longitudinal surface roughness to evaluate surface topology in this investigation.

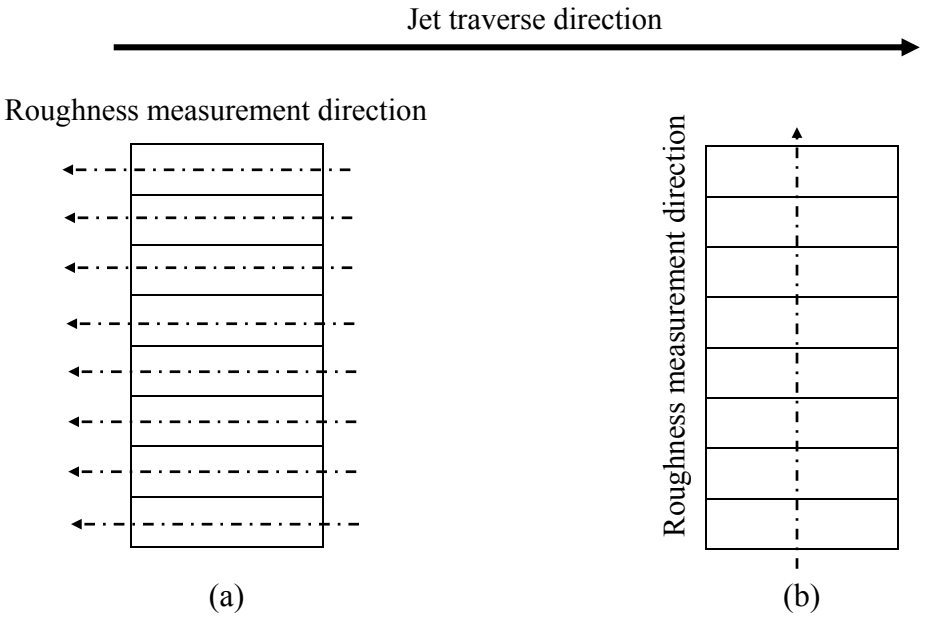

Figure 3.4. Cross sectional view of machined kerf wall depicting (a) Longitudinal, and (b) Transverse roughness measurement direction[1].

Longitudinal Surface roughness

Figure 3.4(a) illustrates the measurement direction of longitudinal surface roughness. Based on the taper results, a 10.5 mm thick specimen was selected and its straight cut profile was measured longitudinally and opposite to jet traverse direction with a total 6 mm traverse length. Also, in order to evaluate the machining quality and understand the effect of AWJ process at different

[1] Diagram is an illustration of measurement directions with number, arrangement and thickness of plies different than the specimens used in the experiments.

curvatures, surface roughness was measured longitudinally and opposite to jet traverse direction. The measurements were recorded for surfaces at three different jet penetration depths - 1.2 mm, 3.75 mm and 6.35 mm for a 7.56 mm thick specimen measured from jet entry side.

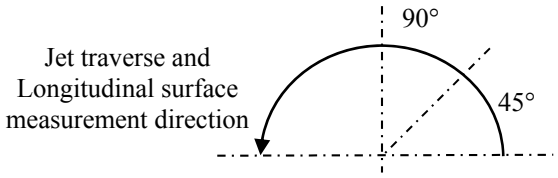

Figure 3.5. Arced profile depicting longitudinal surface roughness measurement direction.

The surfaces were measured with a traverse length span of 3.75-5.6 mm about 90° orientation for arced profiles as depicted in Figure 3.5.

Transverse Surface roughness

Transverse roughness profiles were measured for each profile feature mentioned in Table 3.4 along with the surface machined using diamond saw cutter. A total of 382 profiles were obtained at 12 locations for each of the 32 samples machined with different AWJ experimental conditions. These profiles were measured from jet exit to entry side with a traverse length of 6.5 mm and 9 mm for 7.56 and 10.25 mm thick specimens respectively. Besides, in order to address the issue of water induced composite distortion discussed later in section 4.2.1, transverse surface roughness profiles were measured around large outer arc profile of a 10.5 mm thick specimen at 5° angular offset and 10.5 mm traverse length. The transverse surface measurement direction and layout for the same is depicted in Figure 3.6.

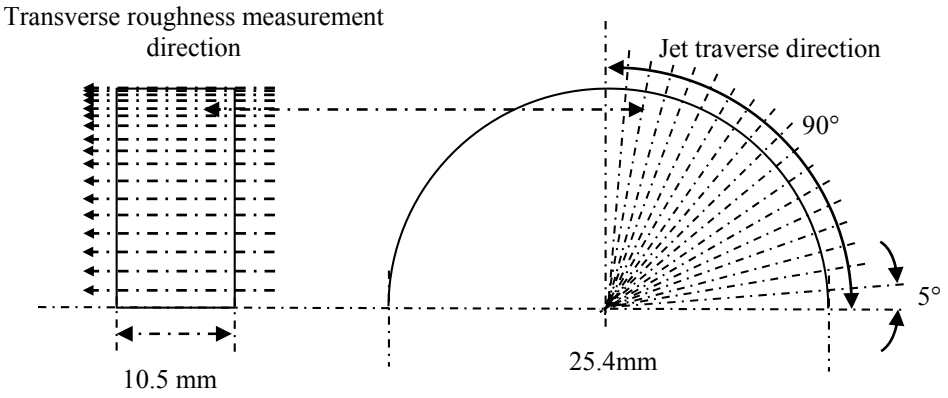

Figure 3.6. Transverse surface roughness measurement profile for AWJ-32 specimen

Roughness 2D amplitude parameters

Several profile amplitude and amplitude distribution parameters were evaluated to quantify, categorize and compare the surface topology. The parameters are described in this section with the help of schematic profile shown in Figure 3.7.

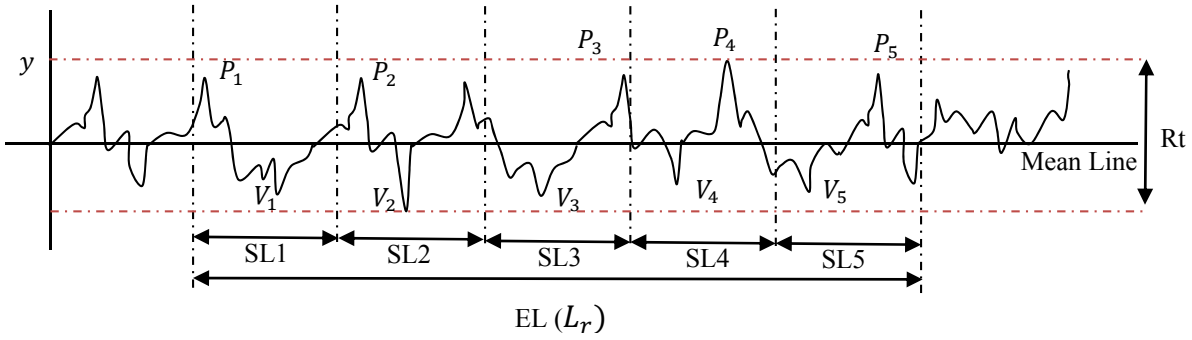

Figure 3.7. Schematic profile depicting various roughness parameters

EL = Evaluation length

$SL_i = i_{th}$ Sampling length

P_i = distance of i_{th} peak from mean line

V_i = distance of i_{th} peak from mean line

Average roughness or Center line average (R_a) is defined under ISO 4287 as the arithmetic mean deviation of the assessed profile. R_a value is incapable of expressing the spatial frequency of the irregularities or shape of the assessed profile. It is valuable when the global evaluation of a surface is to be related to stochastic roughness where there is no special events expected in the machining process.

$$R_a = \frac{1}{n}\sum_{i=1}^{n}|y_i| = \frac{1}{L_r}\int_0^{L_r}|y|\,dx \tag{3.3}$$

RMS average (R_q) is the root mean square deviation of profile from the mean line over the sampling length. R_q, being a standard deviation of the assessed profile, is a statistically significant parameter. R_a and R_q are good average parameters but they are unable to discern between peaks and valleys, and thus not informative about the shape or form of the unit event.

$$R_q = \sqrt{\frac{1}{n}\sum_{i=1}^{n} y_i^2} = \sqrt{\frac{1}{L_r}\int_0^{L_r} y^2 dx} \tag{3.4}$$

R_t (EL peak to valley height) is the maximum distance between highest peak and deepest valley within the evaluation range. It is an extreme parameter and highly susceptible to localized disturbances in the process.

$$R_t = \max(P_i, V_j) \text{ over EL}$$

R_z (SL peak to valley height) is the average of distance between maximum peak and deepest valley measured over each sampling length. $R_z(JIS\ B\ 0601{:}\ 2001)$, also known as ten point average is an alternative method of the extreme averaging where distance between five highest peaks and lowest valleys within sampling length is averaged. It significantly magnifies the dominant irregularities which otherwise would be filtered by sampling length averaging.

$$Rz = \frac{1}{5}\sum_{i=j=1}^{5} |P_i| - |V_i| \tag{3.5}$$

$$Rz\left(JIS\right) = RzJ = \frac{1}{5}\left[\sum_{i=1}^{5} y_{pi} - \sum_{i=1}^{5} y_{vi}\right] \tag{3.6}$$

Skewness (Rsk), defined by ISO 4287 (1997), is a measure of the asymmetry of the amplitude density curve. Mathematically, it is the third moment of height amplitude distribution and generally normalized by standard deviation. It acquires a null value for a completely random surface profile due to uniform distribution of profile amplitudes about the mean line. However, it is an important measure in categorizing the manufacturing processes as it reflects the distribution and shape of unit event(s).

A positively skewed profile exhibit good gripping and locking properties in metallic materials, and helps in improving fatigue life of components, where cracks may initiate from surface defects. Negative skewness indicates a surface with good bearing properties due to valleys acting as lubrication reservoirs.

$$Rsk = \frac{1}{Rq^3}\left[\frac{1}{Lr}\int_0^{Lr} y^3 dx\right] \tag{3.7}$$

With reference to abrasive interaction in AWJ machining, metals with greater resistance to erosion exhibit a negatively skewed roughness profile due to prominent abrasive dents rather than bulk erosion. On the contrary, metals with low resistance to abrasive erosion are found to exhibit positive skewness due to bulk erosion [28].

Kurtosis (Rku), defined by ISO 4287 (1997), also quantifies bearing properties by measuring the peakedness of the amplitude density curve. Mathematically, it is the fourth moment of height amplitude distribution and generally normalized by standard deviation.

$$Rku = \frac{1}{Rq^4}\left[\frac{1}{Lr}\int_0^{Lr} y^4 dx\right] \tag{3.8}$$

A skewness-kurtosis space plot (bearing curve) gives a better understanding of the roughness characteristics, but skewness and kurtosis can be influenced by isolated peaks and valleys, which often limit their usefulness.

3.3.3 Surface Integrity

The new surface generated after material removal in any manufacturing process exhibits certain topological and property modification characteristics that are different from the rest of the bulk. Topological modifications (such as geometric form, waviness, roughness, surface distortion and other profile characteristics) and property modifications (such as residual stress, hardness) influence the part failure strength, especially under variable loading conditions. The scope of surface integrity in the present investigation is limited to the study of machining induced topological surface modification. Proper selection of process parameters is necessary to not only achieve desired material removal rate, but also to minimize surface roughness and other localized defects which may generate cracks under variable loading conditions.

In order to inspect the machined surface integrity, selected specimens were sectioned using Buehler® Isomet™ low speed saw with a diamond cutting wheel. A comparative analysis was made between the diamond saw cut and AWJ machined surface characteristics. Scanning electron microscopy was conducted on straight cut AWJ specimen using FEI XL30 Sirion FEG digital electron scanning microscope at Nano Tech User facility (NTUF). The spot size used was 3. TiGr

specimens were sputter coated in vacuum with about 10 nm thick conductive (Au/Pd) layer to enable discharging of beam current over non-conductive composite constituents.

The machined surfaces were microscopically (optically) inspected at various magnification levels using a Nikon LV 150 and SMZ 1000 optical microscopes with Nikon DS-U1 digital camera directly linked to a Dell Precision 670 computer, using NIS Elements image processing software. This allowed images of the machined surface as well as the morphology of material removal process.

3.4 ANALYSIS OF VARIANCE (ANOVA)

The effect of process parameters on AWJ machined transverse surface roughness and kerf taper ratio was statistically analyzed by employing ANOVA (Analysis of variance) using Design-Expert v9.0.4 software. The responses were modeled with regression analysis and empirical equations for each response were obtained using a 2FI (two factor interaction) curve fit as shown in equation (3.9). Modeling was performed using backward elimination procedure to eliminate non-influential factors by comparing p-value with critical p-value (alpha out = 0.20).

$$\text{Response} = C_0 + C_1 \sum_{i=1}^{n} A_i + C_2 \sum_{i=1}^{n} \sum_{\substack{j=1 \\ i \neq j}}^{n} A_i A_j + \dots \tag{3.9}$$

Where A_i is the ith parameter of total n parameters and C_0-C_5 are the empirical constants corresponding to the raw data of each.

In order to account for the credibility of analysis, the model was verified by plotting diagnostic curves i.e. normal probability and residual plots. A straight line depicted in normal probability plot verifies the distribution of residuals as Gaussian. A Residual vs Run plot is used to check for any consistent trends and thus periodically sustained error(s) in the experimentation. A random scatter of data points verifies the absence of any time-related lurking variable(s) which can be traced back and blocked for a sound analysis. Residual versus Predicted value plot verifies the model assumption of constant variance across the range of predictions. A constant variance is characterized by a randomly scattered data within the control limits and absence of any repetitive

pattern. Besides, Predicted versus experimental curve was plotted depicting 45° line as the predicted ideal case and the experimental points deviated from the line. The percentage contribution of each parameter in the model can be determined as given by equation (3.10).

$$CB_i = \frac{SS_i}{\sum_{i=1}^{n} SS_i + SS_r}$$

$$CB_i = \text{Contribution of } i_{th} \text{ factor}$$

$$SS_i = \text{Sum of squares of } i_{th} \text{ factor} \qquad (3.10)$$

$$SS_r = \text{Sum of squares of residual}$$

$$n = \text{Total number of parameters}$$

3.5 Overview of Experimental Procedure and Analyses

Two TiGr plates were obtained from The Boeing Company with different thicknesses (10.5 and 7.56 mm) and ply layups. A profile geometry encompassing arcs of three different radii and straight segment was decided for AWJ contouring. In order to study and analyze the effect of process parameters mentioned in section 3.2, response surface experimental design was employed using Design Expert software to obtain 32 different experimental conditions, 16 for each thickness level. The experiments were performed at Flow International using UHP AWJ facility of 600 MPa pressure capacity.

The kerf width was measured for each profile feature and for each AWJ specimen at jet entry and jet exit side using MicroVu optical measuring machine. For the same specimens, surface roughness transverse to jet traverse direction was measured. The kerf width measurements were averaged for a given profile feature (arcs of different curvatures and straight cut) of contour geometry, whereas transverse roughness was measured midway of semi-circular features and at specified location for straight cut features. Transverse roughness of large outer arc machined with experiment condition number 32 was measured at 5° angular offset and upto 90° to analyze the effect of contour angle on surface roughness characteristics.

Kerf wall roughness longitudinal to jet traverse direction was measured at three different locations of each profile feature in AWJ specimen machined with experiment number 5. Besides, longitudinal roughness was also measured along each ply for straight cut kerf machined using

AWJ with experiment number 25. This is measured to study the surface roughness behavior along each ply throughout the jet penetration.

The AWJ machined samples were qualitatively characterized by studying surface roughness and associated parameters. Best and worst contouring conditions were identified based on kerf taper and transverse roughness, and performance variance within given part was studied. The kerf taper ratio and transverse roughness were statistically analyzed and characterized in Design Expert software. Effect of process parameters on machining response was determined and expressed by means of predictive empirical models. Besides, sensitivity of each parameter on response model for different profile features was compared. Optimum parameters were determined based on the common industrial goals and practices.

Selected specimens were sectioned using diamond saw cutter for Optical and Scanning Electron microscopic inspection to identify any possible damages. Besides, roughness characteristics of diamond saw cut profiles were determined for comparative analysis with AWJ specimens.

Chapter 4. RESULTS

Abrasive Waterjet contouring experiments were completed on two different thickness Titanium/Graphite FML plates and results are compiled in this Chapter. The observed macro-topographic and micro-topographic features of AWJ machined thick TiGr laminates are discussed in subsequent sections. Kerf taper ratio results along with empirical models are discussed in section 4.1. Surface integrity and morphological characteristics were investigated along longitudinal and transverse directions and results are discussed in section 4.2.

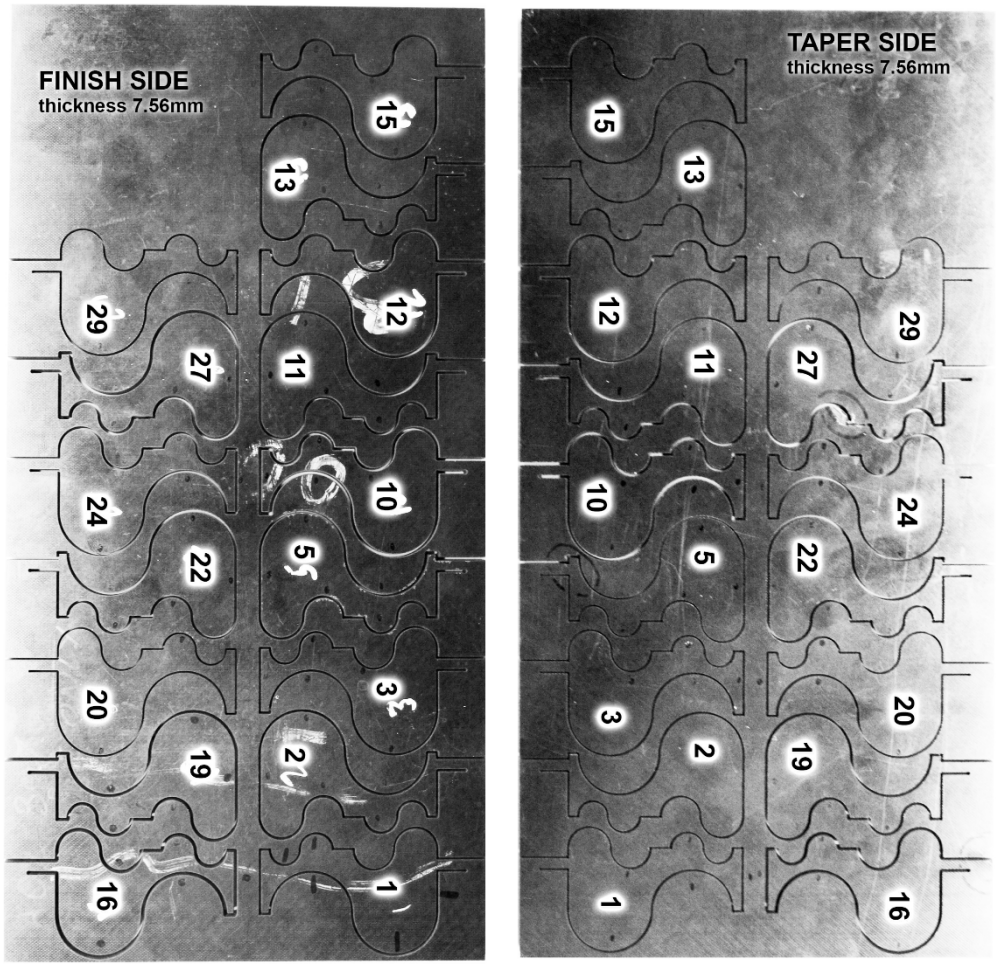

(a) (b)

Figure 4.1. Experimental runs and associated (a) Jet entry, and (b) Jet exit cutting profiles of AWJ machined 7.56 mm thick TiGr specimen.

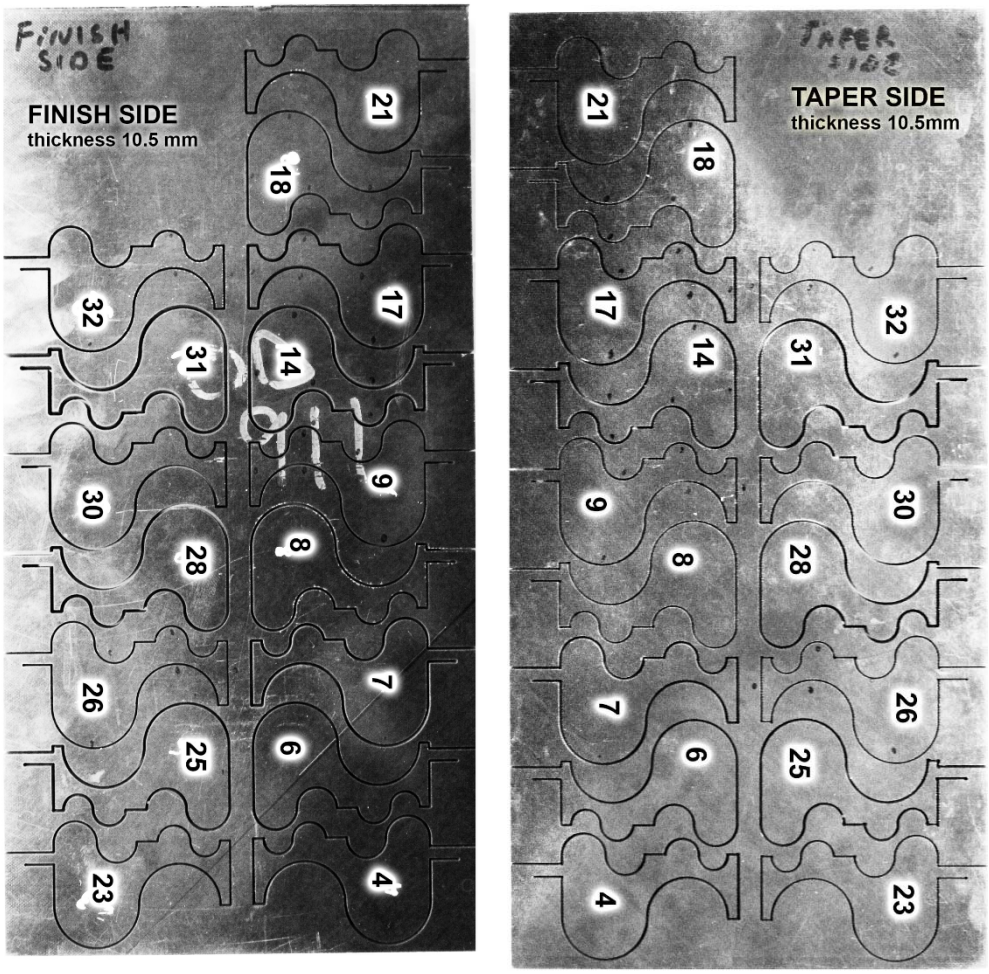

(a) (b)

Figure 4.2. Experimental runs and associated (a) Jet entry, and (b) Jet exit cutting profiles of AWJ machined 10.5 mm thick TiGr specimen.

Figure 4.1 and Figure 4.2 shows jet entry and jet exit side of AWJ machined profiles generated with conditions given by DOE, depicting 16 cuts for each thickness level. Each profile geometry has a total linear length (jet traverse distance) of 216.18 mm.

The obtained composition was verified using Energy Dispersed Spectroscopy and identified as a commonly used industrial grade Titanium alloy (Ti-15V-3Cr-3Al-3Sn) with graphite fiber bonded in thermoplastic PEEK composite. The detected composition of composite matrix material and titanium alloy is depicted by the elemental frequency spectrum in Figure 4.3 along with spectrum location.

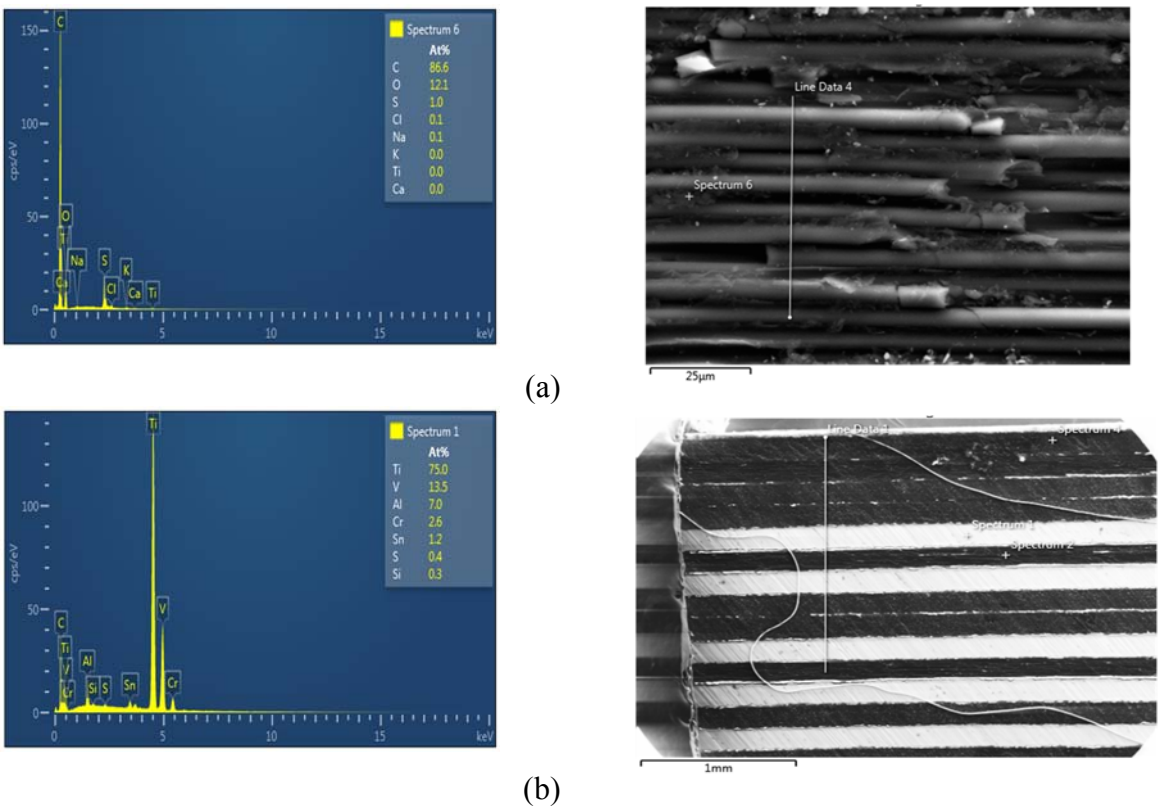

Figure 4.3. EDAX Spectral Analysis for detection of material composition (b) Matrix material, (b) Titanium alloy

Typical macrographs of kerf wall along the profile are shown in Figure 4.4. Distinctive features such as striated marks are evident from the kerf wall macrographs. Also, variation among these macrographs is visually prominent and reflected in the subsequent taper and roughness results. Figure 4.4 also depict the diamond saw cut surface, easily identified by a contrastive abrasive grooves of the cutter. The diamond saw cut surface characteristics are compared with AWJ cut in subsequent results.

Figure 4.5 shows the SEM micrographs of straight cut, 7.56 mm thick AWJ-1 specimen. The micrographs are more focused at the bond line between titanium and composite plies and depict a typical surface topology from jet entry to exit side. Figure 4.6 and Figure 4.7 shows the SEM micrographs of straight cut, 10.5 mm thick AWJ-25 specimen. For the given AWJ machining conditions, no severe interply delamination and grit embedment was observed.

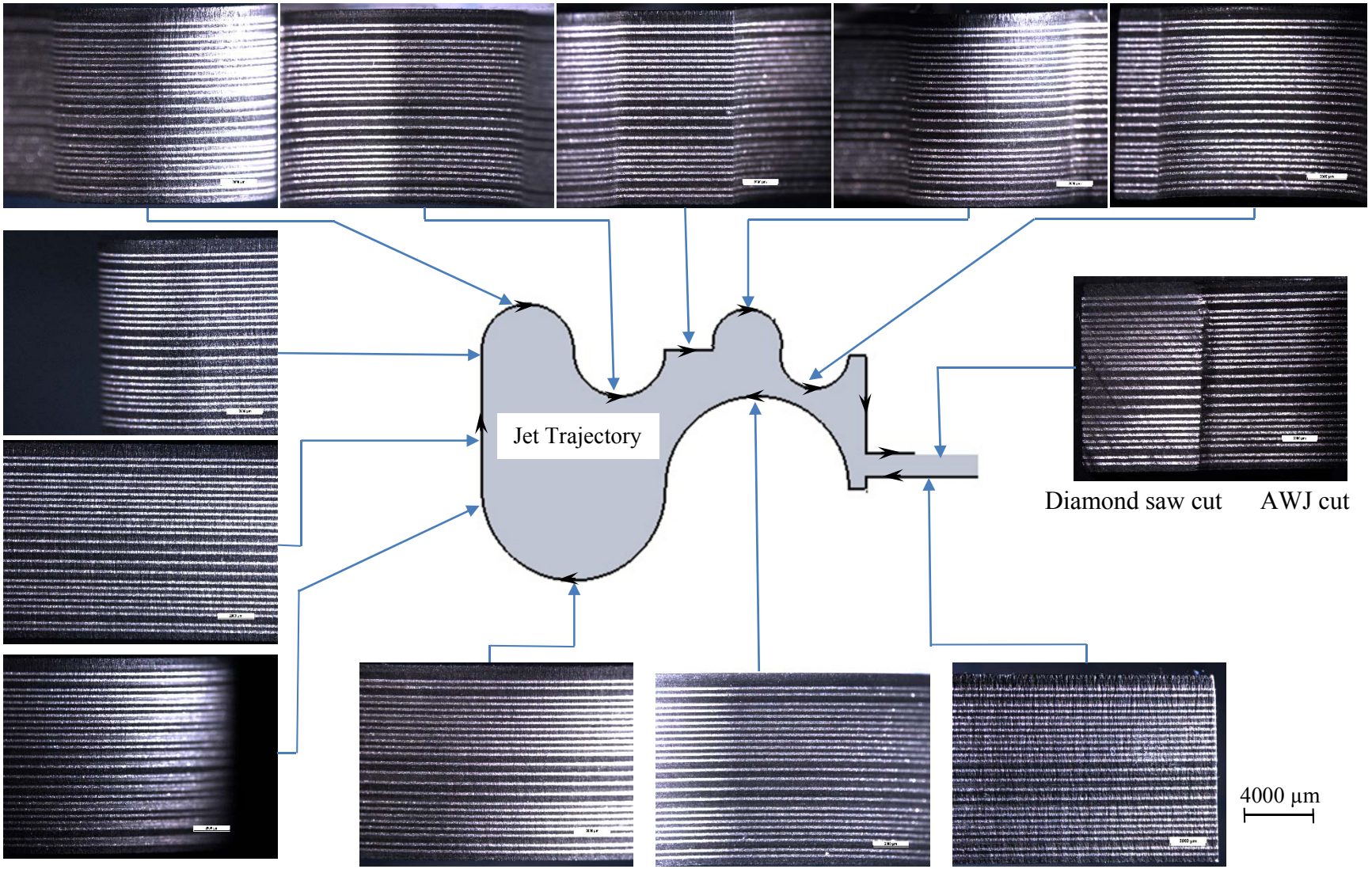

Figure 4.4. Typical macrographs of AWJ-28 machined kerf wall along the cutting trajectory

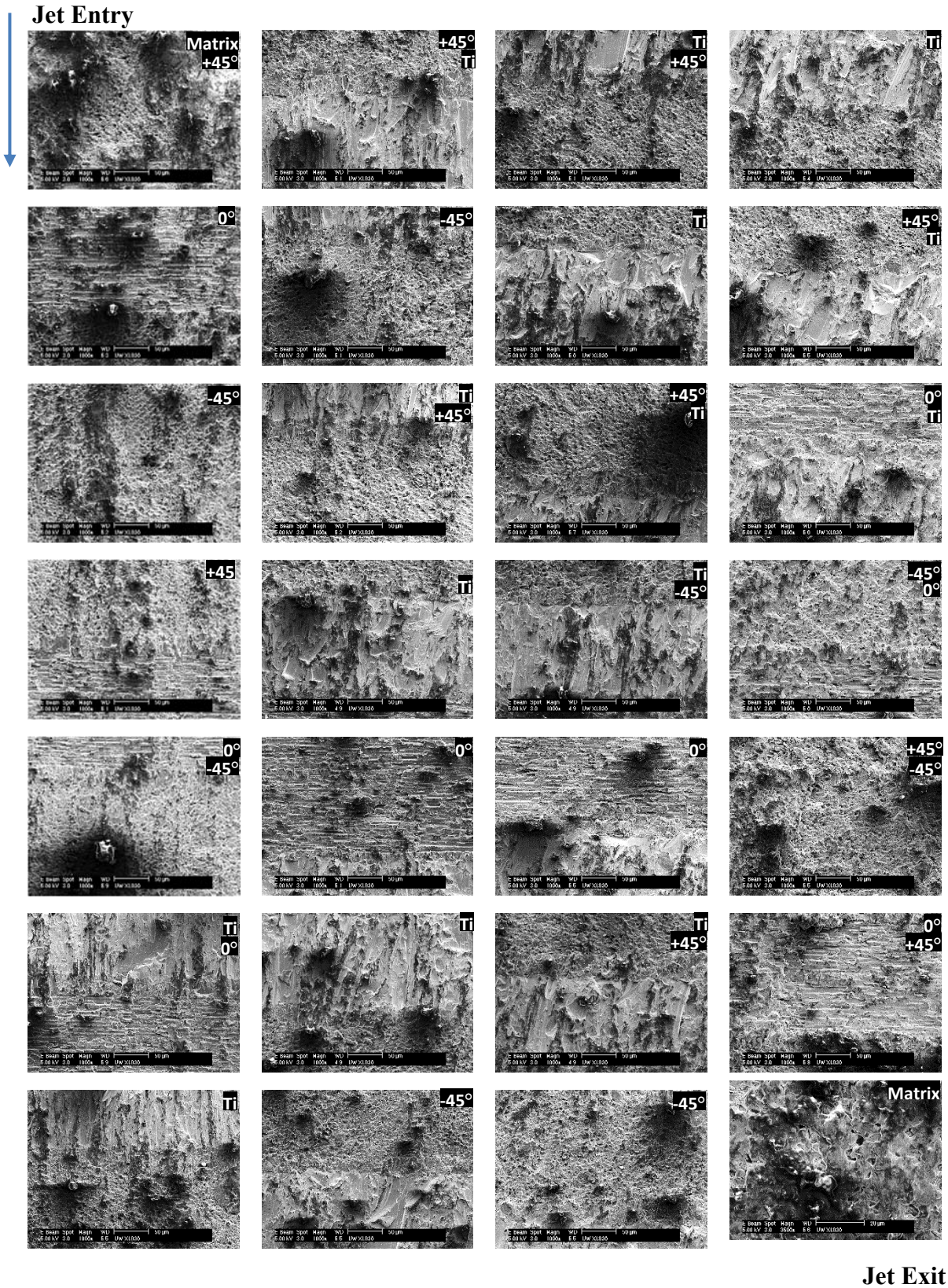

Figure 4.5. SEM micrographs of 7.56 mm thick, straight cut AWJ-1 specimen

Jet Entry

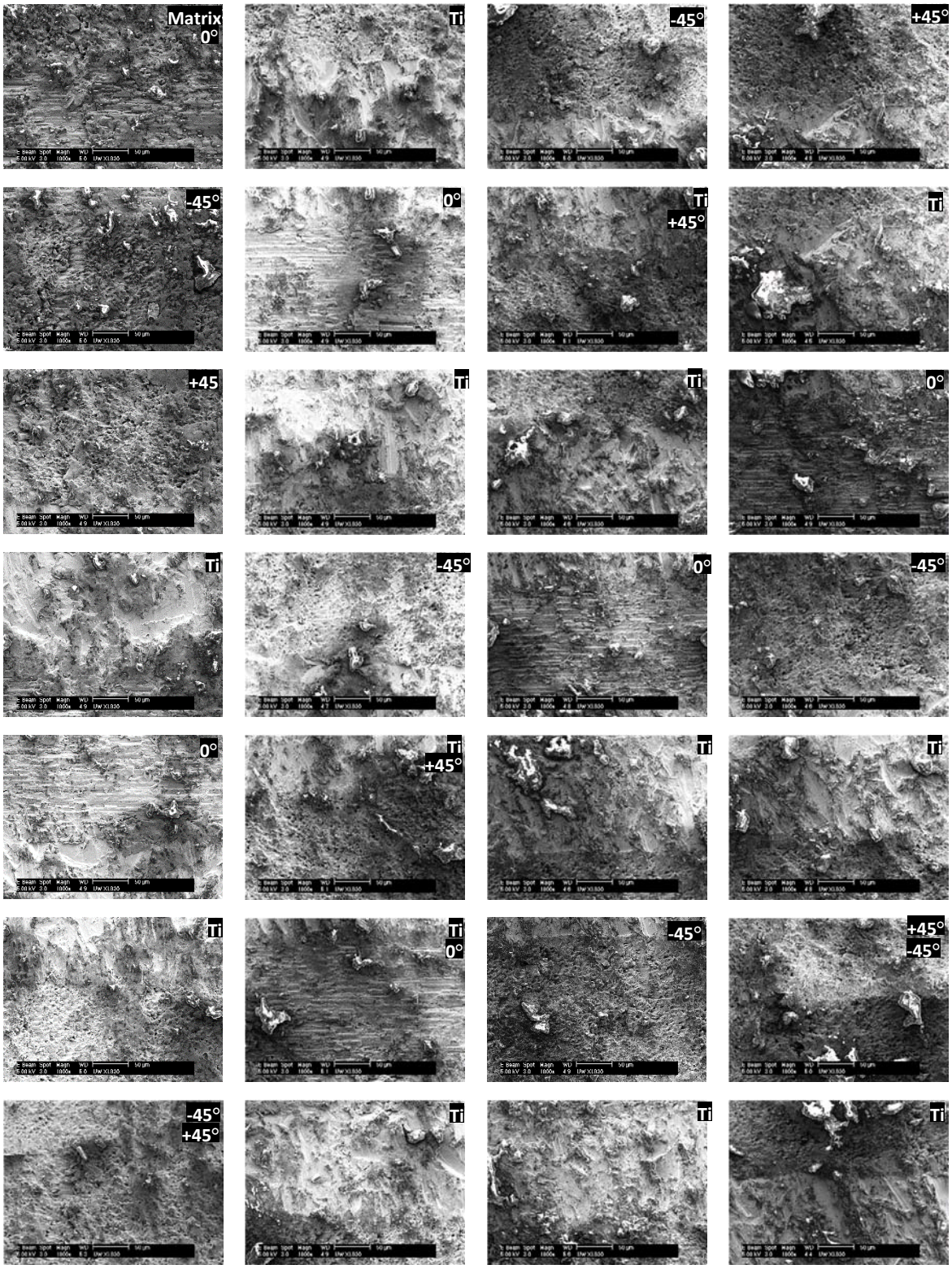

Figure 4.6. SEM micrographs of 10.5 mm thick, straight cut AWJ-1 specimen (Plies 1-33)

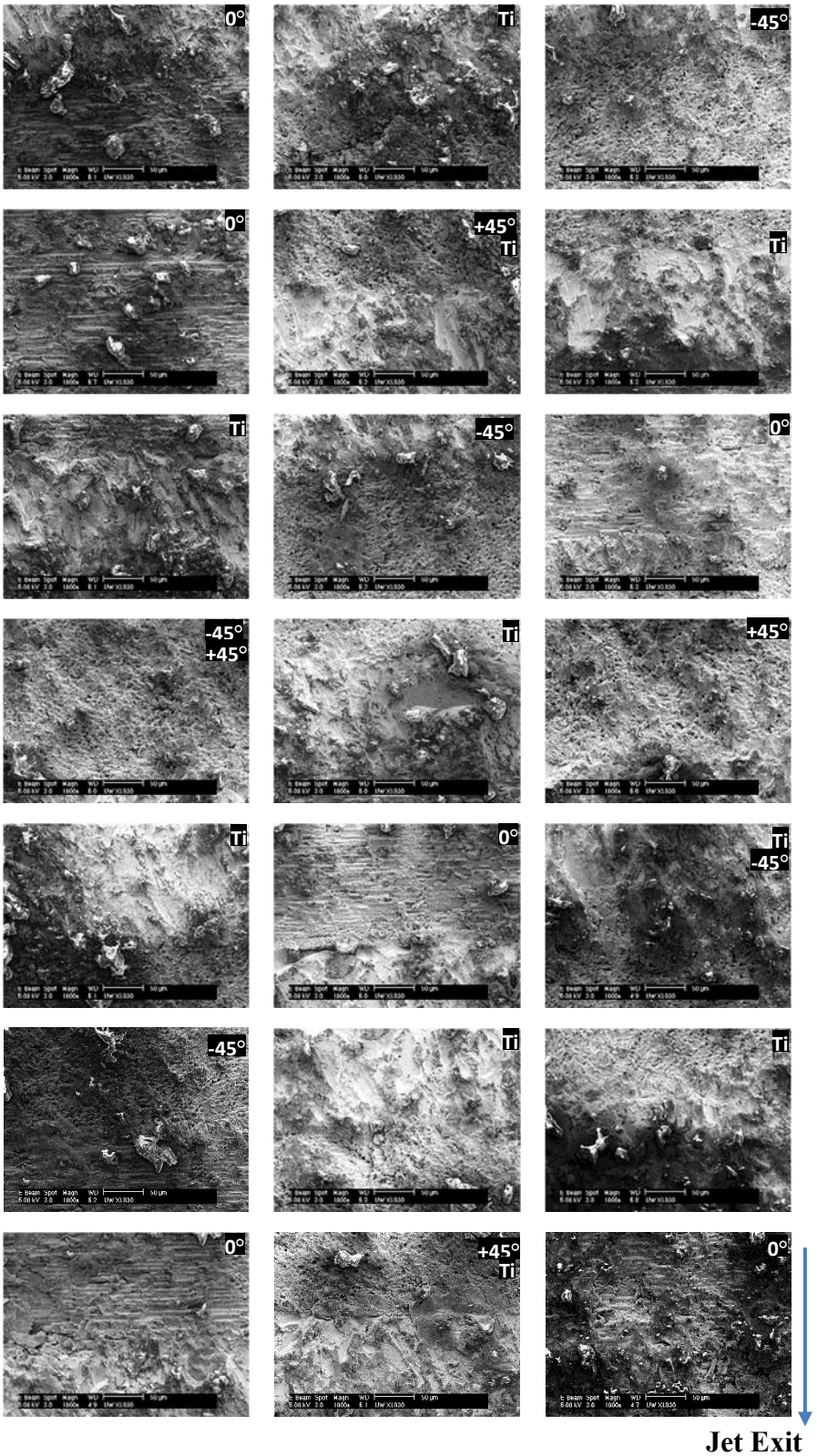

Figure 4.7. SEM micrographs of 10.5 mm thick, straight cut AWJ-1 specimen (Plies 34-58)

4.1 KERF TAPER

The taper angle and taper ratio for each experiment is depicted in Figure 4.8 and Figure 4.9 respectively for 7.56 mm thick specimen, and Figure 4.10 and Figure 4.11 respectively for 10.5 mm thick specimen. The kerf taper angles and kerf taper ratios for all profile features in a given AWJ specimen were averaged. The maximum taper angle observed for thin laminate was 0.67° specimen which dropped down to 0.62° (7.6% reduction) for thicker laminate. As discussed in Chapter 2, the composite ply distortion and removal is significantly affected by water power of the jet, depicting low resistance of composite matrix to curtail the inherent characteristic of jet expansion. For thinner laminates, the jet penetration time was less, giving less time for water to erode the matrix. However, increased thickness demands more energy and jet penetration time, leading to more distortion due to jet expansion and less taper. The reduction in taper was also evident from the increment of maximum exit overcut which is 127 μm for 7.56 mm thick specimen, and 140 μm for 10.5 mm thick specimen.

The average minimum taper angles observed for 7.56 mm thick specimens were -0.02° and 0° for AWJ-20 and AWJ-27 specimens respectively. The average minimum taper angle observed for 10.5 mm thick specimens was 0.1° and 0.19° for AWJ-28 and AWJ-31 specimens respectively. Average maximum taper angles observed for 7.56 mm thick specimens was 0.64° for AWJ-5 and AWJ-15 specimens. For 10.5 mm thick specimens, the observed average maximum taper angle was 0.58 and 0.55 for AWJ-8 and AWJ-14 specimens respectively.

In general, small arc profile features were observed with higher taper when compared to straight and large arc profile features. This can be attributed to nozzle inertial effects. Similar effects of jet acceleration and deceleration were observed for angular corners by Shanmugam et al. [85]. However, at low taper (nearly square cut) conditions, negative taper angle was observed and associated with small profile arc features in AWJ-20 and AWJ-27 specimens, whereas the corresponding large and straight arcs exhibited nearly straight kerf walls with slightly positive taper (< 0.1°). This behavior is a reasonable indication of higher overcut at high energy, especially at small arc features where the effect of jet spreading and curving due to sudden path changes become prominent. The jet cutting energy available can be assumed to be sufficient enough to penetrate easily though the thickness even after jet spreading.

The average taper ratios of all profiles were calculated for each set of experimental conditions, followed by determination of maximum and minimum values. The average minimum taper ratios observed for 7.56 mm thick specimens were 0.99 and 1.00 for AWJ-20 and AWJ-27 specimens respectively. The average minimum taper ratios for 10.5 mm thick specimens were 1.038 and 1.069 for AWJ-28 and AWJ-31 specimens respectively. The average maximum taper ratios observed for 7.56 mm thick specimens were 1.312 and 1.224 for AWJ-5 and AWJ-13 specimens respectively. For 10.5 mm thick specimens, the observed average maximum taper ratios were 1.385 and 1.295 for AWJ-8 and AWJ-32 specimens respectively.

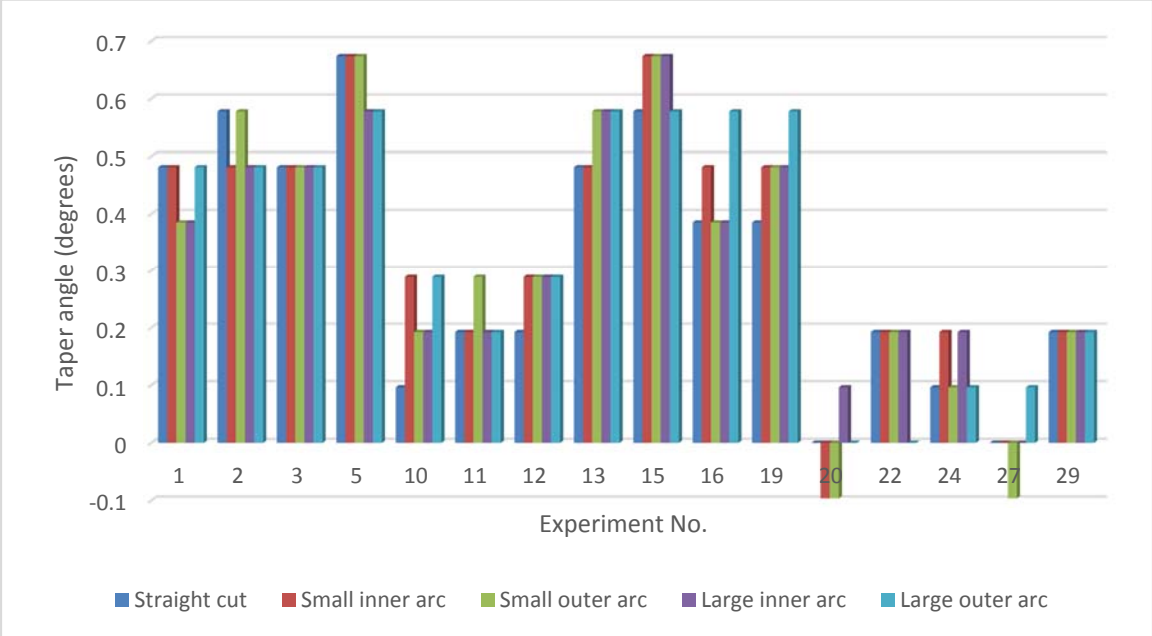

Figure 4.8. Taper angle (degrees) of 5 different profiles at each experiment run for machining 7.56 mm thick specimens

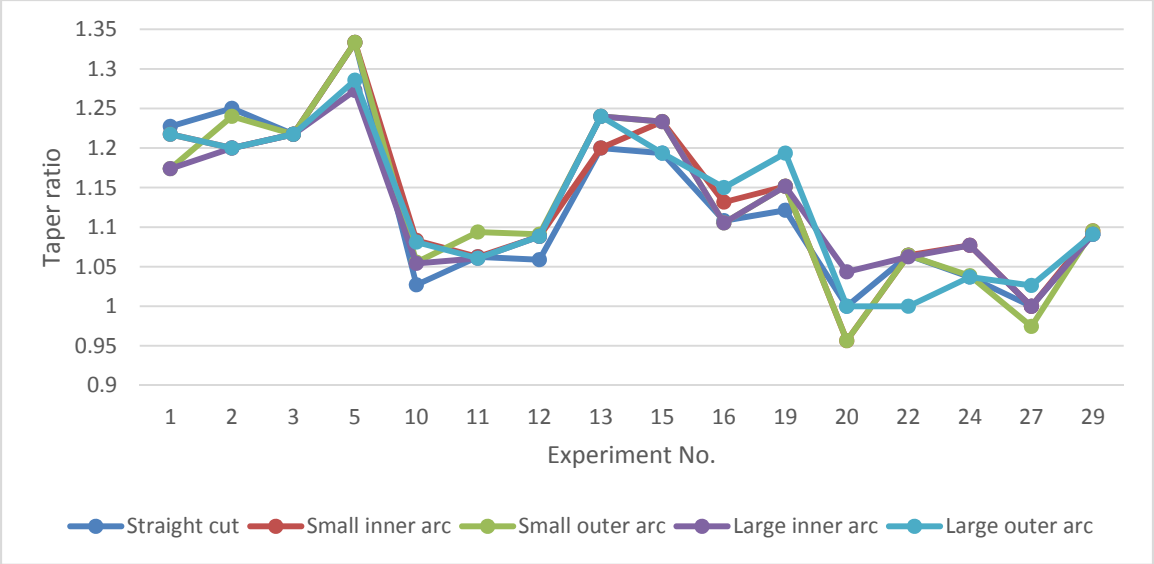

Figure 4.9. Taper ratio of 5 different profiles at each experiment run for machining 7.56 mm thick specimens

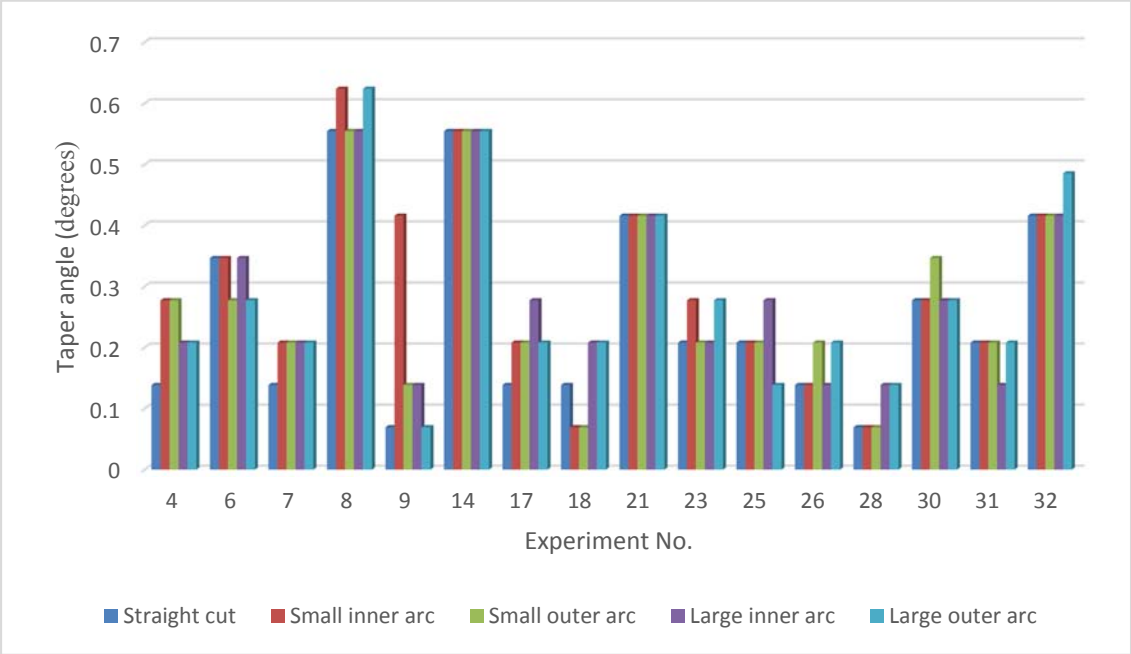

Figure 4.10. Taper angle (degrees) of 5 different profiles at each experiment run for machining 10.5 mm thick specimens

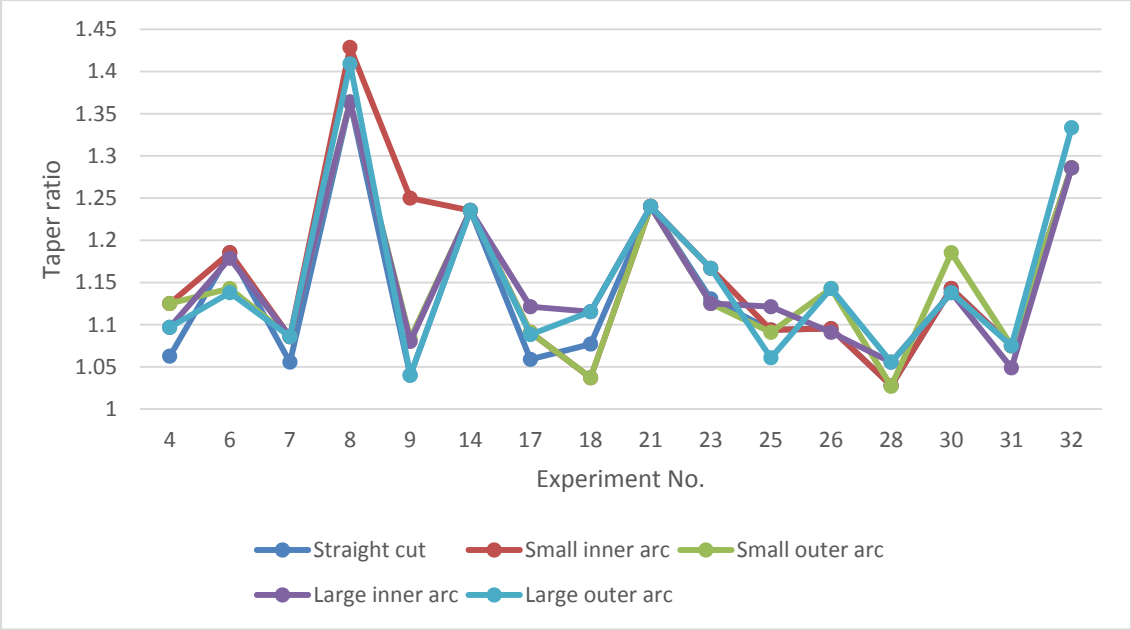

Figure 4.11. Taper ratio of 5 different profiles at each experiment run for machining 10.5 mm thick specimens

Part variation – kerf taper ratio

The variation in taper ratio associated with different profile features in a cutting geometry is a process variability measure and affects the part tolerance. The maximum kerf taper deviation was observed for AWJ-5 and AWJ-9 in 7.56 mm and 10.5 mm thickness levels respectively. For AWJ-5 specimen, kerf taper ratio was observed between 1.27 and 1.33 with 4.76% difference in the extreme values. However, for AWJ-9 specimen, the taper ratio was observed between 1.04 and 1.25 with 20.2% overall difference in the extreme values. In general, taper ratio standard deviation within a part geometry was higher for 10.5 mm thick specimens than 7.56 mm thick specimens.

Figure 4.12 depicts the kerf taper ratio as a function of jet travel distance. The standard deviation of kerf variation in AWJ-5 and AWJ-9 specimen is 0.02 and 0.07 respectively.

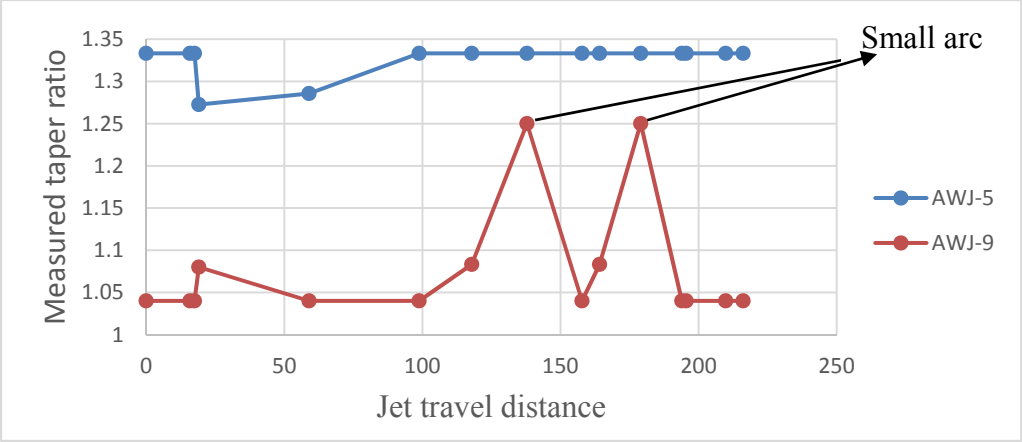

Figure 4.12. Kerf taper ratio variation along the jet trajectory for AWJ-5[2] and AWJ-9[3]

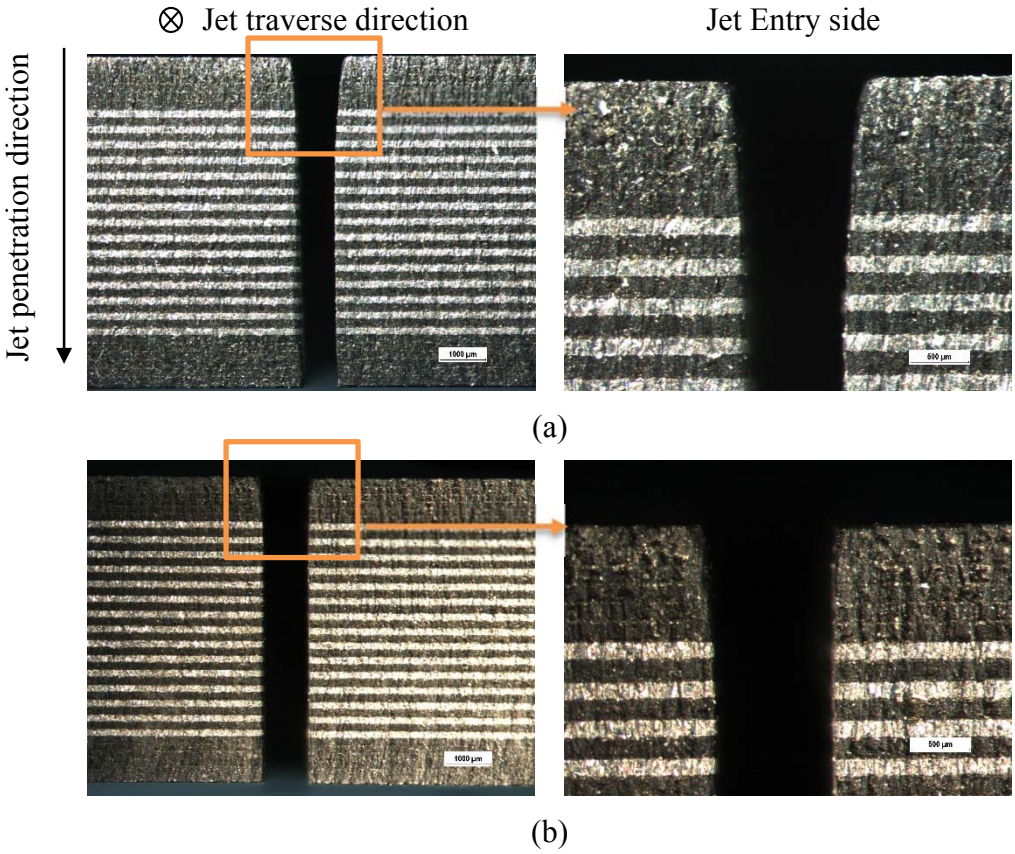

Figure 4.13. (a) Maximum, and (b) Minimum average taper kerf wall associated with 7.56 mm thick AWJ- 5 and AWJ-27 respectively.

[2] Standard deviation : 0.019
[3] Standard deviation : 0.073

Figure 4.13 and Figure 4.14 shows the maximum and minimum kerf wall geometry for 7.56 mm and 10.5 mm thick specimens respectively. The figures depict maximum kerf angle variation and thus maximum damage location at the jet entry side where most of the plies are composite. In general, thinner laminate showed a tendency of slightly curved kerf wall with convexity on both the kerf walls. This can be accounted by the higher composite damage at the exit and entry side in thinner laminate whereas in thick laminate the composite composition is lesser at the entry and exit side, leading up to less damage at the ends.

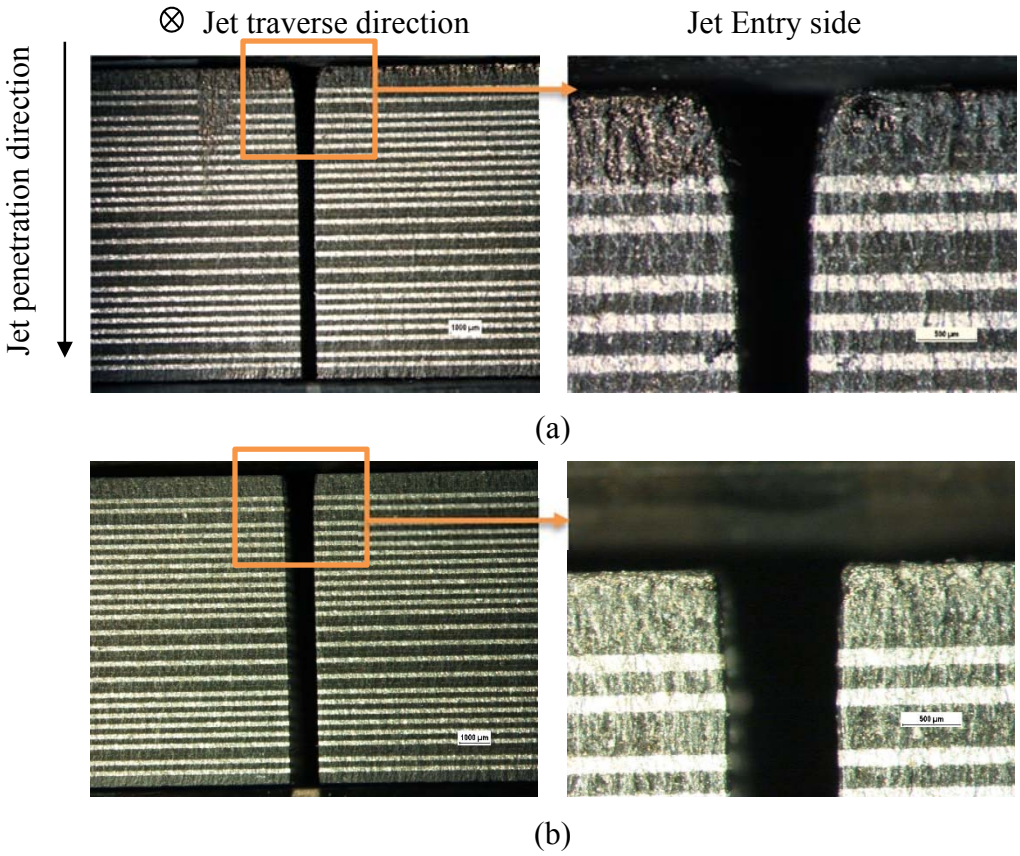

Figure 4.14. (a) Maximum, and (b) Minimum straight cut taper kerf wall associated with 10.5 mm thick AWJ- 32 and AWJ-28 respectively.

4.1.1 Analysis of variance

Kerf taper ratio for each profile feature was statistically analyzed for variance. The parametric effect on kerf taper ratio of straight cut and curved profile features is discussed in sections 4.1.1.1-4.1.1.5. Because of similar behavior of the parametric effect, straight cut taper ratio is discussed in more detail and the relevant ANOVA tables for small inner arc, small outer arc, large inner arc and large outer arc are included in APPENDIX B.

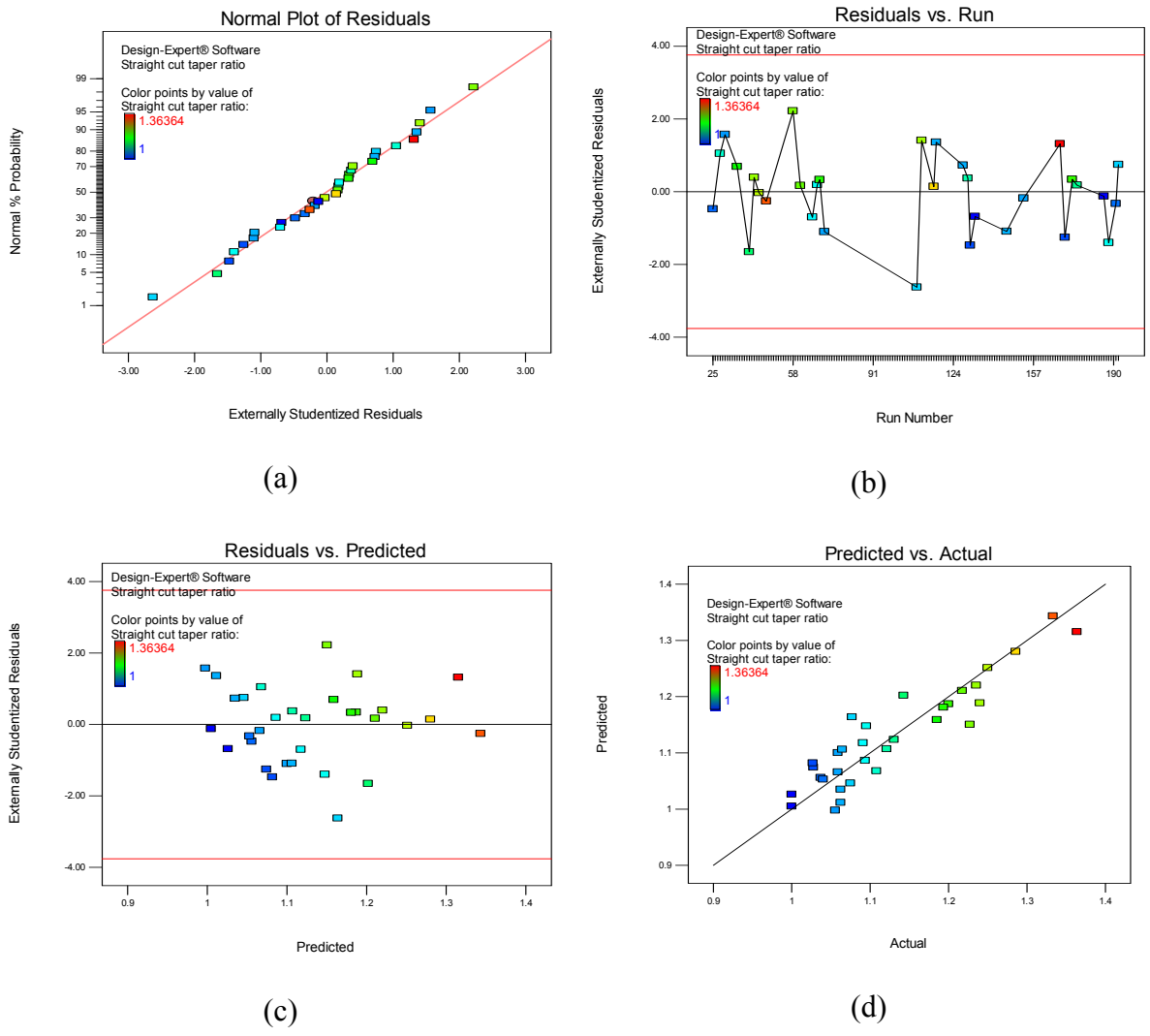

Figure 4.15. Straight cut taper ratio model (a) Normal plot of residuals, (b) Residuals versus Run plot, (c) Residual versus predicted, (d) Leverage versus Run plot

Figure 4.15 depicts the diagnostic curves for straight cut taper ratio modeling. Figure 4.15(a) shows a straight line in normal probability plot depicting Gaussian spread of errors. No pattern was identified in Residual vs run plot depicted in Figure 4.15(b). This verifies the absence of any sustained experimental error. Random scatter in Residual versus Predicted (Figure 4.15(c)) value plot verifies the model assumption of constant variance across the range of predictions. Figure 4.15(d) shows the predicted vs experimental plot. The diagnostic plots for small inner arc, small outer arc, large inner arc and large outer arc are included in APPENDIX C.

Equations (4.1)-(4.5) are the predictive regression models developed using ANOVA for five different profiles. The standard deviation of these models vary from 0.041 to 0.62.

Eq. no.	Regression model equations	R^2
(4.1)	**Straight cut taper ratio =** $0.86773 - 0.0011t - 0.0007P + 0.01683lm$ $-0.1537dm - 7.8432dn + 10.5527R + 0.0038u - 0.0016t \times lm + 0.50269t \times dn$ $+0.00097P \times dm - 0.0104lm \times dm + 0.02747lm \times dn + 0.02053dn \times u - 0.0808R \times u$	0.8451
(4.2)	**Small inner arc taper ratio =** $0.259112 + 0.148332t - 0.0008P + 0.021618lm$ $-1.83392dm - 4.93164dn + 10.8916R + 0.00548u + 9.46 \times 10^{-5} t \times P - 0.00104t \times lm$ $+0.712812t \times dn - 2.94408t \times R - 0.01091lm \times dm - 3.4 \times 10^{-5} lm \times u - 5.29476dm \times dn$ $+36.1432dm \times R + 0.025043dn \times u - 0.08576R \times u$	0.8317
(4.3)	**Small outer arc taper ratio =** $0.202451 + 0.006732t + 0.01927lm + 0.479035dm$ $-6.90767dn + 9.33678R + 0.005678u - 0.00137t \times lm + 0.399286t \times dn$ $-0.01154lm \times dm + 0.026367lm \times dn - 2.5 \times 10^{-5} lm \times u + 0.02298dn \times u - 0.08876R \times u$	0.8480
(4.4)	**Large inner arc taper ratio =** $1.69141 + 0.000531t - 0.0008P + 0.008478lm$ $-1.12484dm - 3.80664dn - 5.60585R + 0.004748u - 0.00131t \times lm + 0.413898t \times dn$ $+1.19 \times 10^{-5} P \times lm - 0.00667lm \times dm + 0.024061lm \times dn - 2 \times 10^{-5} lm \times u$ $-4.29691dm \times dn + 23.6862dm \times R + 0.018497dn \times u - 0.07422R \times u$	0.8934
(4.5)	**Large outer arc taper ratio =** $0.923662 - 0.02238t - 0.00146P + 0.008271lm$ $+0.198391dm - 7.58122dn + 12.8531R + 0.009079u - 0.00097t \times lm + 0.422296t \times dn$ $+1.11 \times 10^{-5} P \times lm + 0.001091P \times dm - 0.01262lm \times dm + 0.029976lm \times dn$ $-2.4 \times 10^{-5} lm \times u - 0.00234dm \times u + 0.024996dn \times u - 0.11561R \times u$	0.9656

4.1.1.1 Straight cut taper ratio

The ANOVA results of parametric effect on straight cut taper ratio are detailed in this section. Figure 4.16 shows the percentage contribution of process variables on the entry and exit kerf width. The mixing tube diameter, traverse speed, thickness-tube length and thickness-orifice bore size contributes to 72.2%, 3.7%, 2.0% and 1.7% respectively for entry kerf width, and 21.6%, 13.4%, 10.7% and 9.1% respectively for exit kerf width. The residual contribution of 16.6% and 7.5% depict the error in predicted and experimental value.

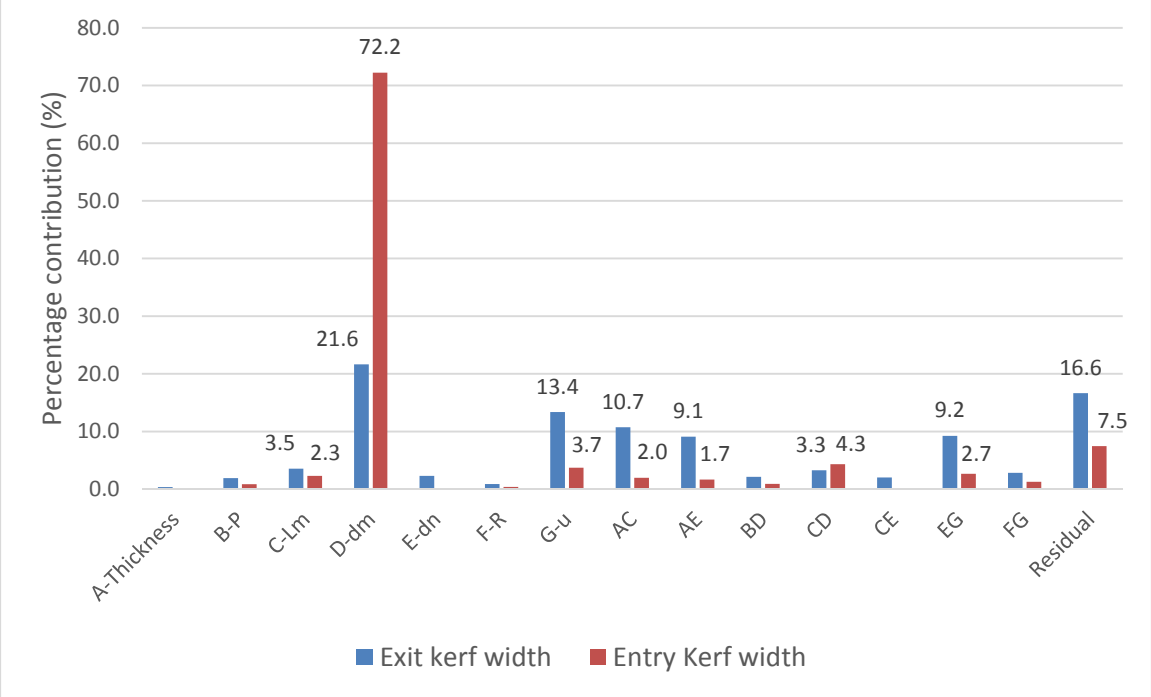

Figure 4.16. Percentage contribution of variables on entry and exit kerf width for AWJ straight cutting of TiGr.

Besides, the exit kerf width was largely influenced by mixing tube length and diameter interaction (4.3% contribution) after mixing tube diameter. Clearly, the nozzle diameter is found to be greatly influencing the entry and exit kerf width of TiGr specimens within the range of experimental conditions and parameters.

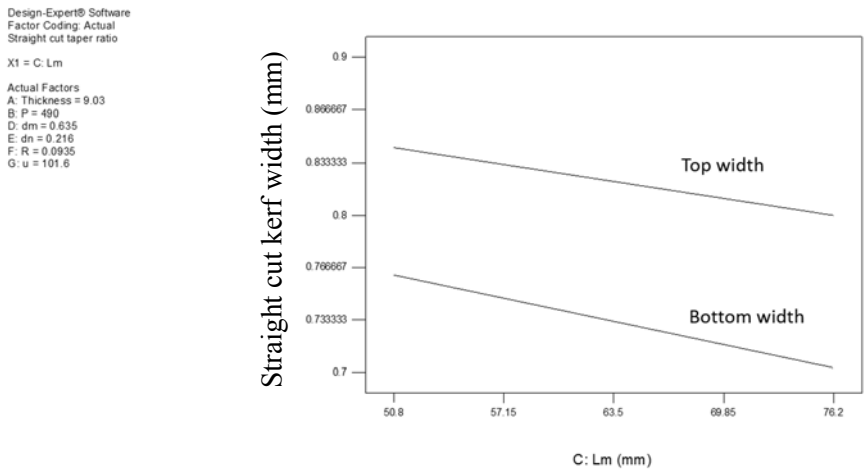

Figure 4.17. One factor effect of mixing tube length on top and bottom width.

Figure 4.17 depicts the effect of mixing tube length on jet entry and exit kerf width. A decrease in kerf width with mixing tube length was found at all penetration depths indicating increased jet energy, producing smallm kerf overcut and allowing the jet to penetrate faster before the radial jet expansion and kerf distortion.

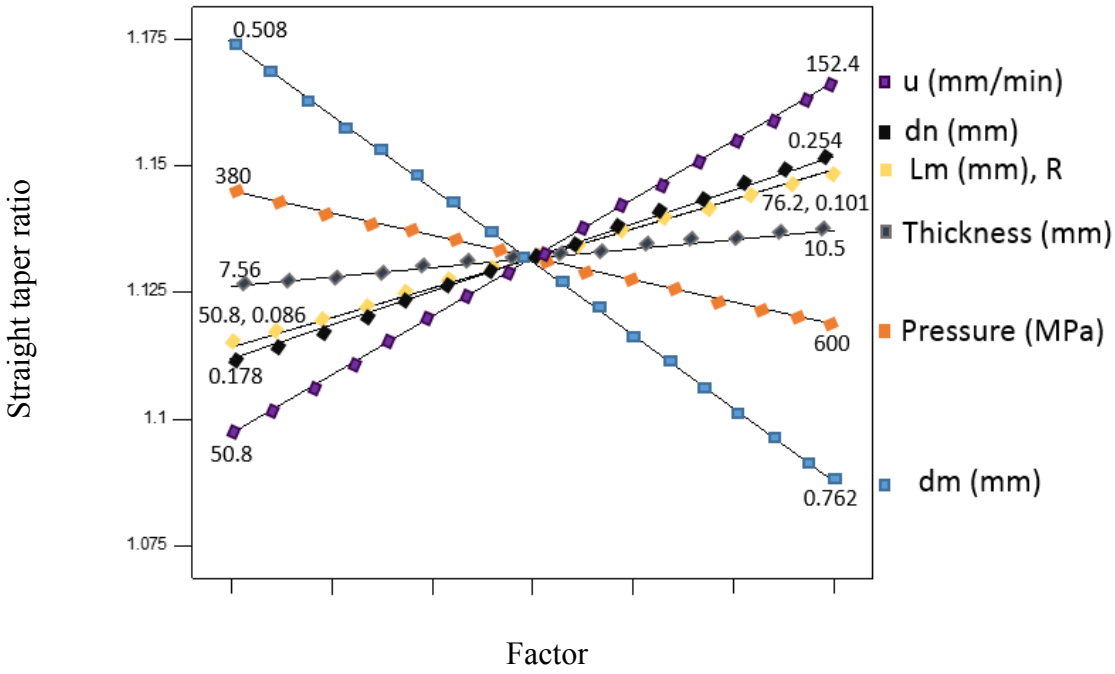

Figure 4.18. Single factor effect (without any interaction) of process variables on straight cut taper ratio.

Figure 4.18 depicts the effect of each process variable in the model without interaction effect. The variables such as length and diameter of mixing ratio, orifice diameter, and jet traverse speed have significant effect on taper ratio even without the consideration of interaction among them. Besides, the exact effect of variable interaction is required for the comprehension and prediction of taper ratio. The main interaction effects and observations are documented below (Figure 4.19).

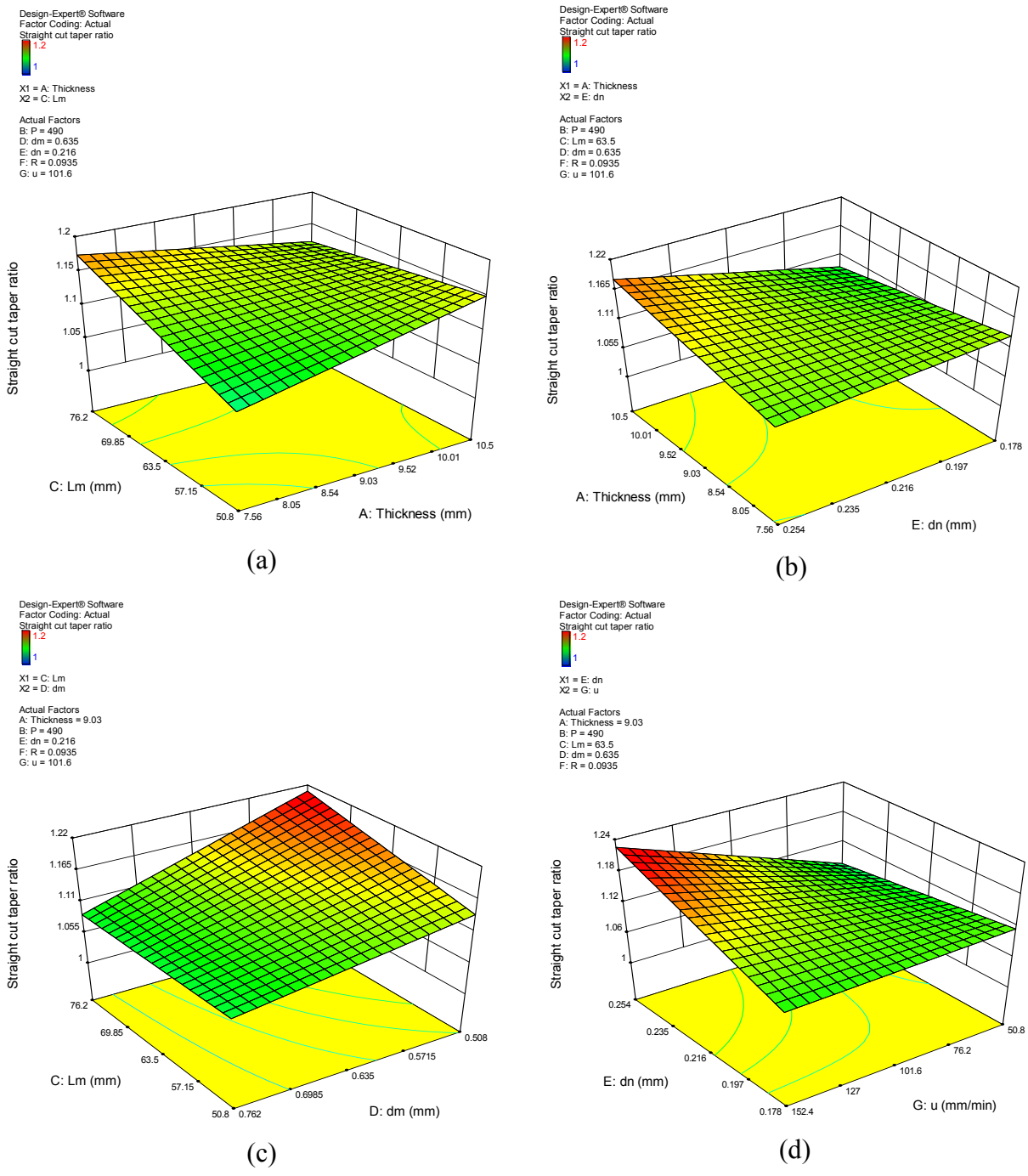

Figure 4.19. Interaction effect between (a) thickness and mixing tube length, (b) thickness and orifice diameter, (c) mixing tube length and diameter, and (c) traverse speed and orifice diameter on kerf taper ratio

Thickness-Mixing tube length interaction

Figure 4.19(a) shows the interaction effect of thickness and mixing tube length on the kerf taper ratio. The kerf ratio was found to exhibit a negative trend with increasing mixing tube length for thicker specimens and vice versa for thinner specimens. For 10.5 mm thick specimens, the kerf taper ratio reduction of 2.31% from 1.149 to 1.123 was observed with 50% increment in mixing tube length from 50.8 mm to 76.2 mm. However, for 7.56 mm thick specimen, kerf taper ratio was increased 8.19% from 1.08 to 1.17 with the increment in tube length.

Overall, this interaction effect can be interpreted as a desirability of higher mixing tube length at higher thickness in order to supplement the higher energy requirement due to increased penetration depth. A longer mixing tube would allow more time for energy transfer from water to abrasive particles and hence producing a more coherent and cutting efficient waterjet slurry. A smaller mixing tube would cause a low energy incoherent jet, leading up to a high taper ratio.

Similarly, low taper can be achieved by using short mixing tube for thin specimens. This can be attributed to less energy requirement of thinner specimens which is easily realized with small mixing tubes. Besides, using a mixing tube longer than the optimum would mean imparting more than the required energy, creating more distortion and significantly high taper ratio, indicating the increased entry damage at prolonged exposure of the high energy jet. An extremely high F-value (10.95) for this combination of parameters emphasize its significant contribution in kerf taper quality, necessitating the use of mixing tube with an optimum length for each thickness level. The result is coeval with the investigations of Jegaraj et al. [52], emphasizing the existence of an optimum mixing tube at which the momentum transfer is maximum.

Thickness - Orifice diameter interaction

Figure 4.19(b) depicts the interaction effect between specimen thickness and orifice bore size on straight cut taper ratio. The taper ratio was found to be decreasing with orifice bore size at lower thickness while a significant 8.12% increase in taper ratio was observed at higher thickness level (10.5 mm). The results were inconsistent with the established reasoning of increased water

flow rate with orifice diameter at a given load ratio, thus increased abrasive flow rate and more cutting power, leading to less kerf taper. However, it can be argued that unlike metals, the mechanism of composite material removal is significantly affected by the water power of the jet. It is evident from the results that a thicker laminate would have more effect of water power assisted by slow penetration and removal of composite plies, especially when the facesheets are composite plies, causing more distortion at the top leading high taper ratio.

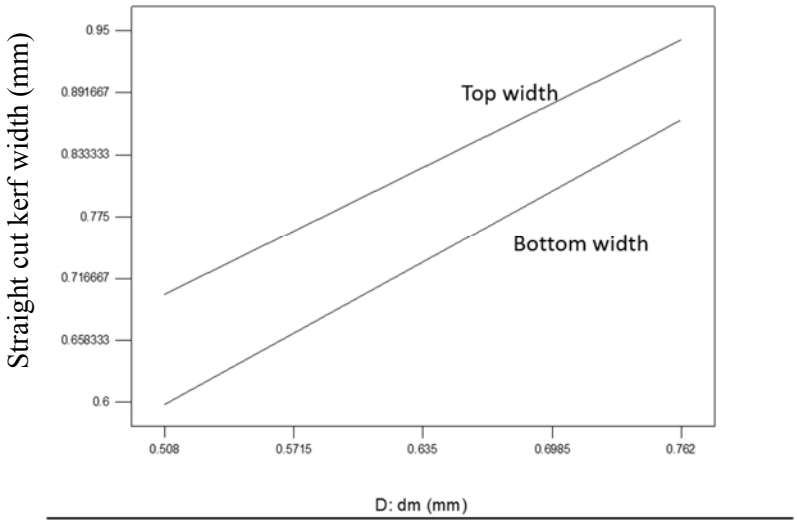

Figure 4.20. One factor effect of mixing tube diameter on top and bottom width.

Mixing tube length – Diameter interaction

Figure 4.19(c) depicts the interaction between mixing tube geometrical features- length and diameter. At 50.8 mm length a 4.7% increase in taper ratio is observed with 33.3% reduction in tube mixing tube diameter. The taper ratio is steeply increased at 76.2 mm tube length with a variability of 9.8% within the chosen diametrical limits.

Overall, higher taper is observed at high aspect ratio (length/diameter) and least at low aspect ratio. Even though jet power imparted per unit area is reduced with higher mixing tube diameter accounting for higher taper, a low taper is observed. This can be justified by the sufficiency of imparted cutting power required to remove the material throughout the diametrical range along with the jet expansion at exit side leading up to higher exit kerf width.

Orifice diameter - Jet traverse speed interaction

The interaction effect of orifice diameter and traverse speed is depicted in Figure 4.19(d). With low orifice diameter and thus low mass flow rate of water as well as abrasive at a given load ratio, an insignificant variation of taper ratio with the traverse speed (-0.52%) was observed. However, the effect of traverse speed is dominating at large orifice diameter with a 14.22% decrease in taper ratio within the experimental limits of high and low traverse speed. The effect clearly indicates an increase in jet exposure time and power transferred to the workpiece material at slower jet traverse speed, allowing a more efficient cut with decreased taper. Also, highest taper ratio was observed at highest orifice diameter (0.254mm) and highest traverse speed (152.4mm/min).

4.1.1.2 Small inner arc taper ratio

Figure 4.21(a) depicts the interaction effect of mixing tube length and thickness on taper ratio. A general trend of increased taper ratio with mixing tube length is observed at all thickness levels. However, the effect is prominent at lower thickness (7.56 mm) where 7.3% increase in taper ratio is observed.

The interaction effect of orifice diameter and specimen thickness is shown in Figure 4.21(b). Similar to straight cut, the taper ratio was observed with a regressing trend, with 2.44% decrease in taper ratio as the orifice diameter was increased while profiling 7.56 mm thick specimen. However, the trend was found to be reversed for thicker specimen, resulting in 10.8% increment in the taper ratio from low to high diametric limits of the orifice. Also, 5.3 % decrease in taper ratio was observed from low to high thickness level at 0.178 mm orifice diameter, whereas, 8.3% increase was observed at 0.254 mm orifice diameter.

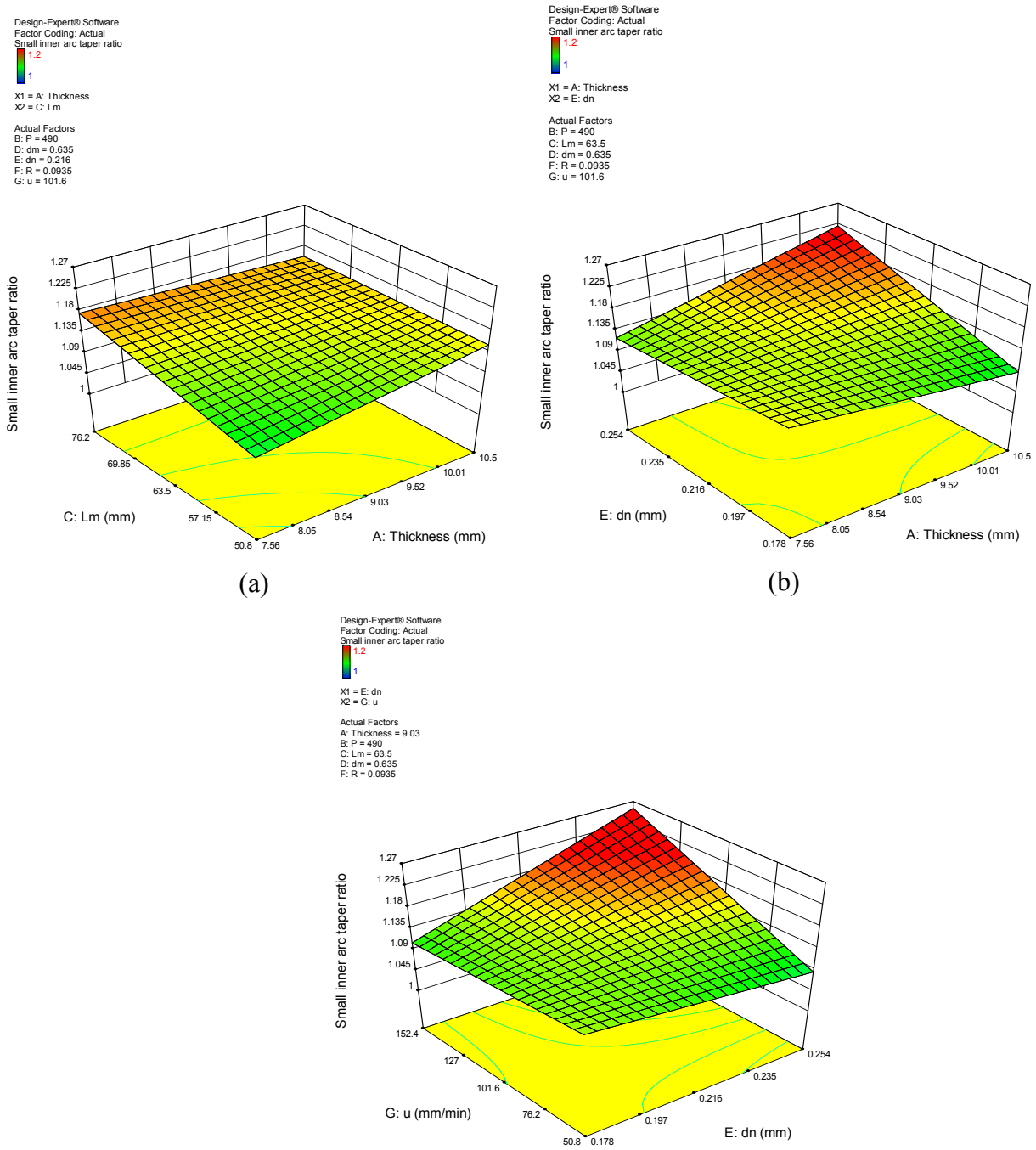

Figure 4.21. Interaction effect between (a) thickness and mixing tube length, (b) thickness and orifice diameter on taper ratio, and (c) traverse speed and orifice diameter

Figure 4.21(c) depicts the interaction effect between traverse speed and orifice diameter. At small orifice diameter, a 2.2 % decrease in taper ratio was observed with increase in traverse speed, however, the effect is reversed at larger orifice diameter, 11.86% increase in taper ratio was observed.

The lowest and highest taper ratio was observed at 0.254 mm orifice diameter and with traverse speed 50.8mm/min and 152.4mm/min respectively. This reinforces the reasoning of composite ply erosion as a dominant factor in deciding kerf taper when compared to abrasive cutting power in thicker laminates.

4.1.1.3 Small outer arc taper ratio

Figure 4.22(a) depicts the effect of thickness and mixing tube length on the kerf taper ratio. Minimum taper ratio observed is 1.07 with 50.8mm long mixing tube for 7.56 mm thick specimen. The taper ratio was increased up to 10.1% and 1.54% with increase in mixing tube length for 7.56 mm and 10.5 mm thick specimen respectively. Besides, the taper ratio was observed to be reduced to 3% with increase in specimen thickness when longer mixing tube is used.

Figure 4.22(b) depicts the interaction effect between thickness and orifice diameter. Similar to observations for straight cut profile, maximum taper ratio was observed at large orifice diameter and for thicker specimen. Around 8.2% increase in taper ratio was observed for 10.5 mm thick specimen which is fairly high than negligible increment at 7.56 mm thick specimen.

The effect of interaction betwwen mixing tube diameter and length depicted in Figure 4.22(c) shows repeatability with straight cut taper ratio. Maximum taper observed was 1.22 at small orifice diameter (0.508mm) and long mixing tube (76.2mm). 8.68% to 9.07% increase in taper ratio was observed when the geometrical parameters – diameter and mixing tube length were explored within the experimental limits.

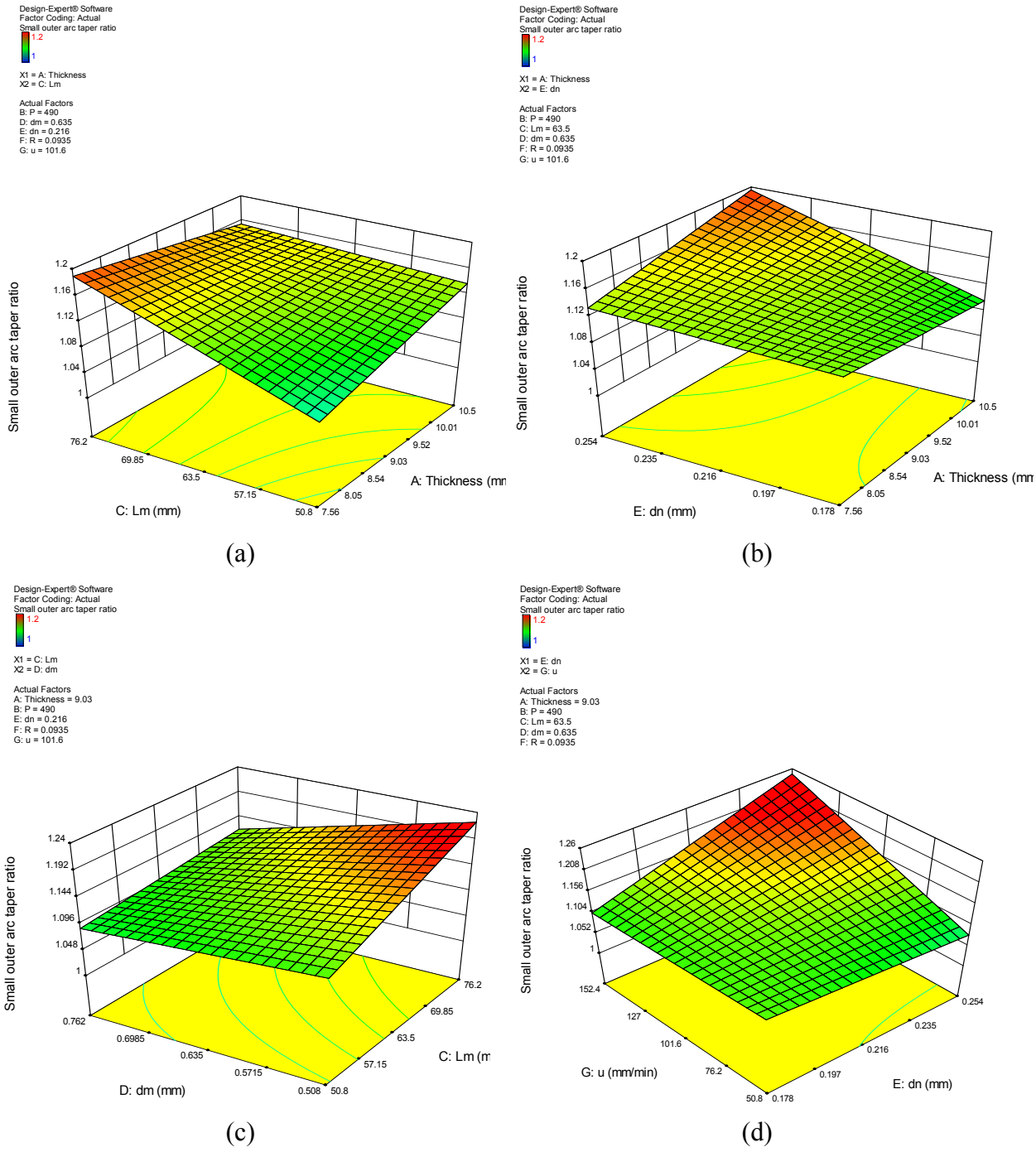

Figure 4.22. Interaction effect between (a) thickness and mixing tube length, (b) thickness and orifice diameter, (c) between mixing tube length and diameter, (d) orifice diameter and traverse speed on taper ratio

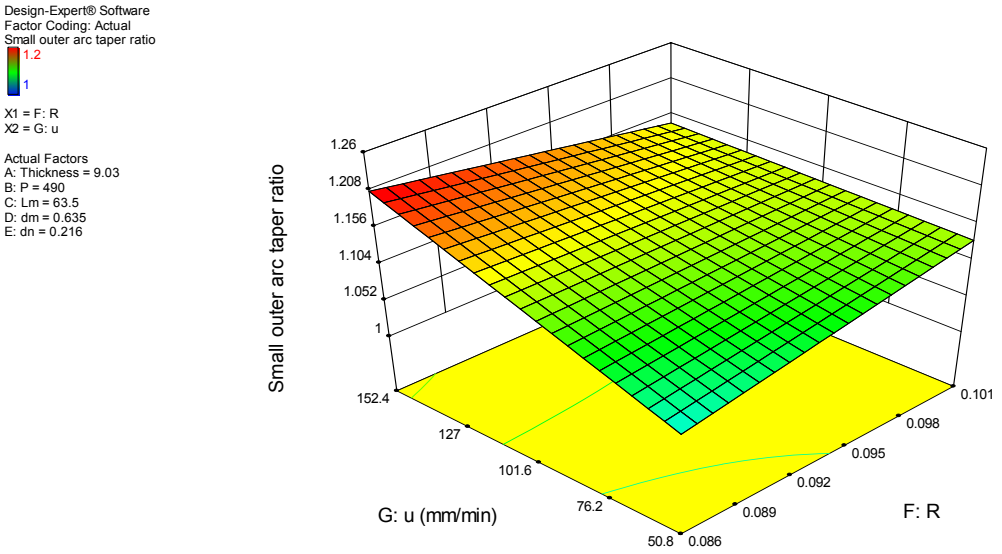

Figure 4.23 Interaction effect between traverse speed and load ratio on taper ratio

Figure 4.22(d) depicts the interaction effect of traverse speed and orifice diameter on taper ratio. 13.36% increase in taper was observed when jet traverse speed is varied from 50.8 mm/s to 152.4 mm/s at 0.254 mm orifice diameter with a negligible variation at small orifice diameter. This confirms the dominant role of orifice diameter and high sensitivity of traverse speed at greater jet power and water flow rate.

The effect of traverse speed and load ratio on taper ratio is depicted in Figure 4.23. Maximum taper ratio was observed at highest traverse speed (152.4 mm/min) and least load ratio (0.086). 12.06% increase in taper was observed at 8.6% load ratio within the experimental traverse speed limits. The results are commensurate to the reasoning of low energy at low load ratio and high traverse speed, leading upto insufficient jet cutting energy at the bottom of penetration affecting the uniformity of cut diameter.

4.1.1.4 Large inner arc taper ratio

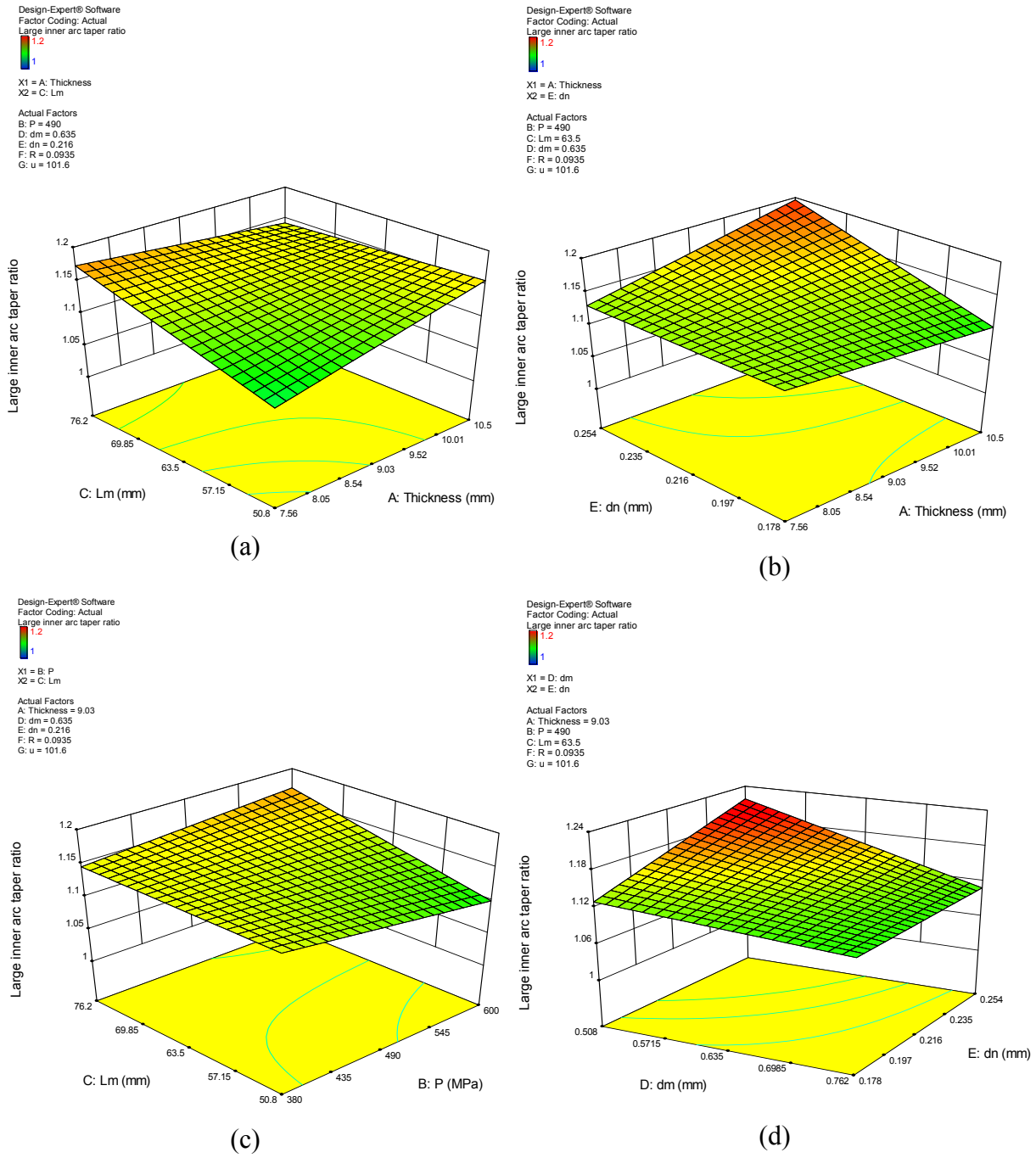

Figure 4.24. Interaction effect between (a) thickness and mixing tube length, (b) thickness and orifice diameter, (c) mixing tube length and water pressure, and (d) orifice and mixing tube diameter on taper ratio

Figure 4.24(a) depicts the effect of thickness and mixing tube length on the kerf taper ratio. Minimum taper ratio observed is 1.09 with 50.8 mm long mixing tube for 7.56 mm thick specimen. The taper ratio was increased up to 7.8% with increase in mixing tube length for 7.56 mm. A negligible 1.14% reduction in taper ration was observed with increase in mixing tube length. Besides, around 2.5% reduction was observed with increase in specimen thickness when longer mixing tube is used.

Figure 4.24(b) depicts the interaction effect between thickness and orifice diameter. Similar to observations for other profiles, maximum taper ratio was observed at large orifice diameter and for thicker specimen. Around 8.38% increase in taper ratio was observed for 10.5 mm thick specimen which is fairly high than negligible increment at 7.56 mm thick specimen.

The interaction effect of water pressure and mixing tube length is shown in Figure 4.24Figure 4.22(c). Lowest taper ratio equivalent to 1.10 is achieved at 600 MPa with 50.8 mm long mixing tube. Taper was increased with mixing tube length with gradient of taper ratio increase higher at high pressure level. The taper ratio was increased 6.3% and 0.22% at 600 MPa and 300 MPa pressure respectively. The effect of interaction between mixing tube diameter and orifice diameter is depicted in Figure 4.24(d). Maximum taper ratio obtained was 1.22 at small nozzle diameter (0.508 mm) and large orifice diameter (0.254 mm). The effect of orifice diameter was negligible at large nozzle diameter. However, 7.77% increase in taper ratio was observed with increase in orifice bore at small nozzle diameter (0.508 mm).

Figure 4.25(a) depicts the interaction effect of traverse speed and orifice diameter on taper ratio. 11.50% increase in taper was observed when jet traverse speed is varied from 50.8mm/s to 152.4mm/s at 0.254mm orifice diameter with a negligible variation at small orifice diameter. This again confirms the dominant role of orifice diameter and high sensitivity of traverse speed at greater jet power and water flow rate.

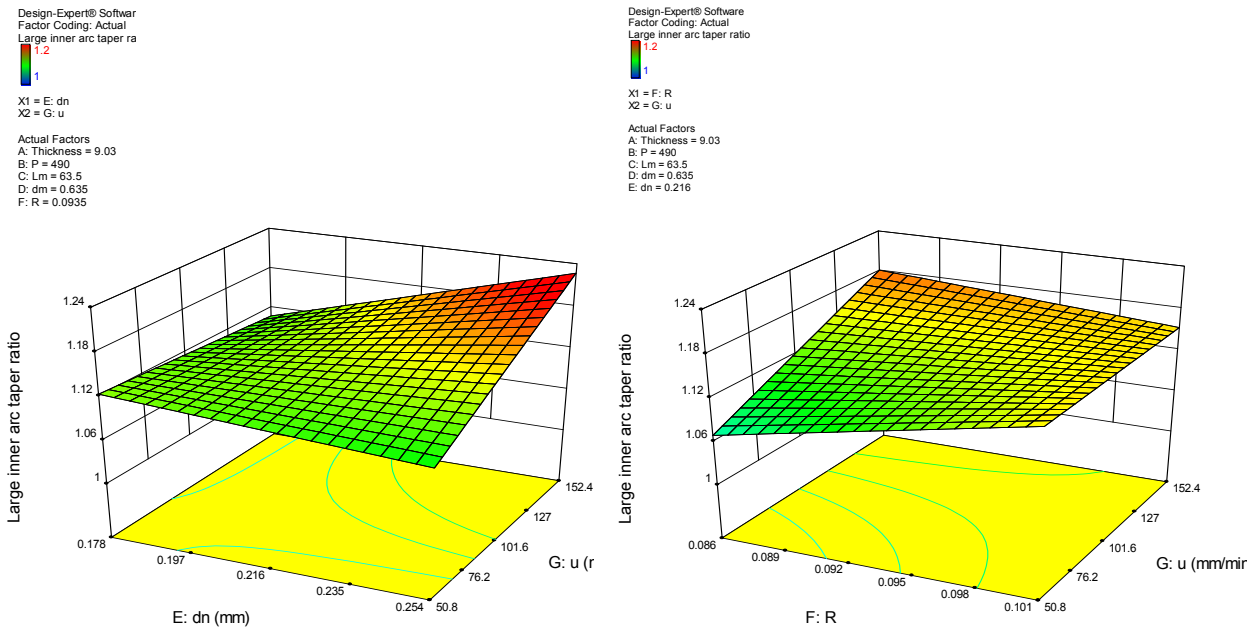

Figure 4.25. Interaction effect between (a) orifice diameter and traverse speed, and (b) load ratio and traverse speed on taper ratio

The effect of traverse speed and load ratio on taper ratio is depicted in Figure 4.25(b). Maximum taper ratio was observed at highest traverse speed (152.4 mm/min) and least load ratio (0.086). 10.43% increase in taper was observed at 8.6% load ratio within the experimental traverse speed limits. The results are commensurate to the reasoning of low energy at low load ratio and high traverse speed, leading upto insufficient jet cutting energy at the bottom of penetration affecting the kerf width.

4.1.1.5 Large outer arc taper ratio

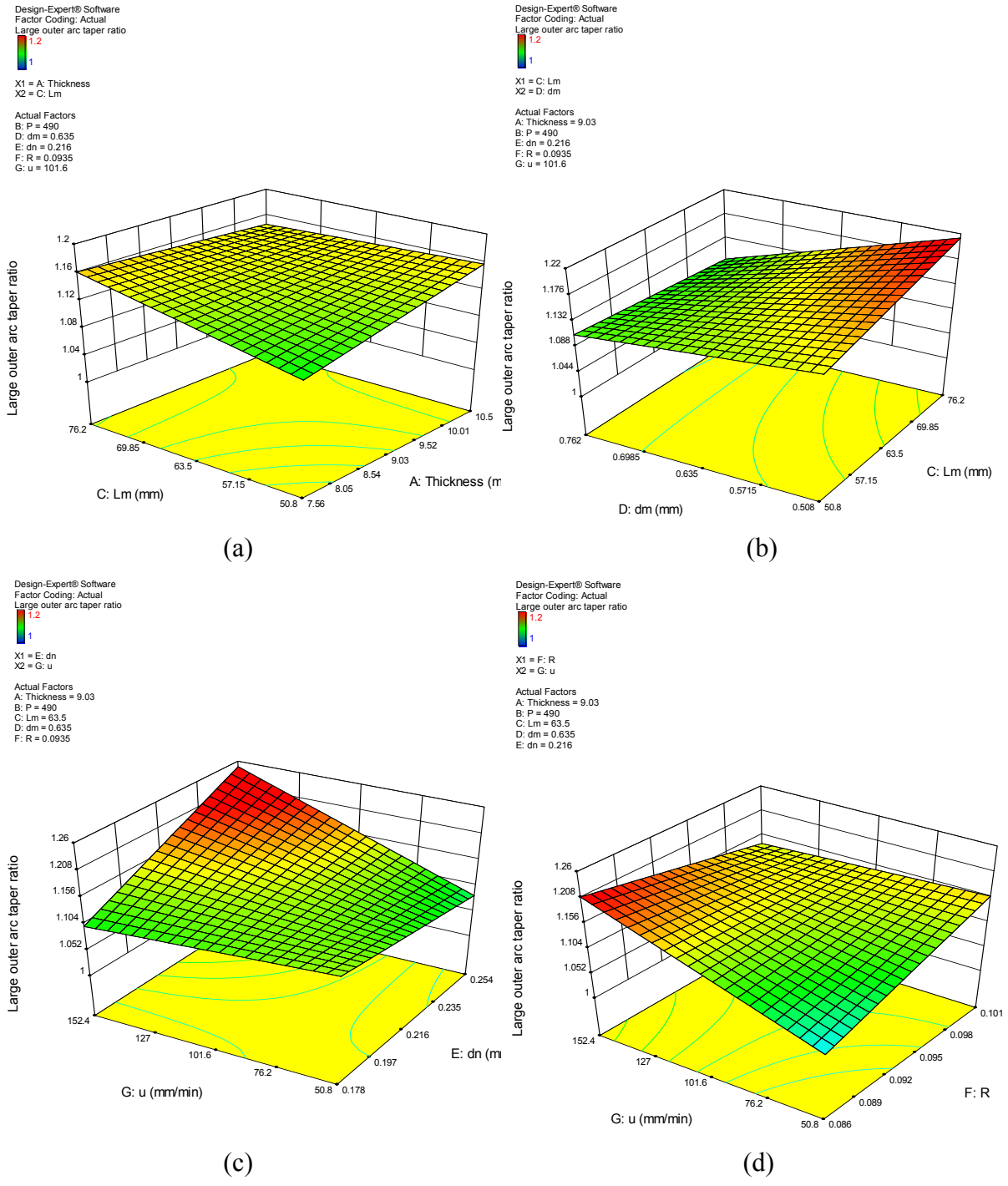

Figure 4.26. Interaction effect between thickness and mixing tube length, (b) mixing tube length and diameter, (c) orifice diameter and traverse speed, and (d) load ratio and traverse speed on taper ratio.

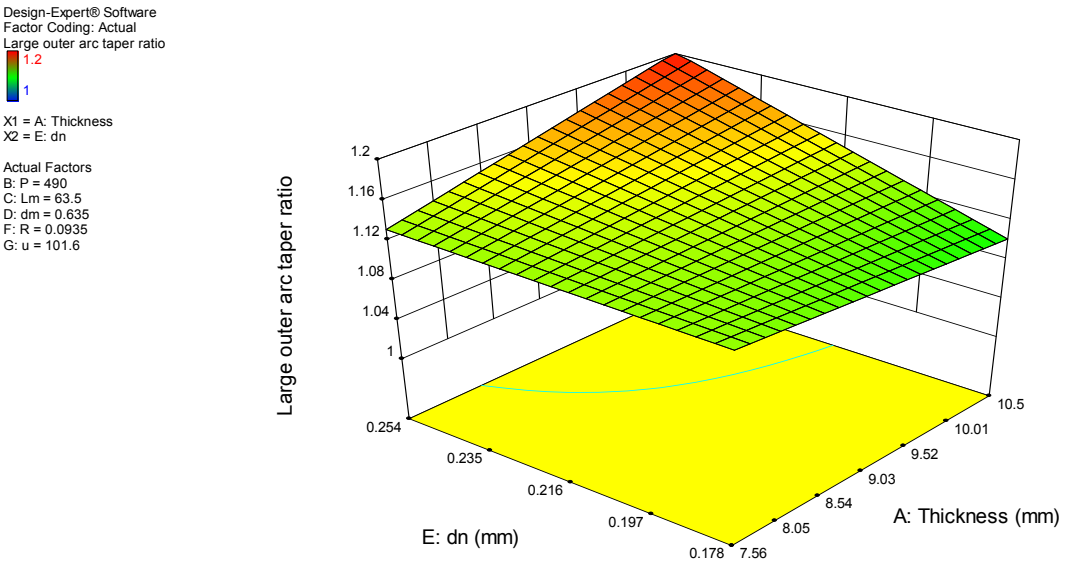

Figure 4.27. Interaction effect between orifice diameter and specimen thickness.

The effects of variables on large outer arc taper ratio were similar to the large inner arc. Figure 4.26 shows the interaction effect between thickness and mixing tube length, mixing tube length and diameter, orifice diameter and traverse speed, and load ratio and traverse speed on kerf taper ratio. A minimum taper ratio was obtained for 7.56 mm thick specimen at 50.8 mm long mixing tube. The taper ratio 1.1 at 50.8 mm long mixing tube is increased to 5.55% at 76.2 mm long mixing tube for 7.56mm thick specimen. Also, maximum taper was observed at lower mixing tube diameter (0.508mm) and longer mixing tube (76.2 mm). This concludes a maximum taper at high aspect ratio (lm/dm=150). Traverse speed and orifice diameter interaction effect was significantly high with maximum taper ratio of 1.25 at 152.4 mm/min speed and 0.254 mm orifice diameter. The effect of traverse speed was negligibly small at 0.178 mm orifice bore size. However, at 0.254 mm orifice bore, the taper ratio increased upto 15.12% with increase in traverse speed from 50.8 mm/min to 152.4 mm/min. Besides, the interaction between traverse speed and load ratio indicated maximum and minimum taper ratio of 1.21 and 1.55 respectively at 8.6% load ratio. Figure 4.27 depicts the interaction effect between orifice diameter and specimen thickness. At large orifice diameter (0.254 mm) the sensitivity of thickness on taper ratio was high with maximum taper ratio of 1.2 at 10.5 thickness and 0.254mm orifice diameter.

4.2 SURFACE INTEGRITY

The surface integrity was determined in terms of kerf wall roughness measured in directions longitudinal and transverse to jet traverse direction. The transverse roughness measured for five different profiles at each experimental condition is compiled in this section. Typical AWJ 2D and 3D kerf wall profiles were constructed and compared with diamond cut profiles. The transverse kerf wall irregularities are discussed in section 4.2.1 and statistically characterized in section 4.2.2. ANOVA and mathematical models for transverse roughness (R_z) are compiled in section 4.2.3. Longitudinal kerf quality evaluation is included in section 4.2.4. The specimens yielding maximum taper (AWJ-5 and AWJ-32) were selected for longitudinal roughness analysis.

The average transverse surface roughness (Ra) of all 5 profile features were calculated for each set of experimental condition, followed by determination of maximum and minimum values. The average maximum transverse surface roughness (Ra) observed for 7.56 mm thick specimens was 3.70 µm and 3.58 µm for AWJ-16 and AWJ-22 specimens respectively. For 10.5 mm thick specimens the average maximum transverse R_a observed was 4.0 µm and 4.93 µm for AWJ-4 and AWJ-25 specimens respectively.

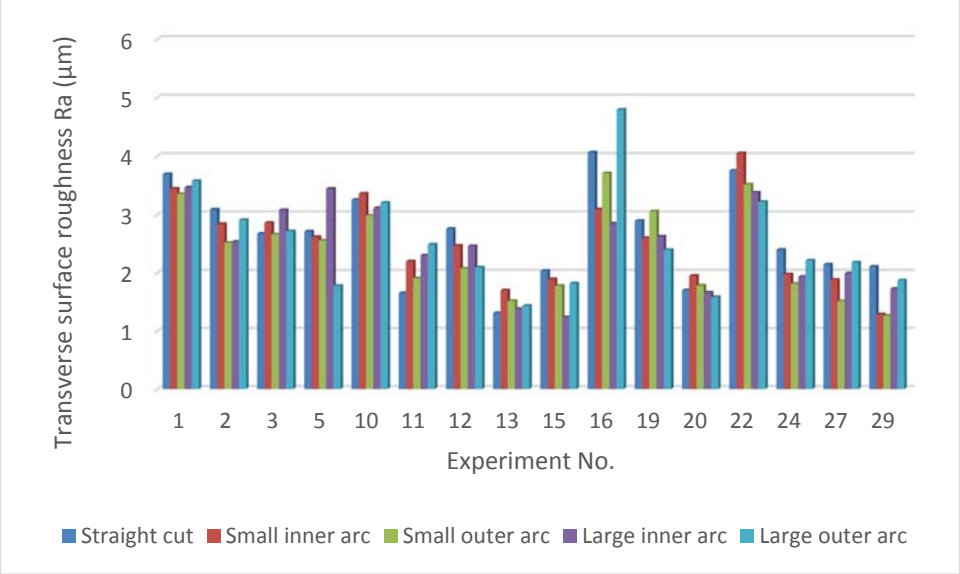

Figure 4.28. Transverse surface roughness (µm) of 5 different profiles at each experiment run for machining 7.56 mm thick specimens

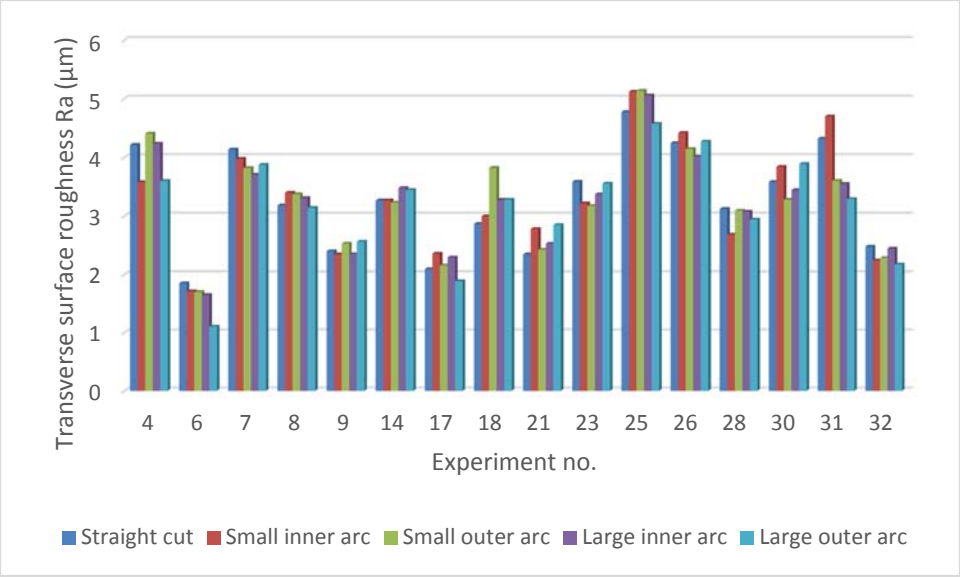

Figure 4.29. Transverse surface roughness (μm) of 5 different profiles at each experiment run for machining 10.5 mm thick specimens

The average minimum transverse surface roughness observed for 7.56 mm thick specimens was 1.47 μm and 1.65 μm for AWJ-13 and AWJ-29 specimens respectively, and for 10.5 mm thick specimens was 1.60 μm and 2.16 μm for AWJ-28 and AWJ-32 respectively. Overall, 235% variation in transverse R_a was observed within the range of experimental conditions.

Part variation – Transverse R_z

The average transverse roughness was found varying with different profile features machined under same experimental conditions. The cutting profile dependence of machining quality in terms of kerf roughness was analyzed by determining the standard deviation of roughness values for all 5 profiles machined with same process parameters. This standard deviation, calculated for each of the 32 experimental conditions, was compared to identify the conditions leading to maximum trajectory dependence in AWJ cutting process.

In general, the standard deviation of transverse R_z was observed to be higher than that of kerf taper ratio. This implies higher profile sensitivity of roughness R_z than taper ratio. The maximum deviation of transverse R_a was observed for 7.56 mm thick AWJ-16 and 10.5 mm thick AWJ-31 specimen. For AWJ-16 specimen, transverse R_z was observed between 18.22 μm and 29.33 μm with 61% difference in the extreme values. However, for AWJ-31 specimen, the taper

ratio was observed between 19.1 µm and 27.33 µm with 43.1% overall difference in the extreme values. In general, standard deviation of transverse R_z within a part geometry was higher for 7.56 mm thick specimens than 10.5 mm thick specimens.

Figure 4.12 depict the transverse roughness R_z as a function of jet travel distance. The standard deviation of kerf variation in AWJ-16 and AWJ-31 specimen is 0.78 and 0.59 respectively. In addition, maximum roughness R_z was observed for straight cut than curved profile.

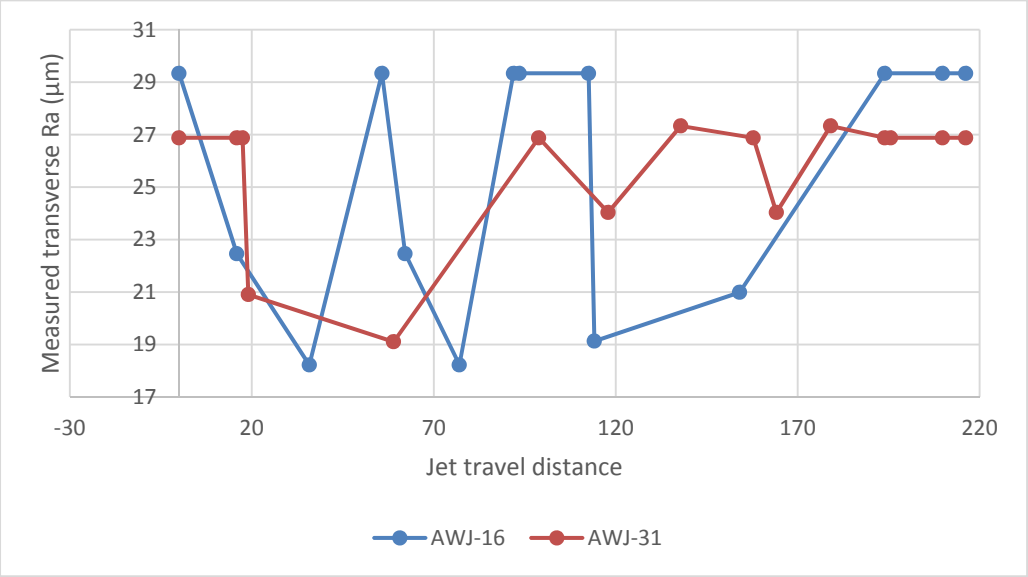

Figure 4.30. Kerf taper ratio variation along the jet trajectory for AWJ-16[4] and AWJ-31[5]

Transverse surface roughness profiles measured at different locations in the cutting geometry for AWJ-16 and AWJ-31 specimens are depicted in Figure 4.31 and Figure 4.32 respectively.

[4] Standard deviation : 0.78
[5] Standard deviation : 0.59

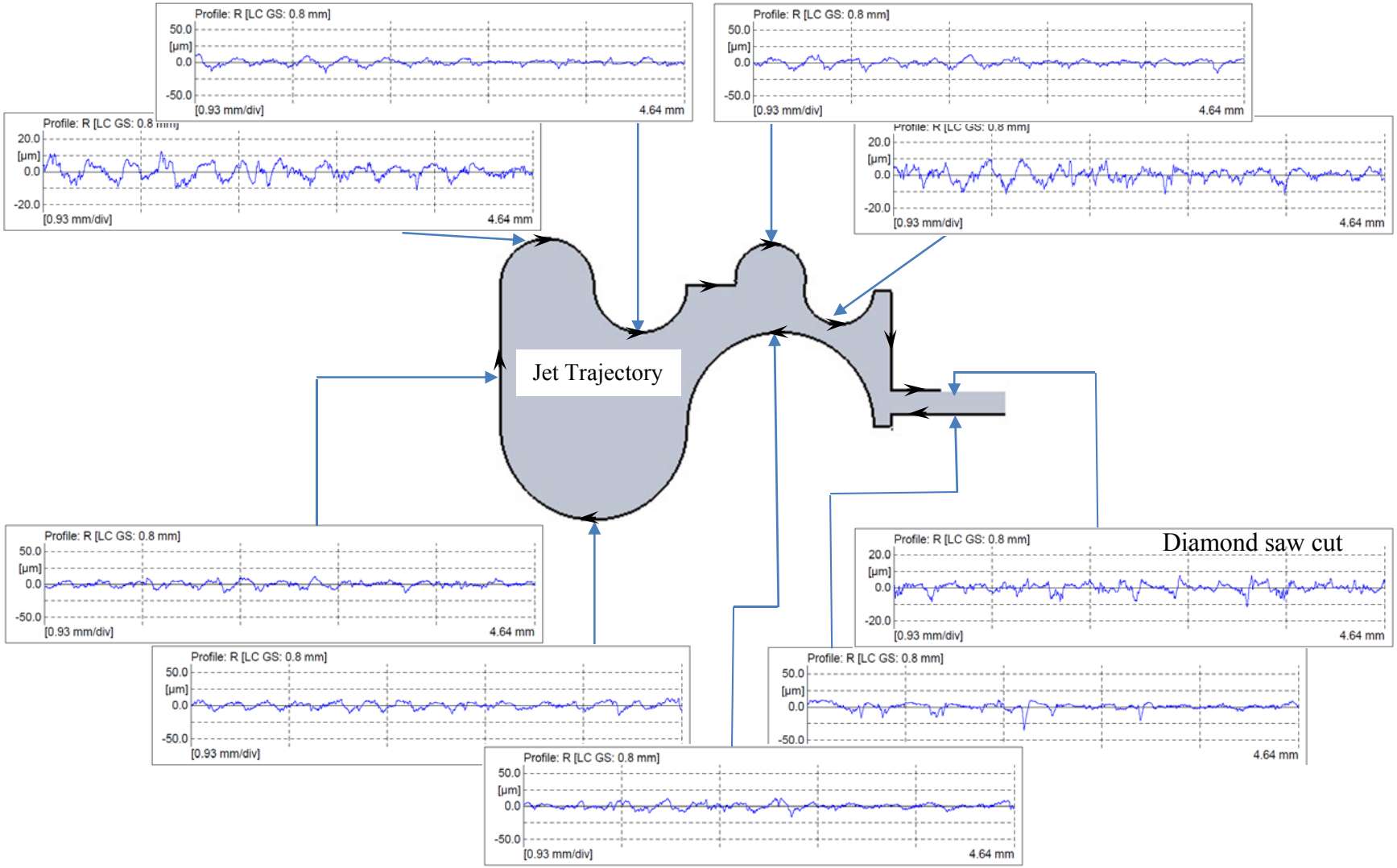

Figure 4.31. Transverse kerf roughness profiles of AWJ-16 specimens at different locations on the contour geometry.

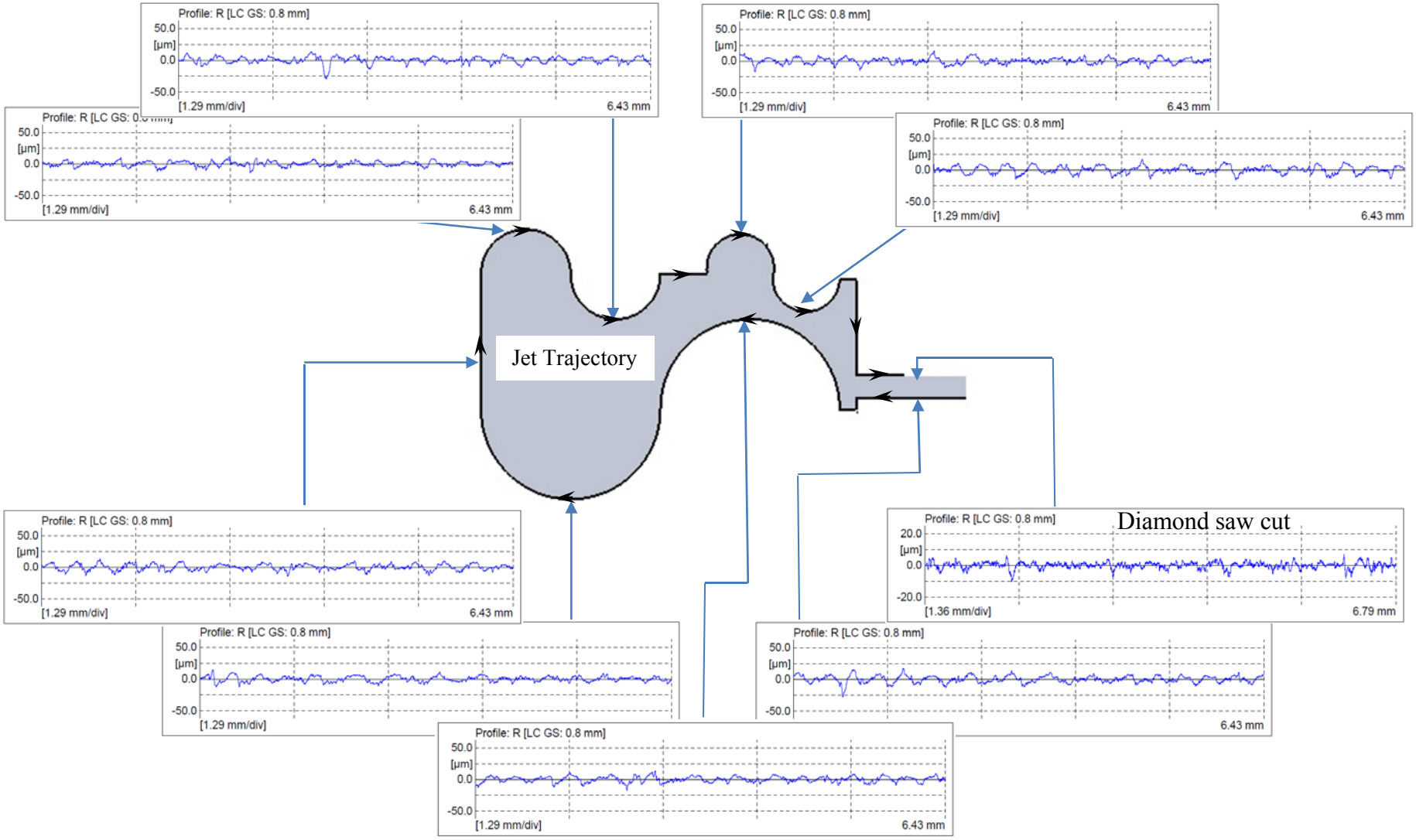

Figure 4.32. Transverse kerf roughness profiles of AWJ-31 specimens at different locations on the contour geometry.

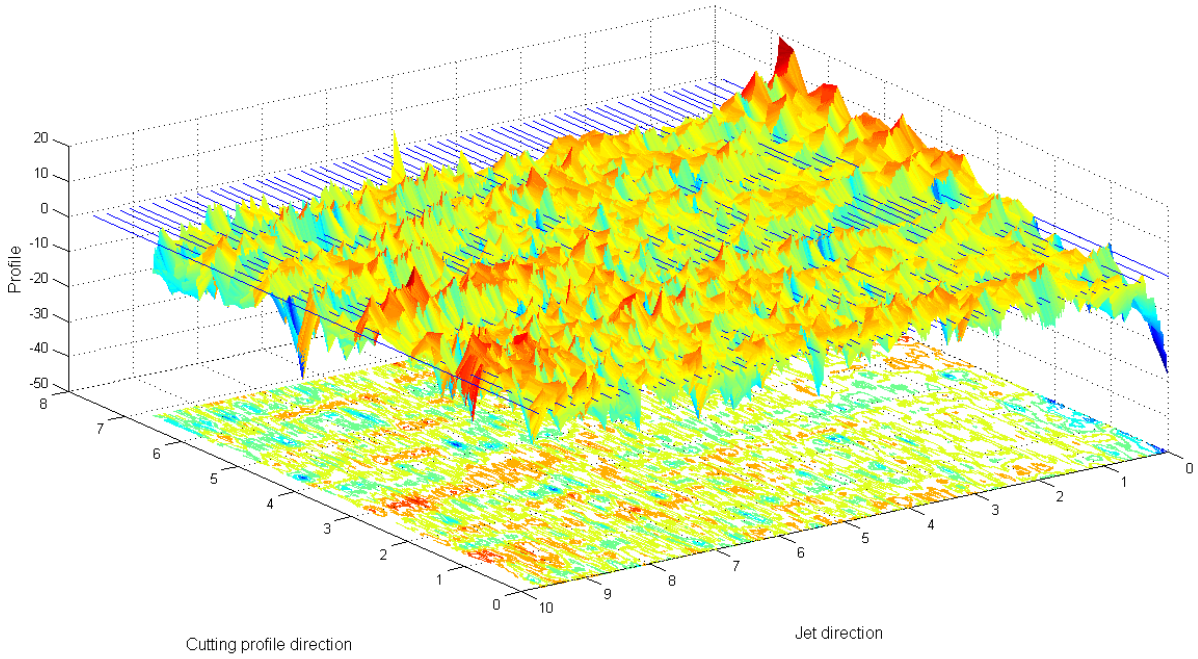

Figure 4.33. 3D Roughness profile of 10.5 mm thick AWJ machined kerf wall of AWJ-32 TiGr specimen.

Figure 4.33 depicts a typical 3D roughness profile of AWJ machined 10.5 mm thick TiGr laminate. Figure 4.34(a) and (b) shows the kerf roughness profile top and side views respectively for Abrasive waterjet machined straight cut of 10.5 mm thick AWJ-32 specimen. A comparison can be drawn with the diamond saw cut roughness profile depicted in Figure 4.34(c) and (d). A striation pattern depicting jet curving can be traced in the top view of AWJ machined surface in comparison to straight abrasive wheel shear marks of diamond cutter. The side views of both the profiles show sharp valleys, indicating the characteristic of solid particle erosion. The peakedness of AWJ machined surface is higher near jet entry and exit side, whereas diamond cut witnesses random peaks and valleys throughout the depth of cutting tool interaction with material.

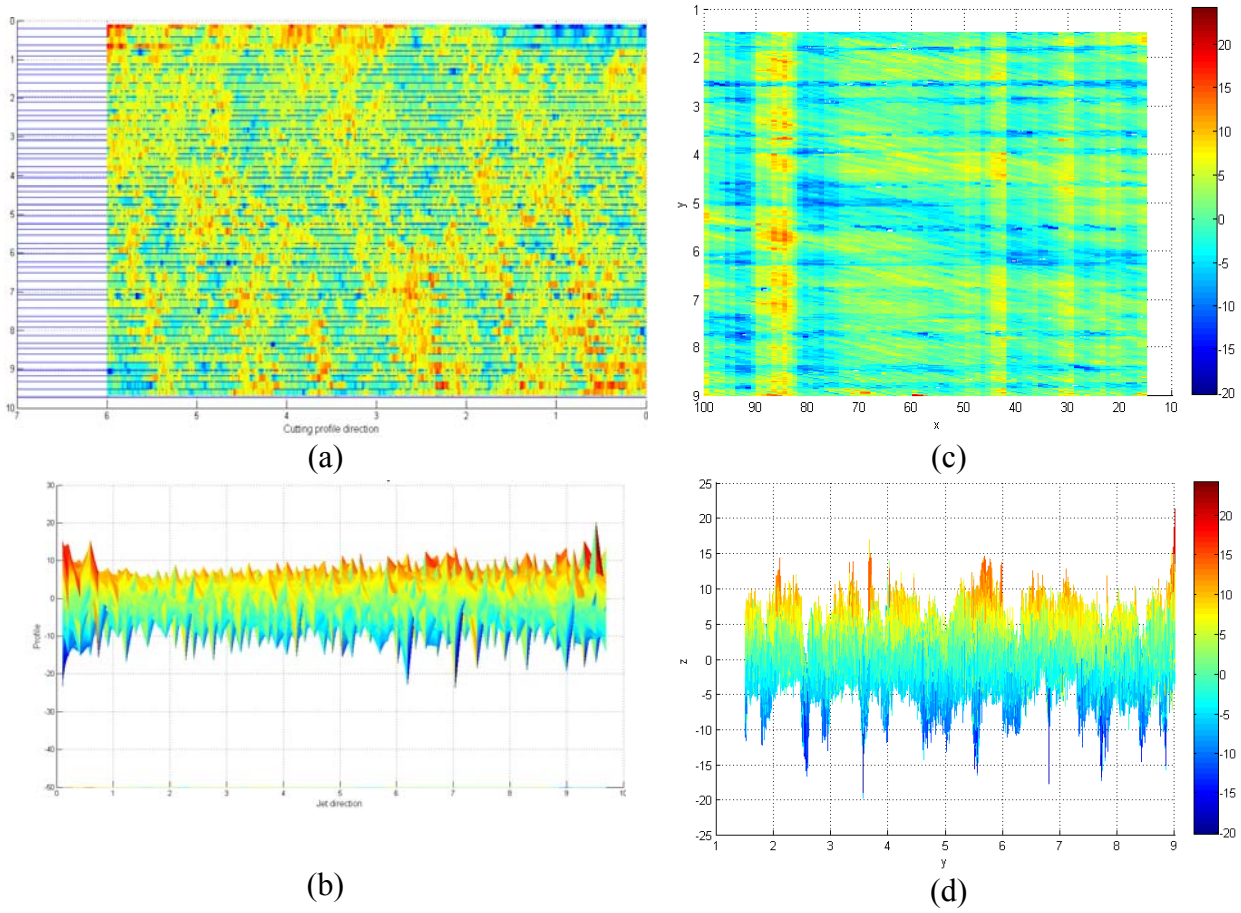

Figure 4.34. Surface Roughness profiles of 10.5 mm thick TiGr Laminate machined using AWJ (a) Top view, (b) Side view, and Diamond saw (c) Top surface, (d) Side view.

4.2.1 Transverse Surface Roughness

The irregularity of kerf wall in the direction of jet penetration is attributed to the difference in material properties, and thus, removal mechanism for different materials. One of the major limitations of AWJ machining of composites is the phenomenon of 'hydrowedging' [45,89] where the water penetrates transverse to the jet penetration and weakens the bonding between composite layers.

A similar detrimental effect of water pressure build up was observed in Titanium-Graphite laminate where erosion of composite ply was found more than the titanium ply. Figure 4.35(b)

illustrates the kerf distortion phenomenon where jet expands sideways and erodes the composite matrix.

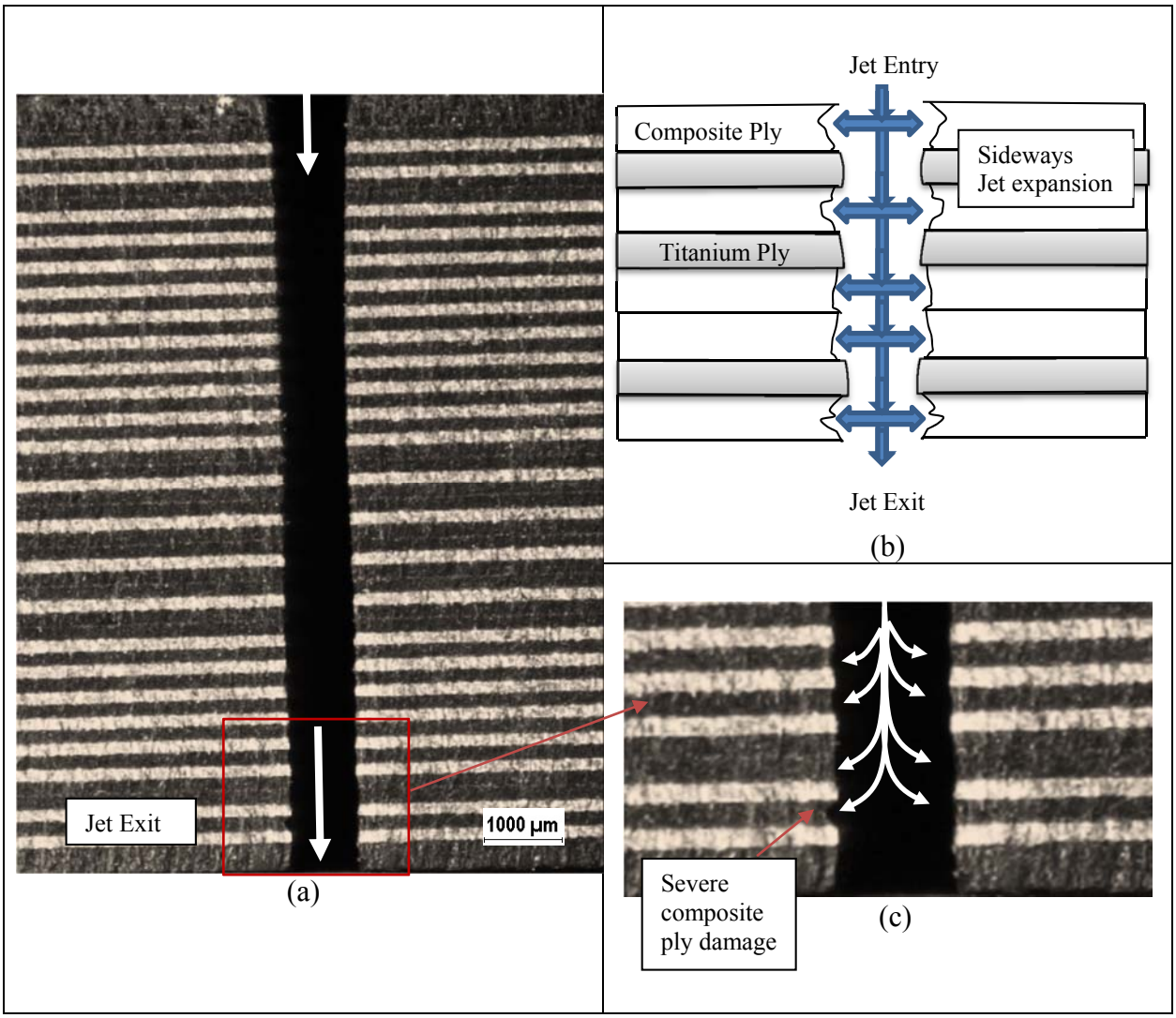

Figure 4.35. Hydro-distortion of 10.5 mm thick specimen machined with AWJ conditions of experiment number 25 depicting (a) kerf wall with jet penetration direction, (b) Graphical illustration of kerf distortion, and (c) Jet exit kerf.

Owing to tendency of jet spreading in composite material, water induced kerf distortion generated a topographically uneven kerf wall throughout the jet penetration depth. Figure 4.35(a) depicts the kerf wall with excessive composite erosion at entry and exit side of the jet for straight AWJ-25 specimen. The severity of composite matrix distortion is shown in Figure 4.35(c) where the matrix

erosion in significant enough to account for possible degradation in structural integrity and require a secondary machining for kerf smoothening.

Traverse roughness along profile arc angle

The effect and influence of water induced kerf distortion along the machining profile was studied by measuring the surface roughness along the thickness direction at 5° angular offset on the large outer arc profile of AWJ-32 specimen.

The average surface roughness R_a along the transverse direction was 1.22 µm with standard deviation of 0.073 µm. The statistical data of average roughness (Ra) depict that there is no significant invariance between the R_a values of profiles at different locations. This can be attributed to the inadequacy of average spatial height distribution in capturing the textural variations of surfaces generated by manufacturing process. The inadequacy of R_a in correlating structural integrity to the surface texture for fiber reinforced plastics has been previously reported by Arola et al. [90]. The ten point average roughness parameter (R_z–JIS) was analyzed for better understanding of the curvature effect in AWJ contour cutting.

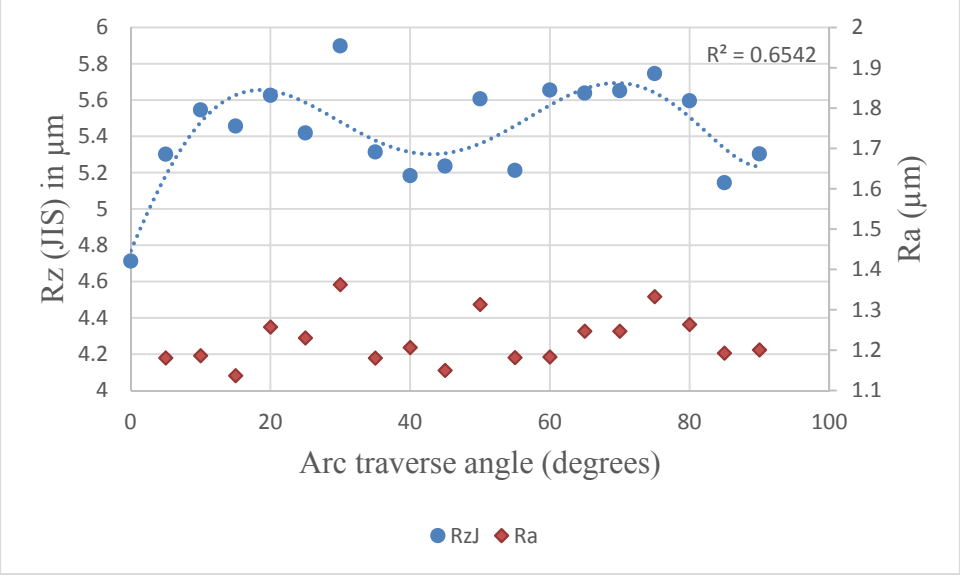

Figure 4.36. Effect of Jet traverse angle on R_a and R_z (JIS) parameter while contouring large outer arc for AWJ-32.

Figure 4.36 shows the R_a and R_z (JIS) values as a function of curvature angle. The R_z (JIS) was found to be varying between 4.7 μm and 5.9 μm with standard deviation of 0.275 μm. The trend indicated minimum values of R_z (JIS) at 0°, 40°-45° and 85°-90° curvature angles. This corresponds to easy removal of the work material and can be attributed to the minimum material resistance due to specific fiber orientation at this radial location, as well as higher jet energy at these profile curvature points. Low roughness at critical locations where profile trajectory changes suddenly can be influenced by the jet spreading due to jet acceleration and deceleration at these locations. If the energy is high enough, the rotational component induced by the jet inertia is expected to erode longitudinally and also reduce the sideways expansion of the jet. This transverse cutting component knocks out the peaks and valleys formed by the erosion during jet penetration from top to bottom ply, generating a smoother profile. The maximum R_z (JIS) value was found to be at 30° and 60°-75° curvature. The overall variation of ten point height parameter is nearly sinusoidal.

Although R_z (JIS) is a good measure of average peaks and valleys, this surface textural quantity doesn't distinguish between the profiles of composite and titanium ply and cannot be successfully employed in understanding the amount of composite removed. A further investigation into the hydro-erosion of composite in RCR (Rough cutting zone) and SCR (Smooth cutting zone) was conducted. The RCR and SCR were assumed to be constant for all profiles measured at different Jet traverse angles. SCR was selected between ply 5 and 35 followed by RCR based on the observation of macroscopic images.

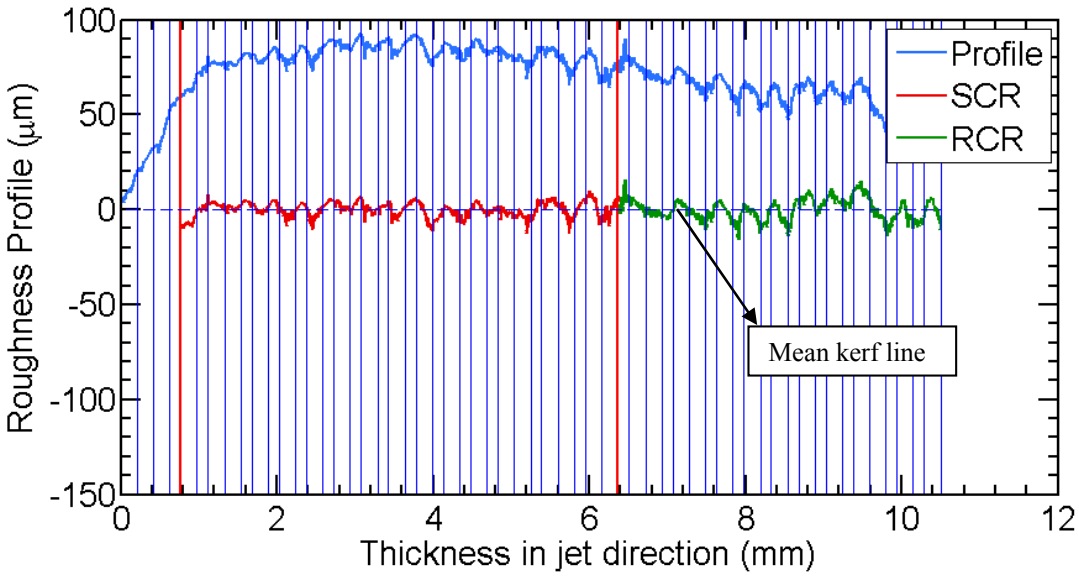

Figure 4.37. Smooth and Rough cutting zone roughness profiles along the thickness direction measured at 0 degree Jet traverse angle

Figure 4.37 depicts the surface roughness in Rough and smooth cutting regions for specimen 32, at 0° Jet traverse angle. The vertical blue lines represent ply layup. Thick and thin plies represent composite and titanium layer respectively. The variation of material area above and below the mean kerf line depicts the excess material available or eroded. The material excess area was determined for composite and titanium layer separately by integration of profile curve above the mean line. The variance of composite and titanium distribution about mean kerf line is about 1.87 in SCR and 2.09 in RCR.

The normalized material distribution in SCR and RCR is depicted in Figure 4.38 and Figure 4.39. The composite layer was found to be mostly below the mean line depicting the significant amount of erosion of composite plies in comparison to titanium plies. The maximum composite erosion was found at 0°, 40°-60° jet traverse angles in smooth cutting region (SCR). The results are in agreement with the aforementioned R_z (JIS) values.

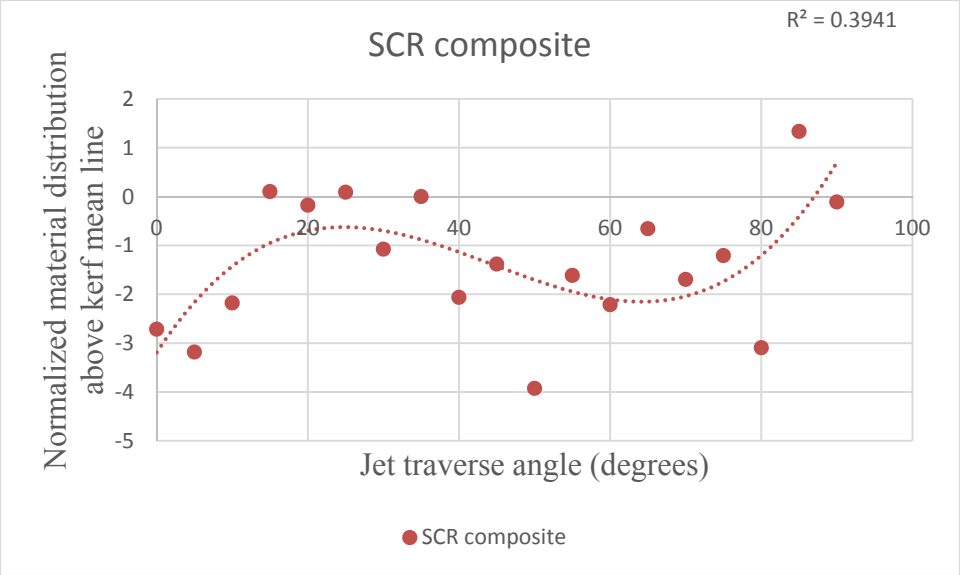

Figure 4.38. Variation of composite area about mean kerf line in SCR

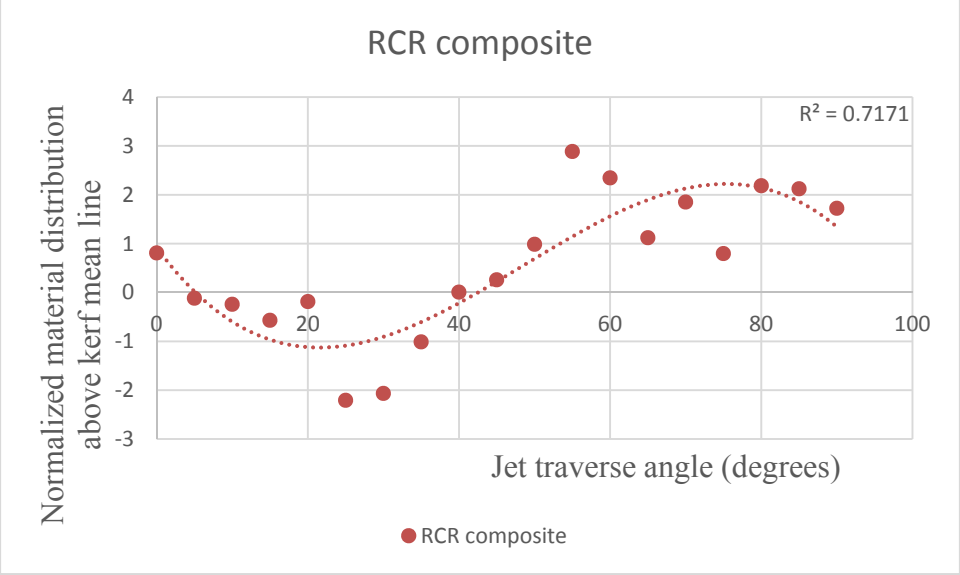

Figure 4.39. Variation of composite area about mean kerf line in RCR

4.2.2 Semi-Analytical modeling

In this section, energy based semi-analytical model proposed by Hoogstrate and Paul (section 2.2.2.6) is modified to predict transverse surface roughness (R_a) of AWJ machined thick TiGr as a function of process variables. As discussed in section 2.2.2.6, the following equations can be derived to determine the power of water jet entering the mixing tube.

By conservation of energy law, velocity of water delivered by high pressure pump can be derived as follows.

$$v_w = \psi \sqrt{\frac{2P_w}{\rho_w}}$$

v_w = Velocity of water
ψ = Velocity coefficient
P_w = Water pressure
ρ_w = Density of water

(4.6)

The power of water jet passing through orifice is given by the product of water flow rate through orifice and water pressure.

$$P_{ow} = \dot{Q}_w \times P_w \tag{4.7}$$

$$\dot{Q}_w = A \times v_{water} \tag{4.8}$$

P_{ow} = Power of Waterjet
P_w = Water Pressure
$\dot{Q}_w$ = Water flow rate
A = Cross-sectional area of orifice

Upon substituting the volume flow rate of water through orifice, given by equation (4.8)

$$\dot{Q}_w = \frac{\pi d_n^2}{4} \times C_d \sqrt{\frac{2P_w}{\rho_w}}$$

d_n = Orifice diamteter
C_d = Coefficient of drag

(4.9)

The power of waterjet at the exit of orifice is given by equation (4.10).

$$P_{ow} = C_d \frac{\pi}{2\sqrt{2\rho_w}} d_n^2 P_w^{3/2} \tag{4.10}$$

The coefficient of drag was found to be a function of pressure and orifice diameter and can be expressed by the following equation within 8% accuracy for a sapphire orifice with a sharp edge entry [91].

$$C_d = 0.785 - 0.00014P - 0.197d_n$$

The water and abrasives enter the mixing chamber alongwith small amount of air and momentum is transferred from entrained air and water to abrasive particles in the control volume. The momentum of entained air is small enough to neglect in further calculations. The abrasives are initially at rest and attain some velocity at the end of mixing chamber. Equation (4.11) is the impulse balance equation without considering any losses in the process.

$$\Sigma\left(\dot{m}v\right)_{before\ mixing} = \Sigma\left(\dot{m}v\right)_{after\ mixing} \tag{4.11}$$

$$\left(\dot{m}_w v_w\right)_{before} = \left(\dot{m}_w v_w + \dot{m}_a v_a\right)_{after} \tag{4.12}$$

It is assumed that the velocity of abrasive particles is the prime contributor to the cutting process and that the average abrasive velocity can be inferred as the average velocity of the abrasive waterjet. A relation between waterjet and abrasive waterjet velocity can be found using:

$$\dot{m}_w v_w = \left(\dot{m}_w + \dot{m}_a\right) v_{awj} \tag{4.13}$$

$$v_{awj} = \frac{\dot{m}_w}{\dot{m}_w + \dot{m}_a} v_w \tag{4.14}$$

$$v_{awj} = \eta \frac{1}{1+R} v_w \tag{4.15}$$

Here R (load ratio) is defined as the ratio of mass flow rate of abrasive particles to mass flow rate of water ($R = \dot{m}_a / \dot{m}_w$) and η is the momentum transfer efficiency. The overall power coefficient that can relate input power to jet cutting power can be derived by taking the ratio of kinetic energy components of abrasive particles after mixing and water before mixing.

$$\kappa = \frac{\frac{1}{2}\dot{m}_a v_{awj}^2}{\frac{1}{2}\dot{m}_w v_w^2}$$

$$\kappa = \frac{\eta^2 R}{(1+R)^2}$$

Conclusively, AWJ power can be determined as

$$P_{o(AWJ)} = \kappa P_{ow}$$

$$P_{o(AWJ)} = \frac{\eta^2 C_d R}{(1+R)^2} \frac{\pi}{2\sqrt{2\rho_w}} d_n^2 P_w^{3/2} \tag{4.16}$$

However, the effect of standoff distance i.e. diametrical expansion of jet between nozzle exit and top surface of the workpiece cannot be neglected [77,83,84,89,92]. From the previous investigations (section 4.1.1) and data from Figure 4.16, a strong correlation between the jet entry diameter and nozzle diameter was found. Assuming the entry diameter is constant for the given experimental range, the following relation was established using linear regression and mathematical approximation.

d_{entry}=1.27d_m

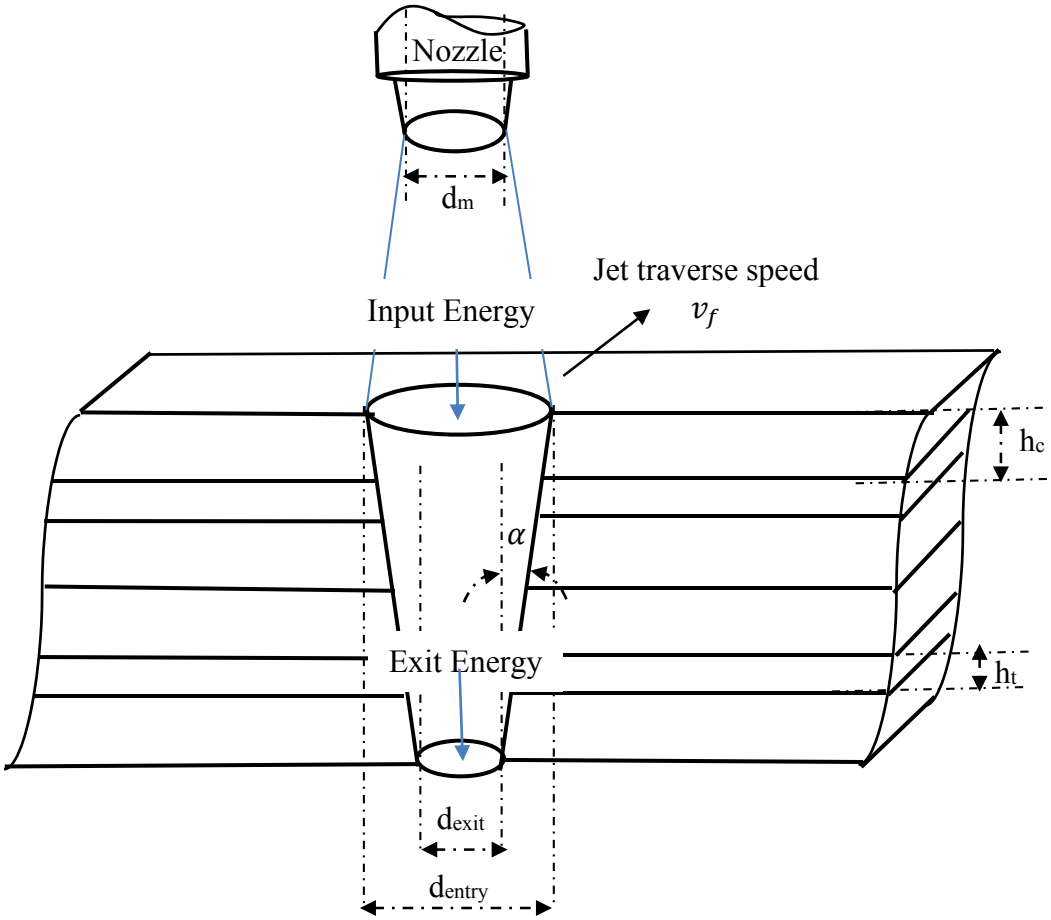

Figure 4.40. Control volume of jet and material interaction

Figure 4.40 illustrates the energy flow in abrasive watrjet cutting process. The energy per unit area imparted to the workpiece by traversing jet can be written as

$$E_o = \frac{P_{o(AWJ)}}{d_{entry} v_f} \tag{4.17}$$

Where v_f is the jet traverse speed. Upon substitution of power relation from equation (4.16)

$$E_o = \frac{\eta^2 C_d R}{(1+R)^2} \frac{\pi}{2\sqrt{2\rho_w}} \frac{d_n^2 P_w^{3/2}}{v_f (1.27 d_m)} \tag{4.18}$$

$$E_o = \lambda_0 \frac{d_n^2 P_w^{3/2}}{v_f d_m} \frac{R}{(1+R)^2} \tag{4.19}$$

For given specimens, it can be assumed that both the composite and titanium plies are sheared by the AWJ. The strain energy per unit volume required to shear a composite and titanium ply can be expressed as following.

$$U = \frac{\sigma_c^2}{2G}$$

Where,

Assuming the effect of ply arrangement and ignoring the jet energy dynamics associated with the material removal behaviour, the total strain energy per unit area required for shearing the entire laminate can be written as

$$E_c = U_c h_c n_c + U_t h_t n_t$$

where,

$h_{c/t}$ = composite/titanium ply thickness

$n_{c/t}$ = Number of composite/titanium plies

Titanium and composite ply thickness is 140 μm and 210 μm respectively. Material strength data tabulated in Table 3.1 can be use to compute the abovementioned critical energy density. The volume of material removed is proportional to the amount of available energy [59]. Thus, phenomenologically the average transverse roughness (Ra) can be assumed to be a function of the ratio of required and available energy per unit cutting area.

$$R_a = f\left(\frac{E_c}{E_o}\right)$$

However, this model doesn't take into account the influence of geometrical dimensions of nozzle on jet energy. For the given material thickness and within the range of experimental conditions, it was found that the role of water power and jet coherency in material removal is significantly large and cannot be ignored. The nozzle dimensions alter the percentage of water and abrasive power in the jet and a jet coherency factor can be defined to incorporate the effect of nozzle geometry.

$$\lambda = \frac{l_m}{d_m}$$

where l_m and d_m are nozzle length and nozzle diameter respectively.

The jet coherency factor was defined a dimensionless quantity and is based on the nature (hydraullic or abrasive), amount and thus cohernecy of jet energy required to remove the material. Since the specimen used in this investigation is significantly influenced by water power, the inverse of jet coherency factor determines the limiting nozzle dimensions required for efficient cut with low taper.

$$R_a = f\left(\frac{1}{\lambda}\frac{E_c}{E_o}\right)$$

It was found that R_a can be best related to the energy components using a power law.

$$\log R_a = a\log\left(\frac{1}{\lambda d_m}\frac{E_c}{E_o}\right) + b \tag{4.20}$$

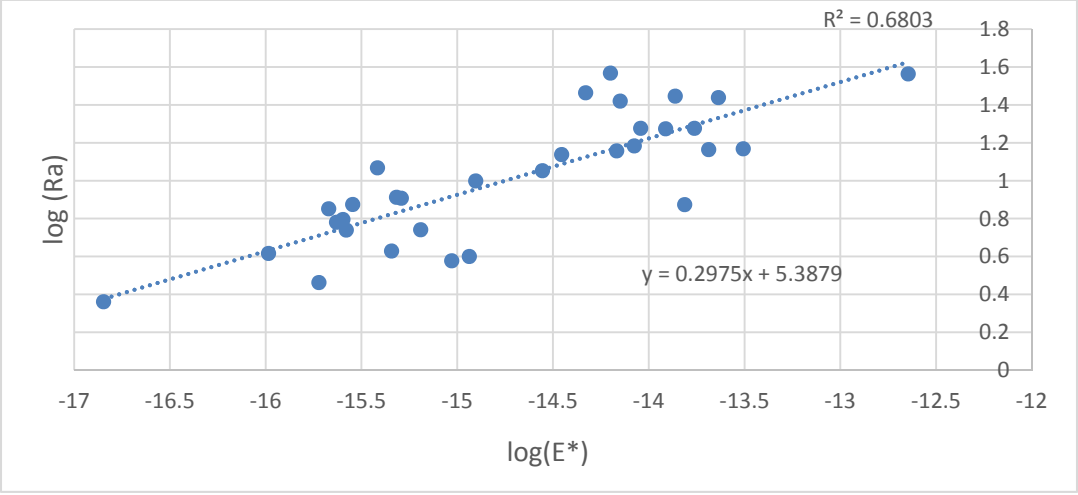

Figure 4.41. Experimental vs analytically predicted transverse roughness (R_a) for TiGr laminate specimen machined with conditions mentioned in Table 3.3.

Here equation (4.20) can be rewritten as

$$\log R_a = a \log\left(E^*\right) + b$$

Figure 4.41 shows the predicted relation between Ra and E* on log-log scale. The empirical constants a and b were found to be 0.298 and 5.388.

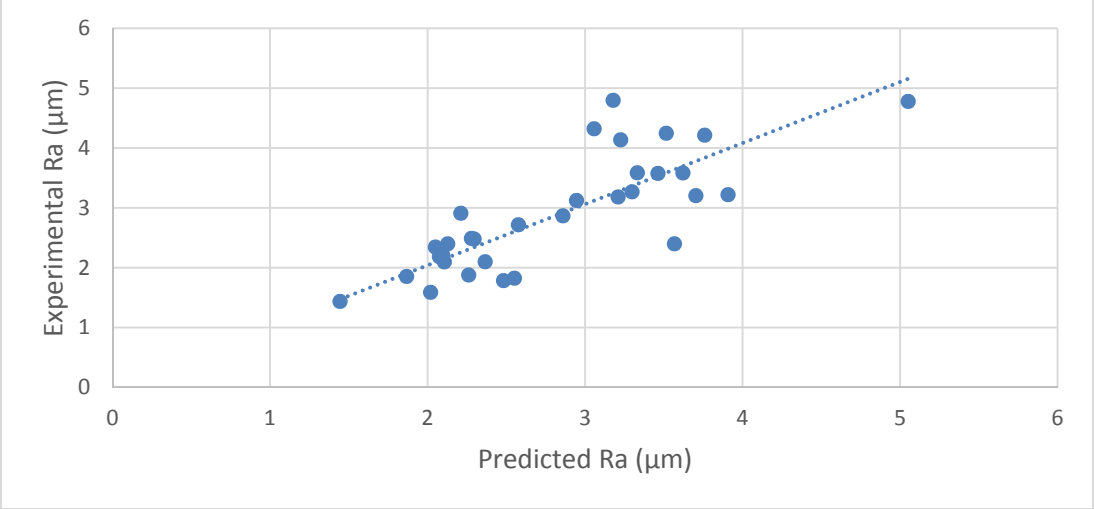

*Satndard deviation of Experimental/predicted ratio is 0.19

Figure 4.42. Experimental vs analytically predicted transverse roughness (R_a) for TiGr laminate specimen machined with conditions mentioned in Table 3.3.

The model successfully predicted the kerf taper ratio and standard deviation of expertimental to predicted ratio equal to 0.19. Although the correlation between predicted and experimental value is not very high, the proposed model is a first attempt to model transverse roughness in ultra high pressure waterjet machining of upto thick TiGr. The model is limited to the predictions within the range of experimental conditions. As discussed in section 4.1, jet coherency is affected by nozzle parameters and jet material interaction properties generalized quantification is difficult without accounting for effect of different ply arrangements. Thus, further investigation into the jet coherency factor is necessiated to modify and incorporate the ply arrangement effect.

Besides, the model is limited to AWJ cutting of straight profiles. A variation of transverse kerf roughness of upto 60% was observed among different profiles which necessiates further modification in the proposed model.

4.2.2 Quantification of Topological characteristics

Statistical and graphical comparison of AWJ machined transverse roughness characteristics depicted that the transverse surface generated by AWJ machining of TiGr laminate was negatively skewed and leptokurtic as depicted in Figure 4.43. The small arc profile kerfs showed the least tendency for positive skewness when machined with Abrasive Waterjet, as depicted in Figure 4.44. As evident from the taper results, the abrasive cutting component is distributed between components parallel and orthogonal to the jet traverse direction. The reduction in energy component parallel to jet direction when jet is traversing in a contour (circle, in this case) is due to the dynamic radial component which tends to reduce the jet coherency. A negatively skewed profile indicates more resistance to abrasive erosion [28], which in this case is the reduced cutting efficiency of the jet in direction of jet penetration.

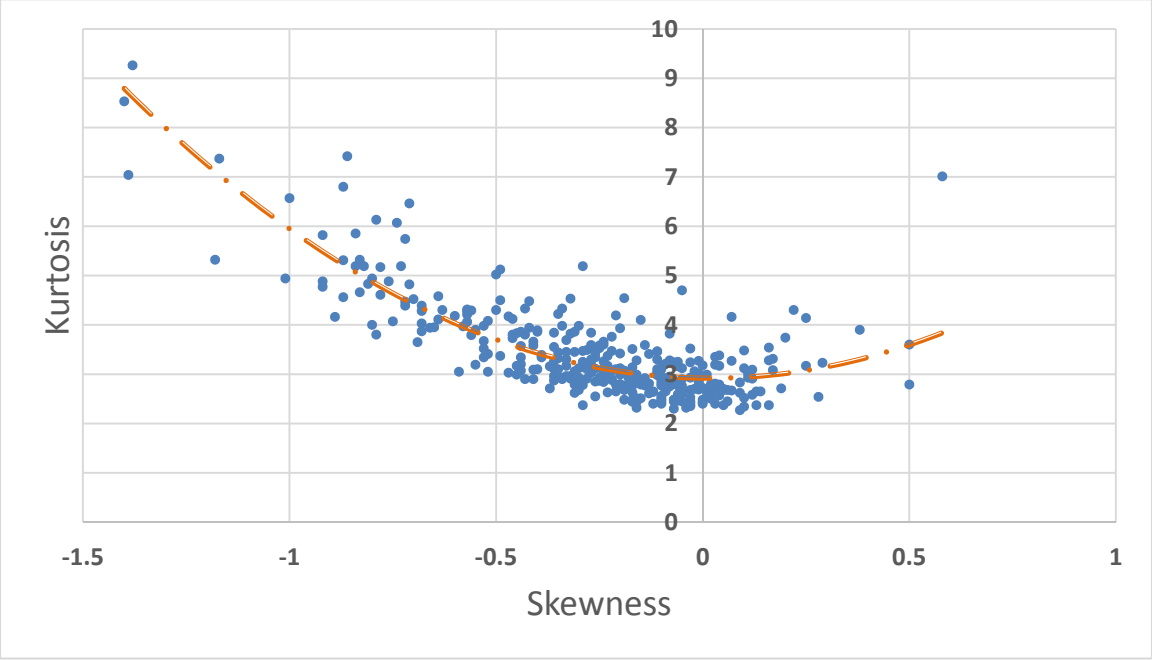

Figure 4.43. Skewness vs. kurtosis curve for all profiles

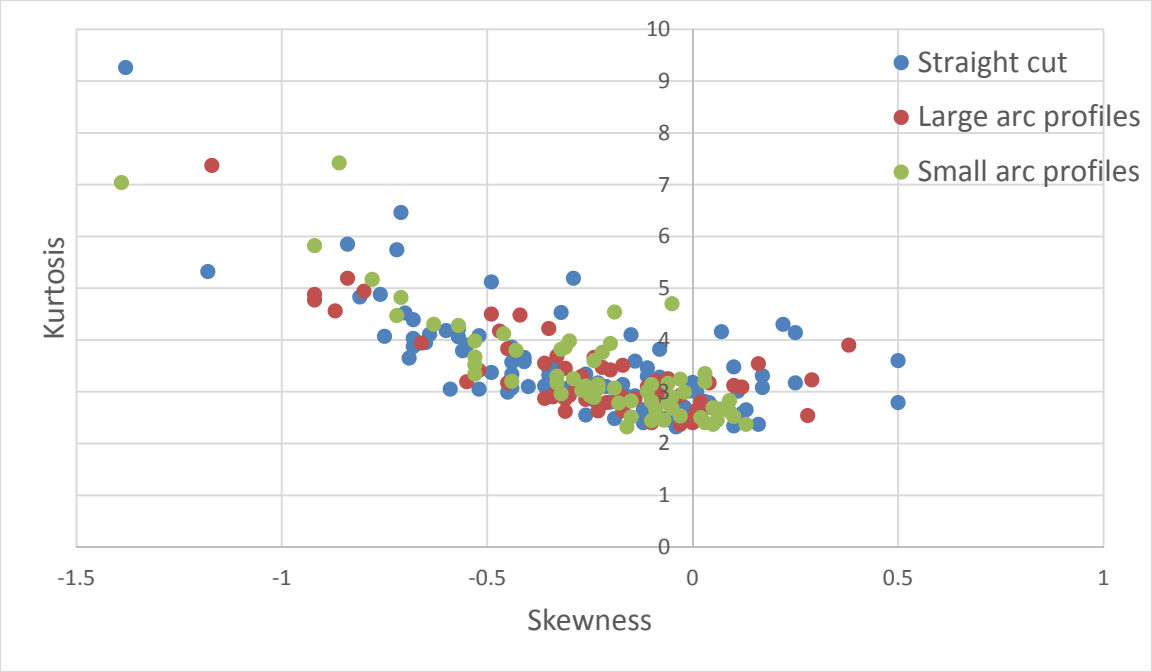

Figure 4.44. Bearing curve characteristic for three different profiles.

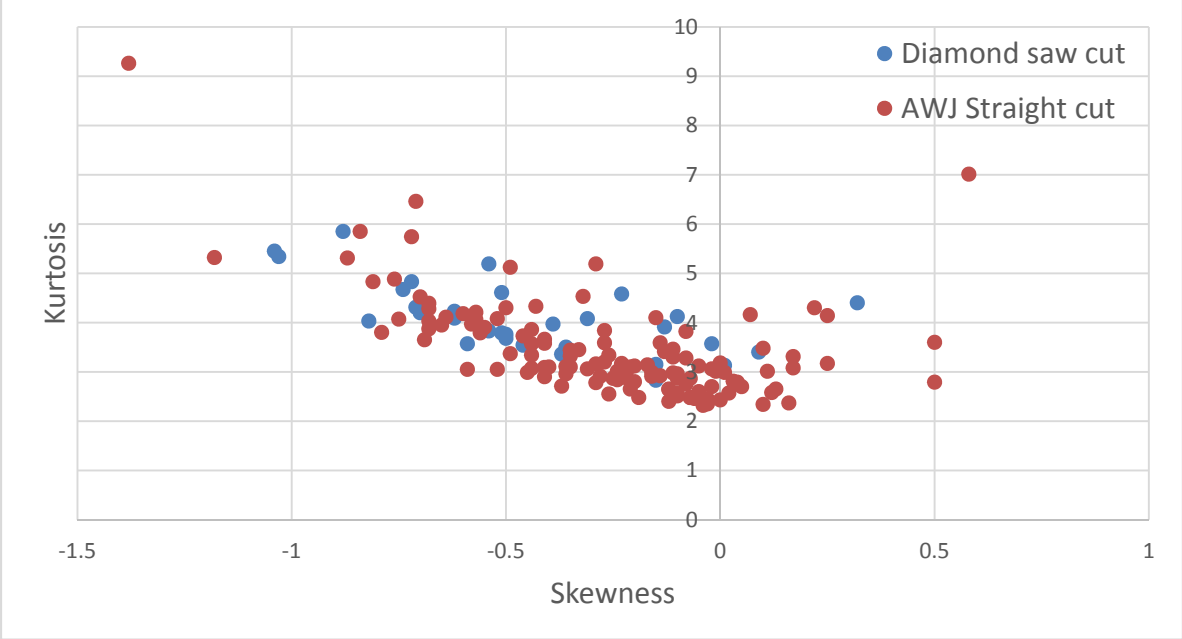

Figure 4.45. Skewness vs. kurtosis comparison of AWJ and diamond saw straight cut.

Figure 4.45 depicts a graphical comparison of skewness-kurtosis space profile for AWJ machined and diamond saw machined surface. Since both the surfaces are generated by the random action of abrasives at microscopic scale, the inherent characteristic describing this unit event accounts for

similar kurtosis and skewness behavior. For a completely random or Gaussian distribution, the kurtosis bears a value of 3, which is similar to the AWJ process.

4.2.3 Analysis of Variance – Transverse Roughness (R_z)

Transverse roughness (R_z) for each profile feature was statistically analyzed for variance. The parametric effect on kerf taper ratio of straight cut and curved profile features is discussed in sections 4.2.3.1-4.2.3.5. Because of similar behavior of the parametric effect, straight cut taper ratio is discussed in more detail and the relevant ANOVA tables and diagnostic curves for all profiles are included in APPENDIX B and APPENDIX C respectively.

Eq. no.	Regression model equations	R^2
(4.21)	**Rz (Straight cut) =** $-89.1873+12.9814t-0.04686P-0.12609lm+52.8824dm$ $-377.942dn+1974.78R-0.10453u+0.003946t\times P+26.9233t\times dn-219.433t\times R$ $+0.014175t\times u-0.43272lm\times dm+1.05496lm\times dn+0.000923lm\times u-0.09481dm\times u$	0.93
(4.22)	**Rz (Small inner arc) =** $-7.39788-0.07376t+0.038779P+0.283306lm$ $+39.1647dm-42.2056dn-158.783R+0.194216u-0.0022t\times P+4.52722t\times dm$ $-0.00034P\times lm-0.00013P\times u-0.51146lm\times dm+0.837391lm\times dn-84.5421dm\times dn$ $-0.16586dm\times u$	0.97
(4.23)	**Rz (Small outer arc) =** $40.132+2.93409t-0.08314P-0.38637lm+17.3195dm$ $-138.416dn+2.9652R+0.100924u+0.004711t\times P-0.0192t\times lm+1.36958t\times dm$ $-34.8129t\times R+0.000377P\times lm-0.48879lm\times dm+7.22769lm\times R+62.772dm\times dn$ $+0.290367dn\times u-1.44206R\times u$	0.98
(4.24)	**Rz (Large inner arc) =** $9.92262-1.93034t-0.05304P+0.272152lm+69.2445dm$ $-43.2878dn-8.95684R+0.047811u+32.4952t\times R+0.005133t\times u+0.000189P\times lm$ $+0.04125P\times dm-0.58323lm\times dm-443.11dm\times R-0.291dn\times u$	0.97
(4.25)	**Rz (Large outer arc) =** $46.7567+1.23523t+0.052143P-0.00804lm-43.1386dm$ $-99.3734dn-355.308R-0.11536u-0.0044t\times P+0.022377t\times lm+0.00784t\times R$ $-0.00044P\times lm+570.249dm\times R+0.346431dn\times u$	0.94

Equations (1.6-1.10) are the regression models developed using ANOVA for five different profiles. The standard deviation of these models vary from 1.06 to 1.97.

4.2.3.1 Straight cut transverse R_z

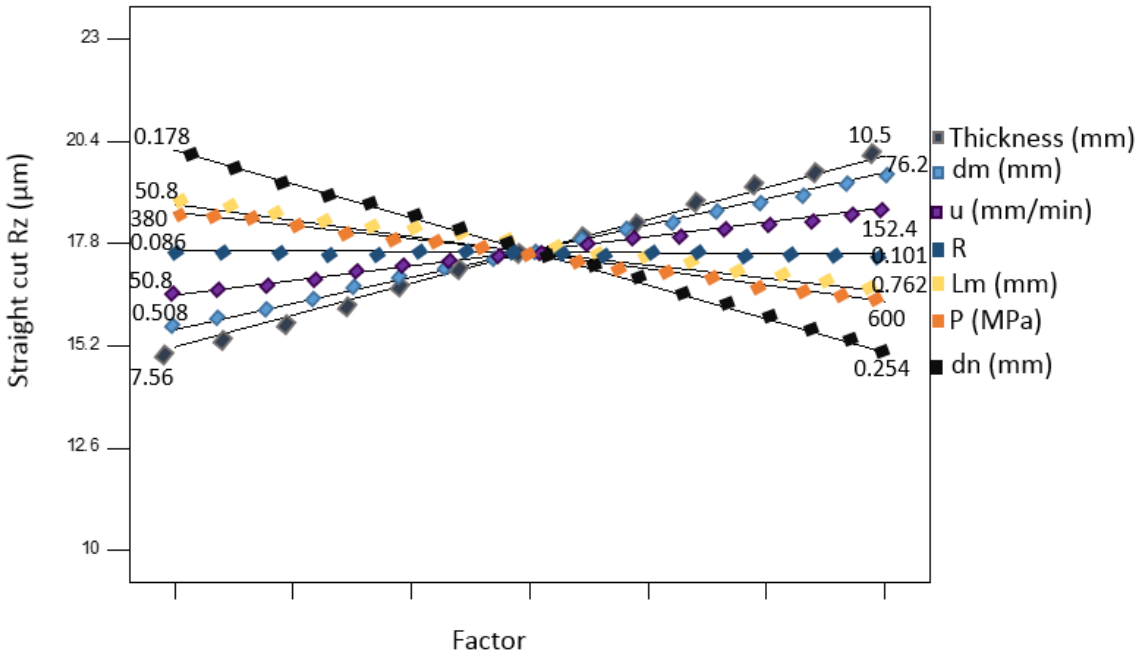

Figure 4.46. Single factor effect (without any interaction) of process variables on straight cut kerf transverse surface roughness parameter (R_z)

Figure 4.46 depicts the effect of each process variable in the model without interaction effect. All the variables except load ratio have significant effect on R_z roughness parameter even without the consideration of interaction among them. Besides, the exact effect of variable interaction is required for the comprehension and prediction of roughness. The main interaction effects and observations below.

Figure 4.47(a) depicts the interaction effect of specimen thickness and orifice diameter. The maximum roughness (R_z) observed was 21.1 µm at small orifice bore size and for thicker specimen. The minimum roughness (R_z) observed was 11.1 µm at large orifice bore size and for thin specimen. The roughness was increased up to 73.6% with reduction in orifice size and up to 70.9% with increase in specimen thickness. A small orifice diameter means less water mass flow rate and thus high roughness. Also, higher thickness represents high penetration depth and more energy loss leading to more erosive wear rather than sharp cutting at the exit side of the jet, generating a spiky, rougher surface.

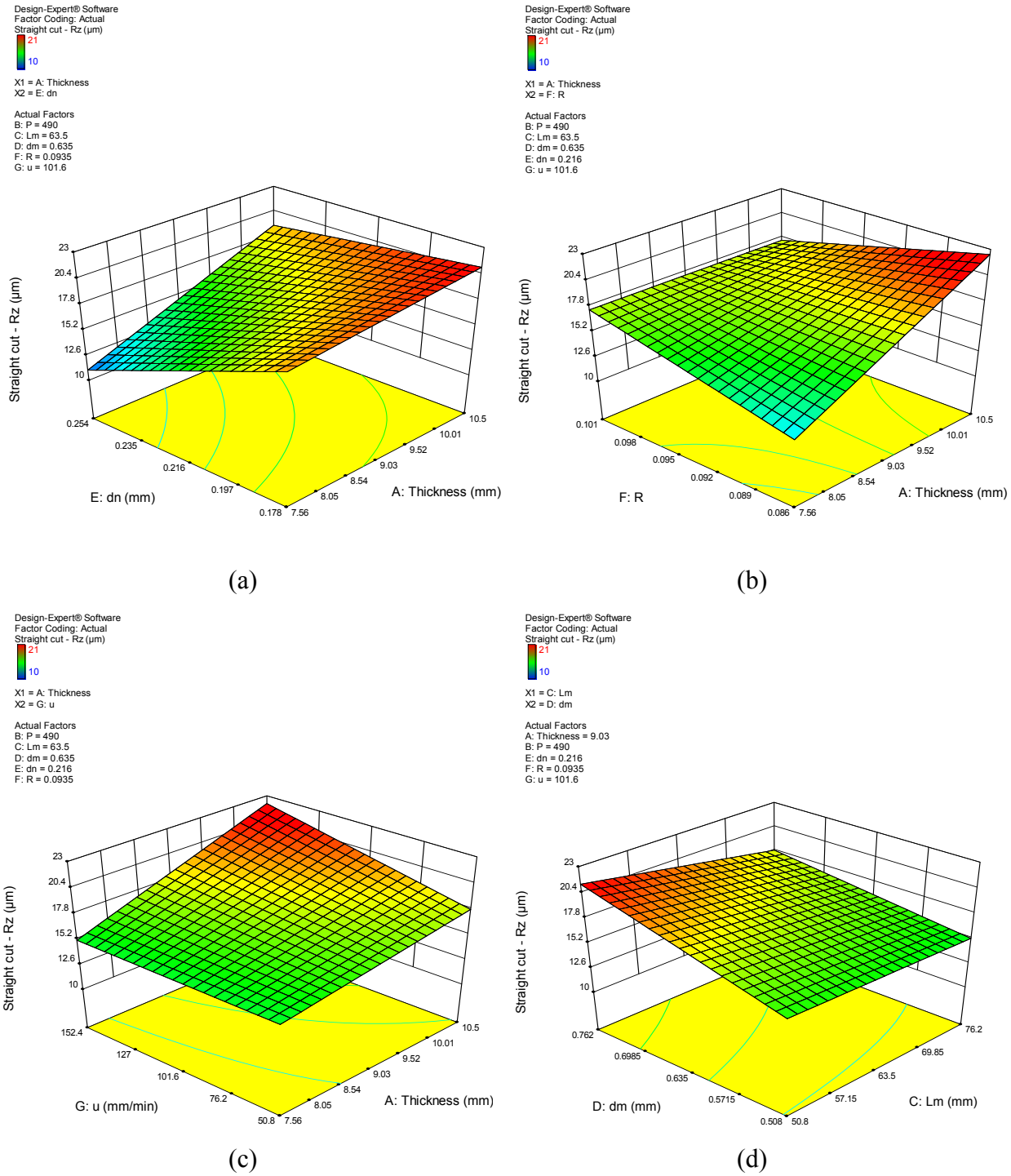

Figure 4.47. Parametric interaction effects on transverse surface roughness in profiling straight cut– (a) Thickness-orifice diameter, (b) Thickness-load ratio, (c) Thickness-traverse speed, and (d) mixing tube length and diameter.

Figure 4.47(b) depicts the interaction effect between specimen thickness and load ratio. The maximum roughness is witnessed at 0.086 load ratio and 10.5 mm thick specimen. A lower load ratio and increased jet penetration requirement represents a higher resistance in machining, justifying high R_z value.

Figure 4.47(c) depicts the interaction effect between traverse speed and specimen thickness. As expected, a rougher surface was obtained at high jet traverse rate (u=152.4 mm/min) and for thicker specimen (10.5 mm) with R_z=22.2 μm. The effect of traverse rate was significant at higher thickness with 24.3% increase in Roughness. Alternatively, the effect of thickness was significant at high traverse speed with 45.8% increase in roughness.

Figure 4.47(d) depicts the interaction effect between mixing tube diameter and length. A rougher surface with R_z=21.3 μm was obtained with short mixing tube (50.8 mm) and large missing tube diameter (0.762 mm). This indicates the high water power component with large diameter, accounting for more roughness. Also, a short mixing tube means less coherent jet with reduced cutting efficiency. A high aspect ratio (Lm/dm=100 to 150) is desirable for low roughness with R_z between 15.3 to 15.9 μm.

4.2.3.2 Small inner arc transverse R_z

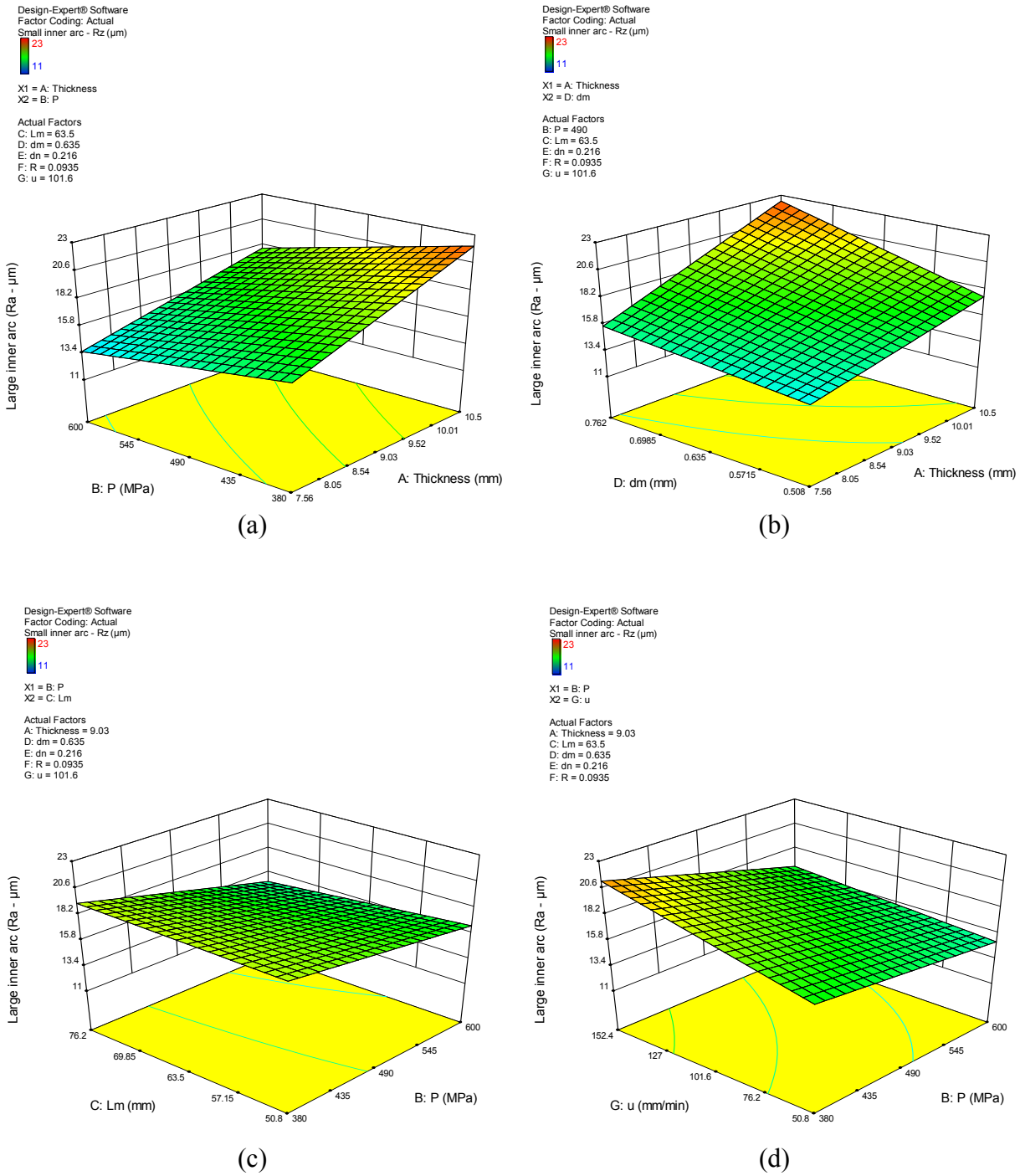

Figure 4.48. Parametric interaction effects on transverse surface roughness in profiling small inner arc – (a) Thickness-pressure, (b) thickness-mixing tube diameter, (c) Pressure-mixing tube length, (d) Pressure-traverse speed

Figure 4.48(a) depicts the pressure and thickness interaction effect on R_z roughness parameter. The maximum roughness is obtained at low pressure (380 MPa) and for thicker specimen. This is consistent with the reasoning of less power and more resistance in jet-material interaction leading to roughness as high as 22.08 µm. About 16.6-18.7% advance in roughness was observed with pressure reduction within the experimental thickness bounds. Also, 32-35.4% advance in roughness with thickness was observed when pressure is varied. This justifies the sensitivity of roughness with thickness more than the pressure variation.

A rougher surface was obtained when mixing tube diameter and thickness were increased, as shown in Figure 4.48(b). A 43.06% increase in R_z was observed with increase in thickness at dm=0.762 mm leading to maximum surface roughness R_z was 22.44 µm under experimental conditions mentioned in the figure.

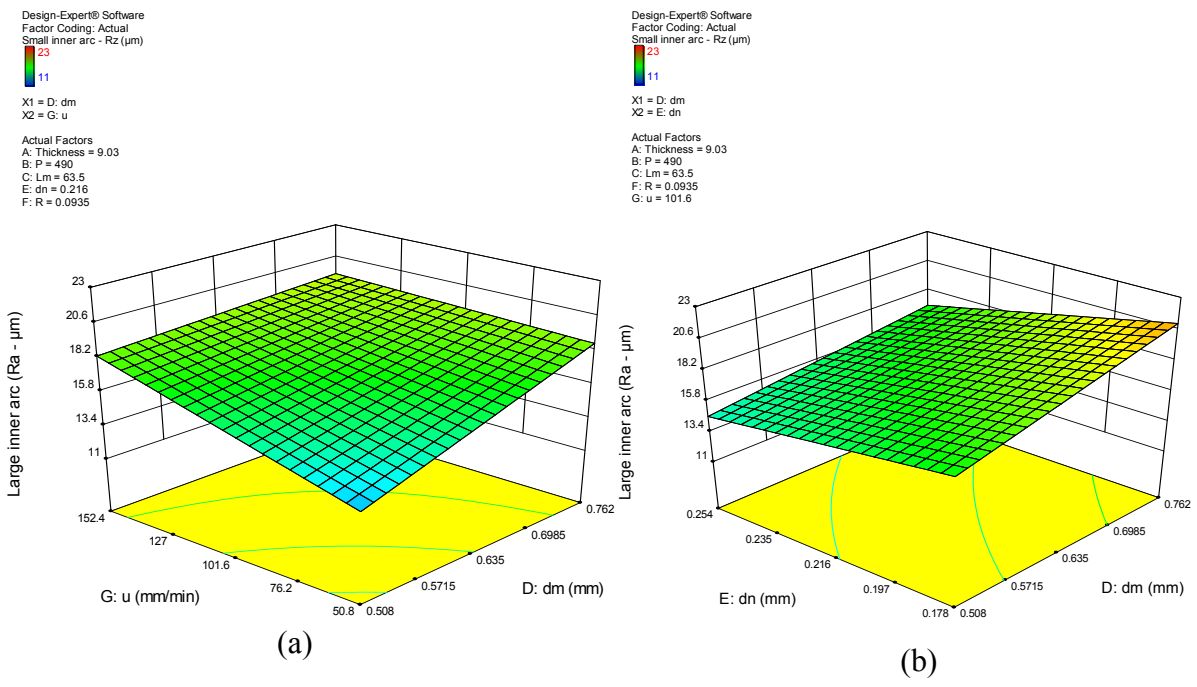

Figure 4.49. Parametric interaction effects on transverse surface roughness in profiling small inner arc – (a) mixing tube diameter-traverse speed, (b) Mixing tube diameter-orifice diameter

Figure 4.48(c and d) depicts the interaction effect between pressure and mixing tube length, pressure and traverse speed on roughness parameter R_z. A rougher surface was obtained at low pressure and high traverse speed.

Figure 4.49(a and b) depicts the interaction effect of mixing tube diameter with traverse speed and orifice diameter. The effect of traverse speed was nearly constant except at small mixing tube diameter where the roughness dropped down to 28.31% with reduction in mixing tube diameter. Also, maximum roughness was obtained at minimum dn/dm ratio = 0.23, whereas minimum roughness was achieved at dn/dm=0.5. A high dn/dm value (~0.5) indicated a high power coherent jet, with roughness as low as 11.63 μm can be obtained given the conditions as depicted in Figure 4.49 (b).

Similar trends were observed in small inner, large inner and large outer profile features. These trends are mentioned in section 4.2.3.3-4.2.3.5.

4.2.3.3 Small outer arc transverse R_z

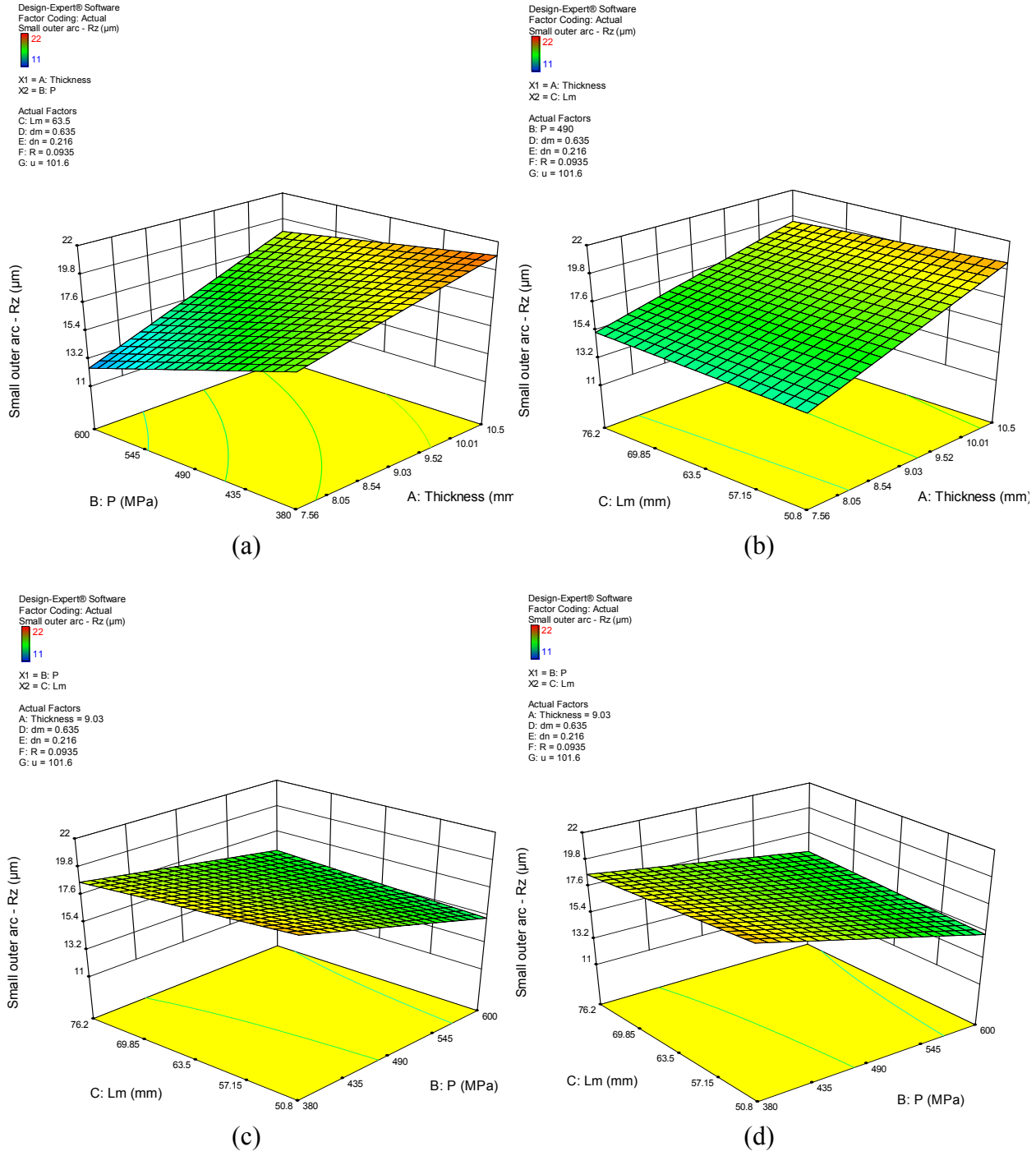

Figure 4.50. Parametric interaction effects on transverse surface roughness in profiling small outer arc – (a) Thickness-nozzle diameter, (b) thickness-orifice diameter, (c) Thickness-traverse speed, (d) Pressure-nozzle length

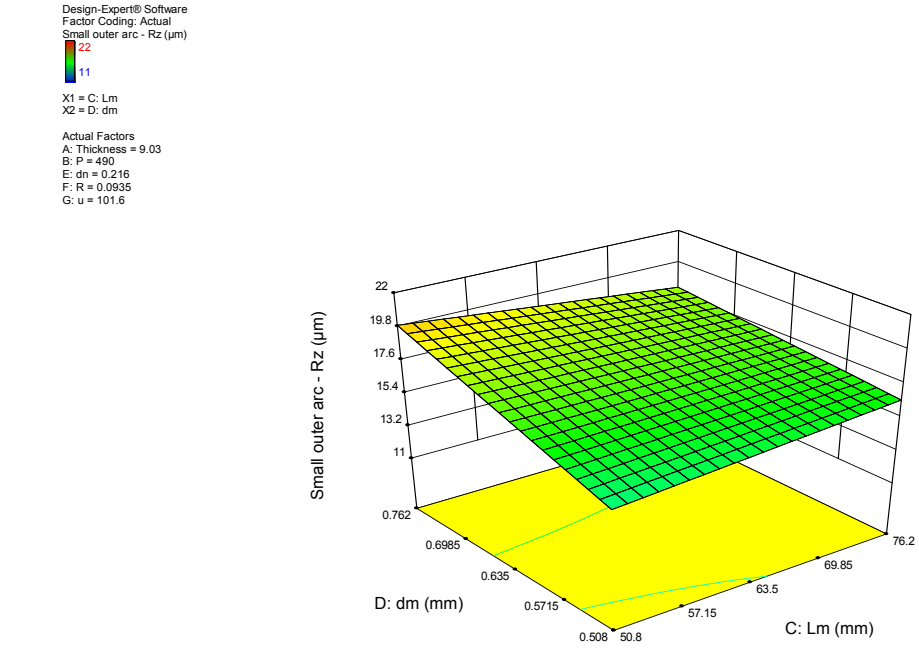

(a)

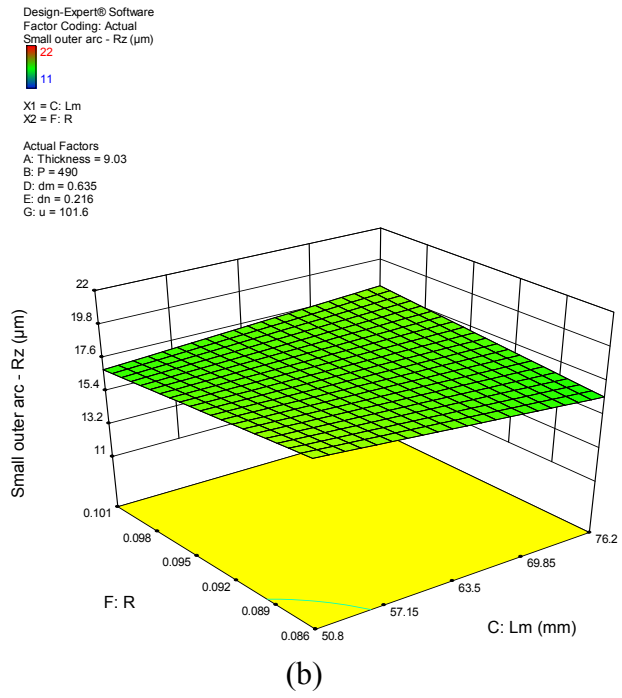

(b)

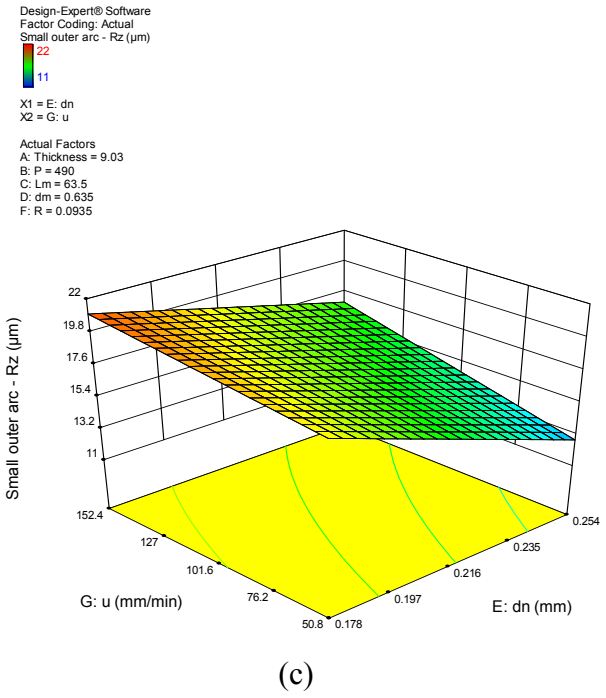

(c)

Figure 4.51. Parametric interaction effects on transverse surface roughness in profiling small outer arc – (a) Nozzle length-diameter, (b) Nozzle diameter-orifice diameter, (c) Traverse speed-load ratio

4.2.3.4 Large inner arc transverse R_z

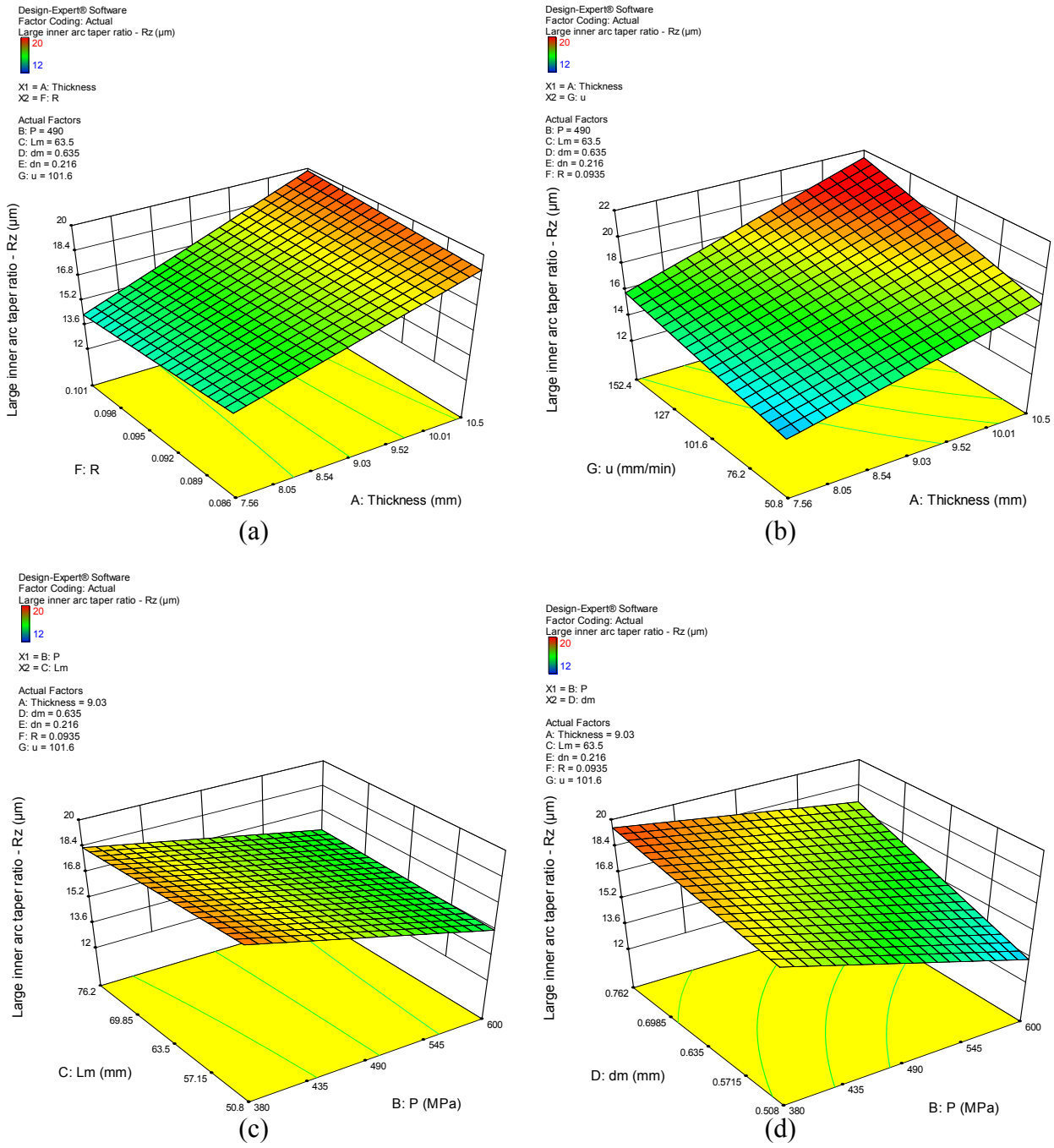

Figure 4.52. Parametric interaction effects on transverse surface roughness in profiling large inner arc – (a) Thickness-nozzle length, (b) thickness-nozzle diameter, (c) Thickness-traverse speed, (d) Pressure-nozzle diameter

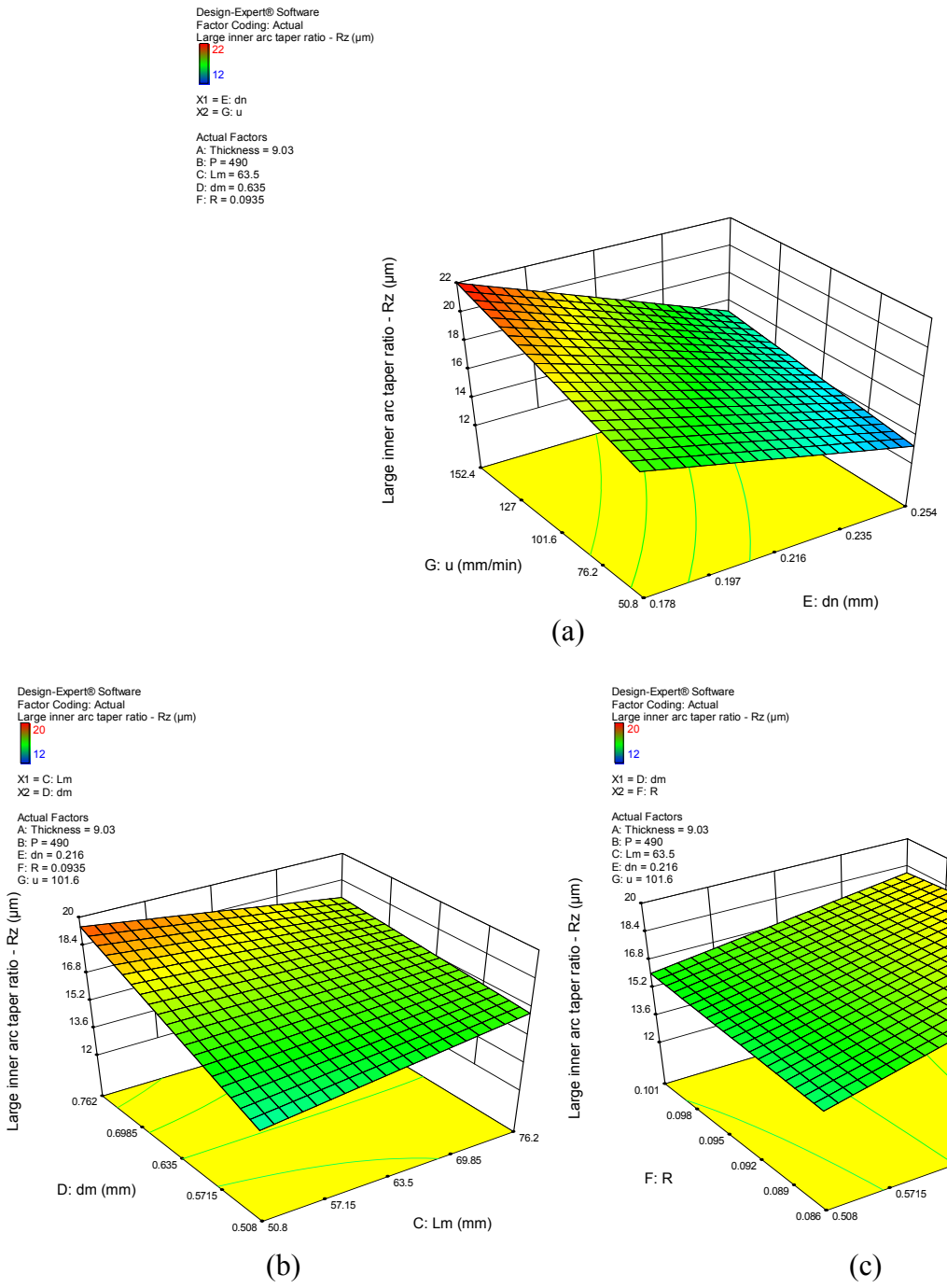

Figure 4.53. Parametric interaction effects on transverse surface roughness in profiling large inner arc – (a) Nozzle length-diameter, (b) Nozzle diameter-traverse speed

4.2.3.5 Large outer arc transverse R_z

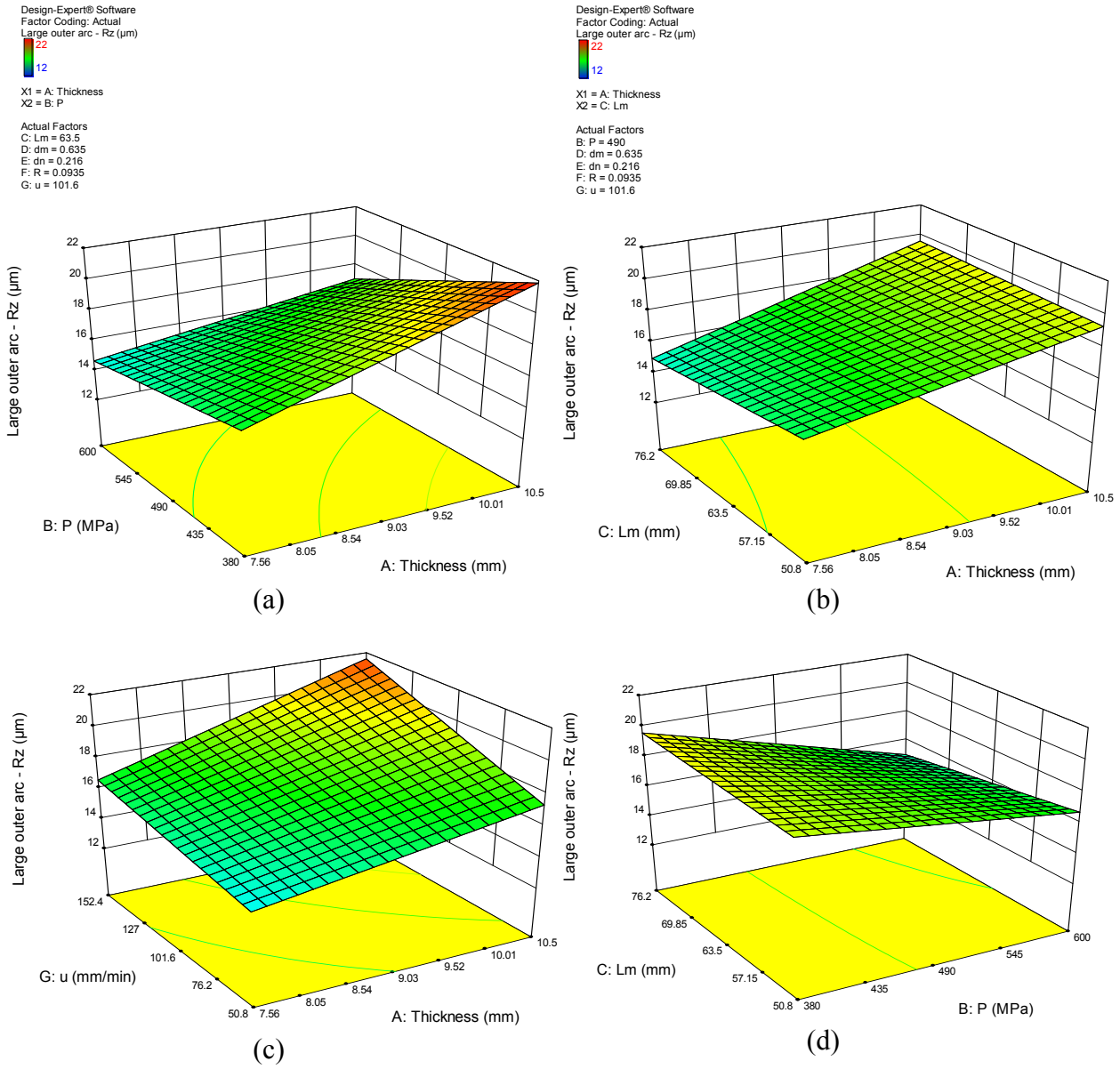

Figure 4.54. Parametric interaction effects on transverse surface roughness in profiling large outer arc – (a) Thickness-Nozzle length, (b) thickness-orifice diameter, (c) Thickness-load ratio, (d) Pressure-Nozzle length

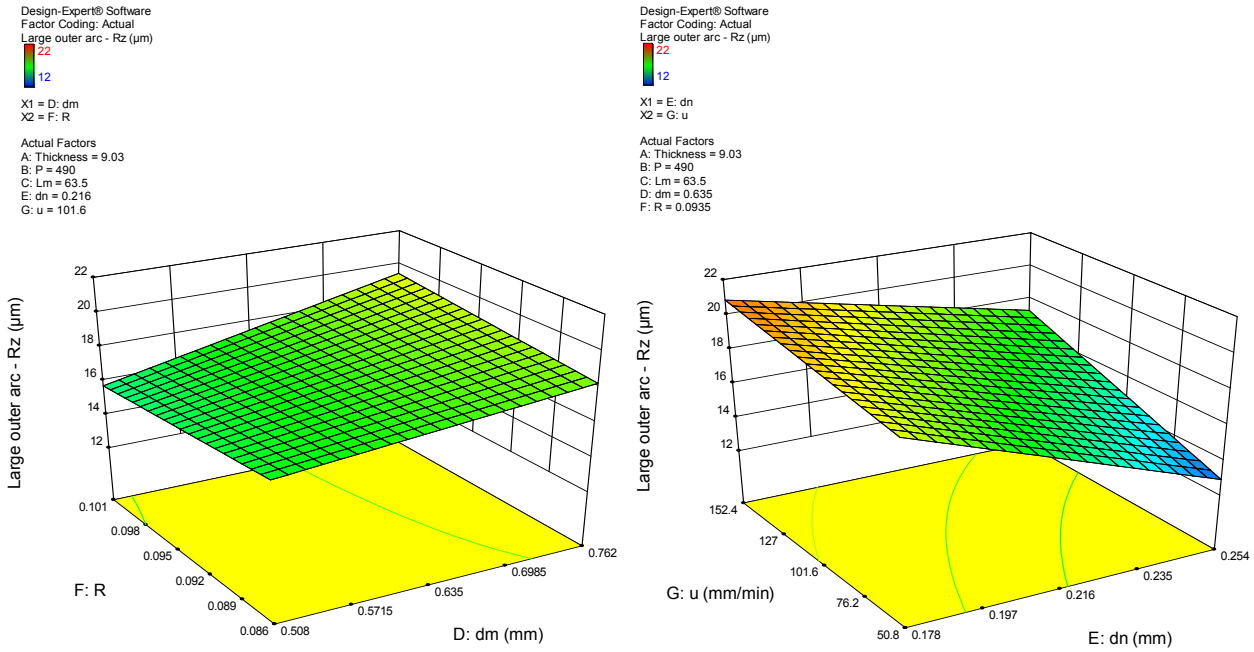

(a) (b)

Figure 4.55. Parametric interaction effects on transverse surface roughness in profiling large outer arc – (a) Nozzle length- diameter, (b) Nozzle diameter-traverse speed

4.2.4 Longitudinal Surface Roughness

In order to qualitatively analyze the longitudinal roughness characteristics of AWJ machined kerf wall, specimen exhibiting maximum kerf taper was selected (AWJ-5). Roughness was measured at three different depths - 1.2 mm, 3.75 mm and 6.35 mm for a 7.56 mm thick AWJ-5 specimen.

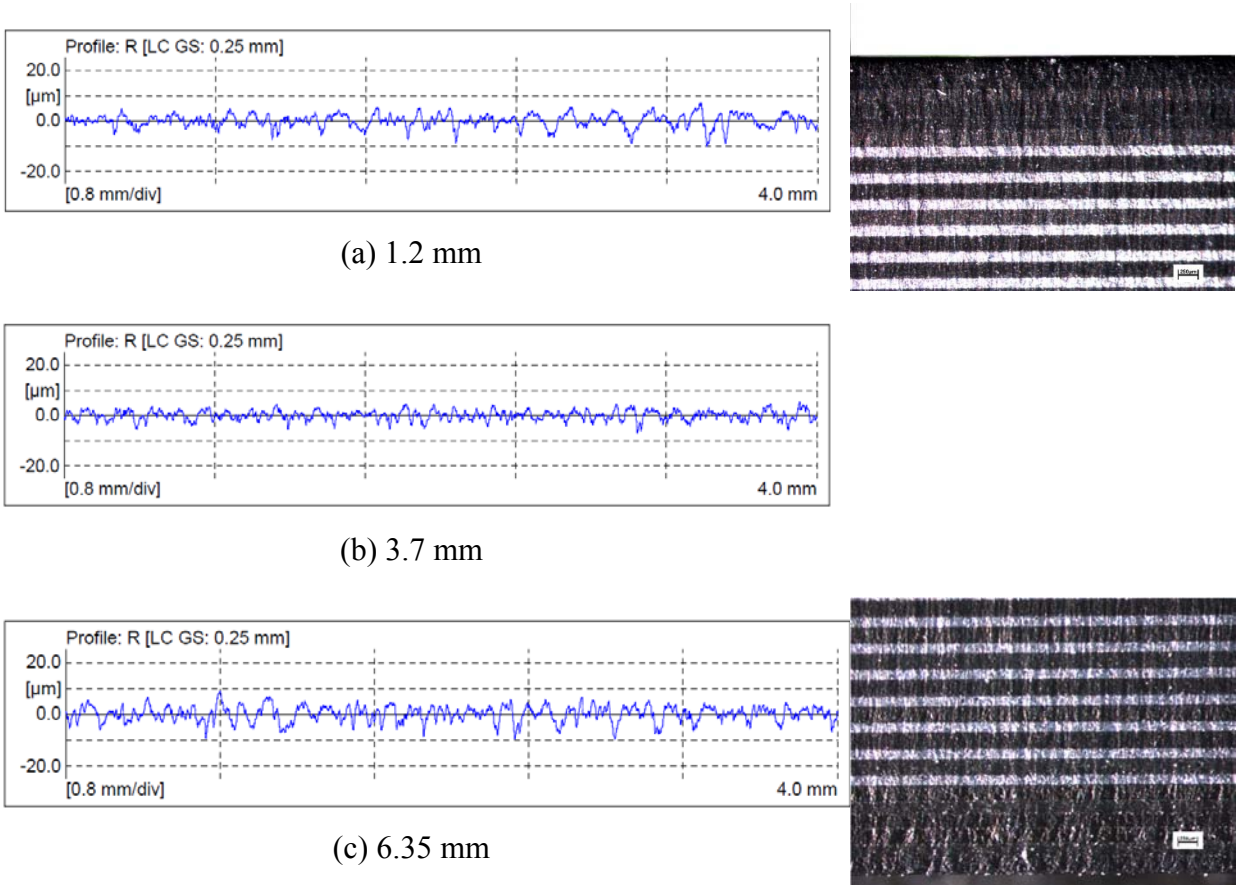

Figure 4.56. Longitudinal surface roughness measured for straight cut AWJ-5 specimen at three different depths (a) 1.2mm, (b) 3.75mm and (c) 6.35mm along with the macrographs depicting surface at jet entry and exit side.

The straight cut longitudinal surface roughness profiles along with the macrographs are depicted in Figure 4.56. Surface roughness measured near jet entry was 1.99 µm which decreased to 1.54 µm in the center, followed by an increased roughness to 2.4µm near the bottom. The high roughness near jet entry and exit side depicts initial damage region (IDR) and rough cutting region (RCR), whereas comparatively lower surface roughness in the middle section depicts the smooth

cutting region (SCR). The macrograph near the jet entry side depicts near orthogonal jet cutting front in initial damage region and the orthogonality is maintained at the jet exit side as well.

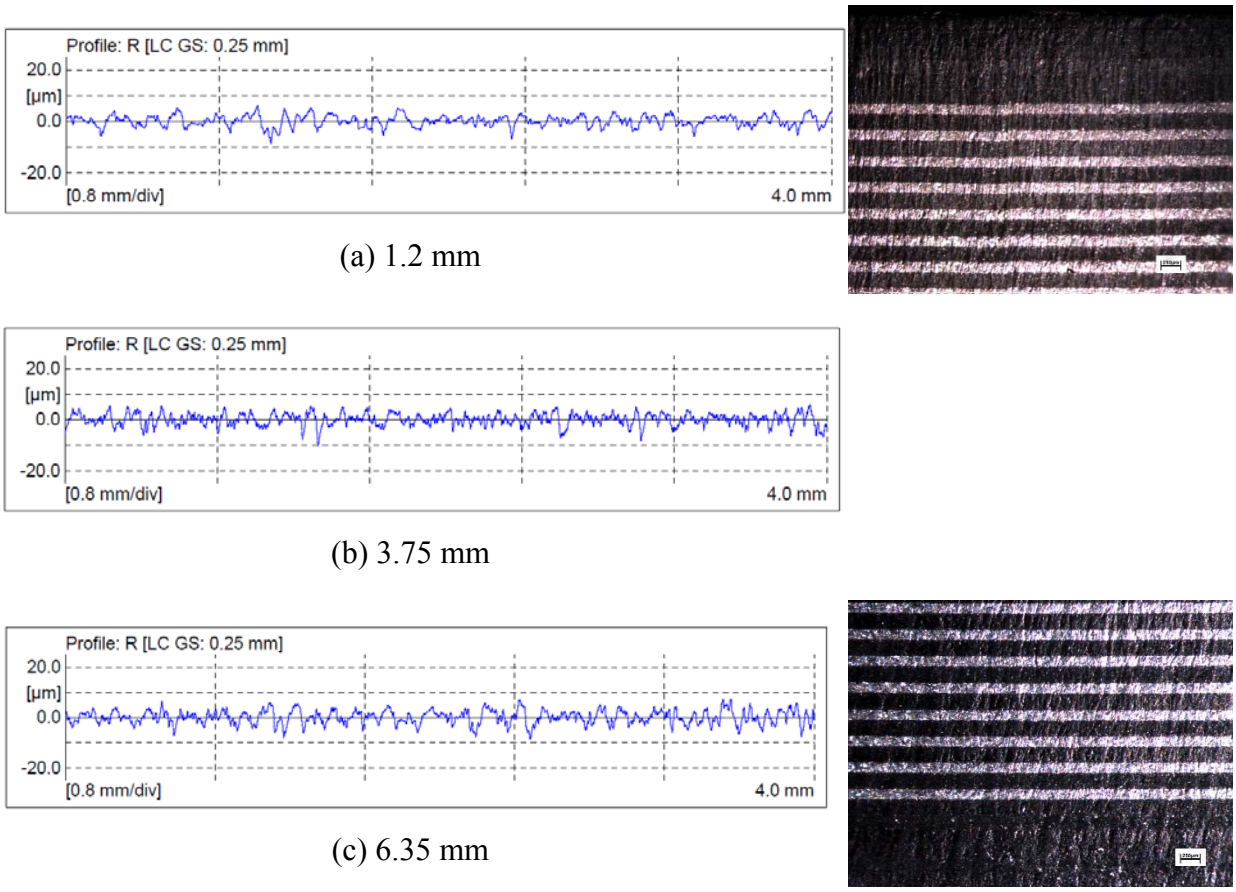

Figure 4.57. Longitudinal surface roughness measured for large outer arc AWJ-5 specimen at three different depths (a) 1.2 mm, (b) 3.75 mm and (c) 6.35 mm along with the macrographs depicting surface at jet entry and exit side.

Figure 4.57 depicts the longitudinal surface roughness profiles for large outer arc AWJ profile at three depths along with the macrographs. Surface roughness measured near jet entry was 1.72 µm with 1.54 µm in the center, and increased to 2.15 µm near the bottom ply.

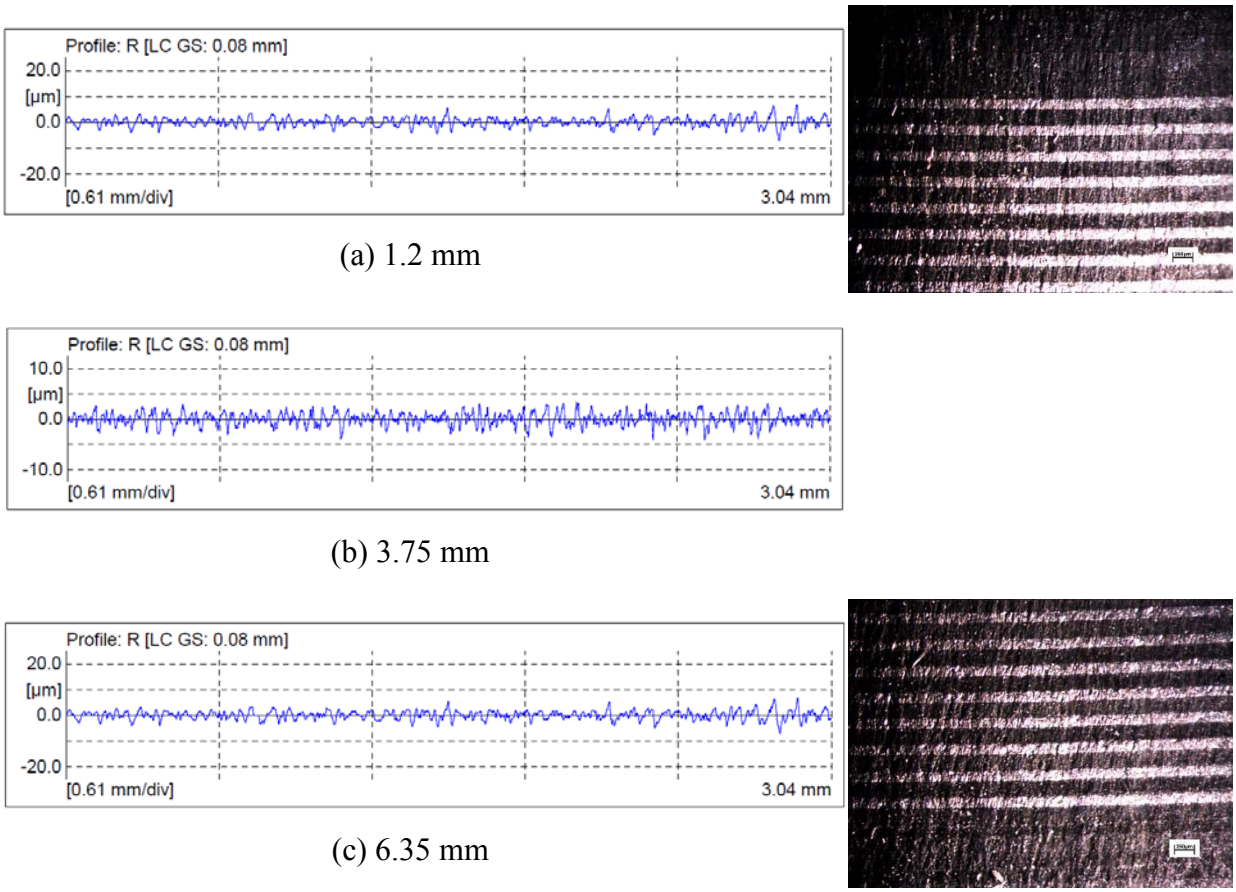

Figure 4.58. Longitudinal surface roughness measured for intermediate outer arc AWJ-5 specimen at three different depths (a) 1.2 mm, (b) 3.75 mm and (c) 6.35 mm along with the macrographs depicting surface at jet entry and exit side.

The small cut longitudinal surface roughness profiles at three depths along with the macrographs are depicted in Figure 4.58. Surface roughness measured near jet entry was 1.00 µm which increased to 1.25 µm in the center, followed by an increased roughness to 1.26 µm near the jet exit side.

For the AWJ-5 specimen 5, yielding maximum average taper, the longitudinal average surface roughness R_a was found varying between 0.96 µm and 2.4 µm with R_t varying between 7.4 µm and 18.8 µm, R_z varying between 6.5 µm and 15.6 µm. Irrespective of the traversed machining profile, the average longitudinal surface roughness was observed to be increasing with the jet penetration depth. The jet exit region observed a 20 to 38% increase in R_a in comparison to the entry region.

The surface roughness observations also exhibited a trend of decreasing surface roughness with reducing arc radius. The R_a values measured for straight cut near the jet exit region were found nearly half of the R_a for smallest arc radius, as depicted in Figure 4.59. Besides, roughness parameter R_t was analyzed along with R_z as it is an extreme parameter and accounts for localized disturbances. Increase in R_t and R_z values (Figure 4.60 and Figure 4.61) to nearly 40% supplement the smoother surface characteristic for smaller arc profiles.

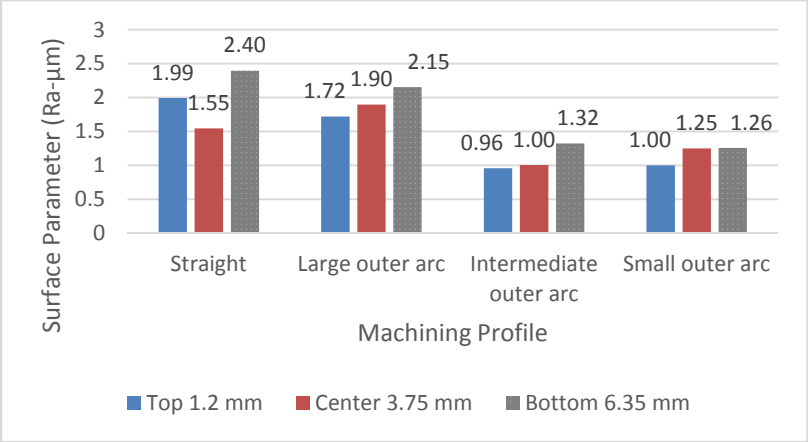

Figure 4.59. Surface roughness parameter R_a measured longitudinally at three different depths for four different profiles.

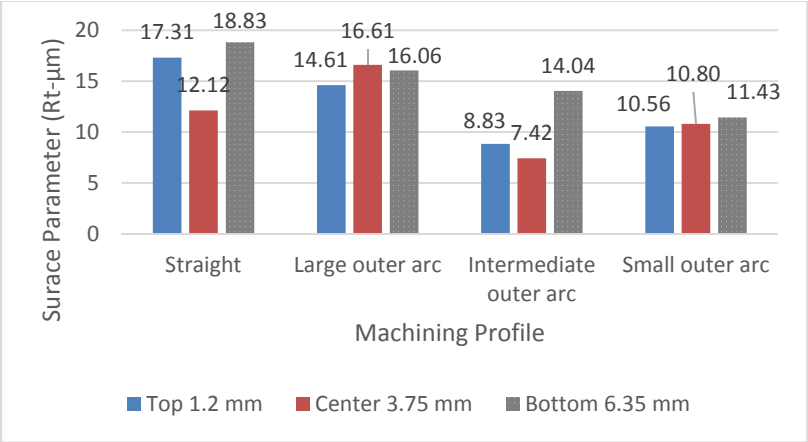

Figure 4.60. Surface roughness parameter R_t measured longitudinally at three different depths for four different profiles.

The microscopic images of the surface were further investigated to reinforce and relate the effect of profiling curvature on the surface quality. An unconventional observation of striations based on visual inspection was made. The trailback striation marks of the jet due to energy loss at the exit side and eventual jet curving in the direction opposite to the jet traverse is a characteristic of rough AWJ cut. This depicts either inadequacy of jet cutting energy or higher material resistance. The jet curving near the bottom is related to incoherency of jet with decelerating sporadic abrasive particles, resulting in an expected behavior of high surface roughness.

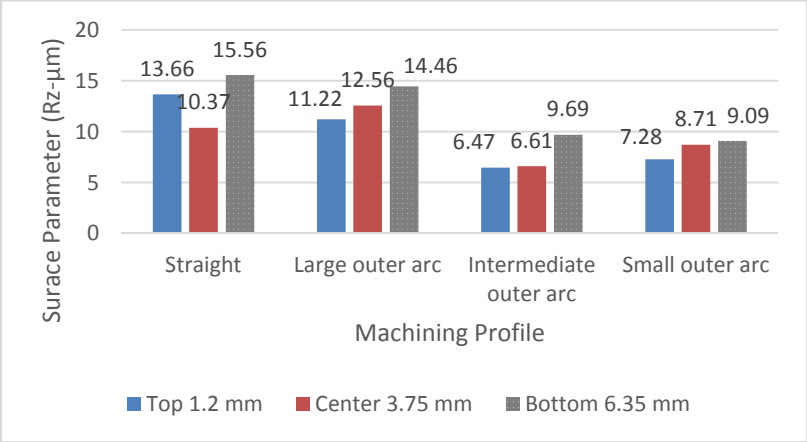

Figure 4.61. Surface roughness parameter R_z measured longitudinally at three different depths for four different profiles.

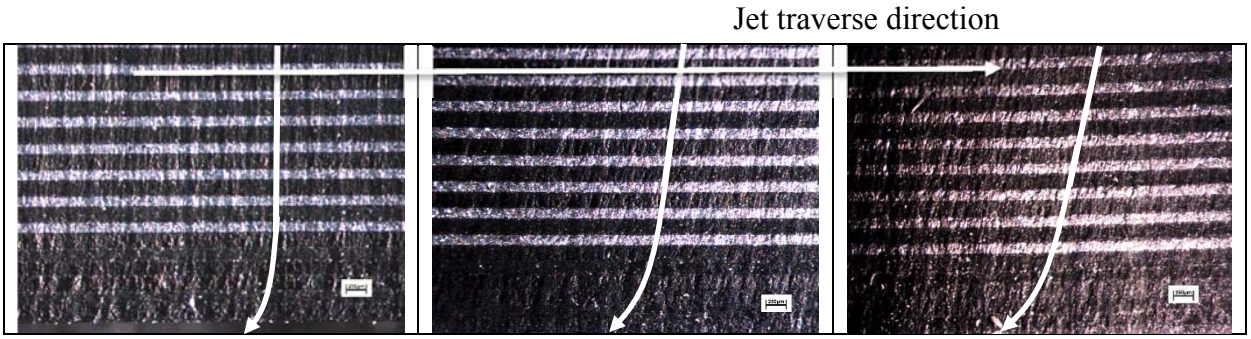

Figure 4.62. Surface quality and curved front striations at the jet exit side for (a) straight cut, (b) large arc profile (c) small arc profile

The curved cutting profile depicted in Figure 4.62 showed prominent curved striations which increases with the reduction in cutting profile curvature. However, the average surface roughness is unexpectedly lower for profiles observed with largely curved jet fronts.

The behavior of longitudinal surface roughness was also investigated in thick laminate (10.5 mm). Surface roughness along the straight cut jet traverse direction and for each ply from entry to exit side was measured and depicted in Figure 4.63. Experiment number 32 was selected for this analysis because a significant variation in surface roughness from top to bottom ply is expected for an AWJ profiled surface with conditions leading up to maximum taper.

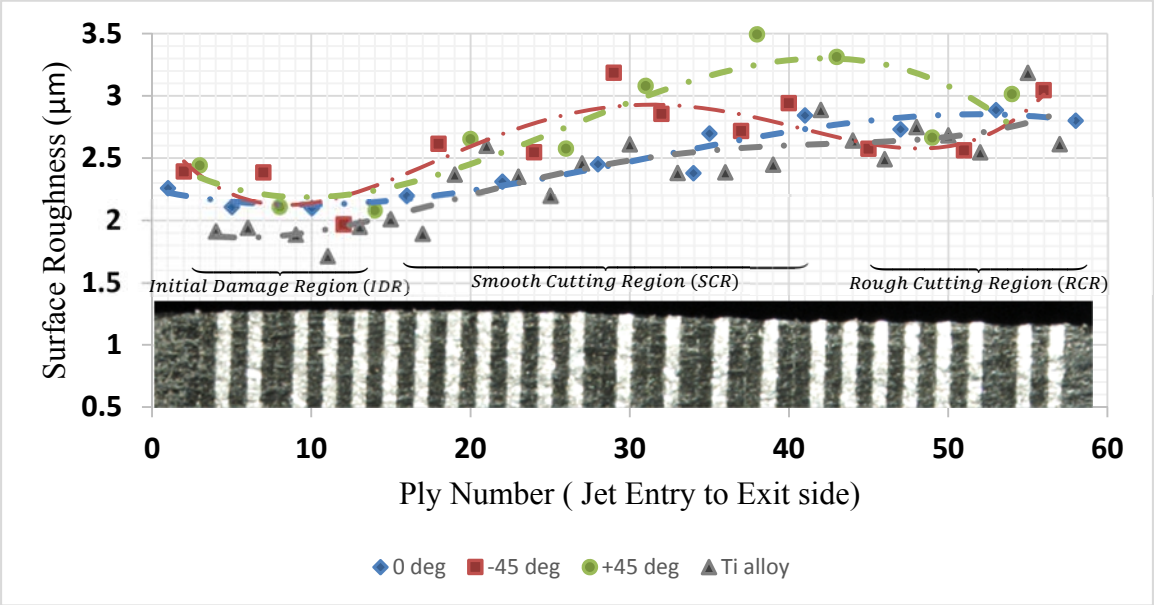

Figure 4.63 Surface Roughness (Ra- µm) along jet traverse direction for each ply in straight cut for AWJ- 32 specimen.

The average roughness values vary from 1.65µm to 3.5µm. As depicted in Figure 4.63, three zones can be identified based on the average surface roughness (Ra) parameter. The first zone - Initial Damage Region (IDR) spans around initial 8-9 plies (~1.2mm) with R_a value varying between 2-2.5µm for composite ply and 1.6-1.8µm for Titanium ply. The value of R_a stabilizes and gradually increases upto the jet penetration depth of ~8mm. The R_a value was observed between 2.25-3.5 µm for composite ply and 2.2-2.45µm for titanium ply. The R_a value steeply increased in the remaining Rough Cutting Region (RCR) to upto 3.18µm.

It was observed that the titanium surface roughness was lower than the composite plies in all the cutting characterized regions with an exception of Rough Cutting Region where titanium depicted surface roughness nearly equivalent to the composite plies (>2.5µm).

Besides, an unusual roughness characteristic was observed at the end of RCR where a discrete layup arrangement spans between ply 27 and 42, with titanium plies interspersed alternatively between two consecutive composite plies. A sudden 8.5% drop in R_a value for titanium and 13% spurge for +45° composite ply suggests the effect of ply layup in machining laminates, significantly affecting the jet-material interaction. This behavior can be attributed to the dominant role of water power in mechanism of material removal in composites, especially the matrix material. The availability of water component earlier than the abrasive particles, at the end of composite layer, accounts for the hydro-pressure build up just before the titanium ply. This pressure is dependent on the jet penetration depth through composite layer before titanium layer and is suddenly released by the erosive impact of abrasive particles on the titanium. The momentary increase in jet energy with increased hydro-pressure accounts for increased cutting efficiency of the jet for titanium plies. This manifests smooth titanium surface on removal with high energy jet, and rougher composite surface due to increased water-induced distortion in composite plies.

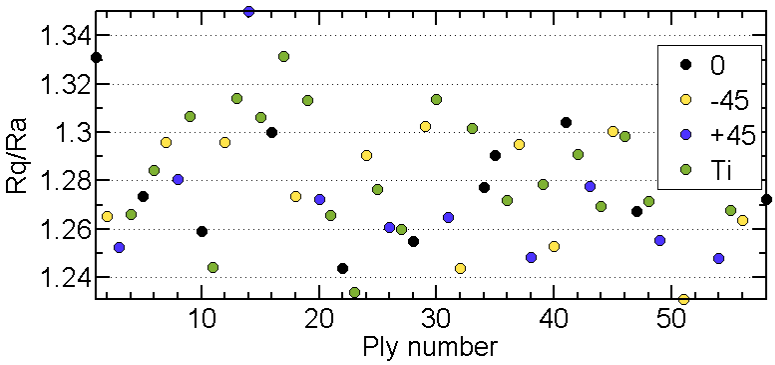

Figure 4.64 Rq/Ra ratio for profile measured along jet traverse direction for each ply in AWJ-32 straight cut specimen

The variation of the ratio of root mean square surface roughness and average surface roughness was found to be randomly varying around 1.28 (±0.025) as shown in Figure 4.64. The R_q/R_a value depicts the inherent characteristic of the machining process.

Skewness and kurtosis are depicted in Figure 4.65 and Figure 4.66 respectively. The graphs suggest a negatively skewed process throughout jet penetration depth, suggesting a surface topography with profound valleys and comparatively flat troughs. The surface topography is also leptokurtic with kurtosis >3 for most of the plies. The region between ply 10 and 20, also the transition zone between IDR and SCR shows a topologically distinct behavior with a sudden low skewness (-0.5 to -1.25μm^3) and high kurtosis (>4μm^4). This is a zone of cutting with jet abrasive energy high enough to produce low average surface roughness but the sharp edges of the abrasives led to negatively skewed profile with highest peakedness.

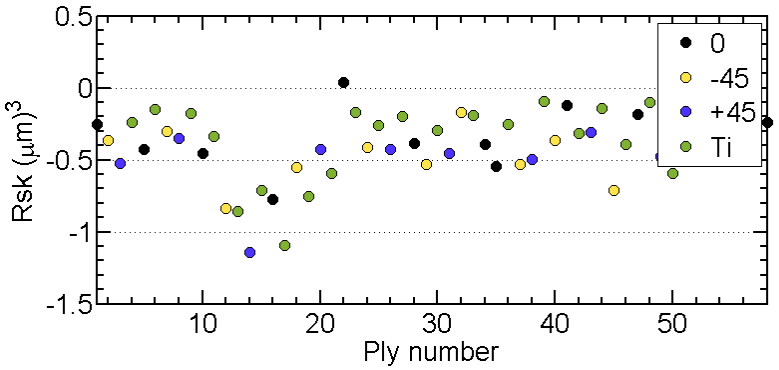

Figure 4.65 Rsk (Skewness) for profile measured along jet traverse direction for each ply in straight cut AWJ- 32 specimen.

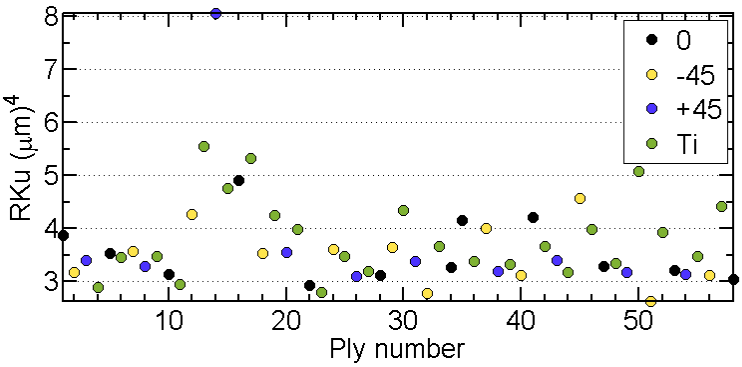

Figure 4.66 Rku (Kurtosis) for profile measured along jet traverse direction for each ply in straight cut AWJ- 32 specimen.

Skewness vs. kurtosis curve was plotted in order to further analyze the surface topography. The plot characteristic was similar to surface generated by grinding, drilling and honing process. Titanium near the jet exit was found to be more negatively skewed in comparison to the composite plies, which corresponds to the deep valleys with high distribution of their peakedness. A negatively skewed profile indicates more resistance to abrasive erosion [28], which in this case is due to reduced cutting efficiency of the jet.

Within the composites, 0° ply showed some positive skewness with weak kurtosis, substantiating the less requirement of cutting energy. +45° composite surfaces exhibit significantly close values in skewness-kurtosis space which correspond to the similarity of jet-material (+45°) interaction throughout the specimen thickness.

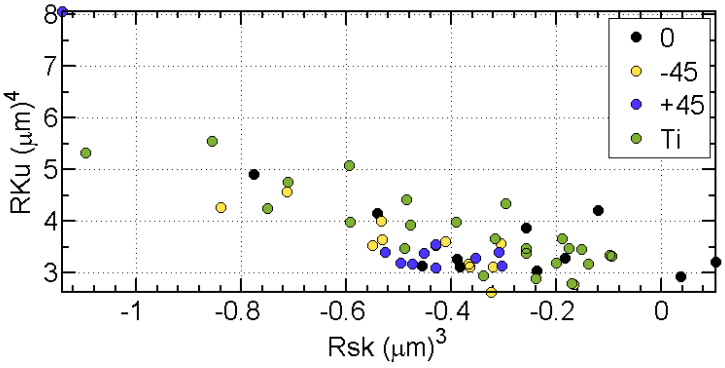

Figure 4.67 Bearing curve for profile measured along jet traverse direction for each ply in straight cut AWJ- 32 specimen.

Chapter 5. DISCUSSION

This investigation is concentrated on the effect of process parameters on AWJ contouring of thick FML. Abrasive Waterjet Technology, hitherto unexplored for thick fiber metal aerospace laminates, exhibit a plausible alternative for conventional machining.

5.1 SURFACE MORPHOLOGY

The kerf wall generated by AWJ machining of TiGr was optically inspected. Typical optical micrographs of rough AWJ kerf wall are depicted in Figure 5.1.

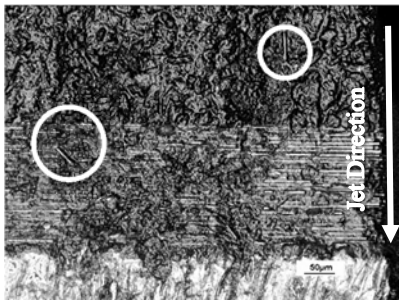

(a) 45/0/Ti ply layup surface

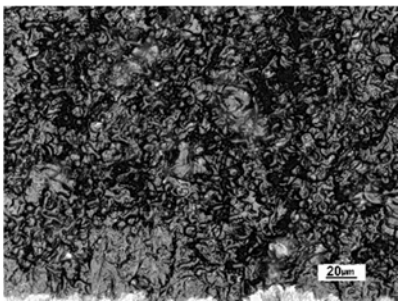

(b) matrix cracking

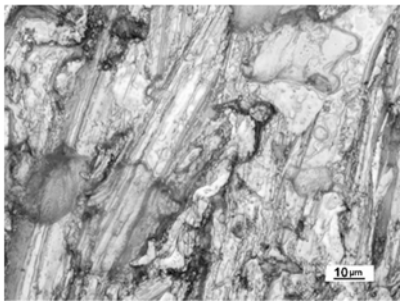

(c) Titanium shearing

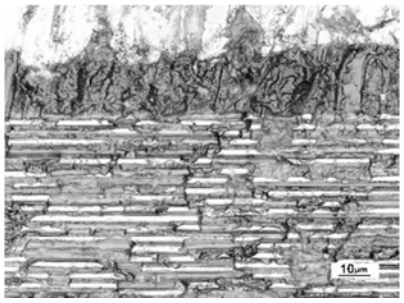

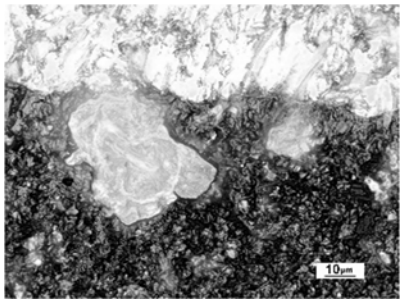

(d) 0° layer fractured fibers, (e) Titanium burr embedment in composite ply

Figure 5.1. Typical rough cut machined kerf surface optical micrographs

Mechanism of material removal was optically inspected for titanium, graphite fiber and thermoplastic matrix as different phases. Within thermoplastic composite-titanium, matrix

material is cut by shearing and plastic deformation as shown in Figure 5.1(a,b,c) and observed by Seo et al. while IM-7 carbon fibers were cut by micro chipping, brittle fracture, and bending failure. The bending and chipping can be easily observed in Figure 5.1(a and d) where interlaminate cracking and the fibers in 0° ply are pulled out and dislocated. Specimens with high abrasive flow rate showed signs of shear deformation on titanium ply concluding that titanium was removed by ductile shearing, abrasive plowing, and scratching action. Figure 5.1(c) depicts shear deformation of Titanium ply similar to what was observed by Seo et al. [68]. The dislodged titanium burrs were also found sticking over composite ply as depicted in Figure 5.1(e).

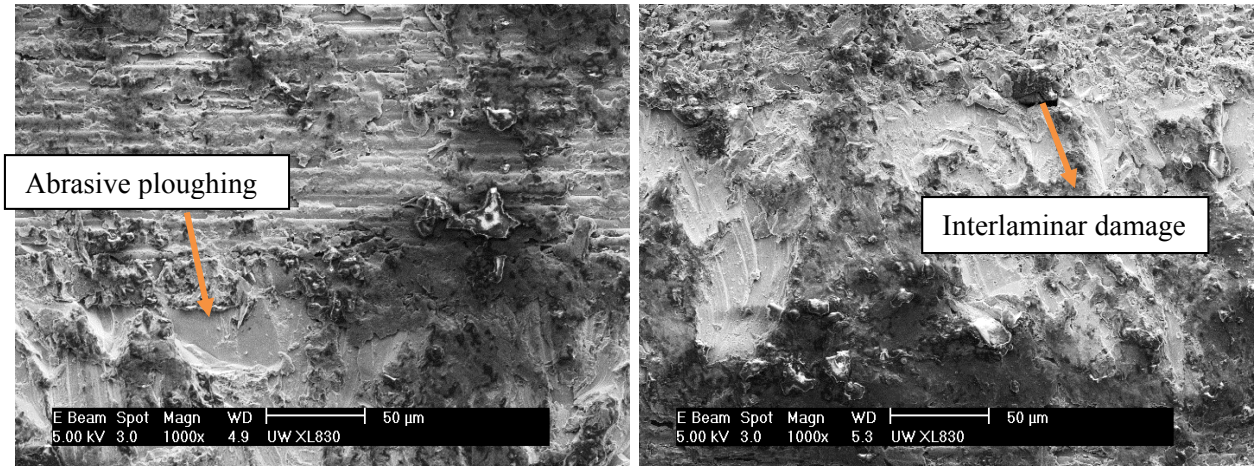

(a) (b)

Figure 5.2. SEM micrograph of (a) fifth ply and from the top, and (b) eighth ply from the bottom of 10.5mm thick, AWJ-25 machined straight cut kerf wall

Figure 5.2 shows the SEM micrograph depicting bond line between 0° and titanium ply for 10.5 mm thick straight cut AWJ-25 specimen. It was observed that the bond line between dissimilar plies viz. composite and titanium was intact near the jet entry region. However, a small Interlaminar damage between -45° and titanium bond was observed at high penetration depth as depicted in Figure 5.2(b). The degraded bond line was only observed between ±45° composite and titanium ply near the jet exit side explaining the role of sideways water intrusion. Besides, the bond defects (although not severe) were found to be the ones between the bonds where titanium was preceded by ±45° ply in the laminate layup.

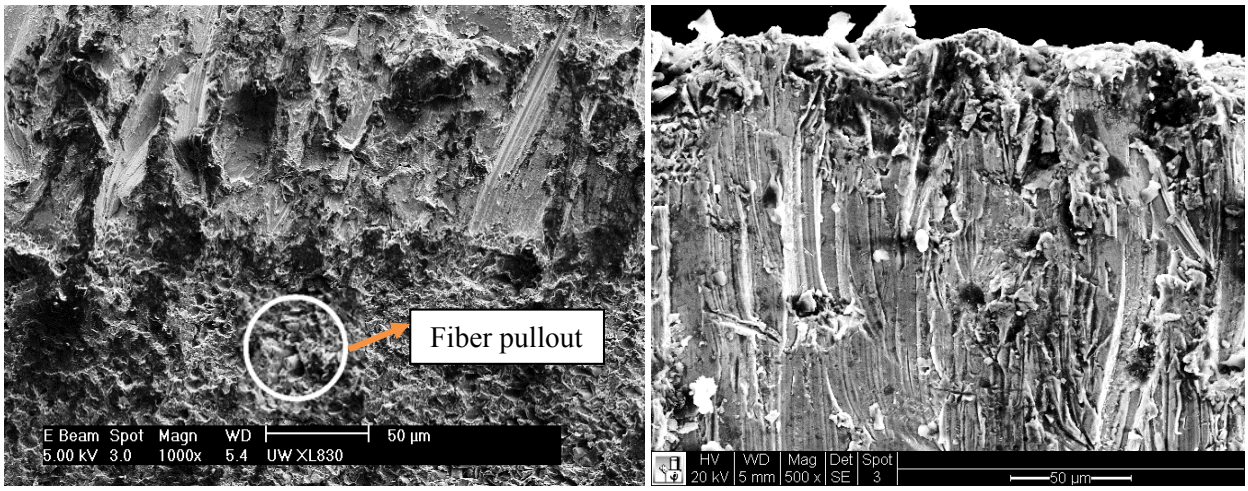

(a) (b)

Figure 5.3. SEM micrograph of AWJ machined straight cut kerf wall under (a) condition number 1 for 7.5mm thick specimen (b) 380 MPa pressure, 4.68g/s abrasive flow rate and 152.4 mm/min traverse speed for 2.52 mm Ti-6Al-4Vsheet.

Figure 5.3(a) shows the SEM micrograph depicting bond line between titanium ply and +45° composite ply for jet exit side straight cut AWJ machining under experimental condition number 1, and for 7.56mm thick laminate specimen. The fiber pullout and random scratching throughout the titanium ply is found to be characteristic of lower jet energy. Figure 5.3(b) depicts the jet entry side of straight AWJ cut Ti-6Al-4Vsheet under 380 MPa pressure, 4.68g/s abrasive flow rate and 152.4 mm/min traverse speed. The contrastive distinction between the titanium shearing with nearly straight scratches at the entry side and randomly oriented scratches near the exit side is evident from the figures.

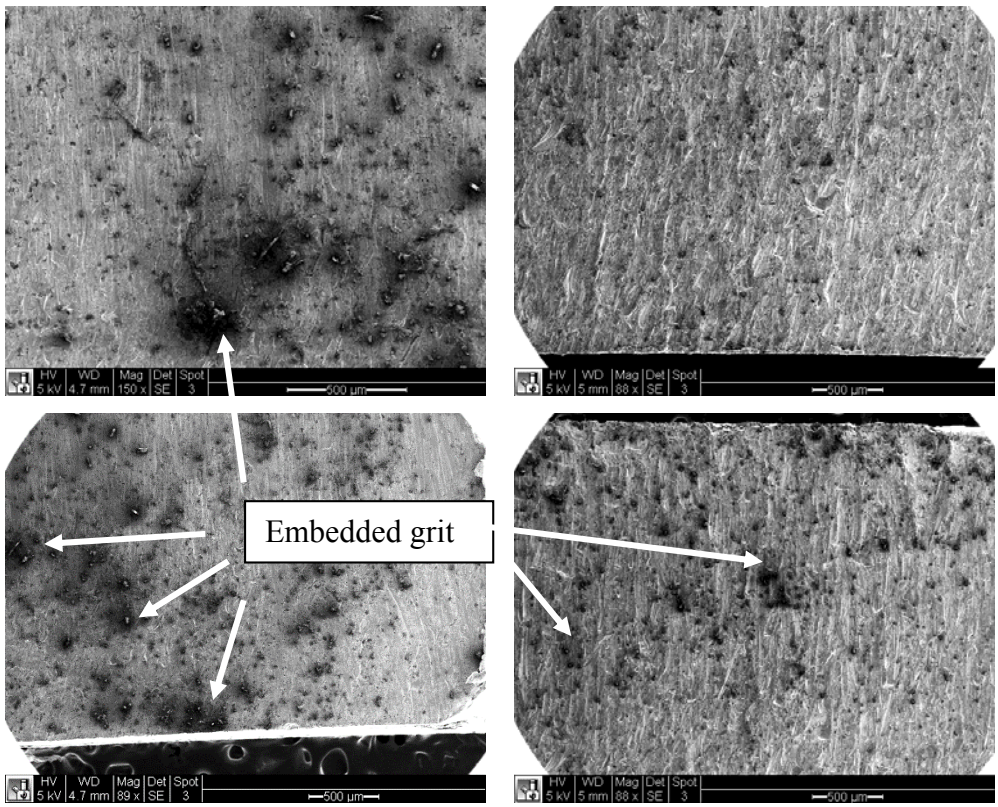

(a) (b)

Figure 5.4. (a) Straight AWJ cut Ti-6Al-4V sheet under 380 MPa pressure, 4.68g/s abrasive flow rate and 152.4 mm/min traverse speed, (b) straight AWJ cut Al 6061-T6 sheet under 380 MPa pressure, 4.68g/s abrasive flow rate and 304 mm/min traverse speed

Overall, as observed from micrographs and SEM pictures, no embedded grit was located in AWJ cutting of TiGr, machined within experimental conditions. AWJ machined FML kerf surface was compared with typical kerf wall surface of common aerospace alloys machined with AWJ. Figure 5.4 depicts SEM micrographs of Ti-6Al-4V and Al 6061-T6 sheet machined at 152.4 mm/min and 304 mm/min traverse speed respectively with 4.68 g/s abrasive mass flow rate and 380 MPa water pressure. The figures shows high level of grit fragmentation and embedment, especially in titanium alloy. However, one of the reasons of low grit embedment in titanium present in TiGr could be that titanium alloy sheets used in this study are 140 μm thick which is comparable to the abrasive diameter size (~125 μm).

5.2 EFFECT OF PLY ARRANGEMENT

The percentage composition and arrangement of titanium plies among composite laminates was found to be an influencing factor in taper as well as surface roughness response. The kerf curving near the exit and entry side depicts an easy removal of composite due to matrix distortion by the high energy jet. This was corroborated by the kerf geometry of high taper specimens as shown in Figure 5.5. Higher damage was observed near the entry and exit side where the composite ply concentration was high, and nearly square cut was observed where titanium was uniformly distributed. This can be attributed to the fact that titanium is removed by shearing, whereas composite plies involve bending and series of fracture failure along with matrix bulk removal by the radial expansion of the jet. A TiGr laminate with titanium as faceplies is expected to show less entry and exit damage.

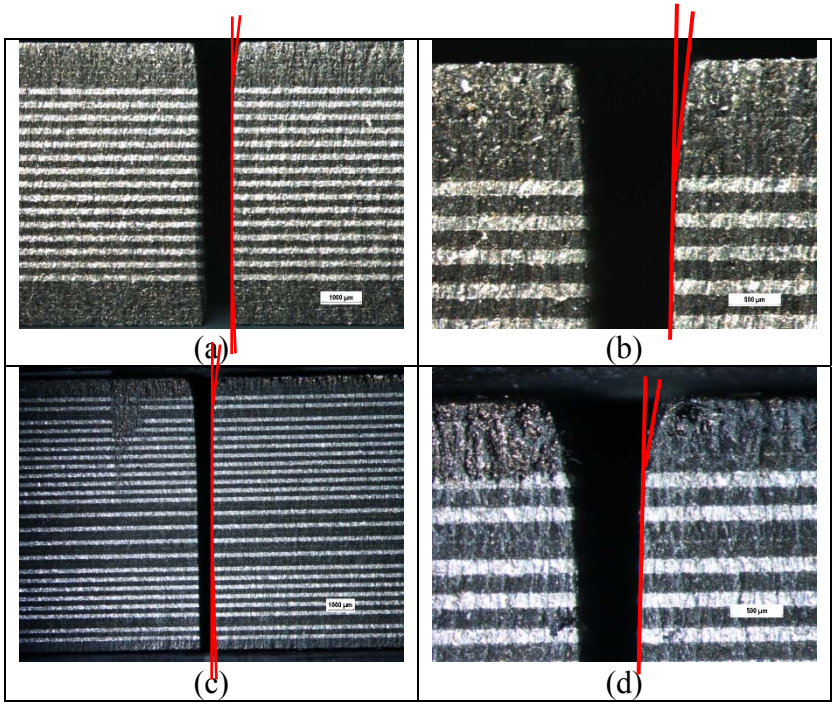

Figure 5.5. Kerf taper of straight cut AWJ-5 (a) Through-the-thickness section, (b) Top cross-section, and AWJ-32 (c) Through-the-thickness section, (d) Top cross-section

The excess composite matrix removal due to inherent characteristic of jet expansion was observed for the sections where two composite plies were interspersed with one titanium ply. This further substantiates the role of titanium distribution in kerf topological characteristics.

5.3 EFFECT OF CUTTING GEOMETRY

AWJ process was concluded as cutting geometry dependent process for machining advanced fiber metal laminates. In order to interpret the taper ratio variation with the cutting profile curvature, a normalized taper (T) can be defined as the ratio of curved surface taper to straight surface taper.

$$\text{Normalized Taper (T)} = \frac{\text{Curved surface taper}}{\text{Straight surface taper}}$$

The normalized taper was calculated based on the predictive models developed in section 4.1.1.

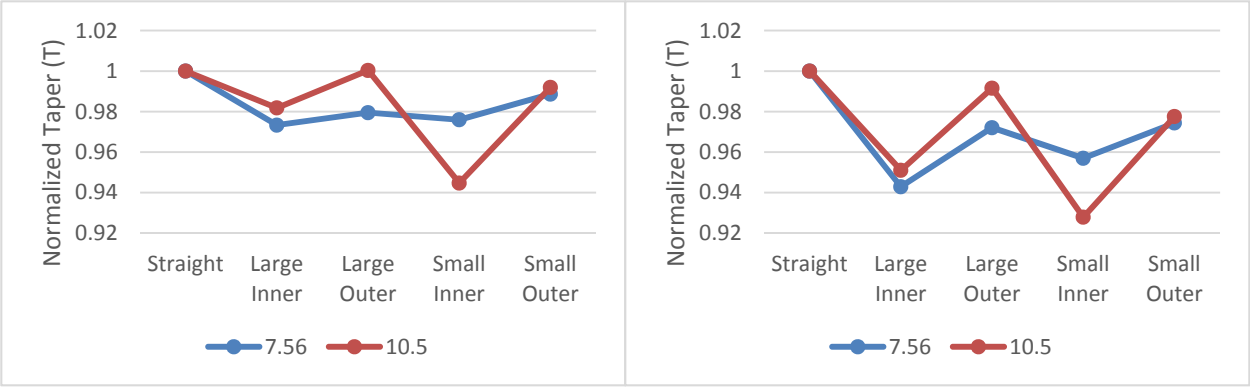

(a) (b)

Figure 5.6. Predicted Normalized taper at Pressure (P) =380 MPa, mixing tube length (Lm) = 76.2 mm, mixing tube diameter (dm) =0.508 mm, orifice bore (dn) =0.254 mm, load ratio (R) =0.101 at jet traverse speed (a) 50.8 mm/min, (b) 152.4 mm/min

Figure 5.6 (a) and (b) shows the normalized taper for different profile curvatures at a given experimental condition with traverse speed 50.8 mm/min and 152.4 mm/min respectively. 10.5 mm thick specimen was more taper sensitive than 7.56 mm thick specimen due to the more resistance and energy loss at higher thickness. Irrespective of the jet traverse speed, the concavity (inner arc) and convexity (outer arc) played a dominant role in taper response. As depicted in Figure 5.6 (a) and (b), the low value of normalized taper for concave (inner) arc profiles in comparison to convex (outer) arc profiles can be attributed to geometric constraints which affect the jet inertial response and thus machining characteristics. For concave curved profiles, the jet traverses in linearly interpolated paths towards the material to be removed and the inertial effect

contributes to more material removal. However, the jet moves away from the curvature in convex profiles, leading to higher taper than inner arc profiles. The effect of concavity was more prominent in smallest arc profiles.

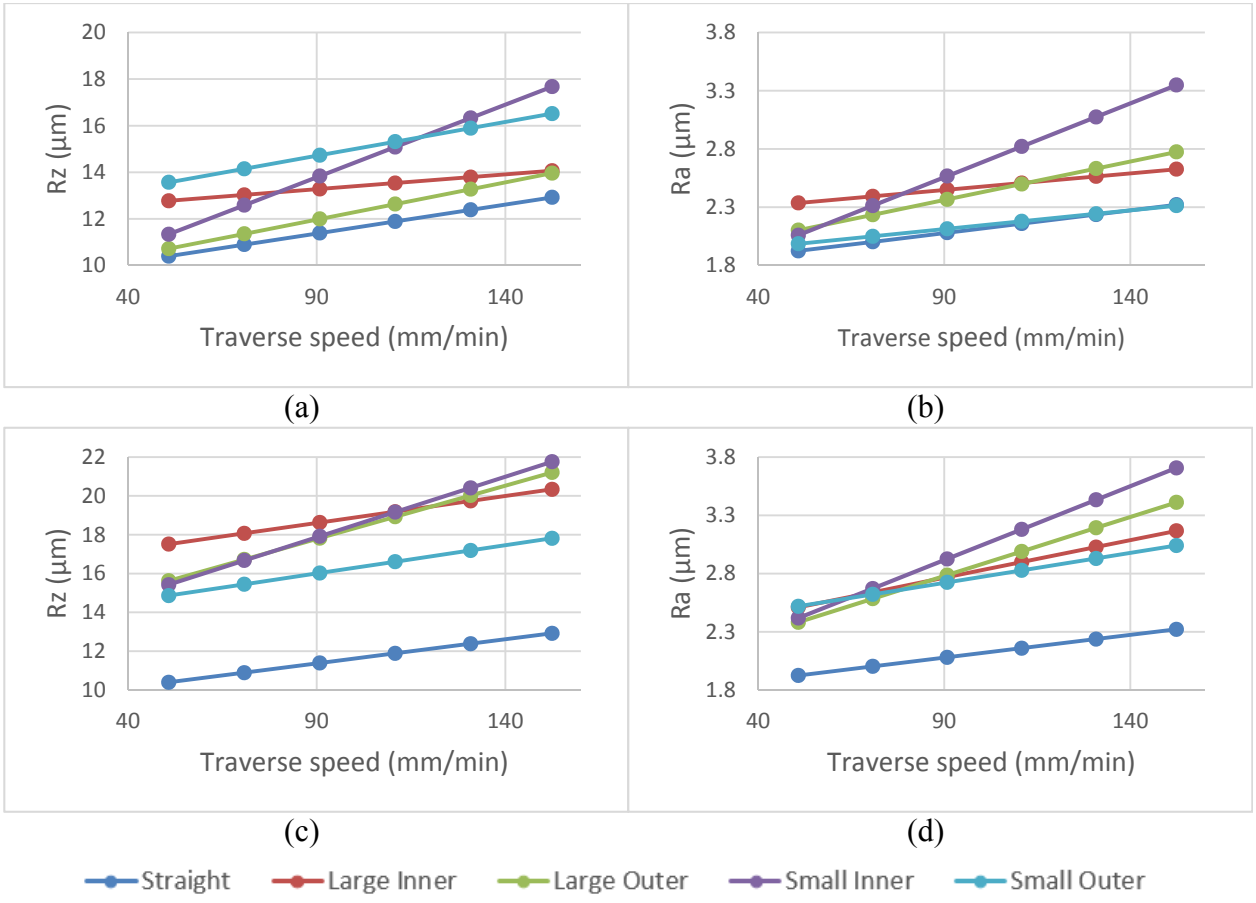

Figure 5.7. Surface roughness for five different profile curvatures as a function of traverse speed at Pressure (P) =380 MPa, mixing tube length (Lm) = 76.2 mm, mixing tube diameter (dm) =0.508 mm, orifice bore (dn) =0.254 mm, load ratio (R) =0.101 for (a) R_z for 7.56 mm thick, (b) R_a for 7.56 mm thick, (c) R_z for 10.5 mm thick, (d) R_a for 10.5 mm thick specimen.

The effect of curvature was also prominent in transverse roughness response. Figure 5.7 (a) and (b) shows R_a and R_z roughness as a function of traverse speed, for 7.56 mm thick specimen machined at constant experimental condition. Similarly, Figure 5.7 (c) and (d) depict the same for 10.5 mm thick specimen. Among all the profile features, straight cut surface was found with least

surface roughness and smaller arc profiles with maximum surface roughness. A high slope of small arc transverse roughness indicates high sensitivity of surface roughness at higher cutting speeds.

Similarly to the taper ratio, normalized surface roughness can be defined as the ratio of longitudinal surface roughness of curved profile to straight profile.

$$\text{Normalized Longitudinal Roughness (S)} = \frac{\text{Curved surface longitudinal roughness}}{\text{Straight surface longitudinal roughness}}$$

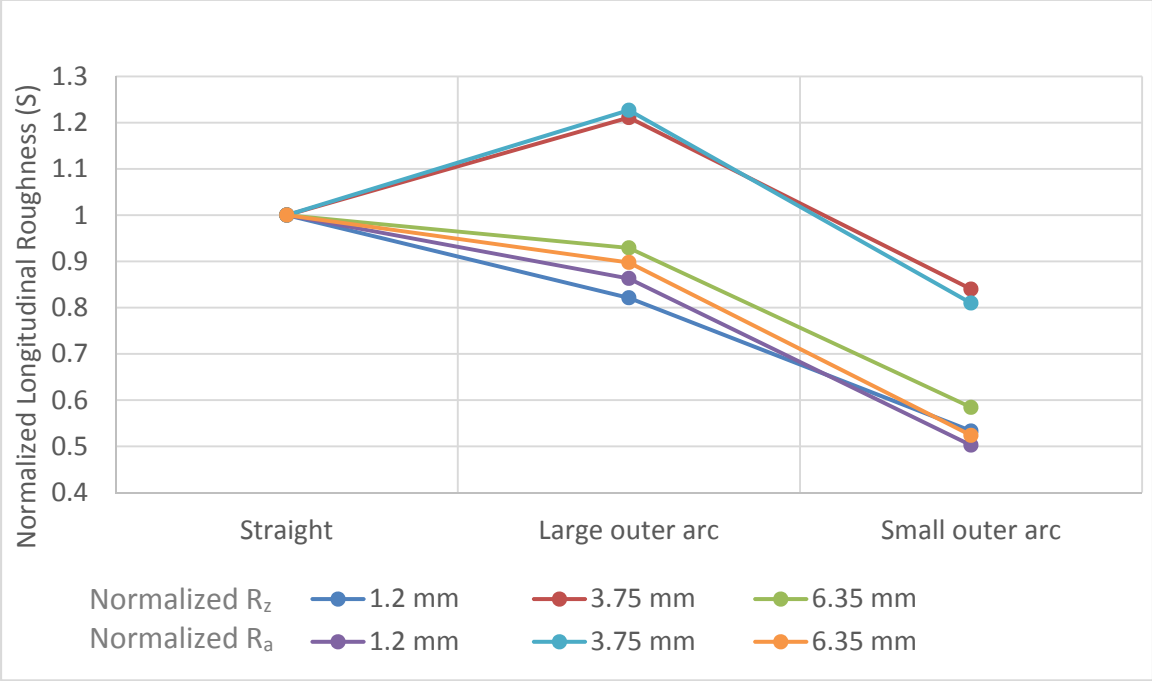

Figure 5.8. Longitudinal surface roughness parameters R_z and R_a measured at three jet penetration depths – 1.2 mm, 3.75 mm, and 6.35 mm normalized with the straight cut surface roughness for AWJ-5 specimens

Figure 5.8 depict the normalized longitudinal surface roughness (S) for AWJ-5 specimen measured at three penetration depths. Both R_a and R_z values were lower for smaller arc profiles due to rotational/longitudinal cutting component of the jet induced by the cutting profile. Besides, the larger arcs at the center of specimen thickness was found to be rougher. Overall, the dependence of roughness and taper performance of AWJ on cutting geometry can be predicted and plots similar to Figure 5.6 and Figure 5.8 can be obtained to relate the cutting performance for straight cut to curved profiles.

5.4 PARAMETRIC EFFECTS

This research study substantiated the feasibility of AWJ process in 2D contouring thick TiGr laminates. The study detailed the effect of six different parameters on kerf taper ratio and transverse surface roughness. The effect of each parameter on machining responses and sensitivity to cutting profile geometry is discussed and summarized in section 5.4.1and 5.4.2.

5.4.1 Parametric Effects on Taper ratio

5.4.1.1 Effect of Pressure

Within the experimental limits, it was determined that the taper ratio is not significantly sensitive to water pressure as it is to the other parameters. This can be justified by the sufficiency of waterjet energy at 380 MPa pressure in efficient machining along with the chosen experimental limits of other parameters. An increase to 600 MPa adds to the jet energy without appreciable variation in taper.

Although low sensitivity of pressure, taper ratio showed negative trend with increase in water pressure, and consistent with the previous investigations for composites [21,84], titanium alloy and glass fiber laminates [23]. However, Wang [78] reported an opposite trend for polymer matrix composites. The results also show inconsistency with some investigations on such as machining of marble [93]. The factor contribution percentage for taper ratio analysis and for different profiles is plotted in Figure 5.9. The predictive empirical models show higher effect of pressure when cutting straight profiles in comparison to contour curvatures and arced profiles. Also, it is noticeable that the water pressure has least significance on taper ratio of smaller arc profiles, which increases as the arc radius increases with maximum effect on straight profile where straight cut profile can be idealized as an arc of infinite radius. This trend can be justified by the gradual acceleration and deceleration at small curvatures, furnishing more jet exposure time and higher power impartation.

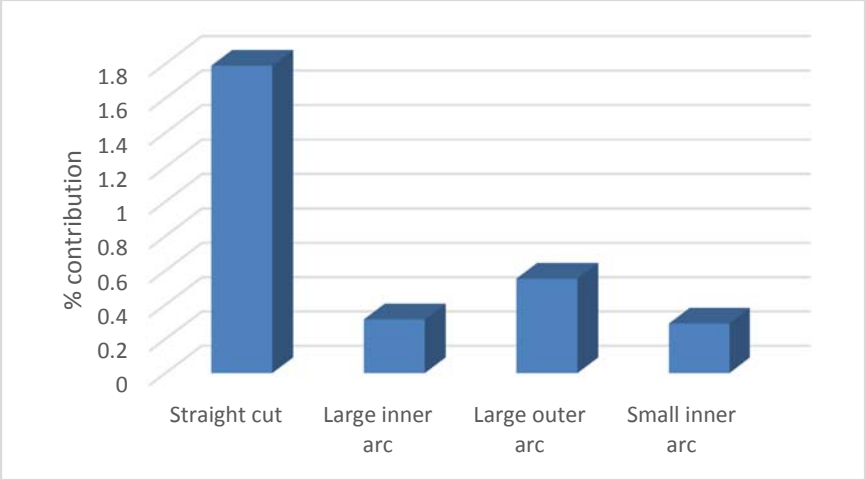

Figure 5.9. Percentage contribution of Pressure as a parameter of empirical model for five different profiles

5.4.1.2 Effect of Mixing Tube geometry

The length and diameter of mixing tube significantly affect the jet coherency and power density [52,94]. Within the experimental limits, it is found that a combination of 76.2 mm length and 0.508 mm diameter mixing tube results in maximum taper. According to the results and previous investigations, an optimum length to diameter (aspect) ratio is necessary for minimun and controlled kerf taper charcteristics. For given experimental conditions, minimisation of taper requires a minimun aspect ratio (Lm/dm=66.67). A large mixing tube diameter shall increase the jet entry kerf width with reduced abrasive cutting energy per unit area. However, high water energy would account for jet tendency to expand while interacting with the material.

Besides, the length of mixing tube needs to be selected based on thickness of the material. In order to machine thinner laminates (~7.56 mm) , a short mixing tube is desirable in comparison to machining thick laminates (~10.5 mm) where a long mixing tube helps in achieving less taper. Using longer mixing tube for specimen thickness ~ 7.56 mm thick laminate would result in high taper due to composite facesheets damage at high energy infusion.

The effect of tube length on thicker specimen is maximum for straight cut which reduces with the radius of profiles. Figure 5.10 depicts the increase in percentage contribution of mixing tube length when profile radius is decreased, and an opposite trend for mixing tube diameter. Also, the

straight cut and large radius profiles are sensitive to length-thickness interaction as depicted in Figure 5.11.

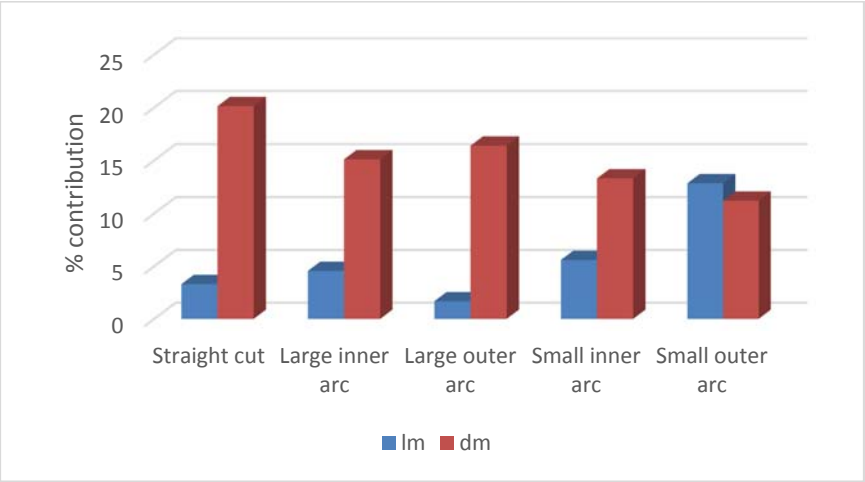

Figure 5.10. Percentage contribution of mixing tube length and diameter as a parameter of empirical model for five different profiles

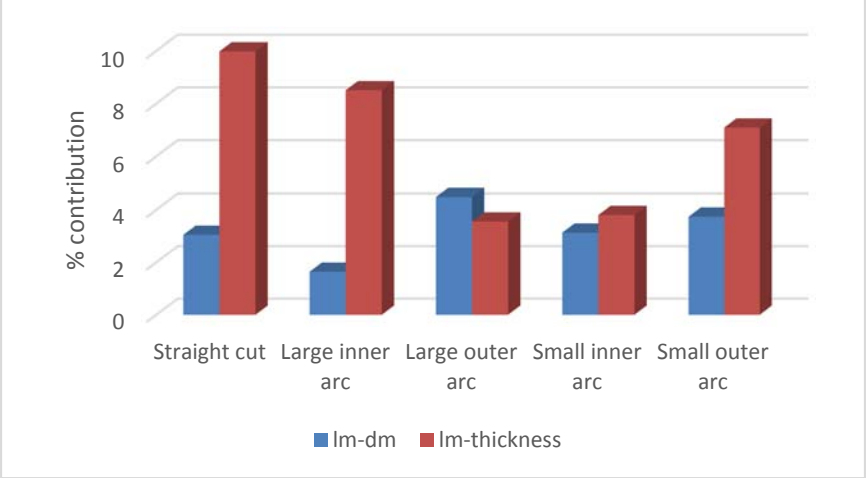

Figure 5.11. Percentage contribution of lm-dm and lm-thickness interaction terms of empirical model for five different profiles.

5.4.1.3 Effect of Orifice diameter

The orifice diameter determine the water flow rate and thus overall cutting power of the jet. A larger orifice diameter (0.254mm) resulted in maximum taper for almost all cutting profiles. This is because of the increased water flow rate at a given load ratio, leading to reduction in abrasive mass flow rate and thus, reduction in jet cutting efficiency. Although, nozzle-orifice diameter interaction effect is not significant in all cutting profiles, taper is found to be minimum for dm=0.762 mm and at all values of dn. This provides an optimum dn/dm ratio between 0.23 and 0.33. Previous investigations determined the minimum requirement of dn/dm ratio equivalent to 0.5 to produce sufficient pressure for abrasive suction [53].

5.4.1.4 Effect of Load ratio and Traverse speed

Taper is significantly increased with increase in traverse speed due to less exposure and less jet power transmission to the workpiece. The load-speed interaction term is significant in the model depicting higher taper ratio at low abrasive load and higher traverse speed because of low power density being transferred to the specimen. The low F-value of speed-load interaction term and high F-value of traverse speed indicates traverse speed as one of the most indispensable factor. The traverse speed is significantly affecting the model for all profiles, especially, the small outer arc, as depicted in Figure 5.12.

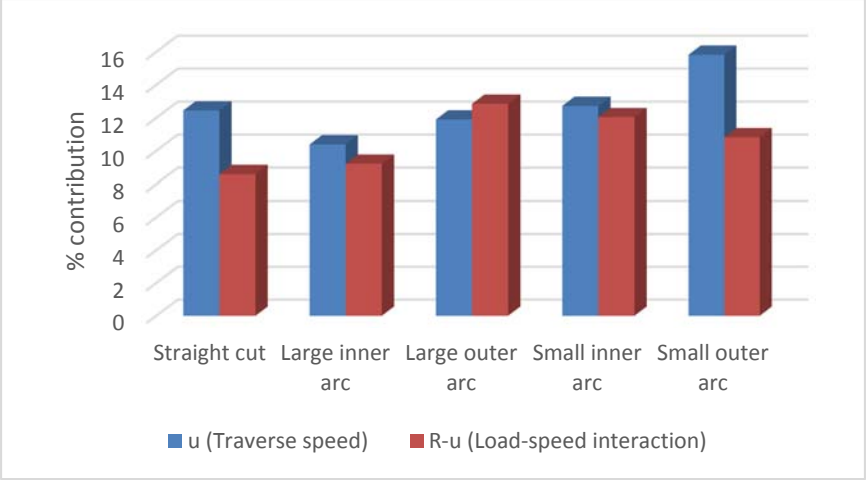

Figure 5.12. Percentage contribution of traverse speed and R-u as a parameters of empirical model for five different profiles

5.4.2 Parametric Effects on Transverse Surface Roughness

5.4.2.1 Effect of Laminate Thickness

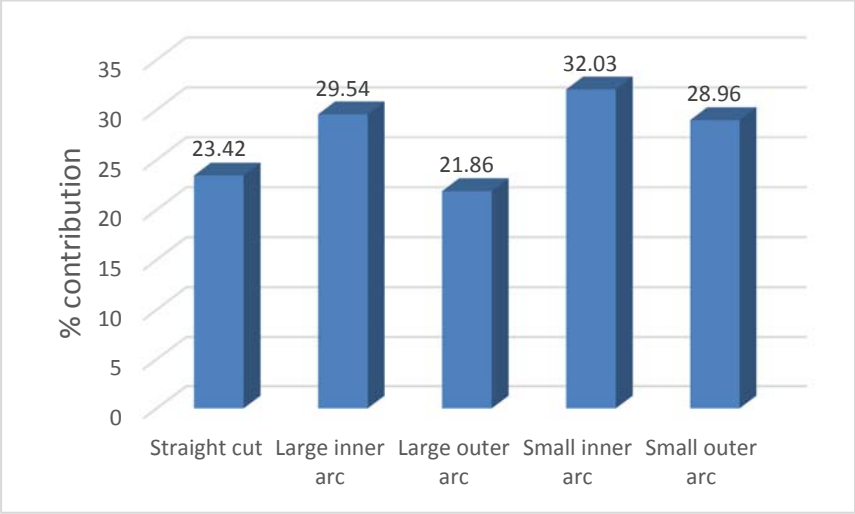

Figure 5.13. Percentage contribution of laminate thickness on transverse surface roughness parameter R_z for five different profiles.

The R_z roughness parameter significantly increases with increase in specimen thickness. This can be supported by the argument that jet energy decreases with the penetration depth, leading to failing cutting strikes of abrasives at the bottom. This abets the water pressure to build up temporarily, which in otherwise would be released by the sharp cutting action of the abrasives, causing the water to flow sideways leading to hydro-distortion of composite plies. An overall mismatch in the material removal of composite and titanium plies generates undesirable peaks and valleys. Figure 5.13 depicts the percentage influence of material thickness on overall roughness value (R_z). Curved profiles, especially smaller arcs are significantly affected by the material thickness in comparison to straight cut profiles.

5.4.2.2 Effect of Pressure

Unlike kerf taper, the transverse roughness is found to be significantly sensitive to pressure. In general, the surface roughness R_z is found to increase with reduction in pressure. This is apparent due to the reduction in cutting energy of the jet amounting to less momentum of sharp abrasives. The percentage contribution of pressure is around 6-17% depending upon the contouring profile and more precisely, the profile curvature.

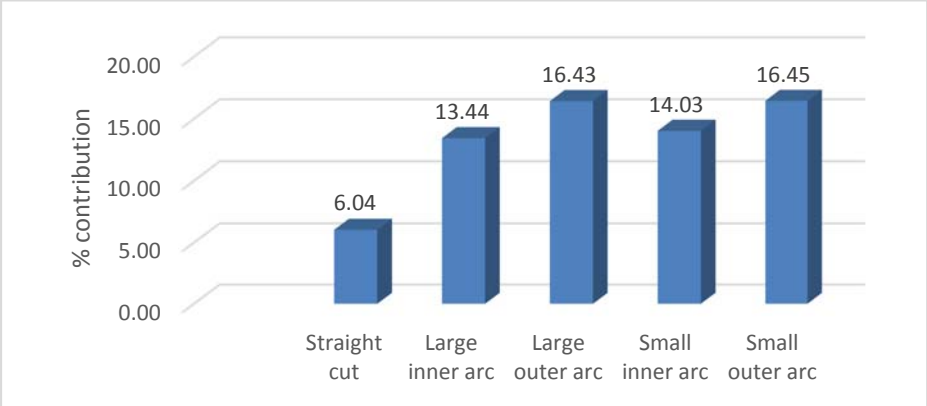

Figure 5.14. Percentage contribution of water pressure on transverse surface roughness parameter R_z for five different profiles.

Figure 5.14 shows the percentage contribution of pressure term in R_z roughness predictive model. The straight cut profile is least sensitive to water pressure. However, the contribution of pressure increases with the reduction in profile curvature. Also, the pressure contribution in transverse roughness is more for outer arc profiles than inner arcs. This involves the effect of jet dynamics and necessity for adequate control mechanism in contouring convex and concave profiles.

5.4.2.3 Effect of Geometric variables

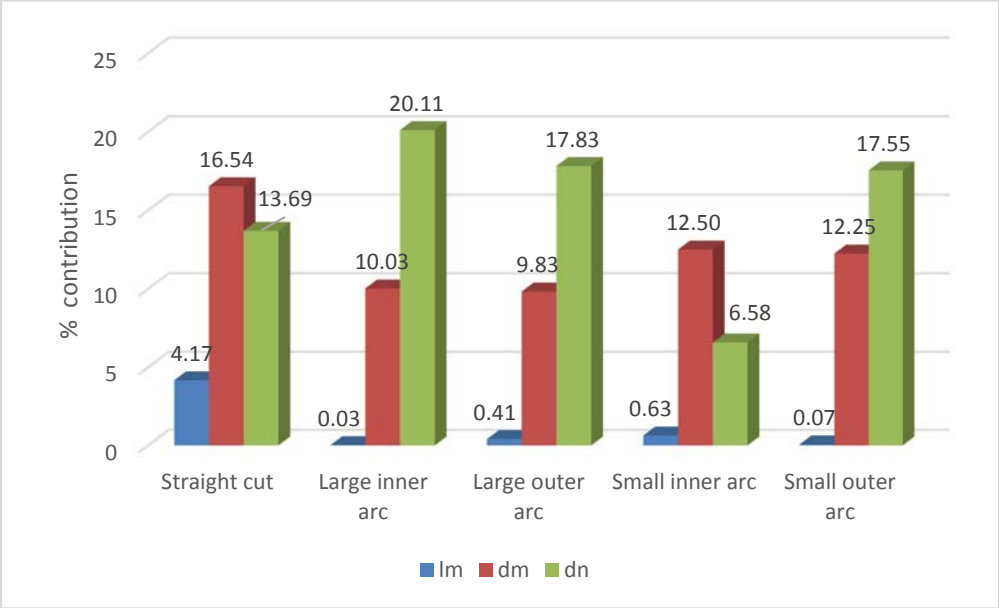

Figure 5.15. Percentage contribution of geometrical parameters on transverse surface roughness parameter R_z for five different profiles.

The length of mixing tube is not significantly affecting the kerf transverse roughness. An increment in mixing tube length is associated with jet coherency and elevation of jet energy level on account of ampleness of control volume during momentum transfer between water and abrasives. However, power transmitted during jet-material interaction is more affected by other parameters than length of mixing tube. Nonetheless, transverse roughness R_z is higher for short mixing tubes. Besides the contribution of mixing tube length is lesser and nearly negligible at smaller contouring profile, as depicted in Figure 5.15. This can be supported by the reasoning that excess power is transmitted when gradual change in cutting direction increases the jet exposure time. Besides, a radial cutting component is expected while sweeping the curved geometry due to centrifugal force component on the jet. This is evident by the large trailback striation marks for small curvature profiles in Figure 4.62. The recirculation and redistribution of abrasives in an incoherent waterjet not only machine the surface transversely, but also the recirculated worn out abrasives erodes the material longitudinally as well. This accounts for a smoother surface of curved geometries.

The diameter of mixing tube is another influencing factor in transverse surface topological characteristics. A larger diameter accounts for low power density of the jet, with increased area of jet-material interaction and reduced cutting ability of the jet. Also, the orifice bore size controls the jet water power by altering the mass flow rate of the water. An increased orifice bore means more water flow rate and more water power of the jet, leading to a smoother surface.

Overall, out of all the three aforementioned geometrical parameters, orifice diameter has the maximum contribution to the transverse surface roughness of the kerf wall for nearly all curvatures as depicted in Figure 5.15. In comparison to straight cutting profile, the transverse roughness characteristics of large arcs are more sensitive to orifice diameter than mixing tube diameter with 17.8-20% contribution in roughness model, and vice versa for small arced profiles with 6.5-17.5% contribution in roughness model.

5.4.2.4 Effect of Traverse speed

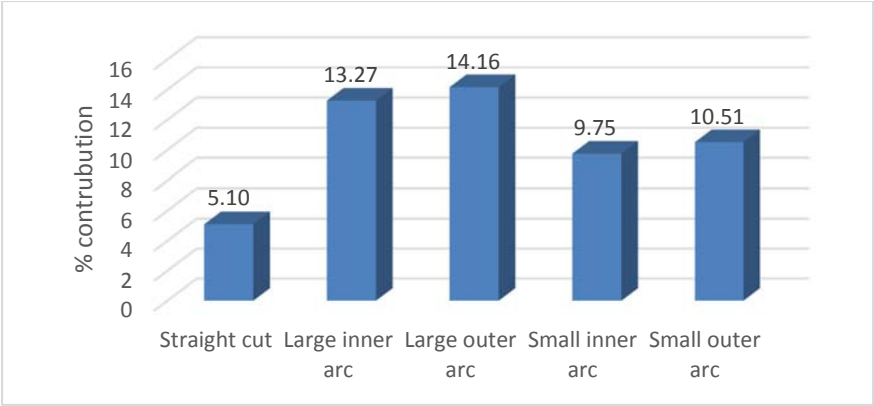

Figure 5.16. Percentage contribution of jet traverse speed on transverse surface roughness parameter R_z for five different profiles.

The transverse surface roughness increases with jet traverse speed due to less exposure time and low power of the jet. The investigation showed higher sensitivity of traverse speed for curved profiles in comparison to straight cut.

5.4.3 Process Optimisation

The taper performance was found to be highly sensitive to geometrical variables. The selection of proper mixing tube and orifice is suggested as the first step in planning the waterjet machining of thick Titanium Graphite. Since, the mixing tube length and diameter show a variable trend with specimen thickness, the dimensions need to be selected based on the same criteria. The orifice diameter is found to exhibit low taper at 0.178 mm irrespective of interaction with other parameters within the experimental limits. The water pressure is suggested to be minimum to account for the availability and reduced energy consumption. Besides, the process economics are significantly dependent on abrasive flow rate (or load ratio) and traverse speed, which are targetted to be low and high respectively for high material removal rate. Table 5.7 depicts the required variable constrains and conditions for output response of statistical optimisation in Design Expert software.

Table 5.7. Constraints used to determine minimum taper and low Roughness (R_z).

Constraints						
Name	*Goal*	*Lower Limit*	*Upper Limit*	*Lower Weight*	*Upper Weight*	*Importance*
A:Thickness	7.56, 10.5	7.56	10.5	1	1	3
B:P	minimize	380	600	1	1	3
C:Lm	is in range	50.8	76.2	1	1	3
D:dm	is in range	0.508	0.762	1	1	3
E:dn	is in range	0.178	0.254	1	1	3
F:R	minimize	0.086	0.101	1	1	3
G:u	maximize	50.8	152.4	1	1	3
Straight cut taper ratio	minimize	1	1.36364	1	1	3
Small inner arc taper ratio	minimize	1	1.42857	1	1	3
Small outer arc taper ratio	minimize	1	1.36364	1	1	3
Large inner arc taper ratio	minimize	1	1.36364	1	1	3
Large outer arc taper ratio	minimize	1	1.40909	1	1	3
Straight cut R_z (µm)	minimize	9.127	29.334	1	1	3
Small inner arc R_z (µm)	minimize	8.612	29.777	1	1	3
Small outer arc R_z (µm)	minimize	8.074	26.959	1	1	3
Large inner arc R_z (µm)	minimize	7.507	27.97	1	1	3
Large outer arc R_z (µm)	minimize	8.302	25.812	1	1	3

The conditions corresponding to aforementioned constraints yielding low taper are depicted in Table 5.8 and that of both low taper and transverse roughness R_z are depicted in Table 5.9.

Table 5.8. Conditions at optimized taper ratio

Variable /Response	Values	
Thickness (mm)	7.56	10.5
P (MPa)	380.001	380.0008
lm (mm)	50.8	76.2
dm (mm)	0.762	0.762
dn (mm)	0.254	0.178
R	0.086	0.086
u (mm/min)	95.597	152.4
Straight cut taper ratio	1.00	1.01
Small inner arc taper ratio	0.97	1.05
Small outer arc taper ratio	1.03	1.06
Large inner arc taper ratio	1.01	1.02
Large outer arc taper ratio	1.05	0.99
Desirability	0.88	0.95

Table 5.9. Conditions for optimized surface taper ratio and Roughness (R_z)

Variable /Response	Values	
Thickness (mm)	7.56	10.50
P (MPa)	437.27	437.53
lm (mm)	50.80	76.20
dm (mm)	0.508	0.762
dn (mm)	0.254	0.254
R	0.086	0.086
u (mm/min)	74.23	70.49
Straight cut taper ratio	1.02	1.04
Small inner arc taper ratio	1.07	1.09
Small outer arc taper ratio	1.00	1.10
Large inner arc taper ratio	1.08	1.05
Large outer arc taper ratio	1.03	1.07
Straight cut R_z (μm)	7.38	21.21
Small inner arc R_z (μm)	12.22	21.63
Small outer arc R_z (μm)	10.25	16.50
Large inner arc R_z (μm)	10.40	16.64
Large outer arc R_z (μm)	12.40	17.62
Desirability	0.79	0.59

The statistical optimization to achieve a trade-off between conditions yielding low taper and low transverse R_z reveals a possible kerf roughness of 7.4-12.4 μm and taper ratio of 1.00-

1.08 for 7.56 TiGr laminate. However, optimized conditions achieved for 10.5mm thick specimen showed higher roughness (17.6-21.2 μm) and high taper ratio (1.04-1.10). The optimisation results emphasize the disagreement within the conditions yielding high surface quality and low kerf taper for thick (~10.5mm) TiGr laminate.

Material removal rate was calculated using the formula

$$MRR = u \times \left(\frac{d_{entry} + d_{exit}}{2}\right) \times t$$

MRR between 5.6-6.9 mm^3/s was achieved with the conditions optimized for high quality.

Chapter 6. CONCLUSION

An investigation was conducted to evaluate the feasibility and machinability of contouring thick TiGr through Abrasive Waterjet (AWJ) in terms of kerf characteristics- taper ratio and surface quality. Two aerospace grade Titanium/Graphite laminate sheets with different thickness (7.56mm and 10.5mm) and different ply layup were machined using AWJ process. The specimens were machined with varying parameters as suggested by a response surface experimental design. The selected machining profile consisted of straight cuts, and arcs of radii 4.8, 6.35 and 12.7 mm to analyze the variation of machining responses with different profile features. A total of 32 profiles were machined at different experimental conditions according to a response surface experimental design obtained using Design Expert software. The process variables included pump pressure, jet traverse speed, load ratio (by varying abrasive flow rate) and nozzle dimensions. Material removal mechanism was studied for three different phase material systems. Kerf characteristics were investigated to qualitatively characterize superior and inferior quality cuts by determining minimum taper conditions. Analysis of Variance (ANOVA) was used to statistically characterize the effect of operating variables on kerf taper ratio and predictive mathematical models were developed.

The topological characteristics of the kerf were also studied with roughness evaluation of surfaces parallel (longitudinal) and orthogonal (transverse) to jet traverse direction. The longitudinal surface roughness of a 10.5 mm thick AWJ straight cut kerf wall was measured along each ply (titanium and composite) machined with condition yielding high taper. The cutting zone identification and characterization was made and a nexus between surface topology and jet-material interaction was established based on several roughness parameters. A qualitative assessment of different profiles was made by measurement of longitudinal roughness at three different penetration depths (near jet entry, jet exit and center) and a comparison was drawn along with the curved jet striations.

Water induced distortion was defined as the phenomenon of excessive material removal composite plies when compared to titanium plies as a result of jet expansion. Hydro-distortion was studied by transverse roughness parameters, especially R_z, R_t and R_z (JIS). The roughness as a function of angular distance on curved profile was investigated to understand the roughness variability, hydro-distortion and material removal pattern. The transverse surface roughness for

each profile was determined to account for the soundness of judgment in cut quality evaluation. Surface roughness was quantitatively characterized for all profiles and statistically analyzed for parametric optimization. Mathematical regression models and semi-analytical model was developed to predict R_z and R_a respectively. The surface topology was plotted in Skewness-kurtosis space to characterize and determine the nature of process in the chosen domain of variables. The AWJ process was characterized in terms of R_q/R_a ratio.

A comparison of difference in machining quality (taper and surface roughness) of curved surfaces relative to straight surface was made. Overall, machinability of thick TiGr laminates was evaluated as a function of kerf taper ratio and surface roughness and statistical optimization was done for machining with low taper and low roughness.

Following conclusions were drawn based on the research study:

1. The material removal mechanism was different for different phases. Titanium was removed by shear deformation, scratching and abrasive ploughing. Within the composite material, matrix was removed by shearing, whereas graphite fibers were removed by micro chipping, brittle fracture, and bending failure. Small interply defects and dislodged titanium burrs were spotted over the composite ply. However the kerf surface were free from grit embedment.

2. The employability of AWJ process is established as an entirely feasible and preferred method for machining of TiGr composite because of impressively faster cut, higher MRR (5.6-6.9 mm^3/s), negligible tool wear, delamination free (with proper setting), no thermal damage, no thermal cracks, smoother machined surface, and large machine work space.

3. The kerf wall geometry was affected by the composite percentage and ply arrangement. Nearly square cut (taper and water distortion free) can be achieved by avoiding continuous stacks of composite plies and maintaining higher percentage and uniform distribution of titanium plies. Low taper can be achieved with using UHP (600 MPa), low traverse speed (50.8 mm/min), high load ratio, high mixing tube to orifice bore ratio (0.23-0.33). An

optimum mixing tube length to diameter ratio is necessary for desirable taper for a given thickness.

4. Low Transverse kerf wall roughness (R_z~9.4 μm) can be achieved using lower pressure (380 MPa), low traverse speed (50.8 mm/min), high load ratio, high mixing tube to orifice bore ratio (0.5) and high mixing tube aspect ratio. The AWJ process was characterized in terms of R_q/R_a ratio and was determined to be 1.28 (±0.025). The process was negatively skewed and leptokurtic, similar to grinding process.

5. The AWJ machining of thick TiGr specimens is not independent of the machining profile. The kerf taper ratio and transverse roughness variation when machined with a given process parameters was as high as 20 and 61% respectively. Smaller arc profile features were identified with low roughness and high taper ratio. Parametric optimization (specifically, traverse speed and water pressure) can be used to negate the contour severity with taper ratio and transverse R_z variation to 5.6% and 20% respectively.

Recommendations for future study

1. A more comprehensive study is required to understand the effect of cutting geometry and contour curvature on the jet structure, especially at the exit side. One of the few ways to understand this is to analyze the frequency spectrum of kerf roughness profile.
2. The effect of ply layup and jet dynamics is required to be decoupled to better understand their individual influence on the machining responses.
3. An extensive set of experimental data needs to be acquired along with the understanding of cutting geometry and ply layup effects to improvise and overcome the limitations of semi-analytical model proposed in this study.
4. Although this research study shows well-behaved cutting responses with the chosen set of experimental conditions, testing of mechanical properties (such as bending test and fatigue test) is suggested to ensure structural integrity along with surface integrity.

BIBLIOGRAPHY

[1] Airbus. A380 Technology Innovation n.d. http://www.airbus.com/aircraftfamilies/passengeraircraft/a380family/innovation/ (accessed April 8, 2015).

[2] Tan W, Falzon BG, Chiu LNS, Price M. Predicting low velocity impact damage and Compression-After-Impact (CAI) behaviour of composite laminates. Compos Part A Appl Sci Manuf 2015;71:212–26. doi:http://dx.doi.org/10.1016/j.compositesa.2015.01.025.

[3] Vlot A, Gunnink JW. Fibre metal laminates: an introduction. Springer Science & Business Media; 2001.

[4] Vogelesang LB, Schijve J, Fredell R. Fibre metal laminates: damage tolerant aerospace materials. Case Stud Manuf with Adv Mater 1995;2:253–71.

[5] Tenney DR, Davis Jr JG, Johnston NJ, Pipes RB, McGuire JF. Structural Framework for Flight: NASA's Role in Development of Advanced Composite Materials for Aircraft and Space Structures 2011.

[6] Kingston WR. Coating alloy with platinum; heating, aging, adhering 1998.

[7] Zonda Cinque. Pagani n.d. http://www.pagani-automobili.de/pagani-zonda-cinque.htm# (accessed January 1, 2015).

[8] Gallo G. Laminated skateboard 2010.

[9] Turner PG, Drake SR. Carbon fiber laminate ski or snowboard with metal rib core dampening system 2011.

[10] Grant WF, Kraus SA, Shahood TW. Fiber-reinforced metal striking insert for golf club heads 2001.

[11] Ramulu M, Stickler PB, McDevitt NS, Datar IP, Kim D, Jenkins MG. Influence of processing methods on the tensile and flexure properties of high temperature composites. Compos Sci Technol 2004;64:1763–72. doi:10.1016/j.compscitech.2003.12.008.

[12] Burianek DA, Spearing SM. Fatigue damage in titanium-graphite hybrid laminates. Compos Sci Technol 2002;62:607–17. doi:10.1016/S0266-3538(02)00027-1.

[13] Li E, Johnson WS, Lowthere SE, St. Clair TL. An evaluation of two fabrication methods for hybrid titanium composite laminates. ASTM Spec Tech Publ 1997;1242:202–14.

[14] Ramulu M. Machining and surface integrity of fibre-reinforced plastic composites. Sadhana 1997;22:449–72. doi:10.1007/BF02744483.

[15] Kim D, Ramulu M. Cutting and drilling characteristics of hybrid Titanium Composite Laminate (HTCL). Int. SAMPE Tech. Conf., vol. 2005, 2005.

[16] Hashish M, Kent WA. TRIMMING OF CFRP AIRCRAFT COMPONENTS n.d.

[17] Hashish M. Machining of advanced composites with abrasive-waterjets. Mach Compos 1988:1–18.

[18] Ramulu M, Jenkins MG, Guo Z. Abrasive water jet machining mechanisms in continuous-fiber ceramic composites. J Compos Technol Res 2001;23:82–91.

[19] Hashish M. Waterjet machining of advanced composites. Mater Manuf Process 1995;10:1129–52.

[20] Hamatani G, Ramulu M. Machinability of high temperature composites by abrasive waterjet. J Eng Mater Technol 1990;112:381–6.

[21] Arola D, Ramulu M. A Study of Kerf Characteristics in Abrasive Waterjet Machining of Graphite/Epoxy Composite. J Eng Mater Technol 1996;118:256–65.

[22] Hashish M. Material properties in abrasive-waterjet machining. J Manuf Sci Eng 1995;117:578–83.

[23] Paul S, Hoogstrate AM, van Praag R. Abrasive water jet machining of glass fibre metal laminates. Proc Inst Mech Eng Part B J Eng Manuf 2002;216 :1459–69. doi:10.1243/095440502320783396.

[24] Ramulu M, Spaulding M, Laxminarayana P. Cutting Characteristics of Titanium Graphite Composite by Wire Electrical Discharge Machining. Adv. Mater. Res., vol. 630, Trans Tech Publ; 2013, p. 114–20.

[25] Herzog D, Jaeschke P, Meier O, Haferkamp H. Investigations on the thermal effect caused by laser cutting with respect to static strength of CFRP. Int J Mach Tools Manuf 2008;48:1464–73. doi:http://dx.doi.org/10.1016/j.ijmachtools.2008.04.007.

[26] Goeke A, Emmelmann C. Influence of laser cutting parameters on CFRP part quality. Phys. Procedia, vol. 5, 2010, p. 253–8. doi:10.1016/j.phpro.2010.08.051.

[27] Das S, Chakraborty S. Selection of non-traditional machining processes using analytic network process. J Manuf Syst 2011;30:41–53. doi:10.1016/j.jmsy.2011.03.003.

[28] Arola D, Ramulu M. Material removal in abrasive waterjet machining of metals Surface integrity and texture. Wear 1997;210:50–8. doi:10.1016/S0043-1648(97)00087-2.

[29] Hoogstrate AM. Towards high definition abrasive water jet cutting. TU Delft, The Netherlands, 2000.

[30] Ramulu M, Isvilanonda V, Laxminarayana P. AWJ Cutting and EDM Edge Finishing on Surface Morphology of Fiber-Metal Composite Laminates. Proc. 21st Int. Conf. Water Jet., Ottawa, Canada: BHR; 2012, p. 47–56.

[31] Hundley JM, Hahn HT, Yang J-M, Facciano AB. Three-dimensional progressive failure analysis of bolted titanium-graphite fiber metal laminate joints. J Compos Mater 2010.

[32] Poodts E, Ghelli D, Brugo T, Panciroli R, Minak G. Experimental characterization of a fibre metal laminate for underwater applications. Compos Struct n.d. doi:http://dx.doi.org/10.1016/j.compstruct.2015.03.046.

[33] Vogelesang LB, Gunnink JW. ARALL, a material for the next generation of aircraft. A state of the art. Delft University of Technology; 1983.

[34] Vlot A. Glare. History of the Development of a New Aircraft Material. Secaucus, NJ, USA: Kluwer Academic Publishers; 2001.

[35] Boeing. 787 Commercial Airplane n.d. http://www.boeing.com/commercial/787/#/design-highlights/visionary-design/composites/advanced-composite-use/ (accessed April 8, 2015).

[36] Johnson WS, Hammond MW. Crack growth behavior of internal titanium plies of a fiber metal laminate. Compos Part A Appl Sci Manuf 2008;39:1705–15. doi:10.1016/j.compositesa.2008.07.017.

[37] W. S. J, Ted Q. C, Sharon L, T. L. St. C. Hybrid Titanium Composite Laminates: A New Aerospace Material. NASA Langley Technical Report Server; 1998.

[38] Johnson WS. Damage Tolerance Evaluation of Adhesively Laminated Titanium. J Eng Mater Technol 1983;105:182–7.

[39] Cortés P, Cantwell WJ. The prediction of tensile failure in titanium-based thermoplastic fibre-metal laminates. Compos Sci Technol 2006;66:2306–16. doi:10.1016/j.compscitech.2005.11.031.

[40] Le Bourlegat LR, Damato CA, da Silva DF, Botelho EC, Pardini LC. Processing and mechanical characterization of titanium-graphite hybrid laminates. J Reinf Plast Compos 2010;29 :3392–400. doi:10.1177/0731684410377541.

[41] Tarpani JR, Maluf O, Gatti MCA. Charpy impact toughness of conventional and advanced composite laminates for aircraft construction. Mater Res 2009;12:395–403.

[42] Camanho PP, Fink A, Obst A, Pimenta S. Hybrid titanium-CFRP laminates for high-performance bolted joints. Compos Part A Appl Sci Manuf 2009;40:1826–37. doi:10.1016/j.compositesa.2009.02.010.

[43] Kolesnikov B, Herbeck L, Fink A. CFRP/titanium hybrid material for improving composite bolted joints. Compos Struct 2008;83:368–80. doi:10.1016/j.compstruct.2007.05.010.

[44] Fink A, Camanho PP, Andrés JM, Pfeiffer E, Obst A. Hybrid CFRP/titanium bolted joints: Performance assessment and application to a spacecraft payload adaptor. Compos Sci Technol 2010;70:305–17. doi:10.1016/j.compscitech.2009.11.002.

[45] Ramulu M, Arola D. Water jet and abrasive water jet cutting of unidirectional graphite/epoxy composite. Composites 1993;24:299–308. doi:10.1016/0010-4361(93)90040-F.

[46] Shipway PH, Fowler G, Pashby IR. Characteristics of the surface of a titanium alloy following milling with abrasive waterjets. Wear, vol. 258, 2005, p. 123–32. doi:10.1016/j.wear.2004.04.005.

[47] Aurich JC, Linke B, Hauschild M, Carrella M, Kirsch B. Sustainability of abrasive processes. CIRP Ann - Manuf Technol 2013;62:653–72. doi:10.1016/j.cirp.2013.05.010.

[48] Orbanic H, Junkar M. Analysis of striation formation mechanism in abrasive water jet cutting. Wear 2008;265:821–30. doi:10.1016/j.wear.2008.01.018.

[49] Hoogstrate AM, Susuzlu T, Karpuschewski B. High performance cutting with abrasive waterjets beyond 400 MPa. CIRP Ann - Manuf Technol 2006;55:339–42. doi:10.1016/S0007-8506(07)60430-2.

[50] Hashish M. Observations on cutting with 600-MPa waterjets. J Press Vessel Technol 2002;124:229–33.

[51] Guo NS, Louis H, Meier G, Ohlsen J. Abrasive water jet Cutting—methods to calculate cutting performance and cutting efficiency. Geomechanics, vol. 93, 1994, p. 291–9.

[52] Rozario Jegaraj JJ, Ramesh Babu N. A soft computing approach for controlling the quality of cut with abrasive waterjet cutting system experiencing orifice and focusing tube wear. J Mater Process Technol 2007;185:217–27. doi:10.1016/j.jmatprotec.2006.03.124.

[53] Hashish M. Special AWJ nozzles. Am. WJTA Conf. Expo, Houston, Texas. WaterJet Technol. Assoc., 2009.

[54] Hashish M. Inside AWJ nozzles. Proc. 12th WJTA Conf., 2003, p. 17–9.

[55] Finnie I. The Mechanism of Erosion of Ductile Metals. Proc Third US Natl Congr Appl Mech Held Brown Univ Provid Rhode Island, June 11-14, 1958 1958:527–32.

[56] Finnie I. Erosion of surfaces by solid particles. Wear 1960;3:87–103. doi:10.1016/0043-1648(60)90055-7.

[57] Bitter JGA. A study of erosion phenomena. Wear 1963;6:169–90. doi:10.1016/0043-1648(63)90073-5.

[58] Raju SP, Ramulu M. Predicting hydro-abrasive erosive wear during abrasive waterjet cutting: Part I-A mechanistic formulation and its solution. ASME-PUBLICATIONS-PED 1994;68:339.

[59] Momber AW. Energy transfer during the mixing of air and solid particles into a high-speed waterjet: an impact-force study. Exp Therm Fluid Sci 2001;25:31–41. doi:10.1016/S0894-1777(01)00057-7.

[60] Momber AW, Kovacevic R. An energy balance of high-speed abrasive water jet erosion. Proc Inst Mech Eng Part J J Eng Tribol 1999;213 :463–72.

[61] Paul S, Hoogstrate AM, van Luttervelt CA, Kals HJJ. Analytical and experimental modelling of the abrasive water jet cutting of ductile materials. J Mater Process Technol 1998;73:189–99. doi:http://dx.doi.org/10.1016/S0924-0136(97)00228-8.

[62] Kikuchi M. The use of cutting temperature to evaluate the machinability of titanium alloys. Acta Biomater 2009;5:770–5. doi:10.1016/j.actbio.2008.08.016.

[63] Yang X, Richard Liu C. Machining titanium and its alloys. Mach Sci Technol 1999;3:107–39.

[64] Ezugwu EO, Wang ZM. Titanium alloys and their machinability—a review. J Mater Process Technol 1997;68:262–74. doi:10.1016/S0924-0136(96)00030-1.

[65] Che-Haron CH, Jawaid A. The effect of machining on surface integrity of titanium alloy Ti-6% Al-4% v. J Mater Process Technol 2005;166:188–92. doi:10.1016/j.jmatprotec.2004.08.012.

[66] Ginting A, Nouari M. Surface integrity of dry machined titanium alloys. Int J Mach Tools Manuf 2009;49:325–32. doi:10.1016/j.ijmachtools.2008.10.011.

[67] Boud F, Carpenter C, Folkes J, Shipway PH. Abrasive waterjet cutting of a titanium alloy: The influence of abrasive morphology and mechanical properties on workpiece grit embedment and cut quality. J Mater Process Technol 2010;210:2197–205. doi:10.1016/j.jmatprotec.2010.08.006.

[68] Seo YW, Ramulu M, Kim D. Machinability of titanium alloy (Ti'6Al'4V) by abrasive waterjets. Proc Inst Mech Eng Part B J Eng Manuf 2003;217 :1709–21. doi:10.1243/095440503772680631.

[69] Madhavan V, Lipczynski G, Lane B, Whitenton E. Fiber orientation angle effects in machining of unidirectional CFRP laminated composites. J Manuf Process n.d. doi:http://dx.doi.org/10.1016/j.jmapro.2014.06.001.

[70] Colligan K, Ramulu M. Edge trimming of graphite/epoxy with diamond abrasive cutters. J Manuf Sci Eng 1999;121:647–55.

[71] Eneyew ED, Ramulu M. Experimental study of surface quality and damage when drilling unidirectional CFRP composites. J Mater Res Technol 2014;3:354–62. doi:10.1016/j.jmrt.2014.10.003.

[72] Hintze Wolfgang W, Hartmann D, Schütte C. Occurrence and propagation of delamination during the machining of carbon fibre reinforced plastics (CFRPs) - An experimental study. Compos Sci Technol 2011;71:1719–26. doi:10.1016/j.compscitech.2011.08.002.

[73] Ramkumar J, Malhotra SK, Krishnamurthy R. Effect of workpiece vibration on drilling of GFRP laminates. J Mater Process Technol 2004;152:329–32. doi:10.1016/S0924-0136(03)00622-8.

[74] Abrate S, Walton DA. Machining of composite materials. Part I: Traditional methods. Compos Manuf 1992;3:75–83. doi:10.1016/0956-7143(92)90119-F.

[75] Boudelier A, Ritou M, Garnier S, Furet B. Investigation of CFRP machining with diamond abrasive cutters. J Compos Adv Mater Vol 2013;23.

[76] Rahmah A, Khan AA, Ramulu M. A study of abrasive waterjet machining of Kevlar composite. Proc. 12th US Water Jet Conf., 2003.

[77] Azmir MA, Ahsan AK, Rahmah A. Effect of abrasive water jet machining parameters on aramid fibre reinforced plastics composite. Int J Mater Form 2009;2:37–44. doi:10.1007/s12289-008-0388-2.

[78] Wang J. A machinability study of polymer matrix composites using abrasive waterjet cutting technology. J Mater Process Technol 1999;94:30–5. doi:http://dx.doi.org/10.1016/S0924-0136(98)00443-9.

[79] Wang J, Guo DM. A predictive depth of penetration model for abrasive waterjet cutting of polymer matrix composites. J Mater Process Technol 2002;121:390–4. doi:10.1016/S0924-0136(01)01246-8.

[80] Conner I, Hashish M, Ramulu M. Abrasive waterjet machining of aerospace structural sheet and thin plate materials. Proc. 2003 WJTA Am. Waterjet Conf. Houston, Texas, 2003, p. 17–9.

[81] Jain NK, Jain VK, Deb K. Optimization of process parameters of mechanical type advanced machining processes using genetic algorithms. Int J Mach Tools Manuf 2007;47:900–19. doi:10.1016/j.ijmachtools.2006.08.001.

[82] Siddiqui TU, Shukla M, Tambe PB. Optimisation of surface finish in abrasive water jet cutting of Kevlar composites using hybrid Taguchi and response surface method. Int J Mach Mach Mater 2008;3:382–402.

[83] Azmir MA, Ahsan AK. Investigation on glass/epoxy composite surfaces machined by abrasive water jet machining. J Mater Process Technol 2008;198:122–8. doi:10.1016/j.jmatprotec.2007.07.014.

[84] Shanmugam DK, Masood SH. An investigation on kerf characteristics in abrasive waterjet cutting of layered composites. J Mater Process Technol 2009;209:3887–93. doi:10.1016/j.jmatprotec.2008.09.001.

[85] Shanmugam DK, Chen FL, Siores E, Brandt M. Comparative study of jetting machining technologies over laser machining technology for cutting composite materials. Compos Struct 2002;57:289–96. doi:10.1016/S0263-8223(02)00096-X.

[86] Isvilanonda V, Ramulu M, Laxminarayana P, Briggs T. Effect of Die Sinker EDM and AWJ Machining Processes on Flexural Properties of Hybrid Titanium Laminates. Proc. SAMPE New Mater. Process. a New Econ., n.d.

[87] Ramulu M, Hwang I, Isvilanonda V. Quality Issues Associated with Abrasive Waterjet Cutting and Drilling of Advanced Composites. Am. WJTA Conf. Expo, Houston, TX, 2009.

[88] Peters ST. Handbook of Composites. Springer US; 2013.

[89] Shanmugam DK, Nguyen T, Wang J. A study of delamination on graphite/epoxy composites in abrasive waterjet machining. Compos Part A Appl Sci Manuf 2008;39:923–9. doi:10.1016/j.compositesa.2008.04.001.

[90] Arola D, Ramulu M. An Examination of the Effects from Surface Texture on the Strength of Fiber Reinforced Plastics. J Compos Mater 1999;33 :102–23. doi:10.1177/002199839903300201.

[91] Hashish M. Pressure Effects in Abrasive-Waterjet (AWJ) Machining. J Eng Mater Technol 1989;111:221–8.

[92] Lee JH, Park KS, Kang MC, Kang BS, Shin BS. Experiments and computer simulation analysis of impact behaviors of micro-sized abrasive in waterjet cutting of thin multiple layered materials. Trans Nonferrous Met Soc China (English Ed 2012;22. doi:10.1016/S1003-6326(12)61817-2.

[93] Gupta V, Pandey PM, Garg MP, Khanna R, Batra NK. Minimization of Kerf Taper Angle and Kerf Width Using Taguchi's Method in Abrasive Water Jet Machining of Marble. Procedia Mater Sci 2014;6:140–9. doi:10.1016/j.mspro.2014.07.017.

[94] Wang R, Wang M. A two-fluid model of abrasive waterjet. J Mater Process Technol 2010;210:190–6. doi:10.1016/j.jmatprotec.2009.06.007.

APPENDIX A

MACROSCOPIC IMAGES – KERF TAPER

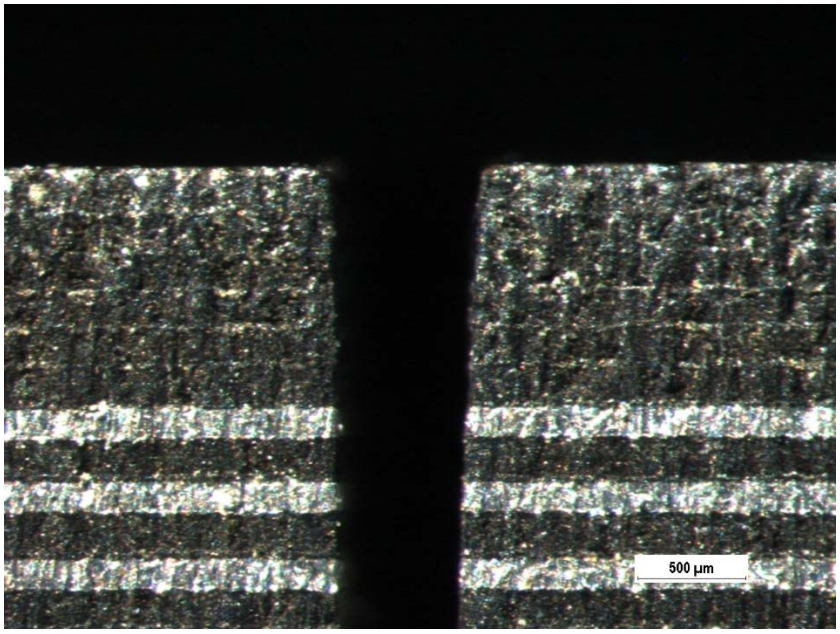

(a)

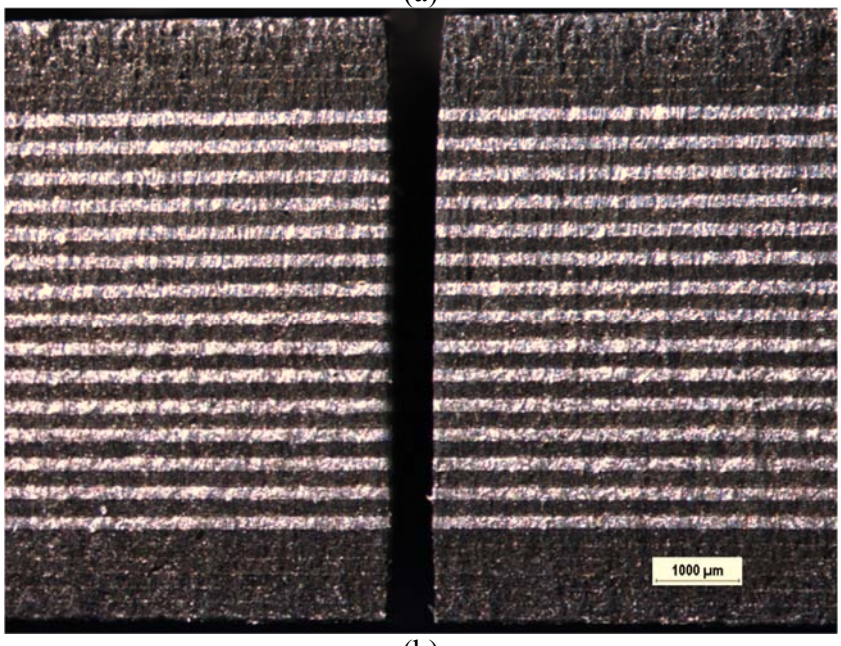

(b)

Figure A.1. **Experiment no. 1** cross-sectional view of AWJ machined kerf geometry depicting (a) Jet entry side damage (8X), and (b) Through the thickness kerf (3X)

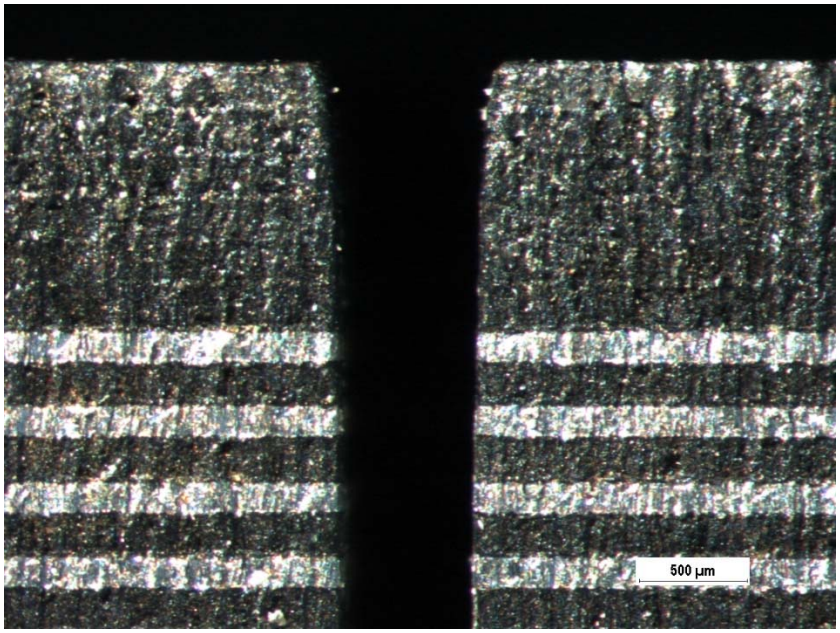

(a)

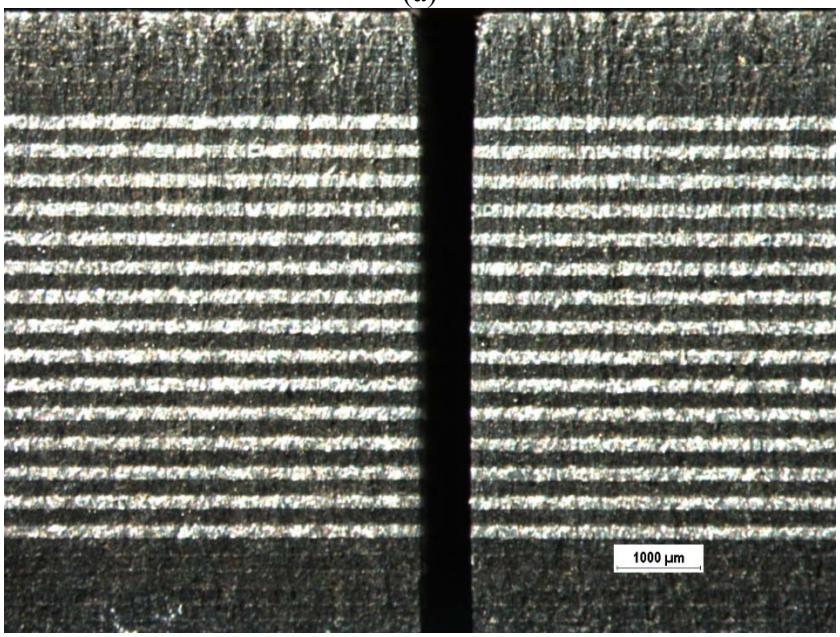

(b)

Figure A.2. **Experiment no. 2** cross-sectional view of AWJ machined kerf geometry depicting (a) Jet entry side damage (8X), and (b) Through the thickness kerf (3X)

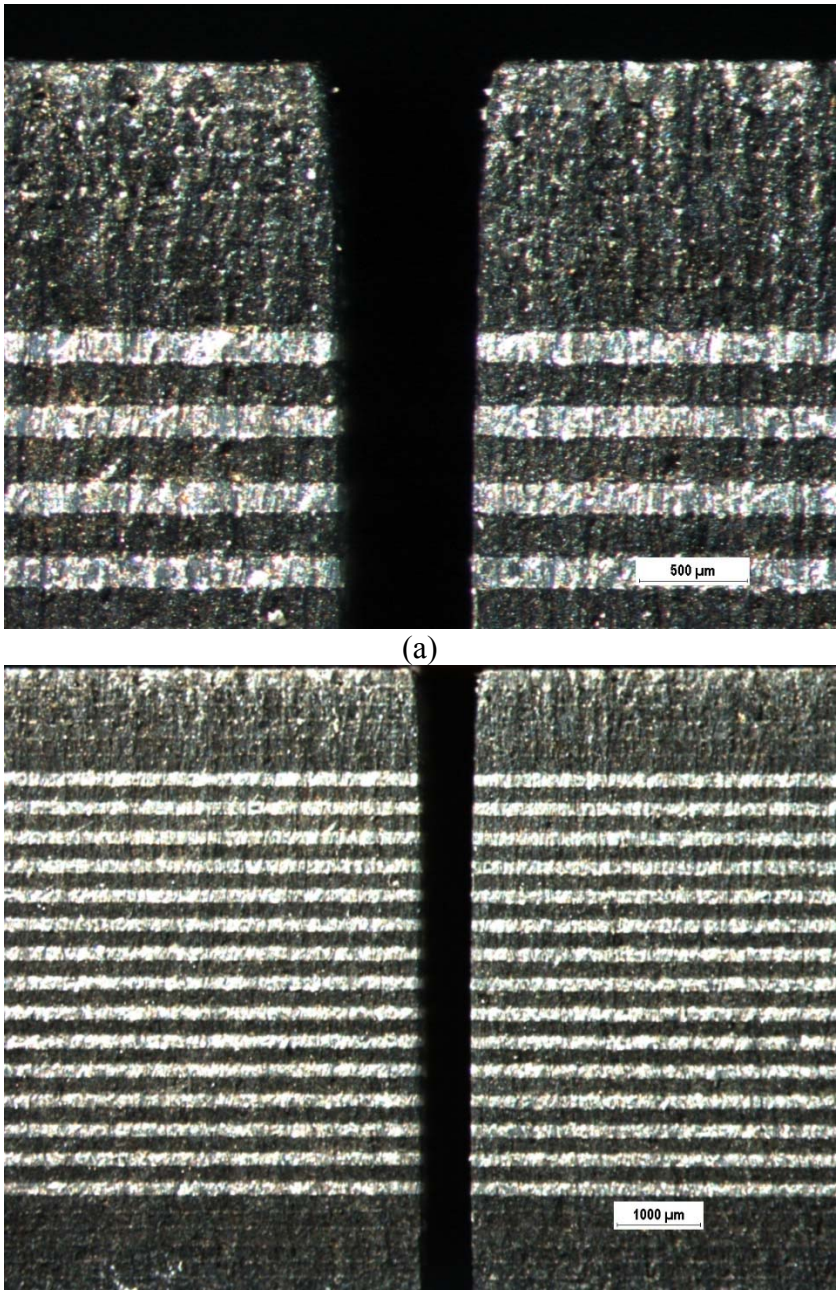

(a)

(b)

Figure A.3. **Experiment no. 3** cross-sectional view of AWJ machined kerf geometry depicting (a) Jet entry side damage (8X), and (b) Through the thickness kerf (3X)

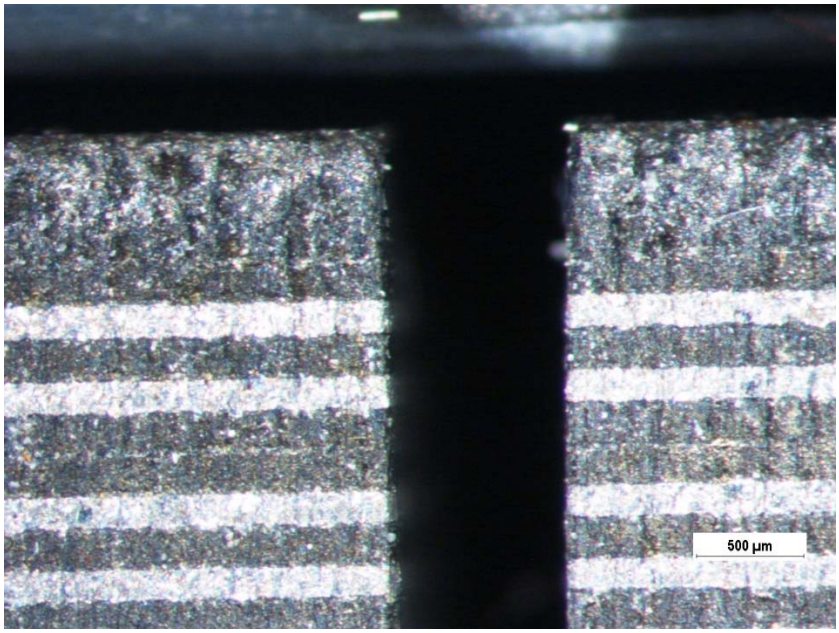

(a)

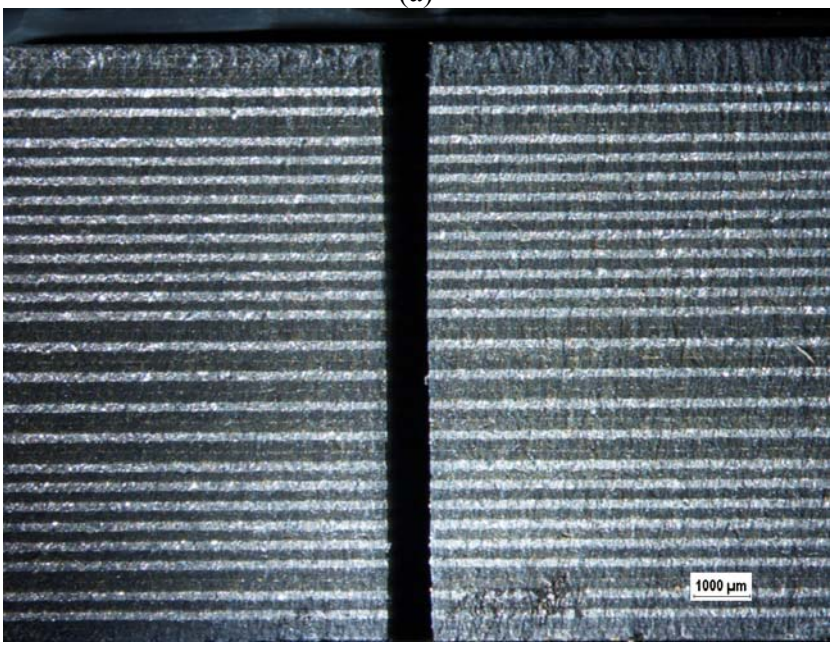

(b)

Figure A.4. **Experiment no. 4** cross-sectional view of AWJ machined kerf geometry depicting (a) Jet entry side damage (8X), and (b) Through the thickness kerf (2X)

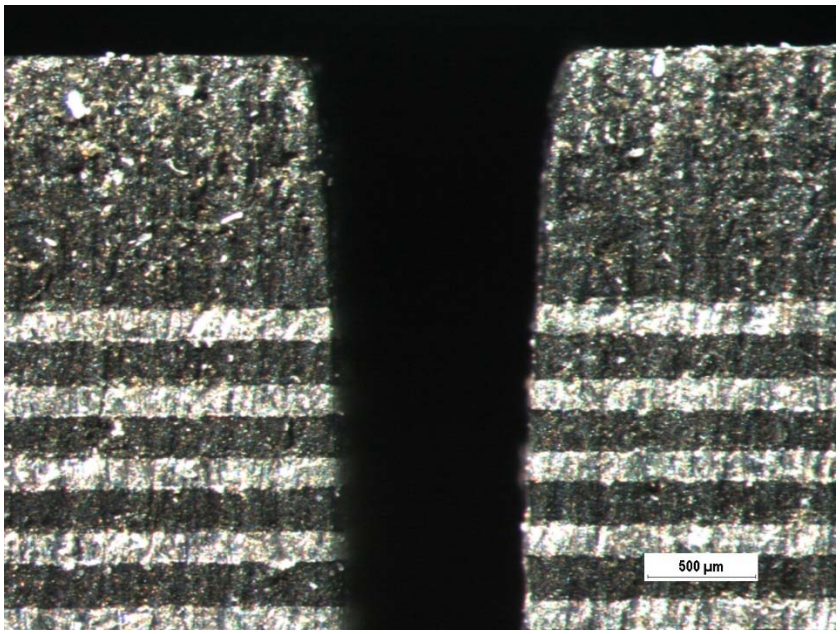

(a)

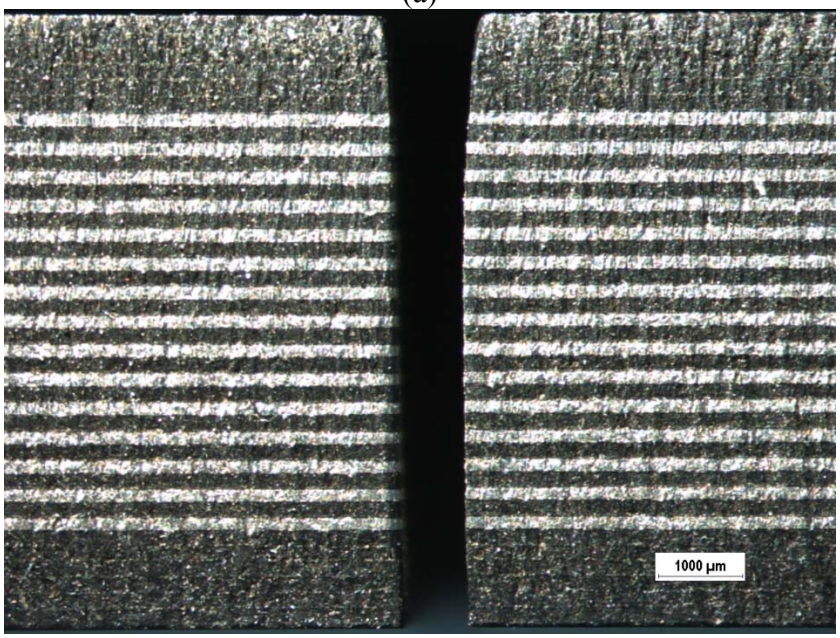

(b)

Figure A.5. **Experiment no. 5** cross-sectional view of AWJ machined kerf geometry depicting (a) Jet entry side damage (8X), and (b) Through the thickness kerf (3X)

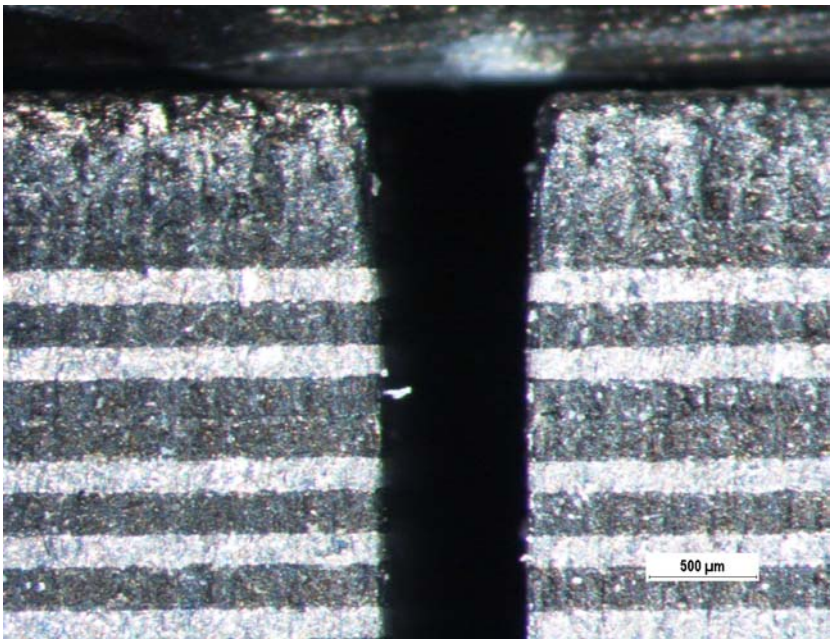

(a)

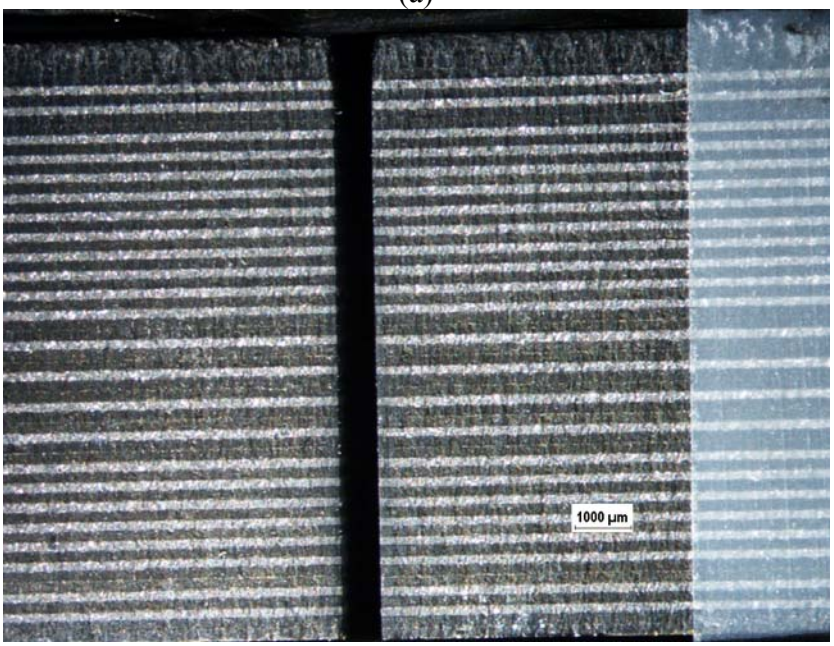

(b)

Figure A.6. **Experiment no. 6** cross-sectional view of AWJ machined kerf geometry depicting (a) Jet entry side damage (8X), and (b) Through the thickness kerf (2X)

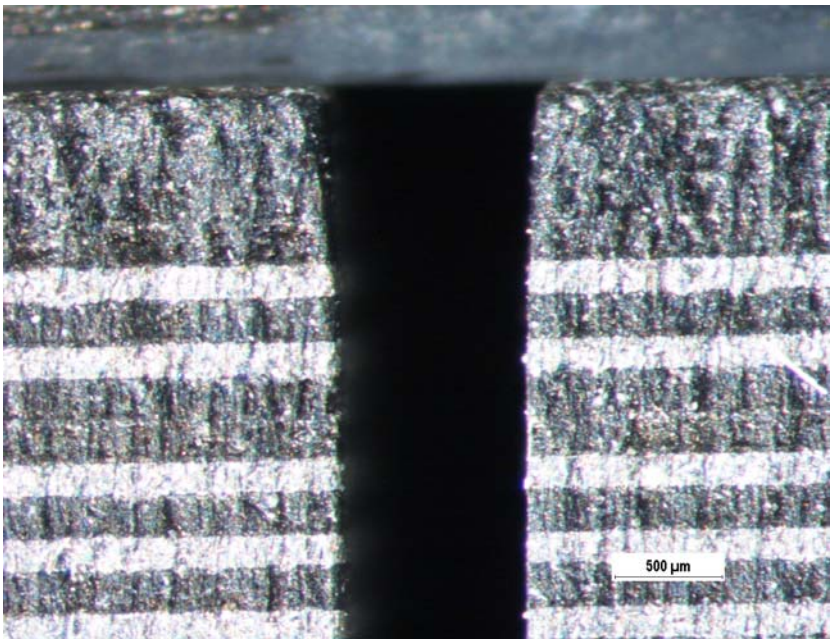

(a)

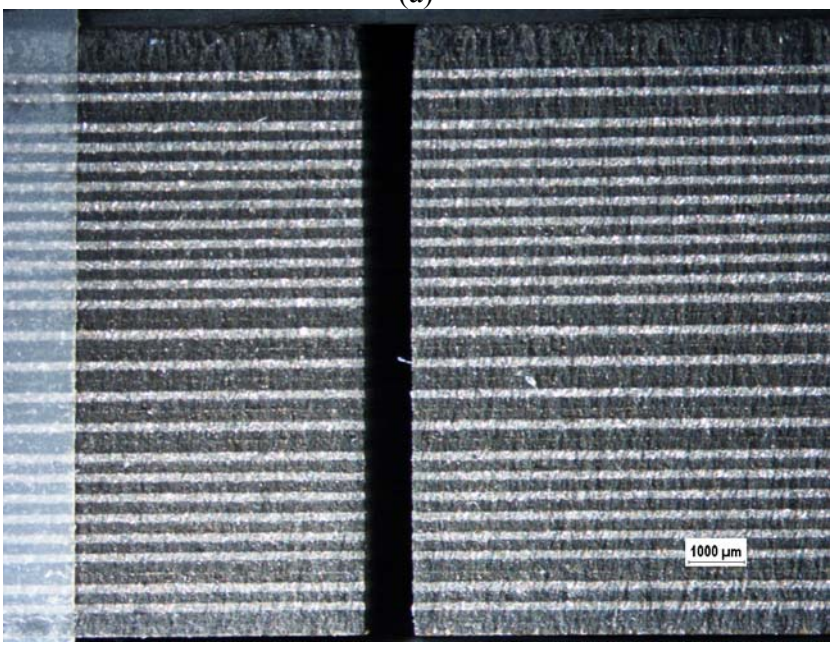

(b)

Figure A.7. **Experiment no. 7** cross-sectional view of AWJ machined kerf geometry depicting (a) Jet entry side damage (8X), and (b) Through the thickness kerf (3X)

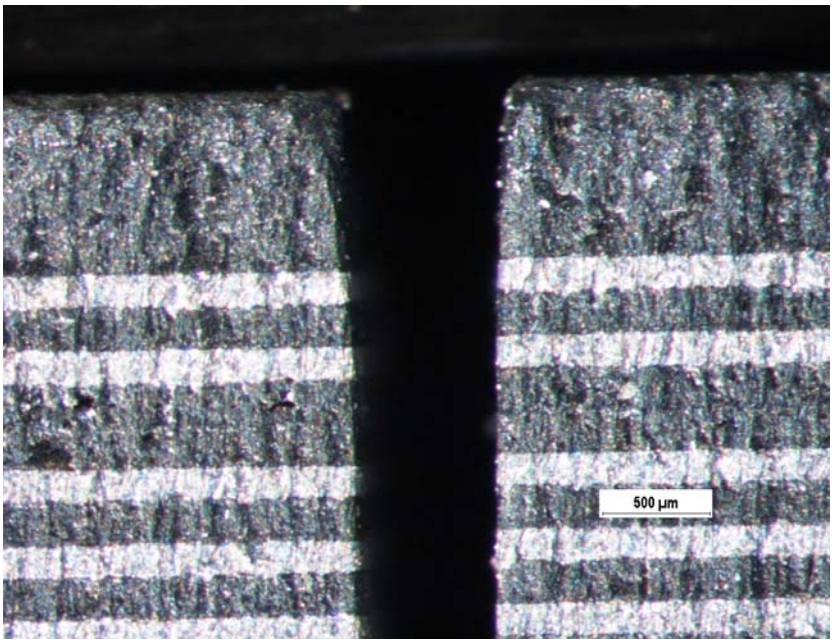

(a)

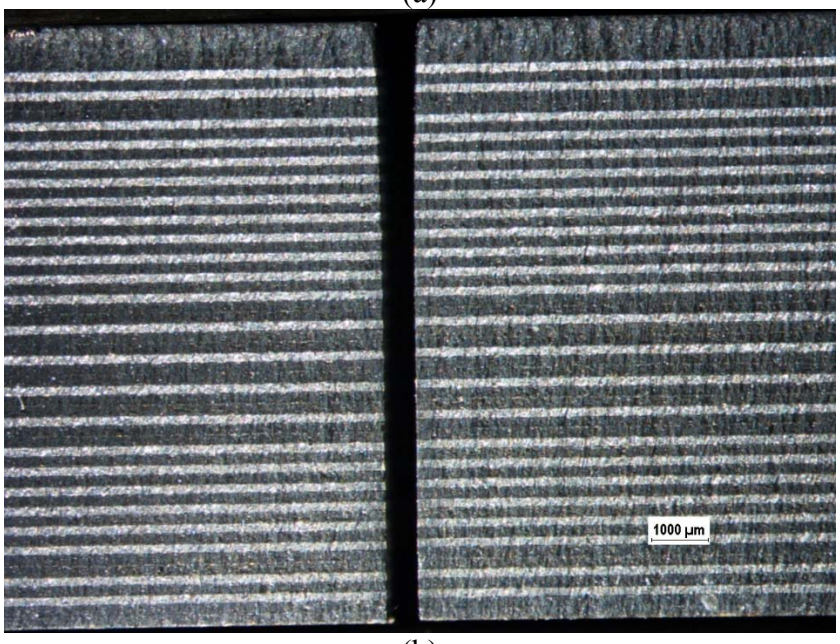

(b)

Figure A.8. **Experiment no. 8** cross-sectional view of AWJ machined kerf geometry depicting (a) Jet entry side damage (8X), and (b) Through the thickness kerf (2X)

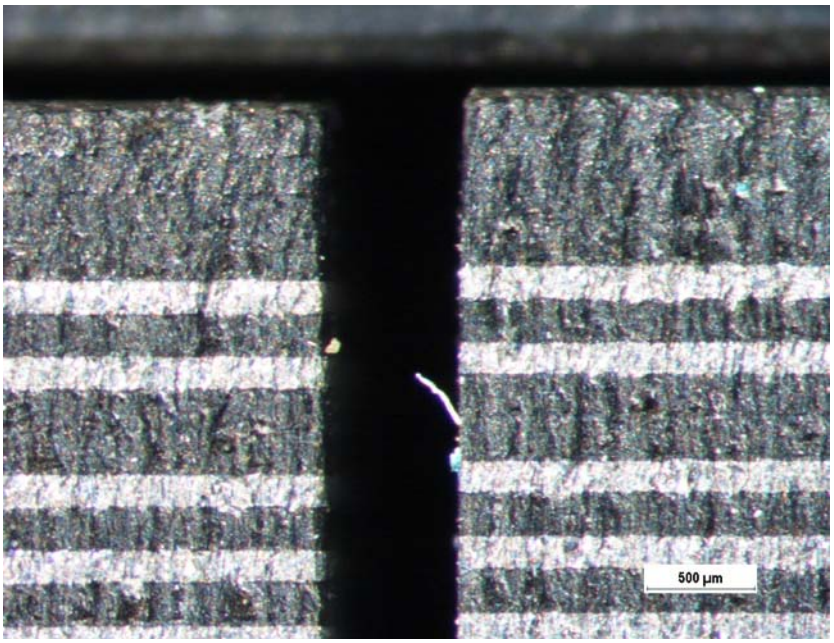

(a)

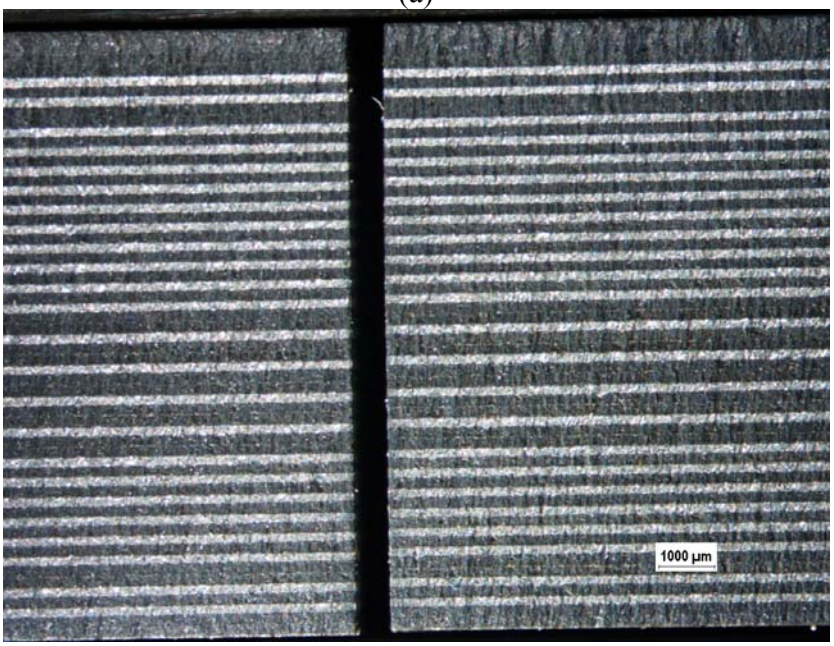

(b)

Figure A.9. **Experiment no. 9** cross-sectional view of AWJ machined kerf geometry depicting (a) Jet entry side damage (8X), and (b) Through the thickness kerf (2X)

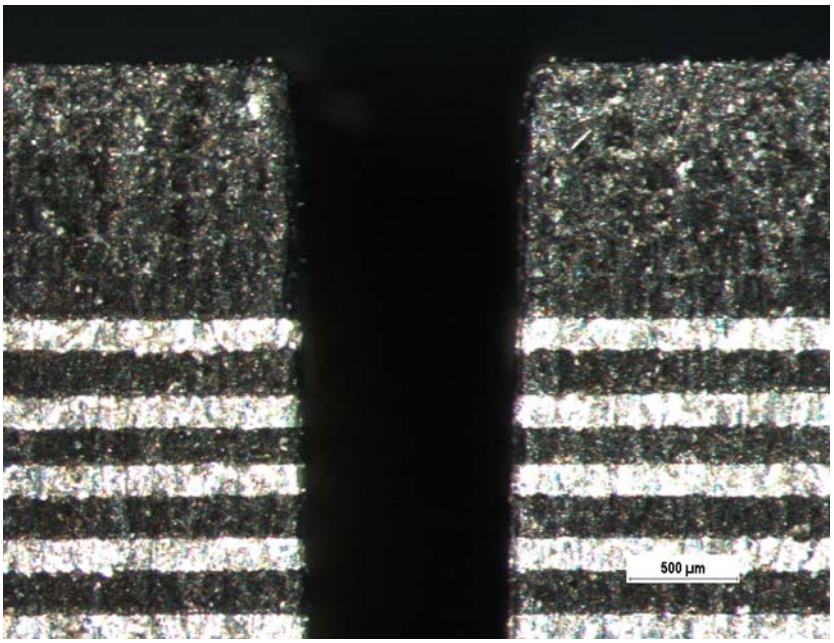

(a)

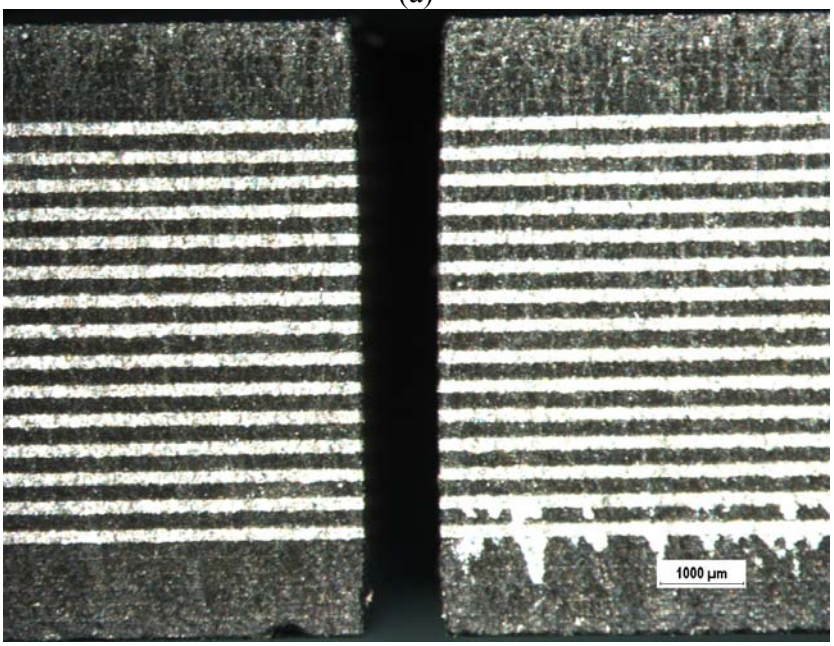

(b)

Figure A.10. **Experiment no. 10** cross-sectional view of AWJ machined kerf geometry depicting (a) Jet entry side damage (8X), and (b) Through the thickness kerf (3X)

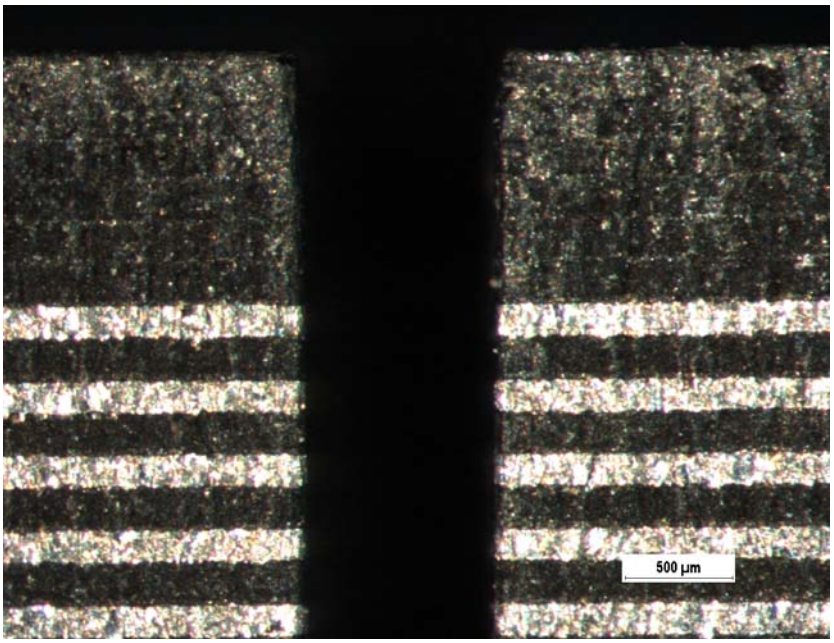

(a)

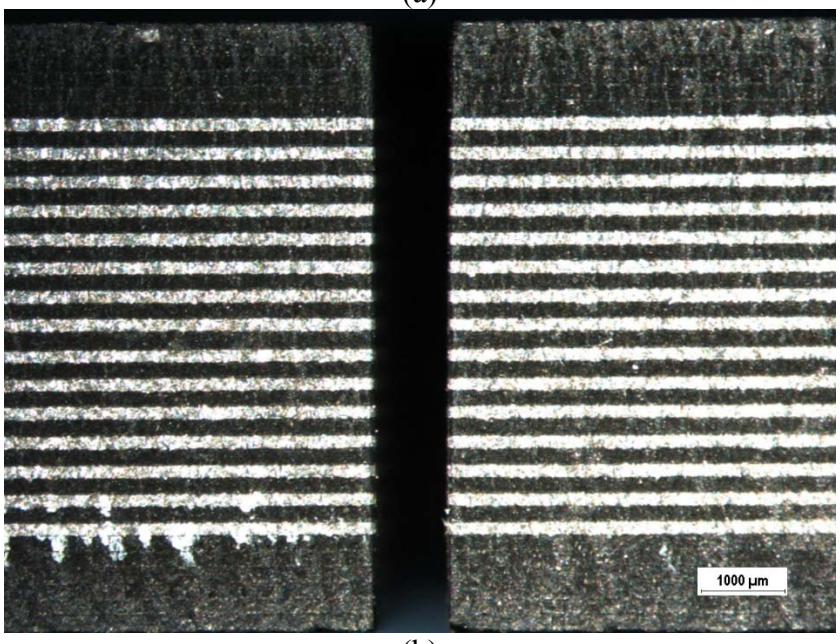

(b)

Figure A.11. **Experiment no. 11** cross-sectional view of AWJ machined kerf geometry depicting (a) Jet entry side damage (8X), and (b) Through the thickness kerf (3X)

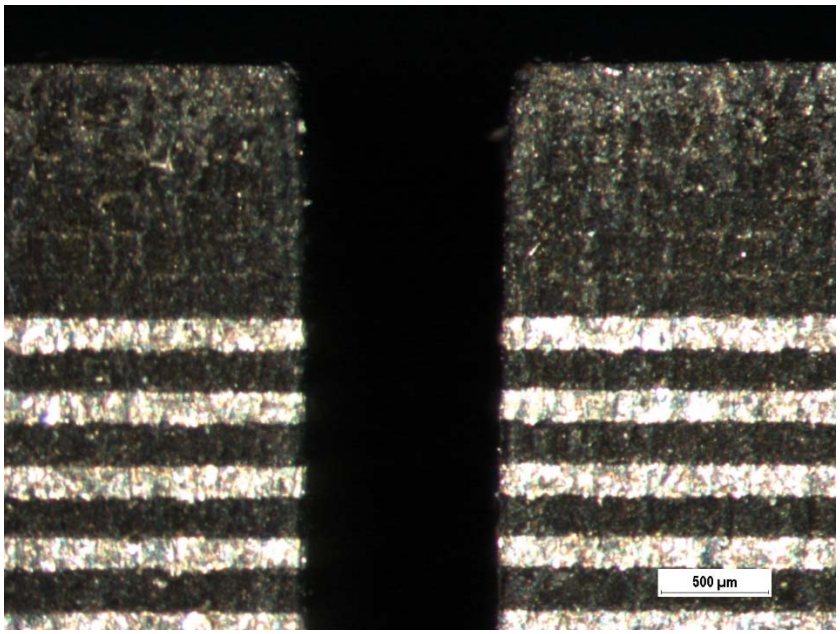

(a)

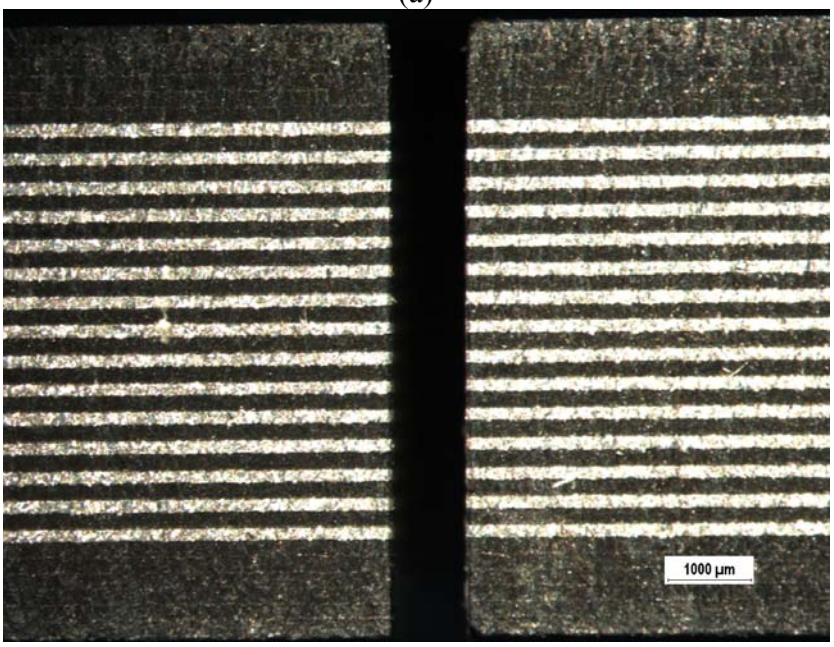

(b)

Figure A.12. **Experiment no. 12** cross-sectional view of AWJ machined kerf geometry depicting (a) Jet entry side damage (8X), and (b) Through the thickness kerf (3X)

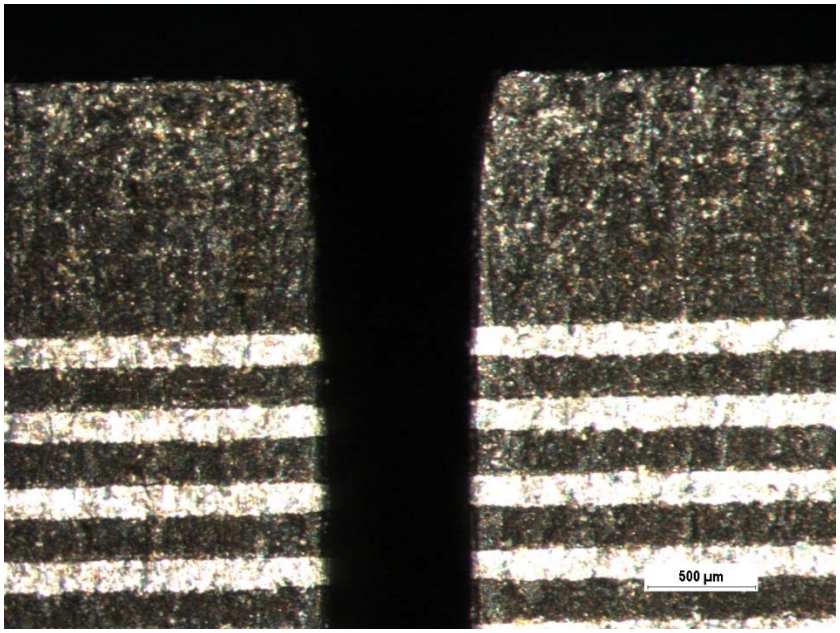

(a)

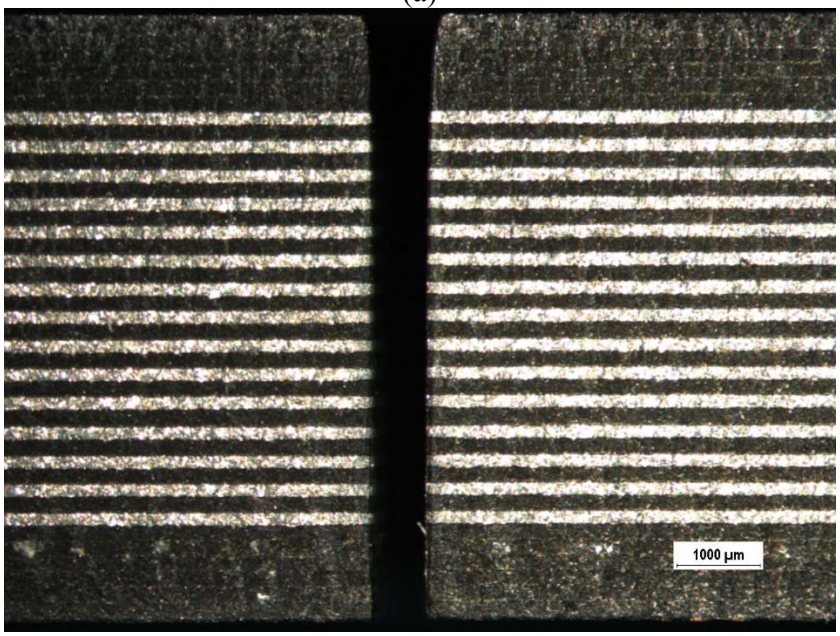

(b)

Figure A.13. **Experiment no. 13** cross-sectional view of AWJ machined kerf geometry depicting (a) Jet entry side damage (8X), and (b) Through the thickness kerf (3X)

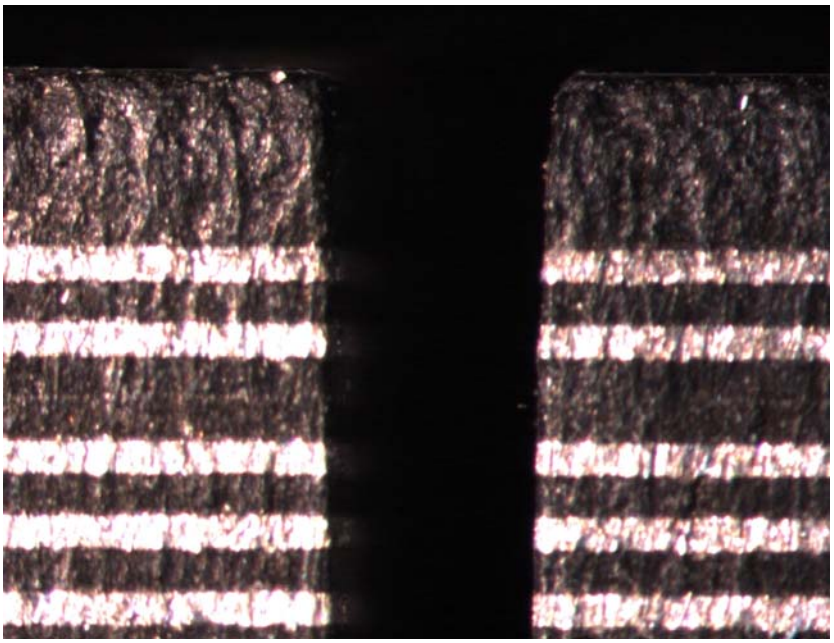

(a)

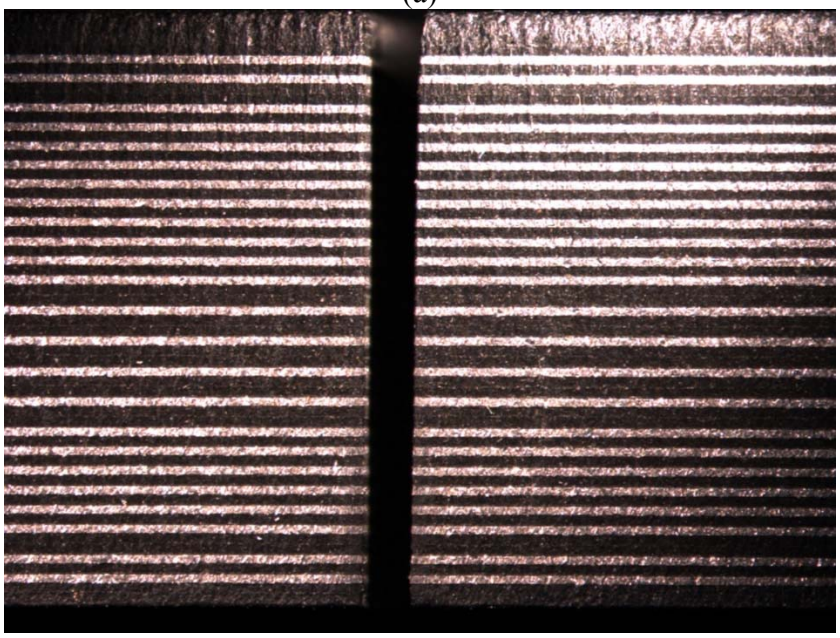

(b)

Figure A.14. **Experiment no. 14** cross-sectional view of AWJ machined kerf geometry depicting (a) Jet entry side damage (8X), and (b) Through the thickness kerf (3X)

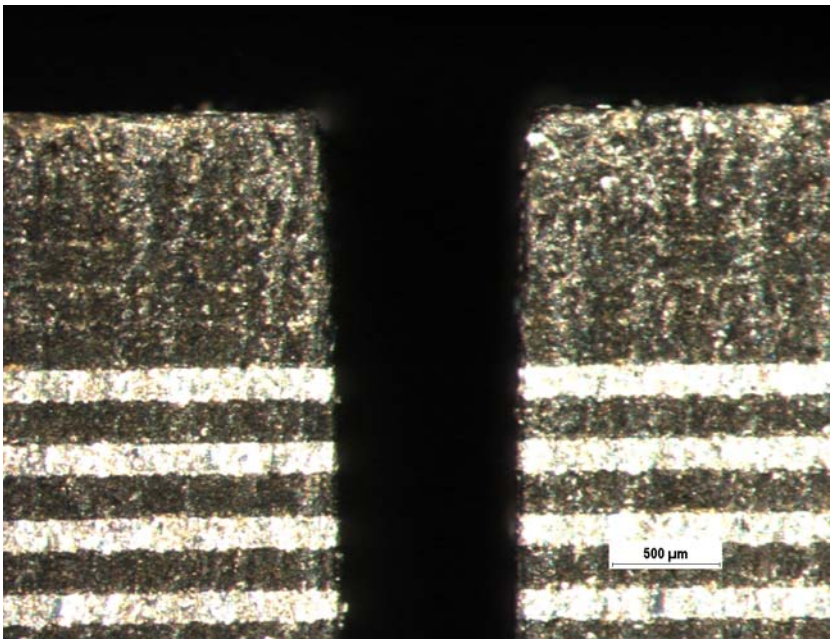

(a)

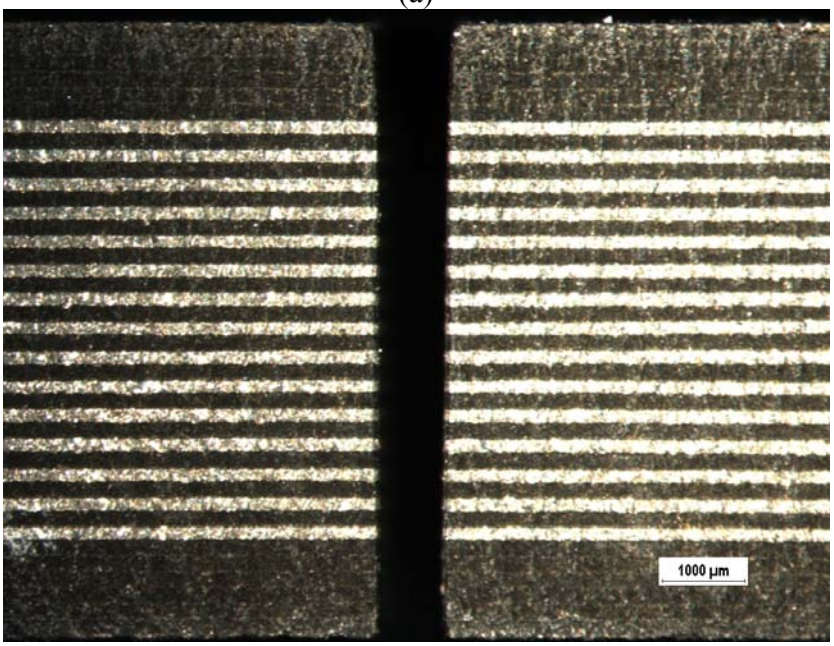

(b)

Figure A.15. **Experiment no. 15** cross-sectional view of AWJ machined kerf geometry depicting (a) Jet entry side damage (8X), and (b) Through the thickness kerf (3X)

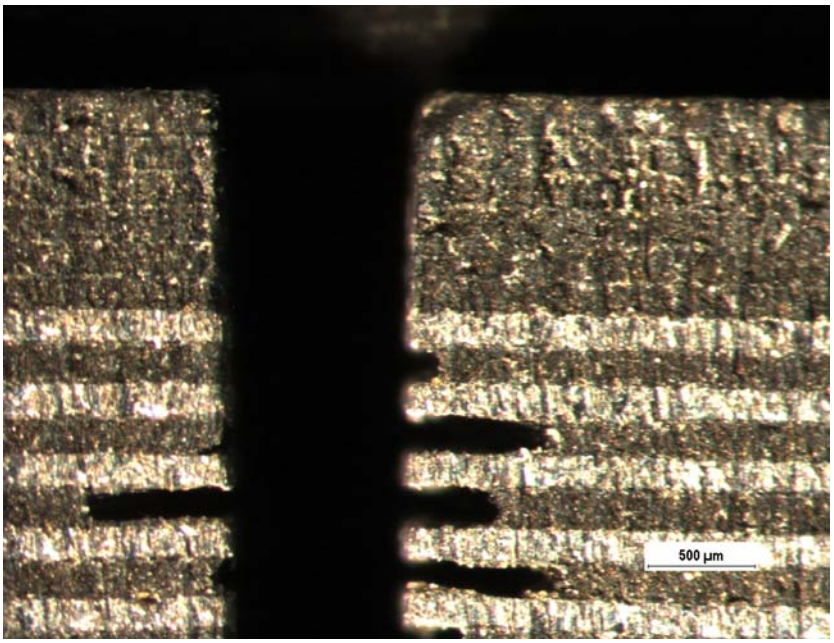

(a)

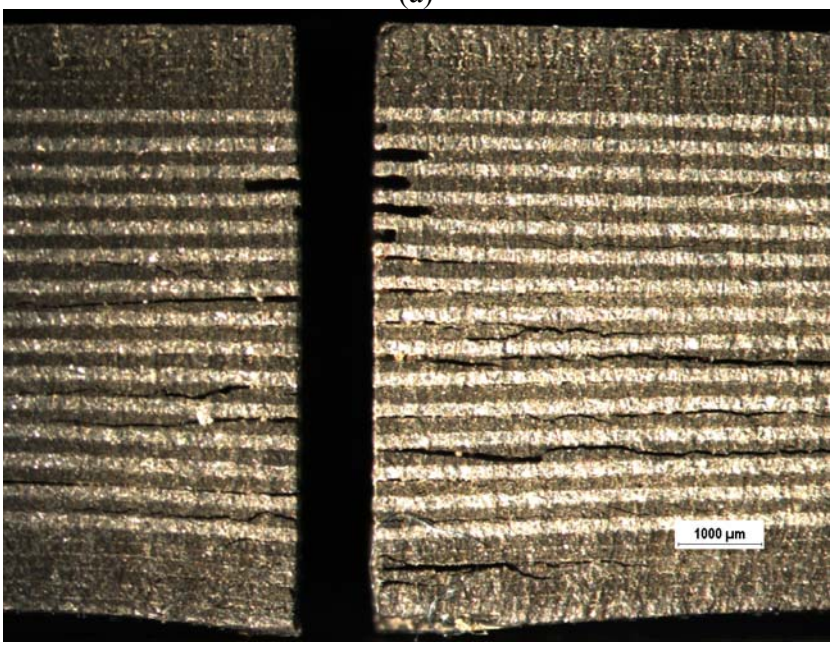

(b)

Figure A.16. **Experiment no. 16** cross-sectional view of AWJ machined kerf geometry depicting (a) Jet entry side damage (8X), and (b) Through the thickness kerf (3X)

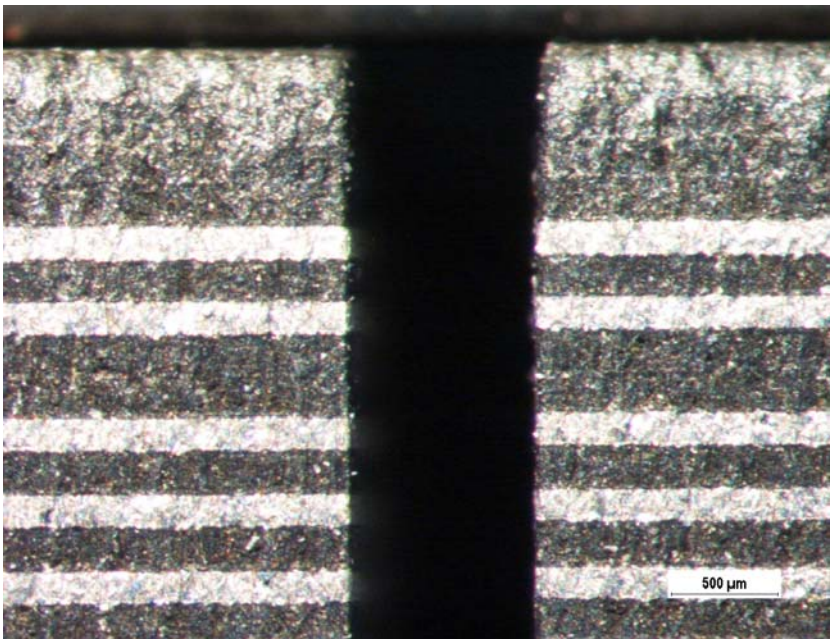

(a)

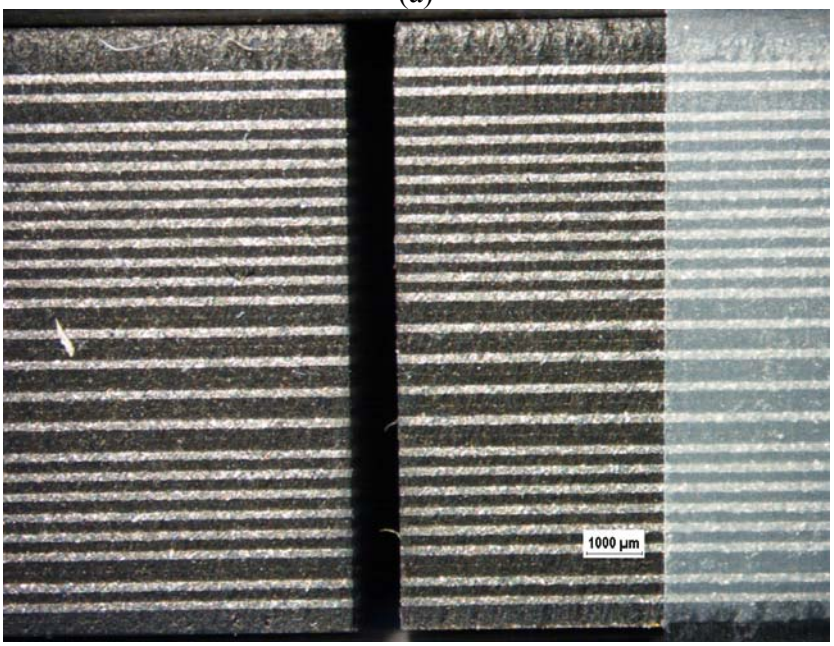

(b)

Figure A.17. **Experiment no. 17** cross-sectional view of AWJ machined kerf geometry depicting (a) Jet entry side damage (8X), and (b) Through the thickness kerf (2X)

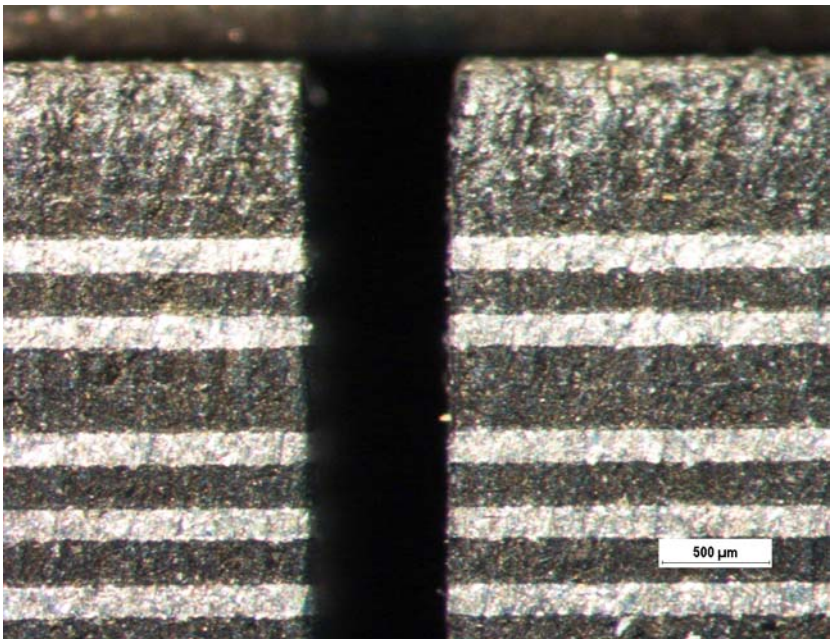

(a)

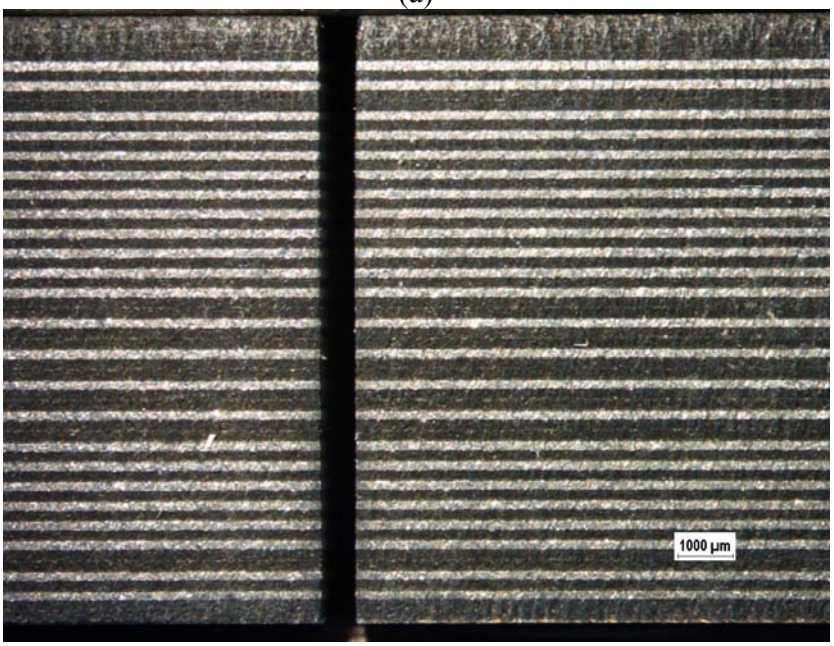

(b)

Figure A.18. **Experiment no. 18** cross-sectional view of AWJ machined kerf geometry depicting (a) Jet entry side damage (8X), and (b) Through the thickness kerf (2X)

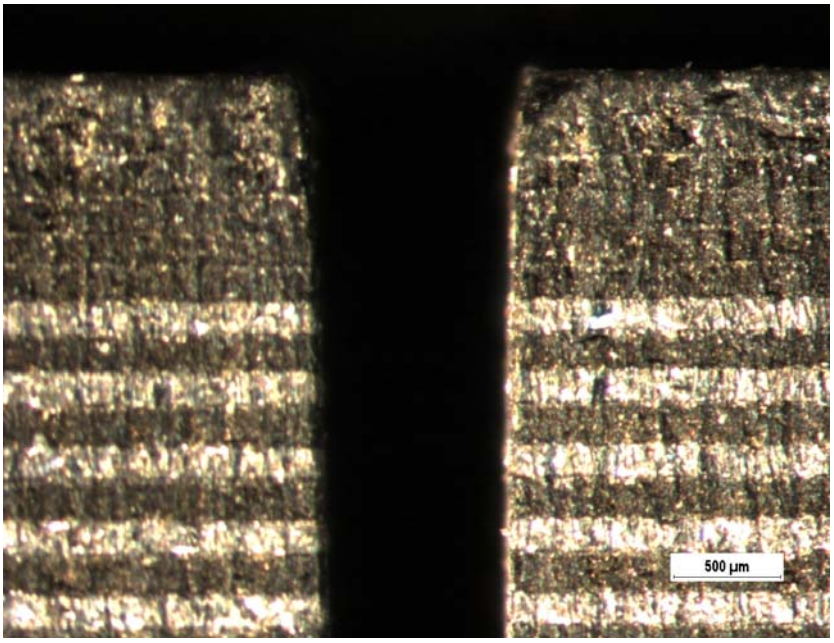

(a)

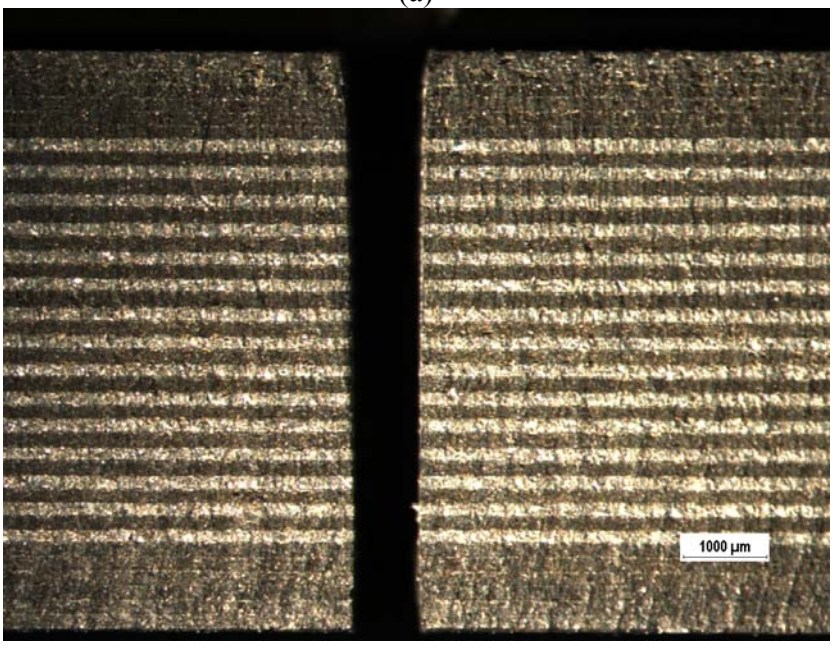

(b)

Figure A.19. **Experiment no. 19** cross-sectional view of AWJ machined kerf geometry depicting (a) Jet entry side damage (8X), and (b) Through the thickness kerf (3X)

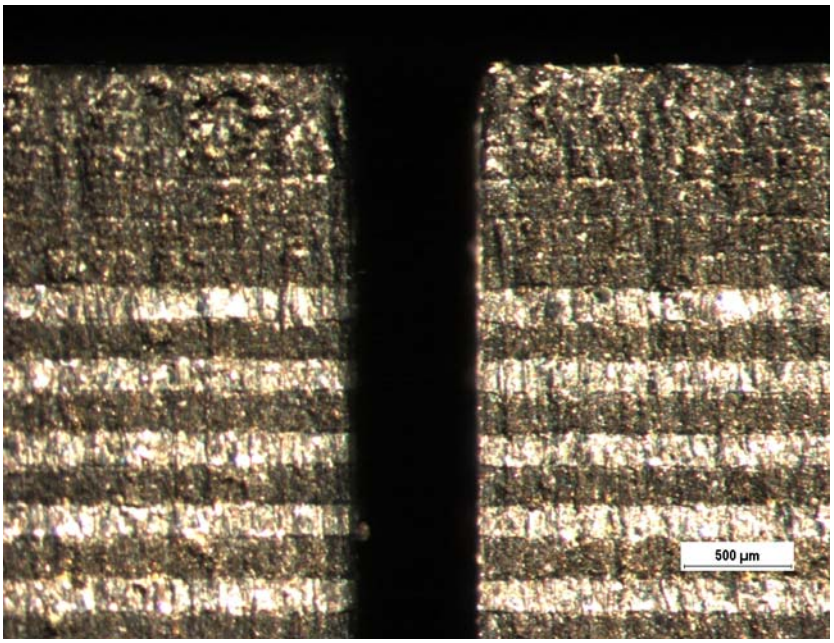

(a)

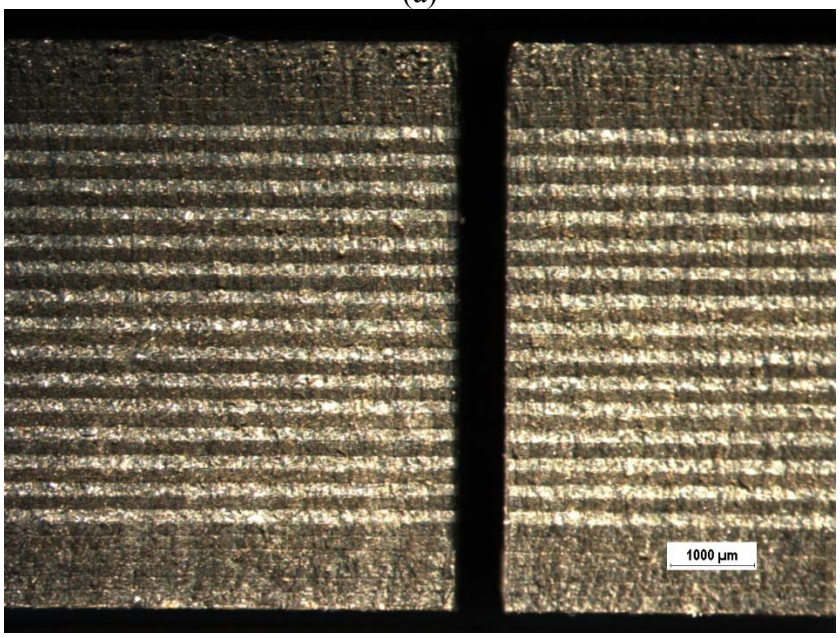

(b)

Figure A.20. **Experiment no. 20** cross-sectional view of AWJ machined kerf geometry depicting (a) Jet entry side damage (8X), and (b) Through the thickness kerf (3X)

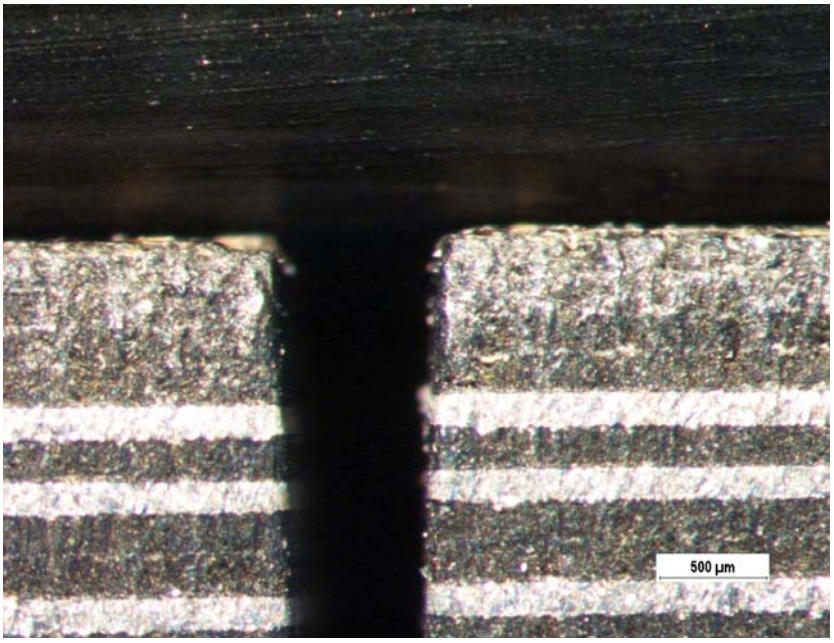

(a)

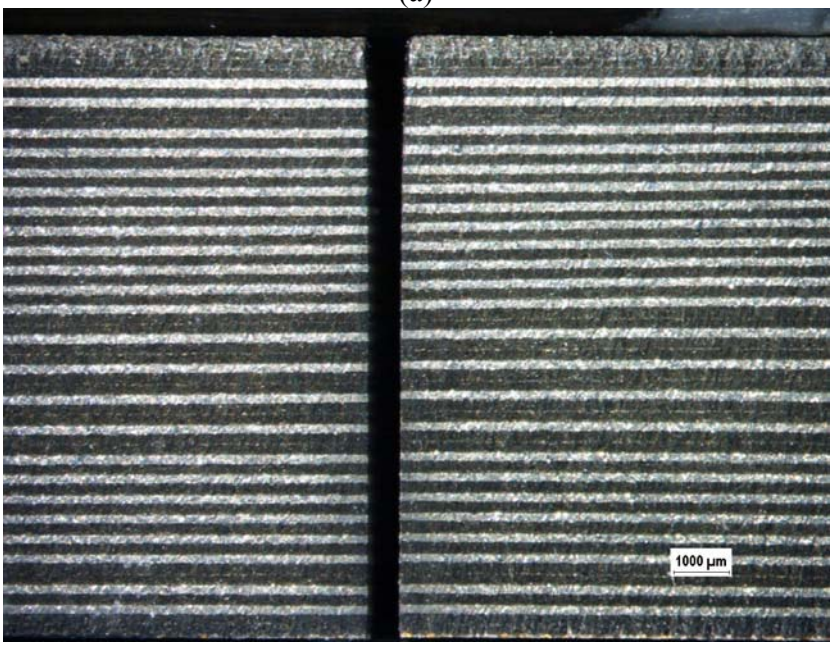

(b)

Figure A.21. **Experiment no. 21** cross-sectional view of AWJ machined kerf geometry depicting (a) Jet entry side damage (8X), and (b) Through the thickness kerf (2X)

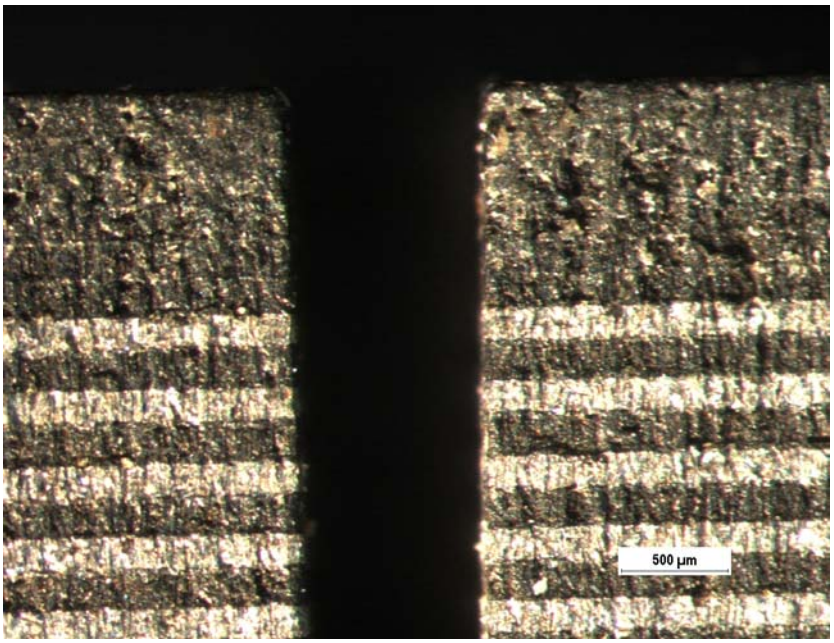

(a)

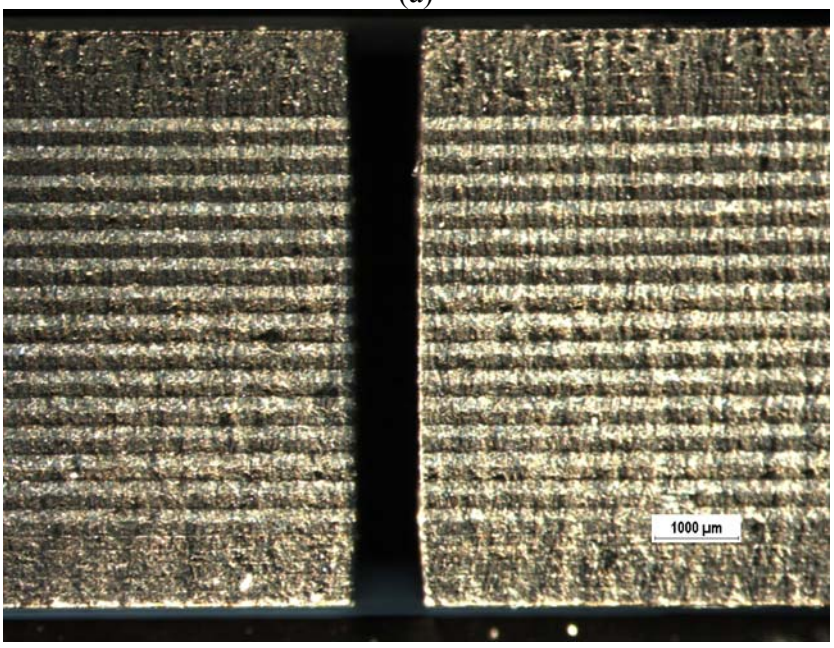

(b)

Figure A.22. **Experiment no. 22** cross-sectional view of AWJ machined kerf geometry depicting (a) Jet entry side damage (8X), and (b) Through the thickness kerf (3X)

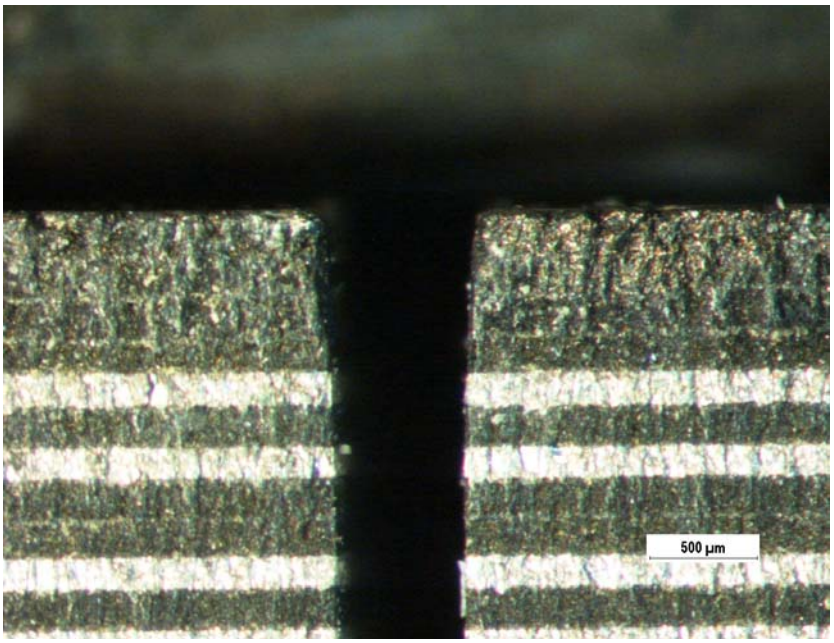

(a)

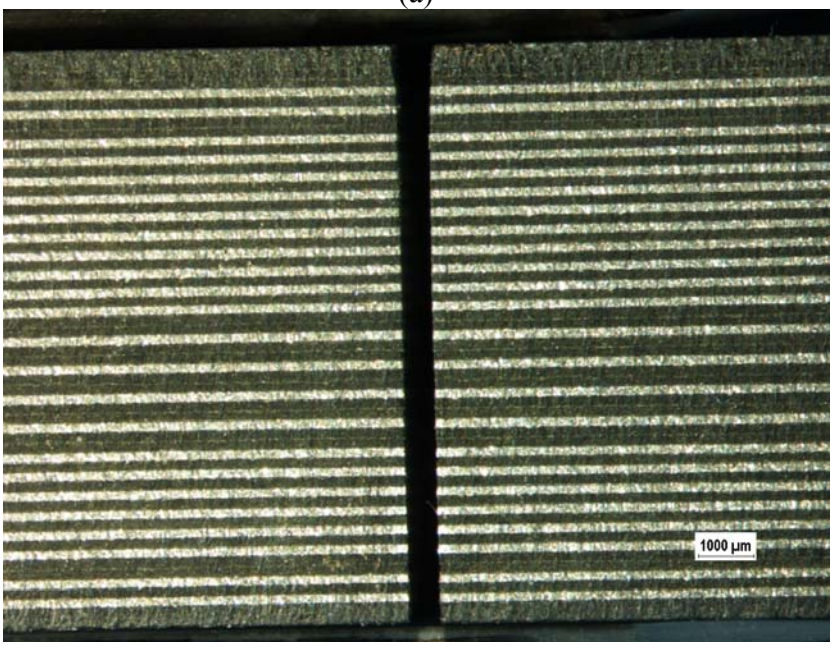

(b)

Figure A.23. **Experiment no. 23** cross-sectional view of AWJ machined kerf geometry depicting (a) Jet entry side damage (8X), and (b) Through the thickness kerf (2X)

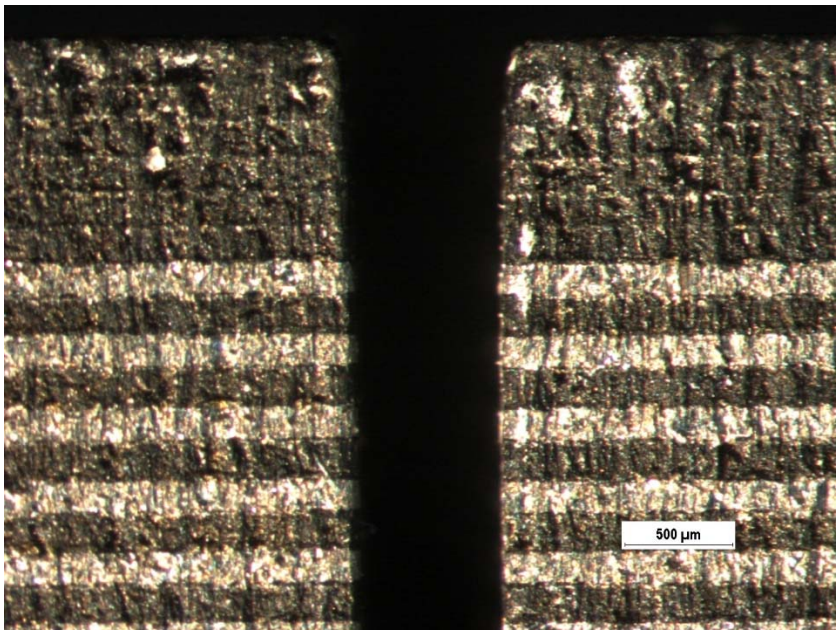

(a)

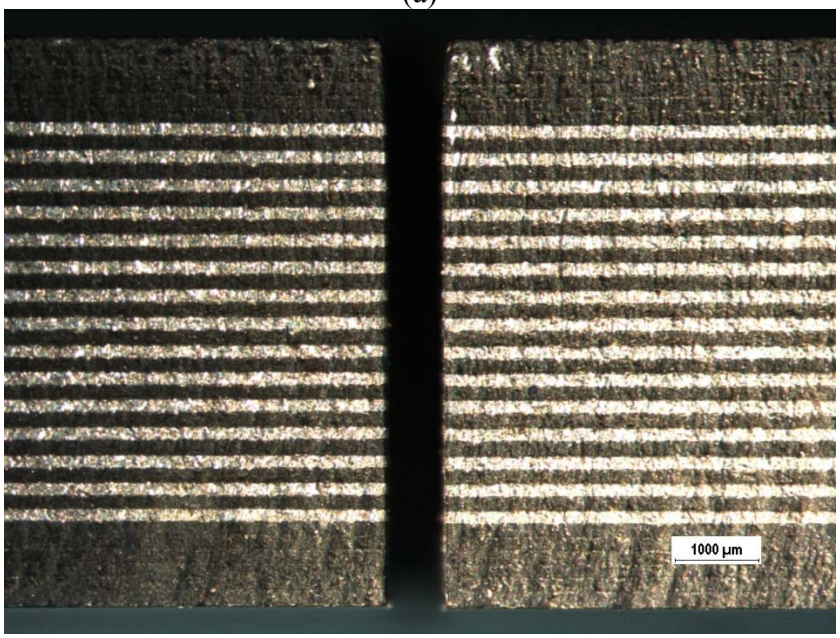

(b)

Figure A.24. **Experiment no. 24** cross-sectional view of AWJ machined kerf geometry depicting (a) Jet entry side damage (8X), and (b) Through the thickness kerf (3X)

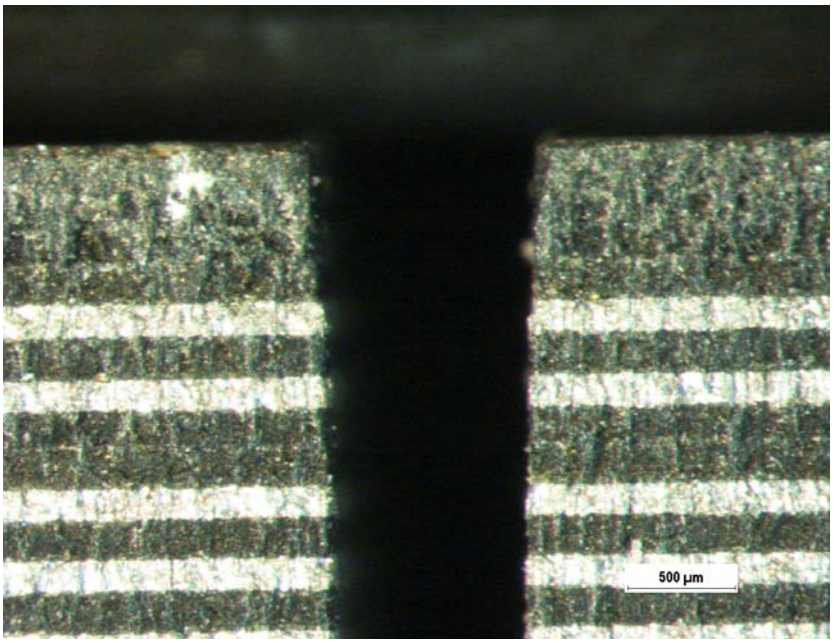

(a)

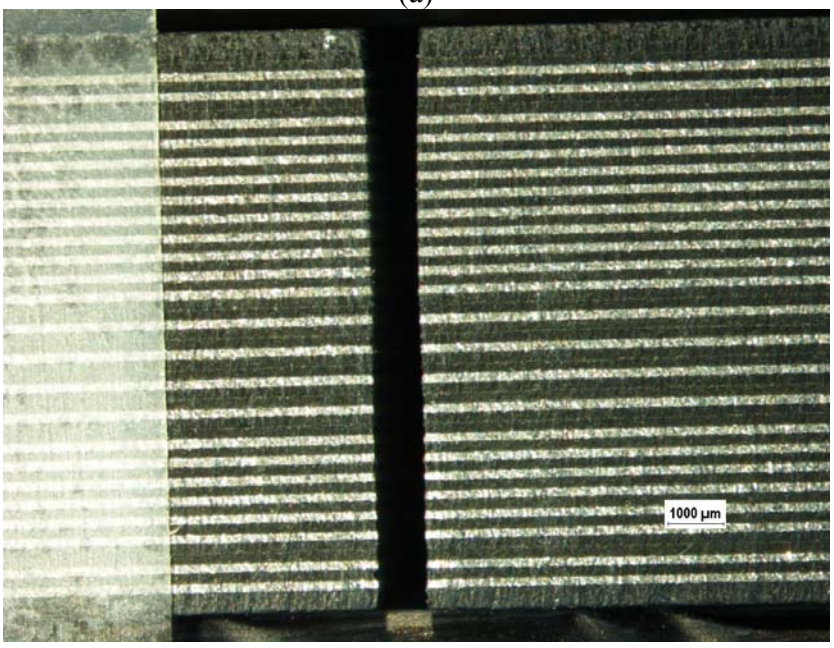

(b)

Figure A.25. **Experiment no. 25** cross-sectional view of AWJ machined kerf geometry depicting (a) Jet entry side damage (8X), and (b) Through the thickness kerf (2X)

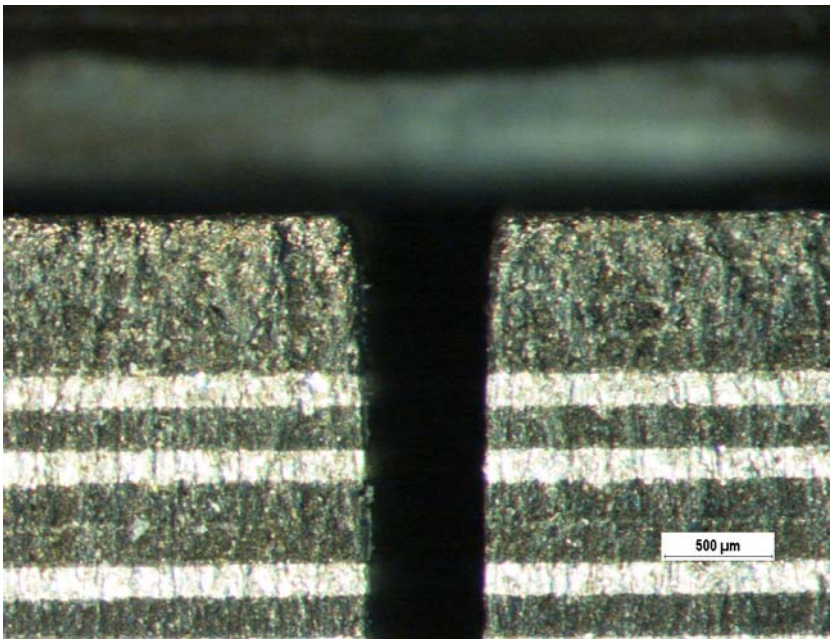

(a)

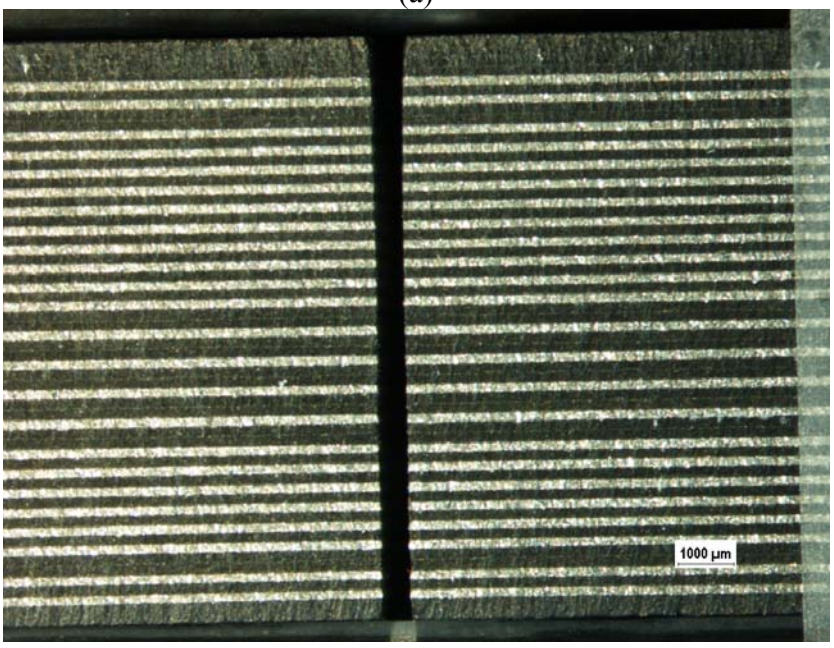

(b)

Figure A.26. **Experiment no. 26** cross-sectional view of AWJ machined kerf geometry depicting (a) Jet entry side damage (8X), and (b) Through the thickness kerf (2X)

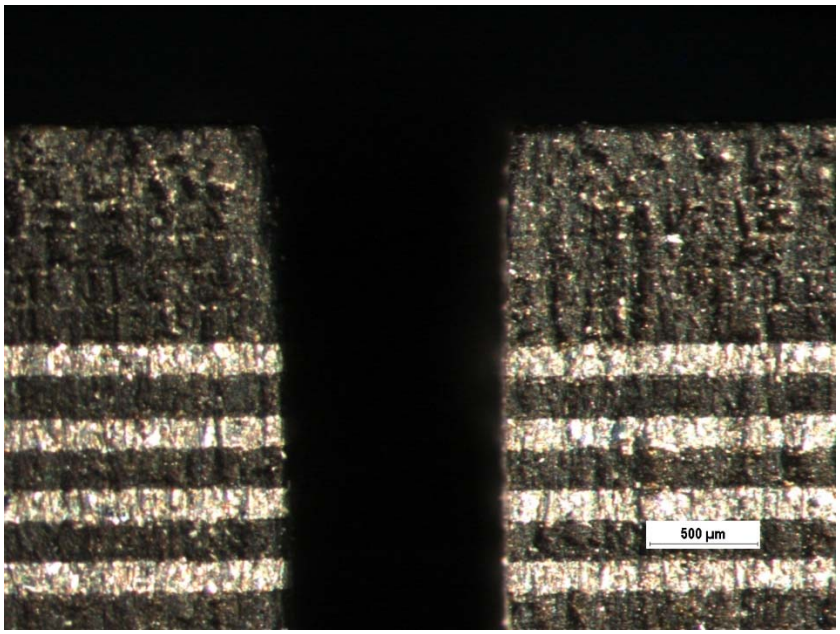

(a)

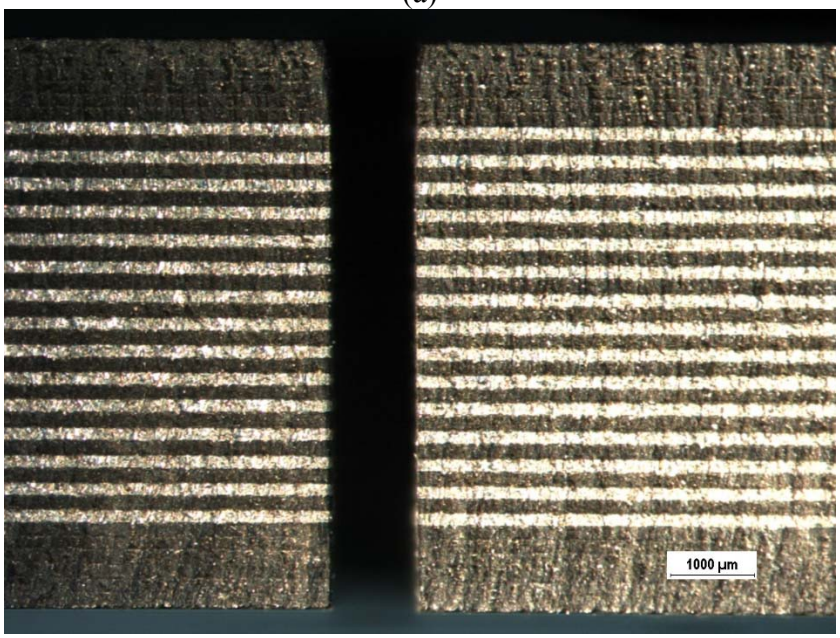

(b)

Figure A.27. **Experiment no. 27** cross-sectional view of AWJ machined kerf geometry depicting (a) Jet entry side damage (8X), and (b) Through the thickness kerf (3X)

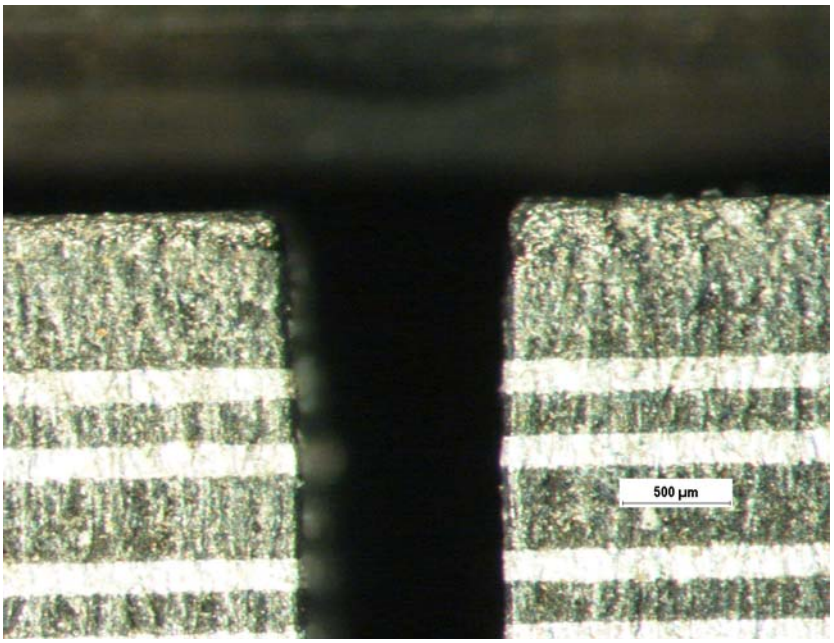

(a)

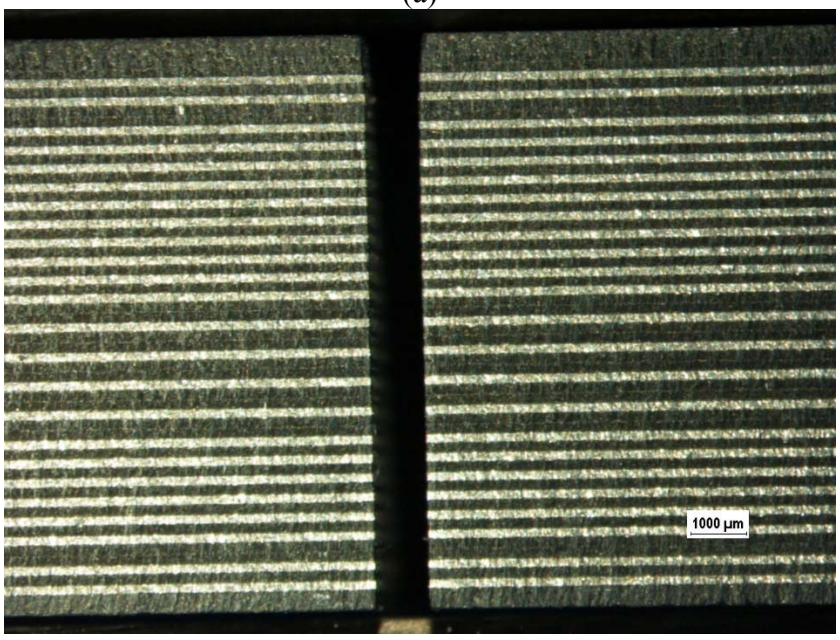

(b)

Figure A.28. **Experiment no. 28** cross-sectional view of AWJ machined kerf geometry depicting (a) Jet entry side damage (8X), and (b) Through the thickness kerf (2X)

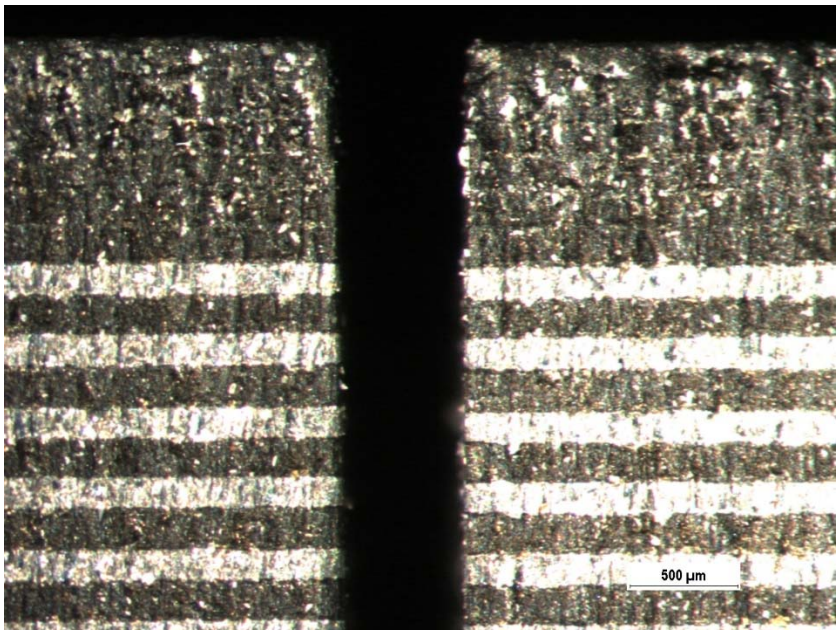

(a)

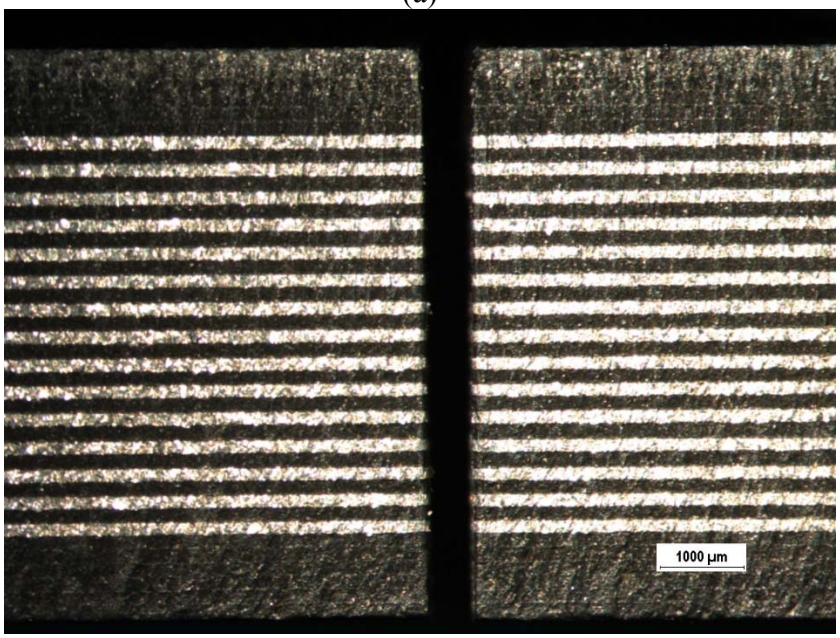

(b)

Figure A.29. **Experiment no. 29** cross-sectional view of AWJ machined kerf geometry depicting (a) Jet entry side damage (8X), and (b) Through the thickness kerf (3X)

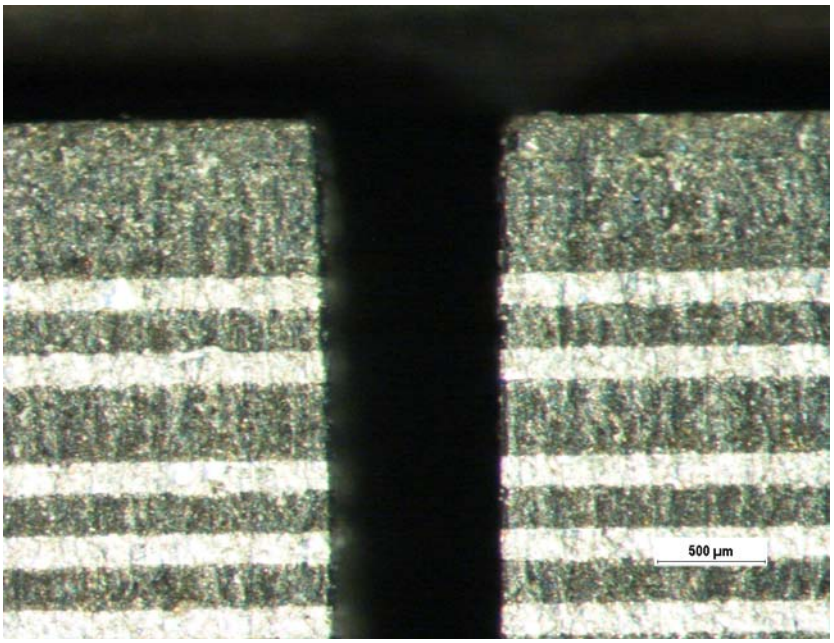

(a)

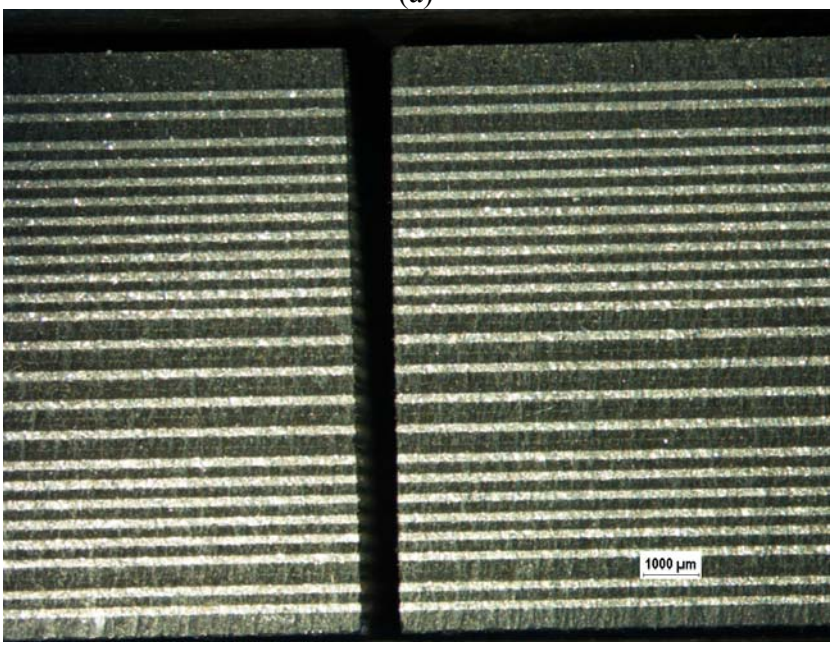

(b)

Figure A.30. **Experiment no. 30** cross-sectional view of AWJ machined kerf geometry depicting (a) Jet entry side damage (8X), and (b) Through the thickness kerf (2X)

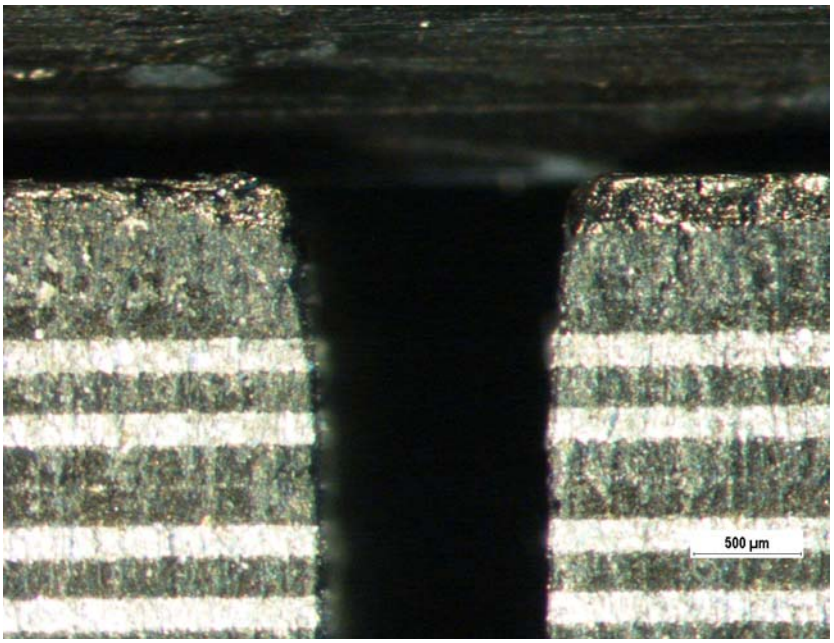

(a)

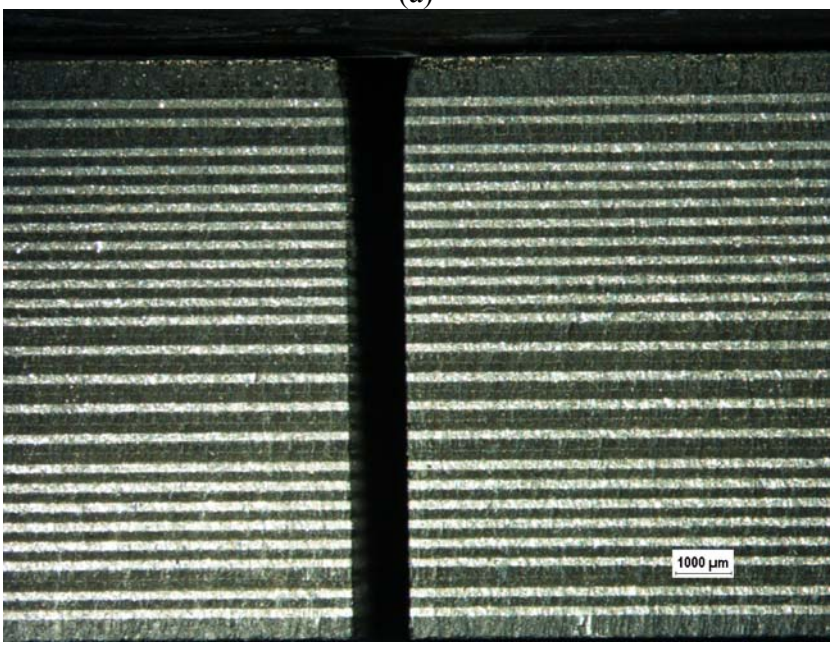

(b)

Figure A.31. **Experiment no. 31** cross-sectional view of AWJ machined kerf geometry depicting (a) Jet entry side damage (8X), and (b) Through the thickness kerf (2X)

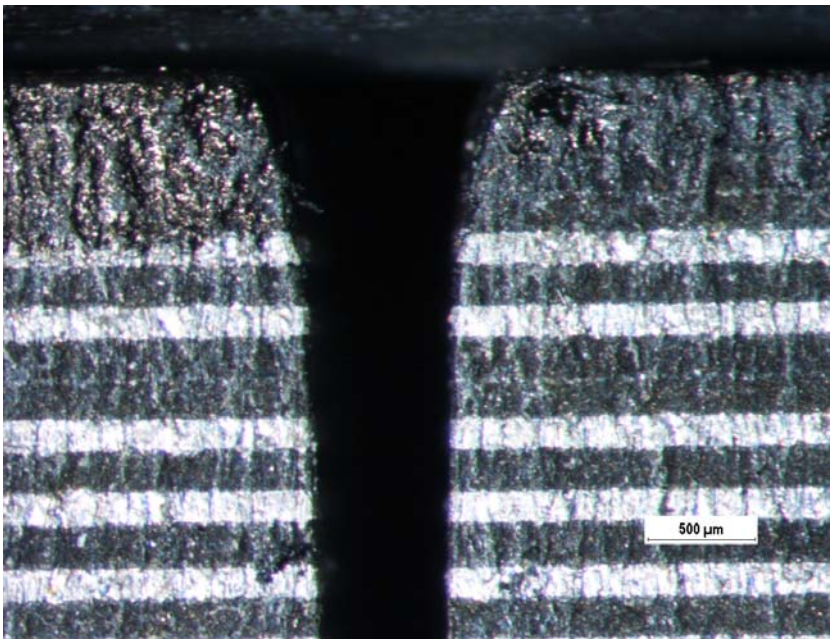

(a)

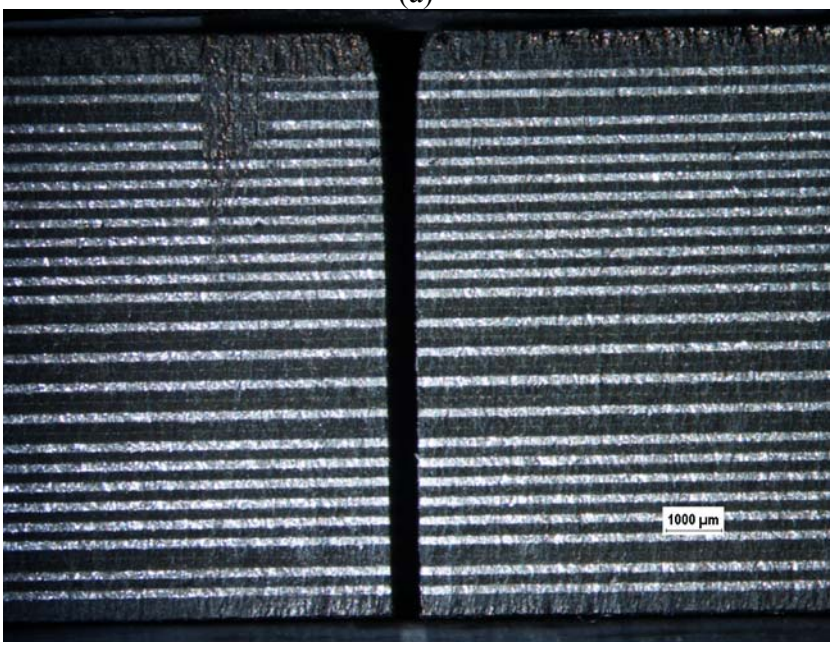

(b)

Figure A.32. **Experiment no. 32** cross-sectional view of AWJ machined kerf geometry depicting (a) Jet entry side damage (8X), and (b) Through the thickness kerf (2X)

APPENDIX B

RAW DATA – KERF TAPER RATIO

Table B.1. Raw data for Kerf Taper

Raw Data- Kerf Taper					
Experiment Number	Straight Surface	Small Inner Arc	Small Outer Arc	Large Inner Arc	Large Outer Arc
	Taper(mm)	Taper(mm)	Taper(mm)	Taper(mm)	Taper(mm)
1	0.127	0.127	0.1016	0.1016	0.127
2	0.1524	0.127	0.1524	0.127	0.127
3	0.127	0.127	0.127	0.127	0.127
4	0.0508	0.1016	0.1016	0.0762	0.0762
5	0.1778	0.1778	0.1778	0.1524	0.1524
6	0.127	0.127	0.1016	0.127	0.1016
7	0.0508	0.0762	0.0762	0.0762	0.0762
8	0.2032	0.2286	0.2032	0.2032	0.2286
9	0.0254	0.1524	0.0508	0.0508	0.0254
10	0.0254	0.0762	0.0508	0.0508	0.0762
11	0.0508	0.0508	0.0762	0.0508	0.0508
12	0.0508	0.0762	0.0762	0.0762	0.0762
13	0.127	0.127	0.1524	0.1524	0.1524
14	0.2032	0.2032	0.2032	0.2032	0.2032
15	0.1524	0.1778	0.1778	0.1778	0.1524
16	0.1016	0.127	0.1016	0.1016	0.1524
17	0.0508	0.0762	0.0762	0.1016	0.0762
18	0.0508	0.0254	0.0254	0.0762	0.0762
19	0.1016	0.127	0.127	0.127	0.1524
20	0	-0.0254	-0.0254	0.0254	0
21	0.1524	0.1524	0.1524	0.1524	0.1524
22	0.0508	0.0508	0.0508	0.0508	0
23	0.0762	0.1016	0.0762	0.0762	0.1016
24	0.0254	0.0508	0.0254	0.0508	0.0254
25	0.0762	0.0762	0.0762	0.1016	0.0508
26	0.0508	0.0508	0.0762	0.0508	0.0762
27	0	0	-0.0254	0	0.0254
28	0.0254	0.0254	0.0254	0.0508	0.0508
29	0.0508	0.0508	0.0508	0.0508	0.0508
30	0.1016	0.1016	0.127	0.1016	0.1016
31	0.0762	0.0762	0.0762	0.0508	0.0762
32	0.1524	0.1524	0.1524	0.1524	0.1778

ANOVA TABLES – KERF TAPER RATIO

Table B.2. ANOVA response table for Straight cut taper model

ANOVA for Response Surface Reduced 2FI model						
Analysis of variance table [Partial sum of squares - Type III]						
	Sum of		**Mean**	**F**	**p-value**	
Source	**Squares**	**df**	**Square**	**Value**	**Prob > F**	
Model	0.25	14	0.018	6.62	0.0002	significant
A-Thickness	*9.792E-004*	*1*	*9.792E-004*	*0.36*	*0.5562*	
B-P	*5.332E-003*	*1*	*5.332E-003*	*1.96*	*0.1792*	
C-Lm	*9.843E-003*	*1*	*9.843E-003*	*3.62*	*0.0741*	
D-dm	*0.060*	*1*	*0.060*	*22.09*	*0.0002*	
E-dn	*6.398E-003*	*1*	*6.398E-003*	*2.35*	*0.1433*	
F-R	*2.473E-003*	*1*	*2.473E-003*	*0.91*	*0.3534*	
G-u	*0.037*	*1*	*0.037*	*13.66*	*0.0018*	
AC	*0.030*	*1*	*0.030*	*10.95*	*0.0041*	
AE	*0.025*	*1*	*0.025*	*9.29*	*0.0073*	
BD	*5.899E-003*	*1*	*5.899E-003*	*2.17*	*0.1589*	
CD	*9.090E-003*	*1*	*9.090E-003*	*3.35*	*0.0850*	
CE	*5.626E-003*	*1*	*5.626E-003*	*2.07*	*0.1683*	
EG	*0.026*	*1*	*0.026*	*9.43*	*0.0069*	
FG	*7.883E-003*	*1*	*7.883E-003*	*2.90*	*0.1067*	
Residual	0.046	17	2.717E-003			
Cor Total	0.30	31				

Std. Dev.	0.052		R-Squared	0.8451
Mean	1.13		Adj R-Squared	0.7175
C.V. %	4.61		Pred R-Squared	0.4577
PRESS	0.16		Adeq Precision	9.685

Table B.3. ANOVA response table for Small inner arc taper model

Analysis of variance table [Partial sum of squares - Type III]						
	Sum of		**Mean**	**F**	**p-value**	
Source	**Squares**	**df**	**Square**	**Value**	**Prob > F**	
Model	0.26	17	0.015	4.07	0.0056	significant
A-Thickness	*3.661E-003*	*1*	*3.661E-003*	*0.96*	*0.3435*	
B-P	*9.188E-004*	*1*	*9.188E-004*	*0.24*	*0.6309*	
C-Lm	*0.018*	*1*	*0.018*	*4.65*	*0.0489*	
D-dm	*0.042*	*1*	*0.042*	*11.07*	*0.0050*	
E-dn	*0.011*	*1*	*0.011*	*2.87*	*0.1126*	
F-R	*9.540E-004*	*1*	*9.540E-004*	*0.25*	*0.6245*	
G-u	*0.040*	*1*	*0.040*	*10.58*	*0.0058*	
AB	*7.203E-003*	*1*	*7.203E-003*	*1.89*	*0.1906*	
AC	*0.012*	*1*	*0.012*	*3.16*	*0.0971*	
AE	*0.025*	*1*	*0.025*	*6.66*	*0.0218*	
AF	*8.428E-003*	*1*	*8.428E-003*	*2.21*	*0.1590*	
CD	*9.917E-003*	*1*	*9.917E-003*	*2.60*	*0.1289*	
CG	*0.015*	*1*	*0.015*	*4.04*	*0.0641*	
DE	*0.011*	*1*	*0.011*	*2.80*	*0.1166*	
DF	*9.861E-003*	*1*	*9.861E-003*	*2.59*	*0.1299*	
EG	*0.038*	*1*	*0.038*	*10.01*	*0.0069*	
FG	*8.883E-003*	*1*	*8.883E-003*	*2.33*	*0.1489*	
Residual	0.053	14	3.808E-003			
Cor Total	0.32	31				

Std. Dev.	0.062		R-Squared	0.8317
Mean	1.15		Adj R-Squared	0.6273
C.V. %	5.38		Pred R-Squared	0.1010
PRESS	0.28		Adeq Precision	7.898

Table B.4. ANOVA response table for Small outer arc taper model

ANOVA for Response Surface Reduced 2FI model						
Analysis of variance table [Partial sum of squares - Type III]						
	Sum of		**Mean**	**F**	**p-value**	
Source	**Squares**	**df**	**Square**	**Value**	**Prob > F**	
Model	0.25	14	0.018	6.99	0.0001	significant
A-Thickness	*2.302E-003*	*1*	*2.302E-003*	*0.89*	*0.3583*	
B-P	*1.179E-003*	*1*	*1.179E-003*	*0.46*	*0.5084*	
C-Lm	*0.038*	*1*	*0.038*	*14.76*	*0.0013*	
D-dm	*0.033*	*1*	*0.033*	*12.86*	*0.0023*	
E-dn	*0.011*	*1*	*0.011*	*4.08*	*0.0594*	
F-R	*1.819E-004*	*1*	*1.819E-004*	*0.070*	*0.7939*	
G-u	*0.047*	*1*	*0.047*	*18.18*	*0.0005*	
AC	*0.021*	*1*	*0.021*	*8.14*	*0.0110*	
AE	*0.016*	*1*	*0.016*	*6.16*	*0.0238*	
CD	*0.011*	*1*	*0.011*	*4.29*	*0.0538*	
CE	*5.181E-003*	*1*	*5.181E-003*	*2.01*	*0.1747*	
CG	*8.186E-003*	*1*	*8.186E-003*	*3.17*	*0.0929*	
EG	*0.032*	*1*	*0.032*	*12.43*	*0.0026*	
FG	*9.516E-003*	*1*	*9.516E-003*	*3.68*	*0.0719*	
Residual	0.044	17	2.583E-003			
Cor Total	0.30	31				

Std. Dev.	0.050		R-Squared	0.8480
Mean	1.14		Adj R-Squared	0.7382
C.V. %	4.40		Pred R-Squared	0.5251
PRESS	0.14		Adeq Precision	10.974

Table B.5. ANOVA response table for Large inner arc taper model

ANOVA for Response Surface Reduced 2FI model						
Analysis of variance table [Partial sum of squares - Type III]						
	Sum of		**Mean**	**F**	**p-value**	
Source	**Squares**	**df**	**Square**	**Value**	**Prob > F**	
Model	0.20	17	0.012	6.90	0.0004	significant
A-Thickness	*3.019E-003*	*1*	*3.019E-003*	*1.76*	*0.2063*	
B-P	*7.091E-004*	*1*	*7.091E-004*	*0.41*	*0.5311*	
C-Lm	*0.010*	*1*	*0.010*	*5.98*	*0.0283*	
D-dm	*0.034*	*1*	*0.034*	*19.84*	*0.0005*	
E-dn	*8.582E-003*	*1*	*8.582E-003*	*4.99*	*0.0423*	
F-R	*1.615E-003*	*1*	*1.615E-003*	*0.94*	*0.3488*	
G-u	*0.023*	*1*	*0.023*	*13.64*	*0.0024*	
AC	*0.019*	*1*	*0.019*	*11.17*	*0.0048*	
AE	*0.017*	*1*	*0.017*	*9.95*	*0.0070*	
BC	*8.868E-003*	*1*	*8.868E-003*	*5.16*	*0.0394*	
CD	*3.704E-003*	*1*	*3.704E-003*	*2.16*	*0.1642*	
CE	*4.315E-003*	*1*	*4.315E-003*	*2.51*	*0.1354*	
CG	*5.255E-003*	*1*	*5.255E-003*	*3.06*	*0.1023*	
DE	*7.015E-003*	*1*	*7.015E-003*	*4.08*	*0.0629*	
DF	*4.235E-003*	*1*	*4.235E-003*	*2.46*	*0.1388*	
EG	*0.021*	*1*	*0.021*	*12.10*	*0.0037*	
FG	*6.653E-003*	*1*	*6.653E-003*	*3.87*	*0.0693*	
Residual	0.024	14	1.719E-003			
Cor Total	0.23	31				

Std. Dev.	0.041		R-Squared	0.8934
Mean	1.14		Adj R-Squared	0.7639
C.V. %	3.64		Pred R-Squared	0.4350
PRESS	0.13		Adeq Precision	10.887

Table B.6. ANOVA response table for Large outer arc taper model

ANOVA for Response Surface Reduced 2FI model						
Analysis of variance table [Partial sum of squares - Type III]						
	Sum of		**Mean**	**F**	**p-value**	
Source	**Squares**	**df**	**Square**	**Value**	**Prob > F**	
Model	0.25	17	0.015	4.57	0.0032	significant
A-Thickness	*3.583E-003*	*1*	*3.583E-003*	*1.11*	*0.3097*	
B-P	*1.634E-003*	*1*	*1.634E-003*	*0.51*	*0.4881*	
C-Lm	*4.963E-003*	*1*	*4.963E-003*	*1.54*	*0.2351*	
D-dm	*0.048*	*1*	*0.048*	*15.03*	*0.0017*	
E-dn	*0.011*	*1*	*0.011*	*3.27*	*0.0922*	
F-R	*5.519E-004*	*1*	*5.519E-004*	*0.17*	*0.6853*	
G-u	*0.035*	*1*	*0.035*	*10.91*	*0.0052*	
AC	*0.011*	*1*	*0.011*	*3.26*	*0.0925*	
AE	*0.018*	*1*	*0.018*	*5.52*	*0.0340*	
BC	*7.689E-003*	*1*	*7.689E-003*	*2.39*	*0.1448*	
BD	*7.433E-003*	*1*	*7.433E-003*	*2.31*	*0.1512*	
CD	*0.013*	*1*	*0.013*	*4.11*	*0.0621*	
CE	*6.697E-003*	*1*	*6.697E-003*	*2.08*	*0.1715*	
CG	*7.583E-003*	*1*	*7.583E-003*	*2.35*	*0.1474*	
DG	*7.317E-003*	*1*	*7.317E-003*	*2.27*	*0.1542*	
EG	*0.038*	*1*	*0.038*	*11.78*	*0.0040*	
FG	*0.016*	*1*	*0.016*	*5.01*	*0.0420*	
Residual	0.045	14	3.224E-003			
Cor Total	0.30	31				

Std. Dev.	0.057		R-Squared	0.8473
Mean	1.14		Adj R-Squared	0.6619
C.V. %	4.98		Pred R-Squared	0.1909
PRESS	0.24		Adeq Precision	8.156

RAW DATA – TRANSVERSE ROUGHNESS (R_Z)

Table B.7. Raw data for Transverse Roughness (R_z)

Raw Data- Roughness R_z (µm)					
Experiment Number	Straight Surface	Small Inner Arc	Small Outer Arc	Large Inner Arc	Large Outer Arc
	Taper(mm)	Taper(mm)	Taper(mm)	Taper(mm)	Taper(mm)
1	19.096	20.119	20.121	19.628	18.292
2	15.802	14.793	18.509	15.501	16.525
3	15.61	17.884	16.792	16.726	14.88
4	26.241	20.462	23.869	25.092	21.614
5	10.262	18.424	14.086	16.021	15.377
6	12.503	11.012	10.374	11.069	8.302
7	21.188	24.775	21.939	21.134	23.297
8	21.063	22.163	19.276	18.029	19.11
9	16.247	15.778	17.878	15.596	16.702
10	19.608	19.65	17.452	19.73	18.333
11	14.349	15.997	14.012	12.396	12.263
12	12.566	15.907	13.473	16.62	18.024
13	9.127	8.612	10.702	10.239	8.338
14	20.548	19.348	20.545	20.077	21.576
15	12.053	9.641	13.453	10.447	12.667
16	29.334	18.221	22.461	19.126	20.987
17	14.313	15.918	15.905	14.623	13.499
18	18.803	17.853	21.597	20.632	22.234
19	14.629	15.882	20.342	16.26	16.583
20	10.729	10.539	10.582	10.4	11.251
21	15.583	16.572	14.592	15.47	17.564
22	18.39	18.334	20.758	21.07	21.694
23	22.568	18.426	21.575	18.934	21.495
24	12.274	13.243	11.213	11.935	15.956
25	25.266	29.777	26.959	27.97	24.603
26	23.547	24.524	23.3	26.73	25.812
27	14.89	12.797	8.842	11.86	14.236
28	19.386	19.886	19.598	20.269	18.065
29	10.287	11.029	8.074	7.507	14.981
30	24.182	22.962	21.171	18.651	24.212
31	26.877	27.331	24.032	20.903	19.104
32	16.223	15.299	16.53	15.791	14.306

ANOVA TABLES – TRANSVERSE SURFACE ROUGHNESS

Table B.8. ANOVA response table for Straight cut transverse roughness (R_z)

ANOVA for Response Surface Reduced 2FI model						
Analysis of variance table [Partial sum of squares - Type III]						
	Sum of		**Mean**	**F**	**p-value**	
Source	**Squares**	**df**	**Square**	**Value**	**Prob > F**	
Model	832.65	15	55.51	14.26	< 0.0001	significant
A-Thickness	*181.83*	*1*	*181.83*	*46.70*	*< 0.0001*	
B-P	*46.91*	*1*	*46.91*	*12.05*	*0.0032*	
C-Lm	*32.36*	*1*	*32.36*	*8.31*	*0.0108*	
D-dm	*128.38*	*1*	*128.38*	*32.97*	*< 0.0001*	
E-dn	*106.31*	*1*	*106.31*	*27.30*	*< 0.0001*	
F-R	*0.020*	*1*	*0.020*	*5.188E-003*	*0.9435*	
G-u	*39.61*	*1*	*39.61*	*10.17*	*0.0057*	
AB	*12.53*	*1*	*12.53*	*3.22*	*0.0918*	
AE	*36.19*	*1*	*36.19*	*9.29*	*0.0077*	
AF	*46.82*	*1*	*46.82*	*12.02*	*0.0032*	
AG	*35.86*	*1*	*35.86*	*9.21*	*0.0079*	
CD	*15.59*	*1*	*15.59*	*4.00*	*0.0627*	
CE	*8.29*	*1*	*8.29*	*2.13*	*0.1638*	
CG	*11.36*	*1*	*11.36*	*2.92*	*0.1070*	
DG	*11.97*	*1*	*11.97*	*3.07*	*0.0986*	
Residual	62.30	16	3.89			
Cor Total	894.96	31				

Std. Dev.	1.97		R-Squared	0.9304
Mean	17.61		Adj R-Squared	0.8651
C.V. %	11.21		Pred R-Squared	0.7215
PRESS	249.22		Adeq Precision	13.512

Table B.9. ANOVA response table for Small inner arc transverse roughness (R_z)

ANOVA for Response Surface Reduced 2FI model						
Analysis of variance table [Partial sum of squares - Type III]						
	Sum of		**Mean**	**F**	**p-value**	
Source	**Squares**	**df**	**Square**	**Value**	**Prob > F**	
Model	746.25	15	49.75	29.98	< 0.0001	significant
A-Thickness	*205.10*	*1*	*205.10*	*123.61*	*< 0.0001*	
B-P	*89.82*	*1*	*89.82*	*54.13*	*< 0.0001*	
C-Lm	*4.06*	*1*	*4.06*	*2.45*	*0.1375*	
D-dm	*80.07*	*1*	*80.07*	*48.25*	*< 0.0001*	
E-dn	*42.16*	*1*	*42.16*	*25.41*	*0.0001*	
F-R	*11.35*	*1*	*11.35*	*6.84*	*0.0188*	
G-u	*62.41*	*1*	*62.41*	*37.61*	*< 0.0001*	
AB	*4.06*	*1*	*4.06*	*2.44*	*0.1375*	
AD	*22.86*	*1*	*22.86*	*13.78*	*0.0019*	
BC	*7.29*	*1*	*7.29*	*4.39*	*0.0523*	
BG	*15.69*	*1*	*15.69*	*9.46*	*0.0072*	
CD	*21.78*	*1*	*21.78*	*13.12*	*0.0023*	
CE	*5.23*	*1*	*5.23*	*3.15*	*0.0950*	
DE	*5.33*	*1*	*5.33*	*3.21*	*0.0921*	
DG	*36.64*	*1*	*36.64*	*22.08*	*0.0002*	
Residual	26.55	16	1.66			
Cor Total	772.80	31				

Std. Dev.	1.29		R-Squared	0.9656
Mean	17.60		Adj R-Squared	0.9334
C.V. %	7.32		Pred R-Squared	0.8626
PRESS	106.19		Adeq Precision	21.765

Table B.10. ANOVA response table for Small outer arc transverse roughness (R_z)

ANOVA for Response Surface Reduced 2FI model						
Analysis of variance table [Partial sum of squares - Type III]						
	Sum of		**Mean**	**F**	**p-value**	
Source	**Squares**	**df**	**Square**	**Value**	**Prob > F**	
Model	742.46	17	43.67	39.02	< 0.0001	significant
A-Thickness	*181.84*	*1*	*181.84*	*162.45*	*< 0.0001*	
B-P	*103.25*	*1*	*103.25*	*92.24*	*< 0.0001*	
C-Lm	*0.46*	*1*	*0.46*	*0.41*	*0.5322*	
D-dm	*76.91*	*1*	*76.91*	*68.71*	*< 0.0001*	
E-dn	*110.17*	*1*	*110.17*	*98.43*	*< 0.0001*	
F-R	*4.961E-004*	*1*	*4.961E-004*	*4.432E-004*	*0.9835*	
G-u	*66.01*	*1*	*66.01*	*58.97*	*< 0.0001*	
AB	*18.20*	*1*	*18.20*	*16.26*	*0.0012*	
AC	*4.11*	*1*	*4.11*	*3.67*	*0.0759*	
AD	*2.09*	*1*	*2.09*	*1.87*	*0.1931*	
AF	*2.36*	*1*	*2.36*	*2.11*	*0.1688*	
BC	*8.71*	*1*	*8.71*	*7.78*	*0.0145*	
CD	*19.89*	*1*	*19.89*	*17.77*	*0.0009*	
CF	*7.58*	*1*	*7.58*	*6.77*	*0.0209*	
DE	*2.94*	*1*	*2.94*	*2.62*	*0.1276*	
EG	*5.13*	*1*	*5.13*	*4.58*	*0.0505*	
FG	*2.51*	*1*	*2.51*	*2.24*	*0.1564*	
Residual	15.67	14	1.12			
Cor Total	758.13	31				

Std. Dev.	1.06		R-Squared	0.9793
Mean	17.50		Adj R-Squared	0.9542
C.V. %	6.05		Pred R-Squared	0.8861
PRESS	86.39		Adeq Precision	25.486

Table B.11. ANOVA response table for Large inner arc transverse roughness (R_z)

ANOVA for Response Surface Reduced 2FI model						
Analysis of variance table [Partial sum of squares - Type III]						
	Sum of		**Mean**	**F**	**p-value**	
Source	**Squares**	**df**	**Square**	**Value**	**Prob > F**	
Model	713.00	14	50.93	39.14	< 0.0001	significant
A-Thickness	*180.07*	*1*	*180.07*	*138.38*	*< 0.0001*	
B-P	*81.92*	*1*	*81.92*	*62.95*	*< 0.0001*	
C-Lm	*0.15*	*1*	*0.15*	*0.12*	*0.7348*	
D-dm	*61.13*	*1*	*61.13*	*46.98*	*< 0.0001*	
E-dn	*122.63*	*1*	*122.63*	*94.23*	*< 0.0001*	
F-R	*4.325E-003*	*1*	*4.325E-003*	*3.323E-003*	*0.9547*	
G-u	*80.93*	*1*	*80.93*	*62.19*	*< 0.0001*	
AF	*2.09*	*1*	*2.09*	*1.61*	*0.2216*	
AG	*4.70*	*1*	*4.70*	*3.61*	*0.0744*	
BC	*2.24*	*1*	*2.24*	*1.72*	*0.2073*	
BD	*10.42*	*1*	*10.42*	*8.01*	*0.0116*	
CD	*28.32*	*1*	*28.32*	*21.76*	*0.0002*	
DF	*2.85*	*1*	*2.85*	*2.19*	*0.1572*	
EG	*10.10*	*1*	*10.10*	*7.76*	*0.0127*	
Residual	22.12	17	1.30			
Cor Total	735.12	31				

Std. Dev.	1.14		R-Squared	0.9699
Mean	17.08		Adj R-Squared	0.9451
C.V. %	6.68		Pred R-Squared	0.8938
PRESS	78.04		Adeq Precision	26.381

Table B.12. ANOVA response table for Large outer arc transverse roughness (R_z)

ANOVA for Response Surface Reduced 2FI model						
Analysis of variance table [Partial sum of squares - Type III]						
	Sum of		**Mean**	**F**	**p-value**	
Source	**Squares**	**df**	**Square**	**Value**	**Prob > F**	
Model	584.38	13	44.95	20.12	< 0.0001	significant
A-Thickness	*116.69*	*1*	*116.69*	*52.22*	*< 0.0001*	
B-P	*87.68*	*1*	*87.68*	*39.24*	*< 0.0001*	
C-Lm	*2.17*	*1*	*2.17*	*0.97*	*0.3374*	
D-dm	*52.46*	*1*	*52.46*	*23.47*	*0.0001*	
E-dn	*95.16*	*1*	*95.16*	*42.58*	*< 0.0001*	
F-R	*0.021*	*1*	*0.021*	*9.312E-003*	*0.9242*	
G-u	*75.61*	*1*	*75.61*	*33.84*	*< 0.0001*	
AB	*16.16*	*1*	*16.16*	*7.23*	*0.0150*	
AC	*5.58*	*1*	*5.58*	*2.50*	*0.1313*	
AG	*10.97*	*1*	*10.97*	*4.91*	*0.0399*	
BC	*11.97*	*1*	*11.97*	*5.36*	*0.0327*	
DF	*4.81*	*1*	*4.81*	*2.15*	*0.1594*	
EG	*14.31*	*1*	*14.31*	*6.40*	*0.0209*	
Residual	40.22	18	2.23			
Cor Total	624.60	31				

Std. Dev.	1.49		R-Squared	0.9356
Mean	17.56		Adj R-Squared	0.8891
C.V. %	8.51		Pred R-Squared	0.7892
PRESS	131.69		Adeq Precision	18.839

APPENDIX C

ANOVA DIAGNOSTIC PLOTS FOR KERF TAPER RATIO

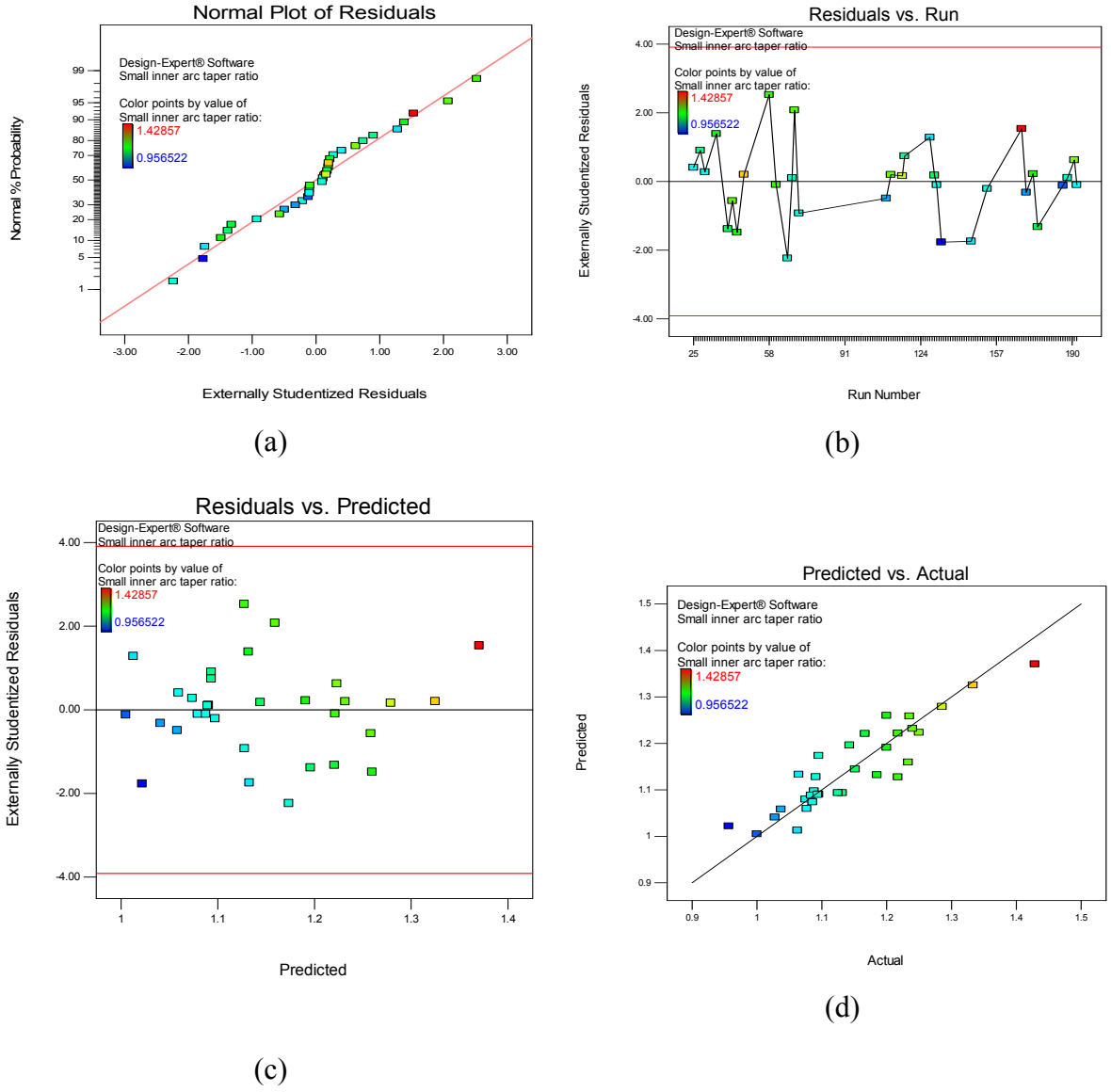

Figure C.1. Small inner arc taper ratio model (a) Normal plot of residuals, (b) Residuals versus Run plot, (c) Residual versus predicted, (d) Predicted versus experimental plot

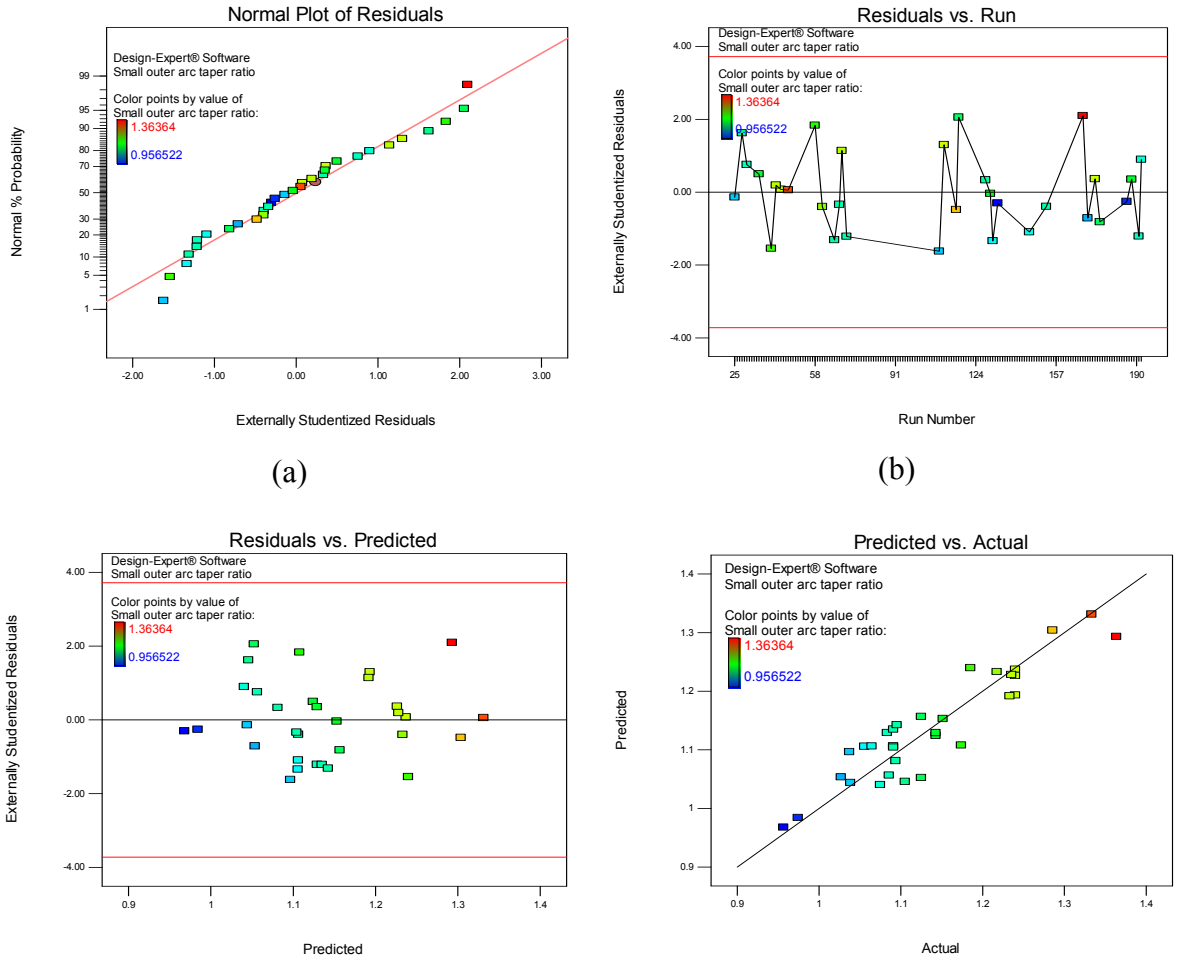

Figure C.2. Small outer arc taper ratio model (a) Normal plot of residuals, (b) Residuals versus Run plot, (c) Residual versus predicted, (d) Predicted versus experimental plot

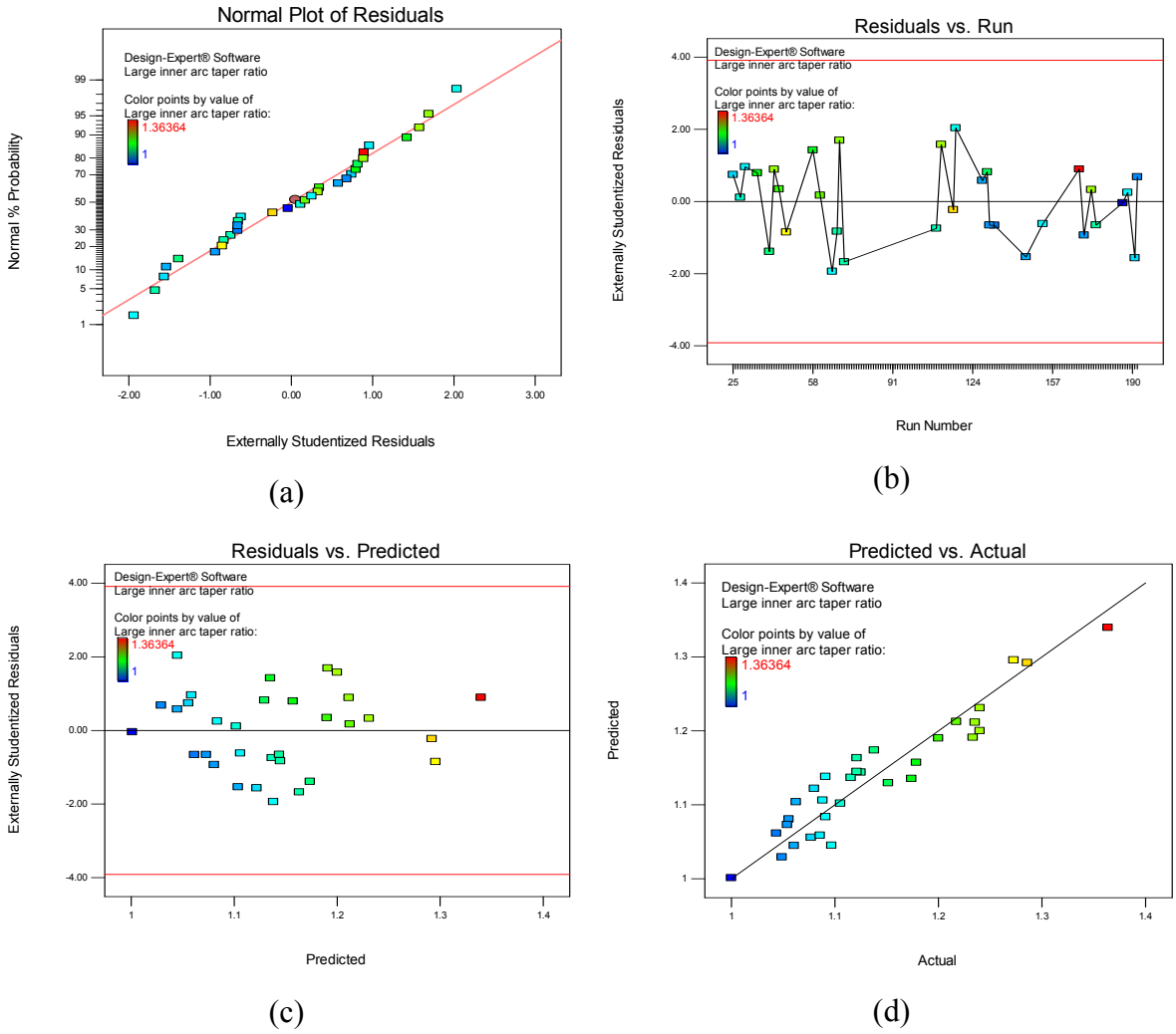

Figure C.3. Large inner arc taper ratio model (a) Normal plot of residuals, (b) Residuals versus Run plot, (c) Residual versus predicted, (d) Predicted versus experimental plot

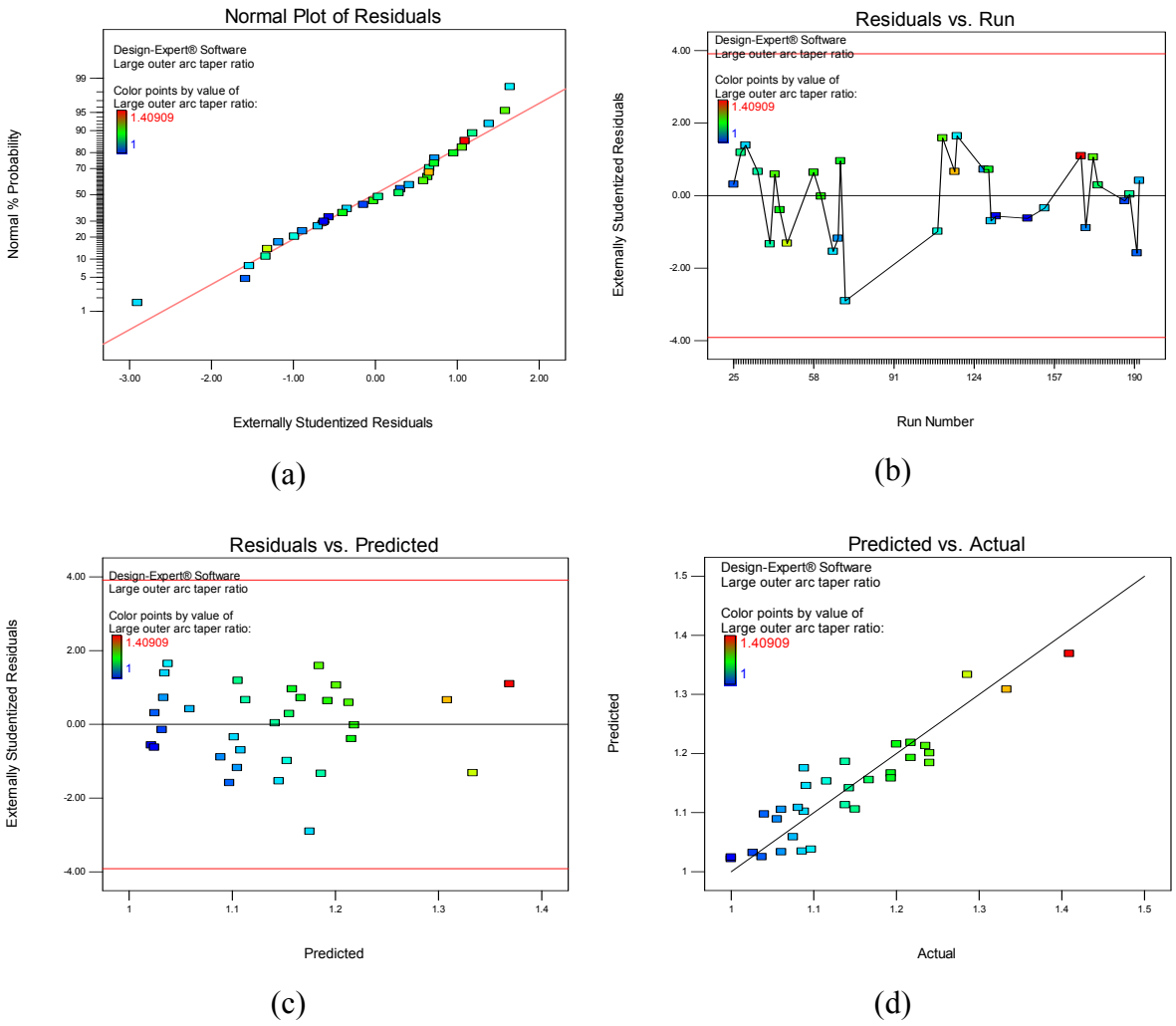

Figure C.4. Large outer arc taper ratio model (a) Normal plot of residuals, (b) Residuals versus Run plot, (c) Residual versus predicted, (d) Predicted versus experimental plot

ANOVA DIAGNOSTIC PLOTS FOR TRANSVERSE SURFACE ROUGHNESS

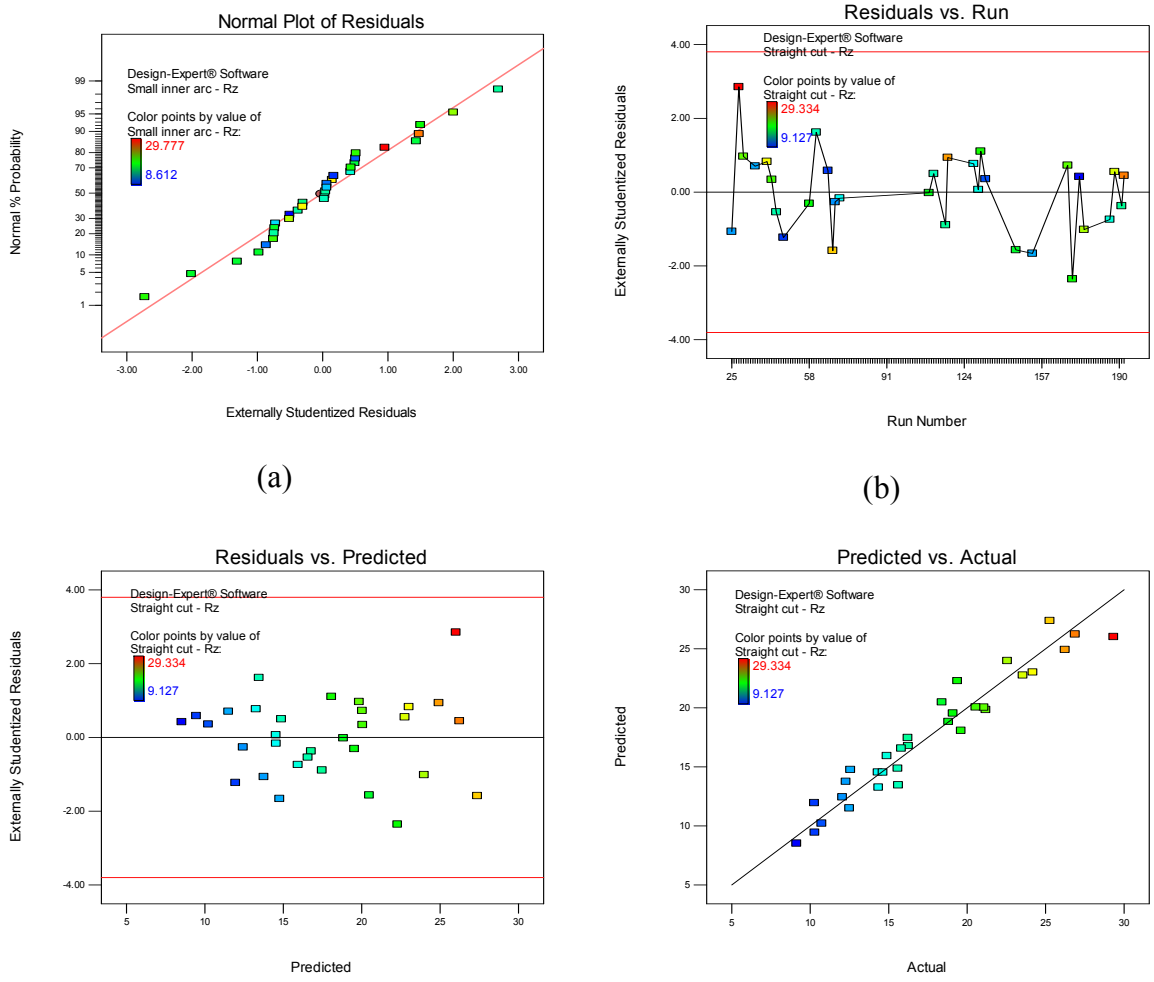

Figure C.5. Straight cut transverse roughness (R_z) model (a) Normal plot of residuals, (b) Residuals versus Run plot, (c) Residual versus predicted, (d) Predicted versus experimental plot

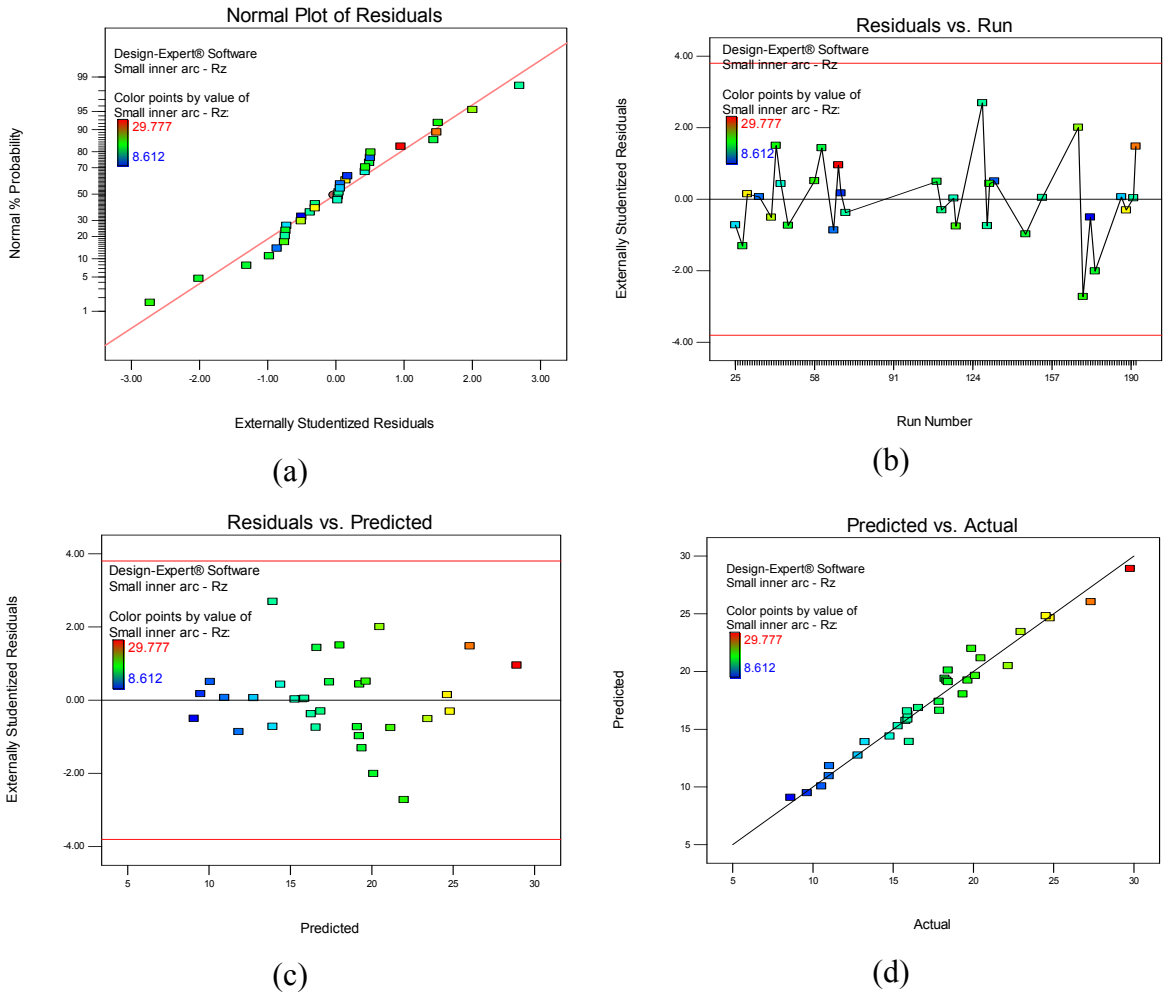

Figure C.6. Small inner arc transverse roughness (R_z) model (a) Normal plot of residuals, (b) Residuals versus Run plot, (c) Residual versus predicted, (d) Predicted versus experimental plot

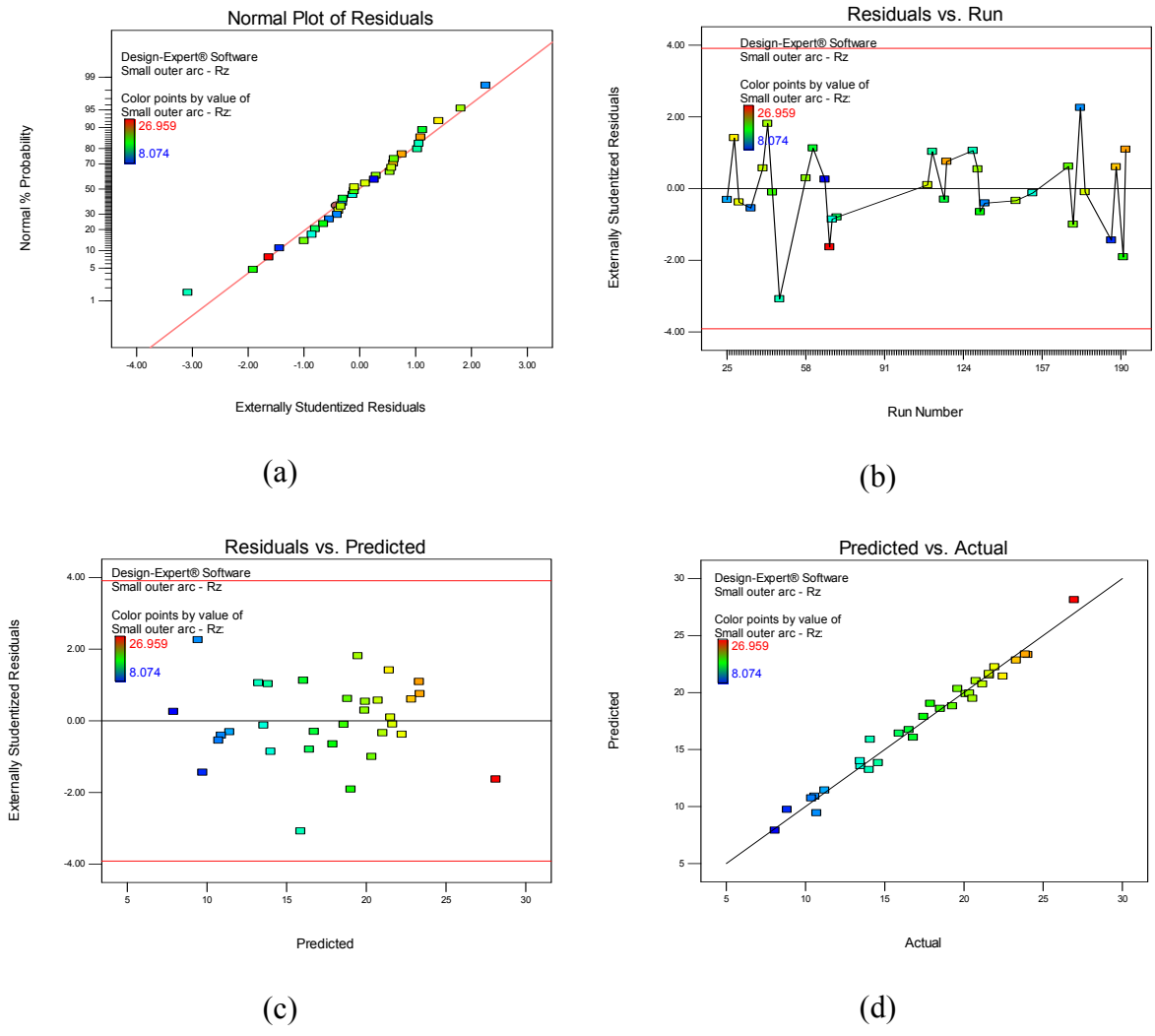

Figure C.7. Small outer arc transverse roughness (R_z) model (a) Normal plot of residuals, (b) Residuals versus Run plot, (c) Residual versus predicted, (d) Predicted versus experimental plot

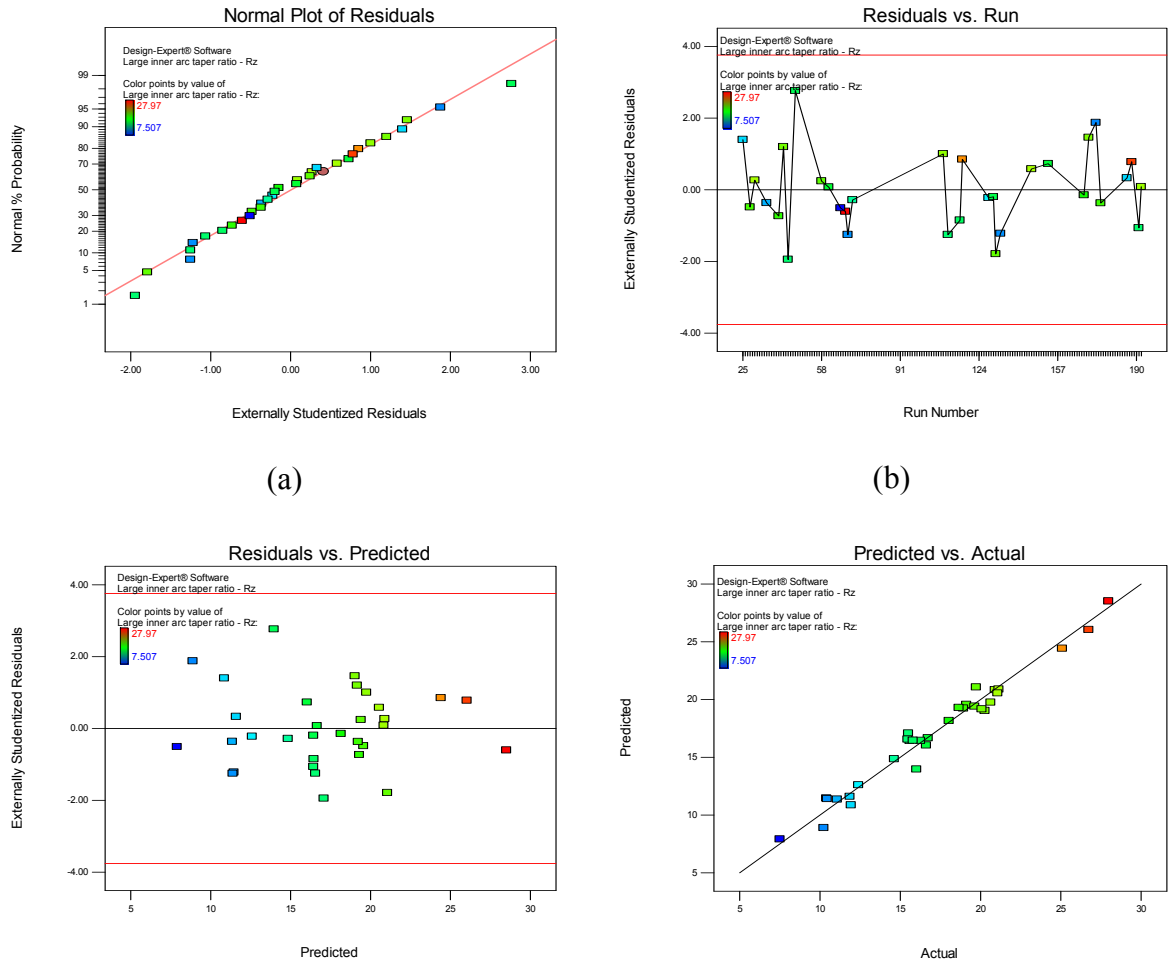

Figure C.8. Large inner arc transverse roughness (R_z) model (a) Normal plot of residuals, (b) Residuals versus Run plot, (c) Residual versus predicted, (d) Predicted versus experimental plot

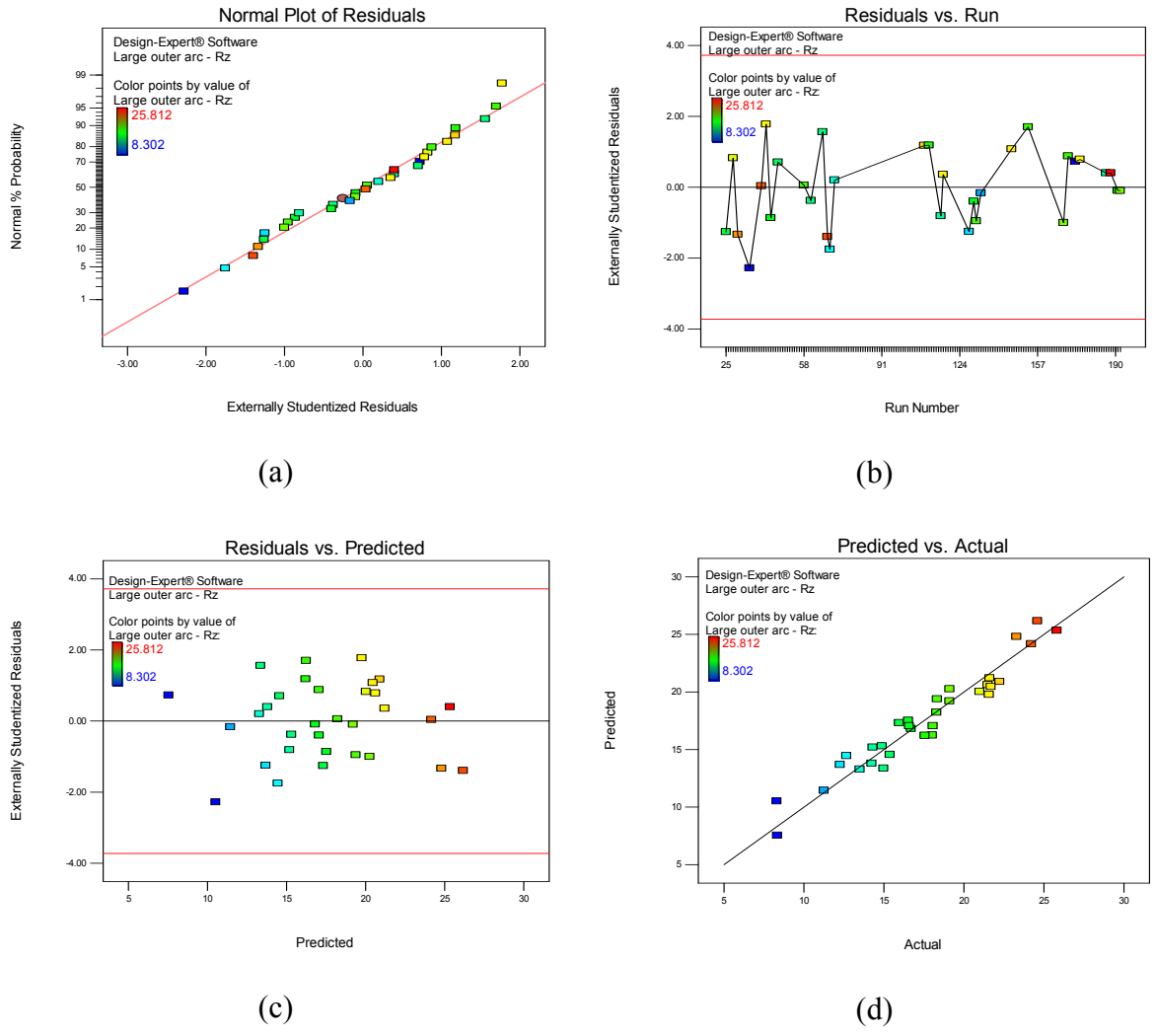

Figure C.9. Large outer arc transverse roughness (R_z) model (a) Normal plot of residuals, (b) Residuals versus Run plot, (c) Residual versus predicted, (d) Predicted versus experimental plot

APPENDIX D

LONGITUDINAL ROUGHNESS PROFILES FOR AWJ-32 SPECIMEN

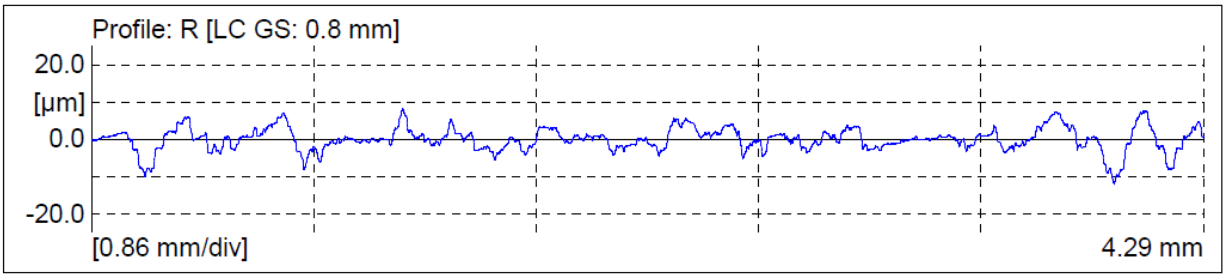

Ply number 1

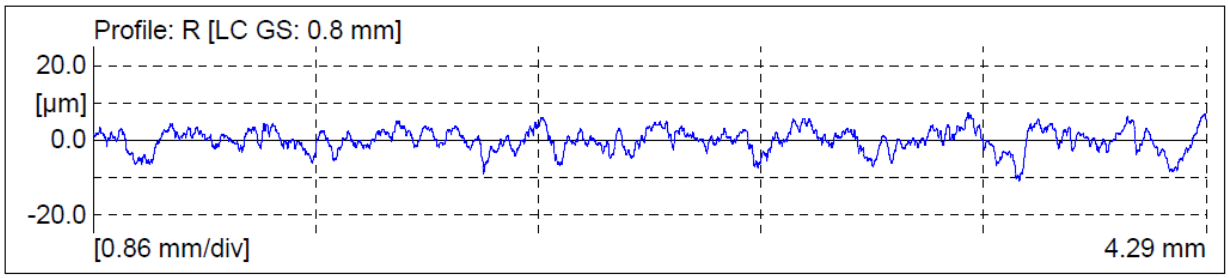

Ply number 2

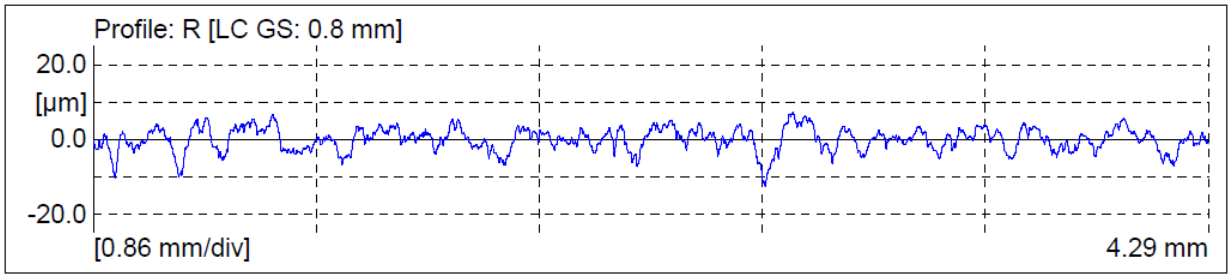

Ply number 3

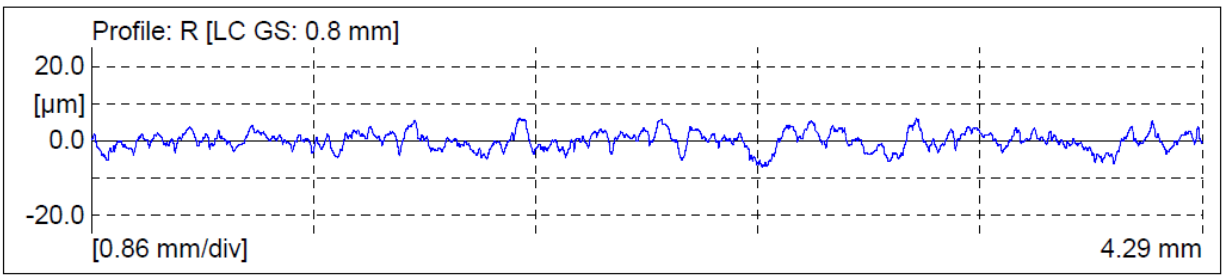

Ply number 4

Figure D.1. AWJ-32 longitudinal surface roughness along ply number 1-4

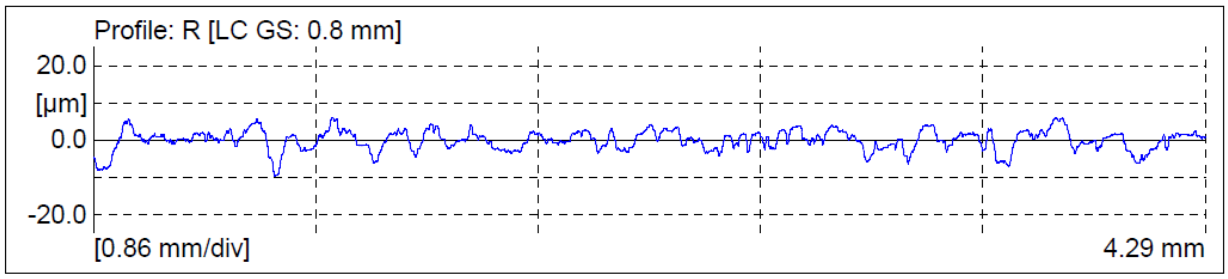

Ply number 5

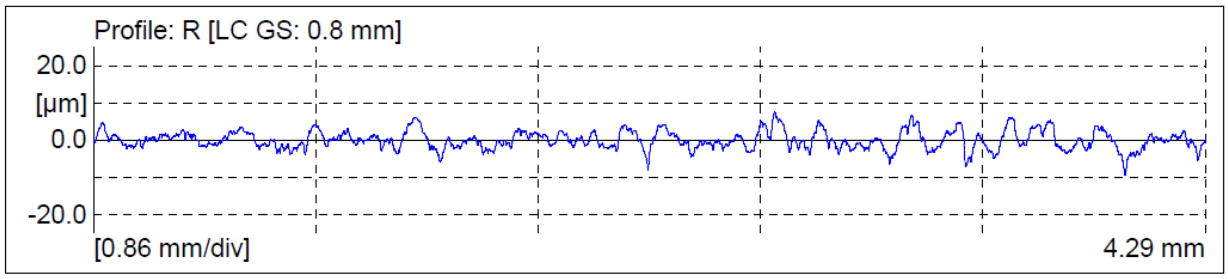

Ply number 6

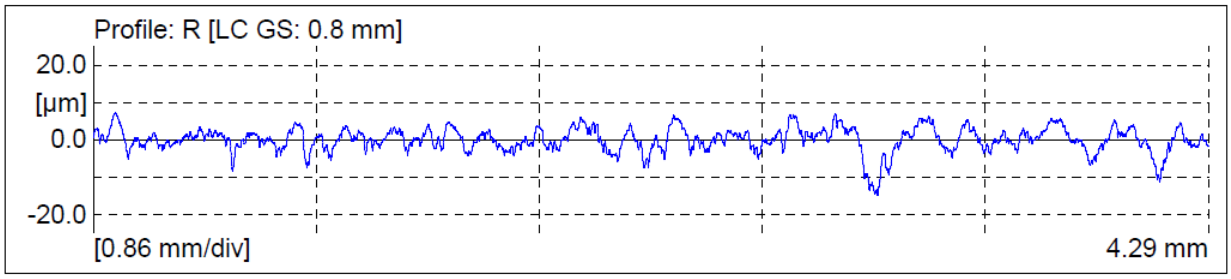

Ply number 7

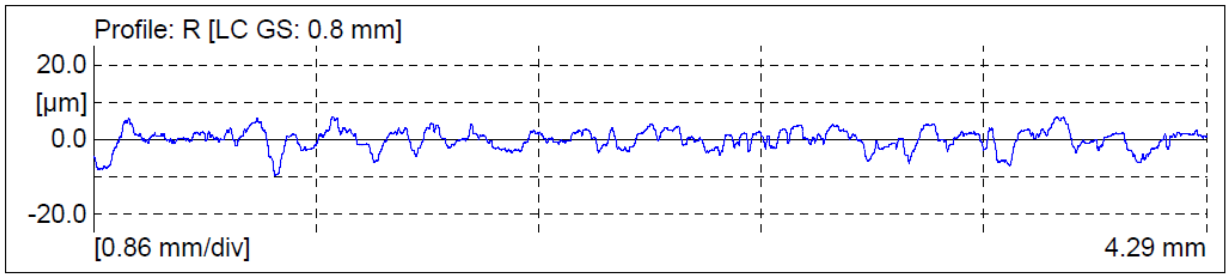

Ply number 8

Figure D.2. AWJ-32 longitudinal surface roughness along ply number 5-8

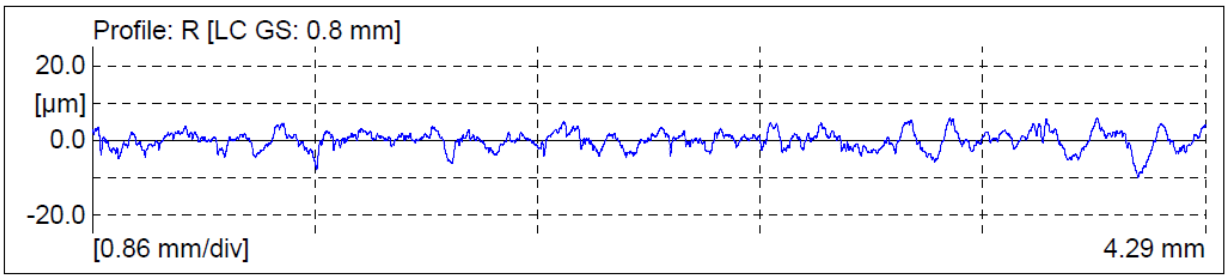

Ply number 9

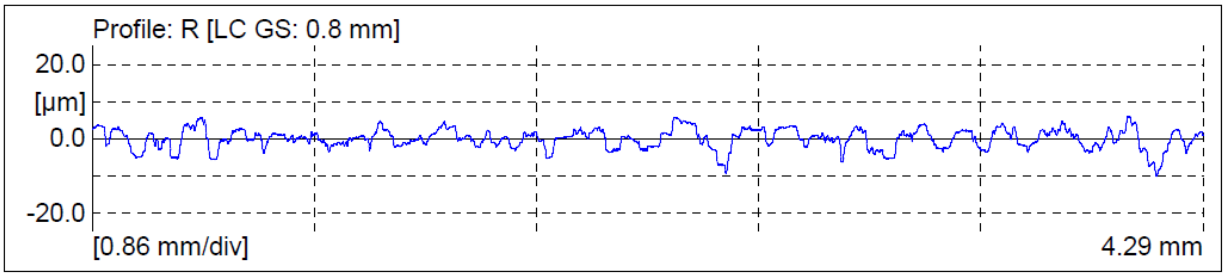

Ply number 10

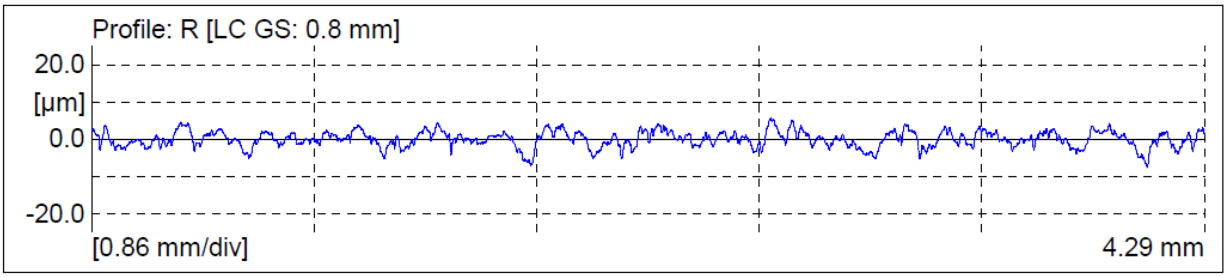

Ply number 11

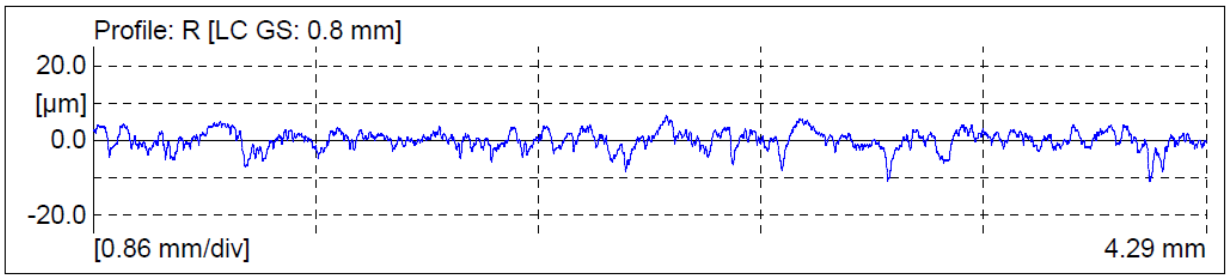

Ply number 12

Figure D.3. AWJ-32 longitudinal surface roughness along ply number 9-12

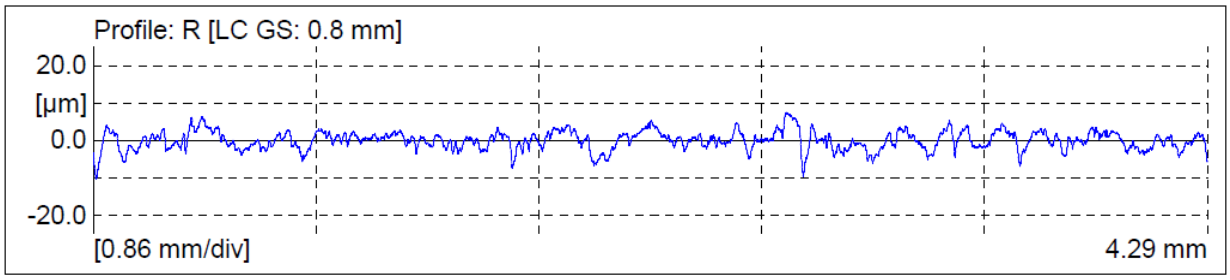

Ply number 13

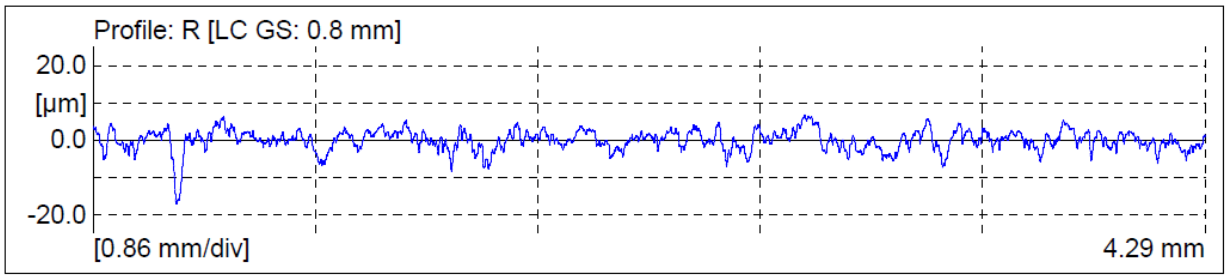

Ply number 14

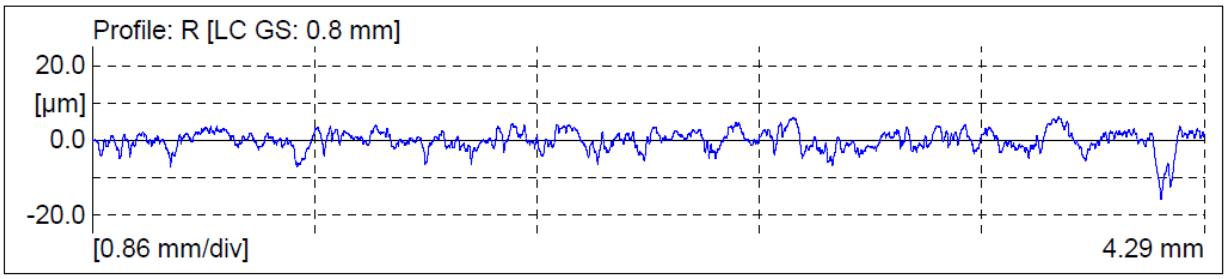

Ply number 15

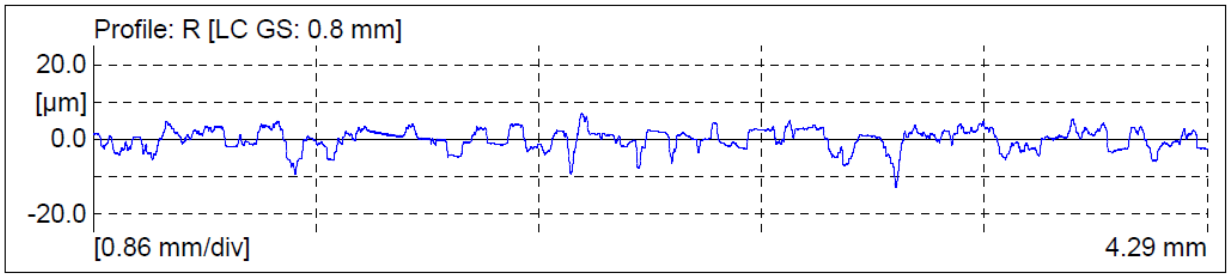

Ply number 16

Figure D.4. AWJ-32 longitudinal surface roughness along ply number 13-16

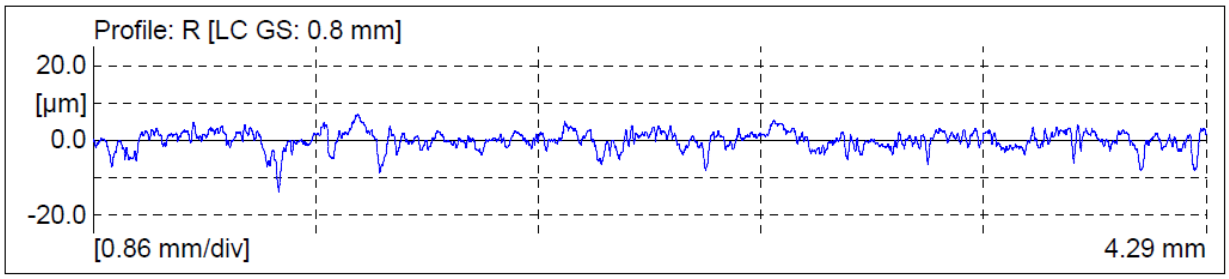

Ply number 17

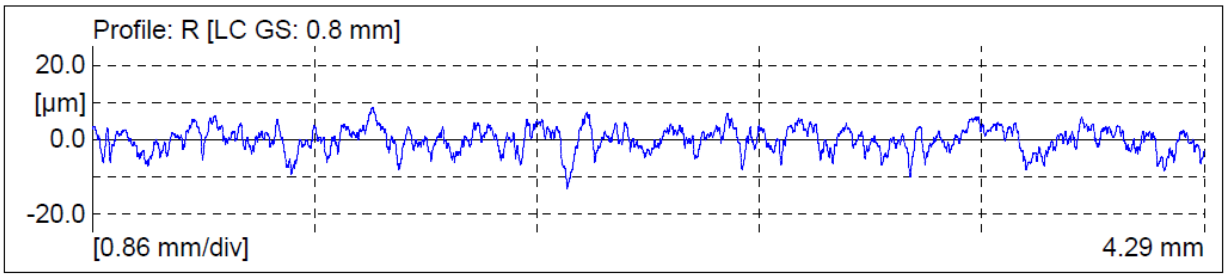

Ply number 18

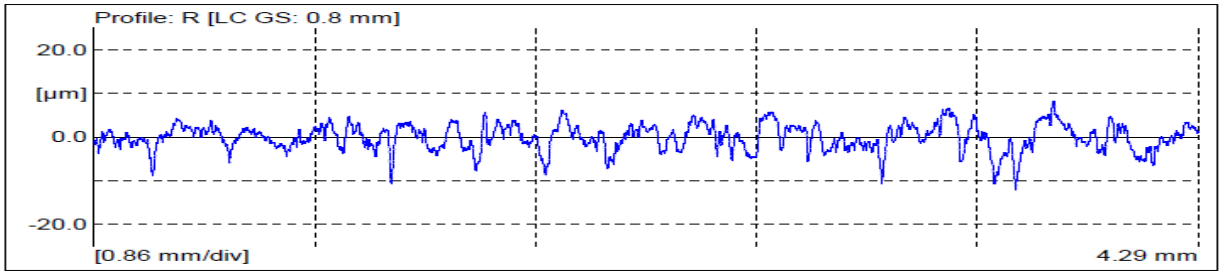

Ply number 19

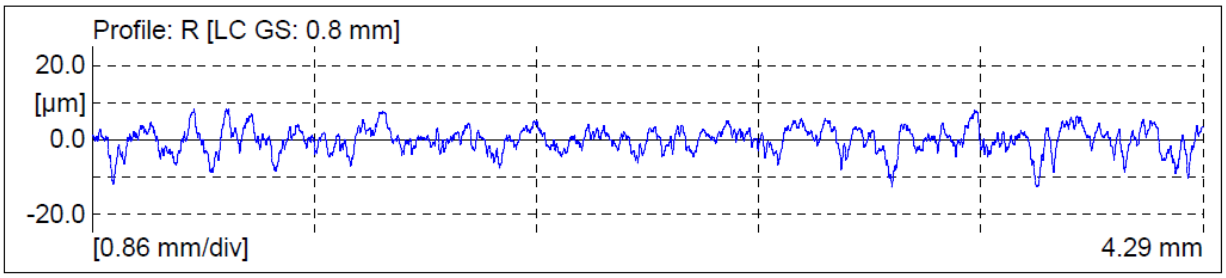

Ply number 20

Figure D.5. AWJ-32 longitudinal surface roughness along ply number 17-20

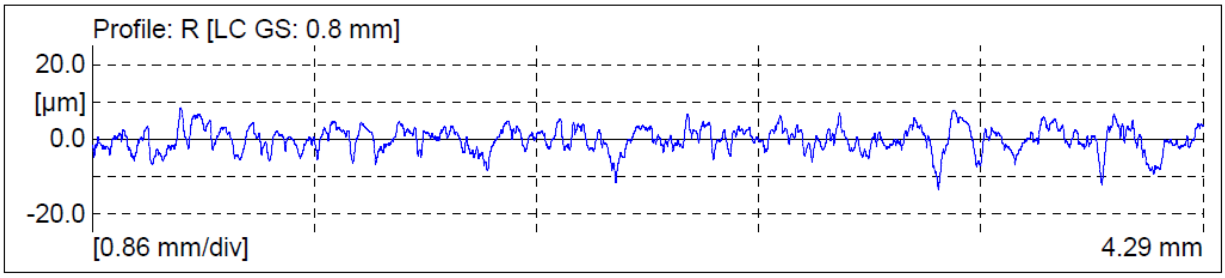

Ply number 21

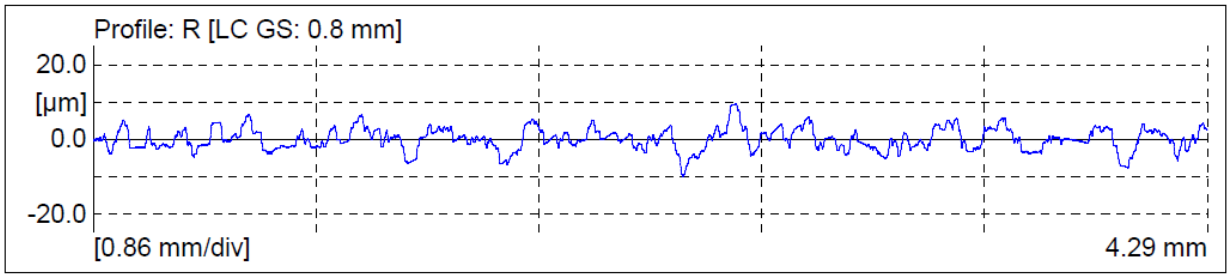

Ply number 22

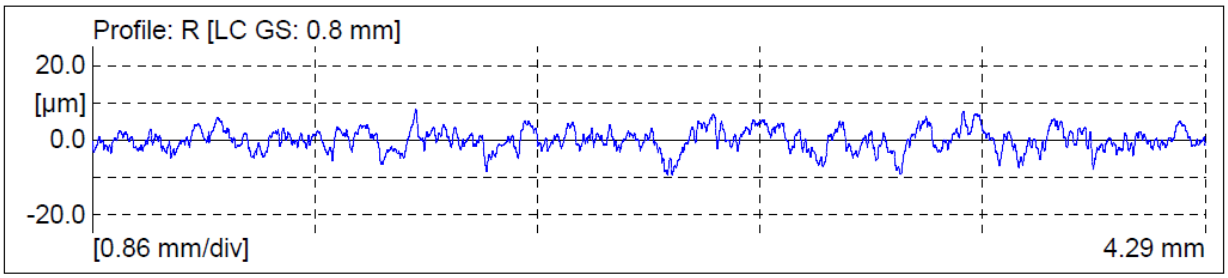

Ply number 23

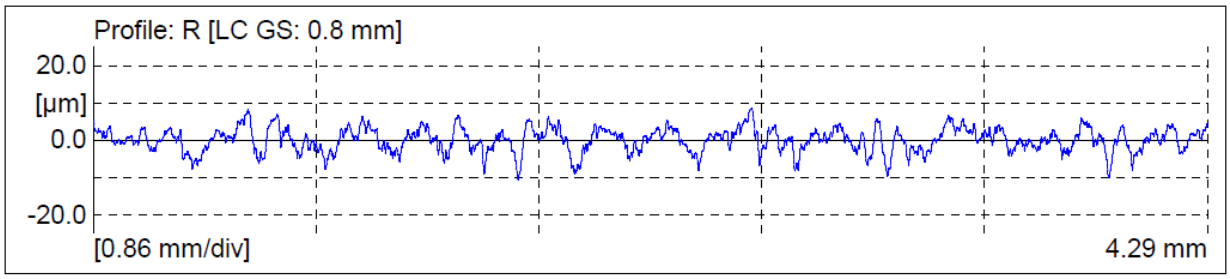

Ply number 24

Figure D.6. AWJ-32 longitudinal surface roughness along ply number 21-24

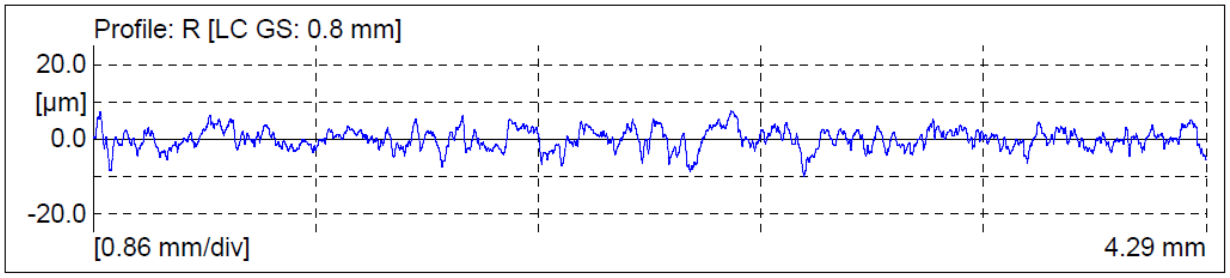

Ply number 25

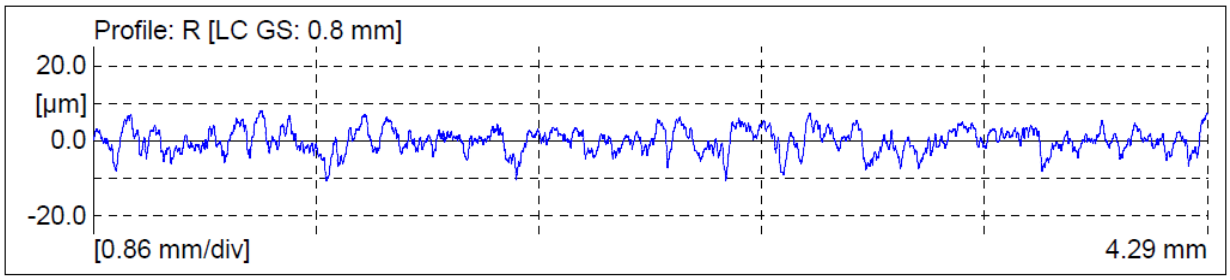

Ply number 26

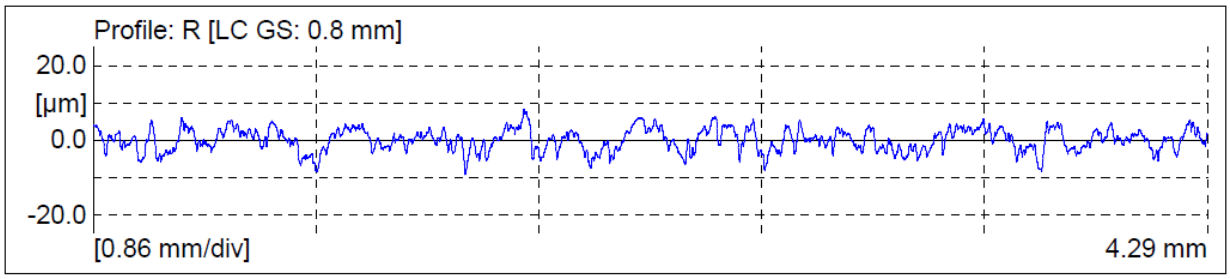

Ply number 27

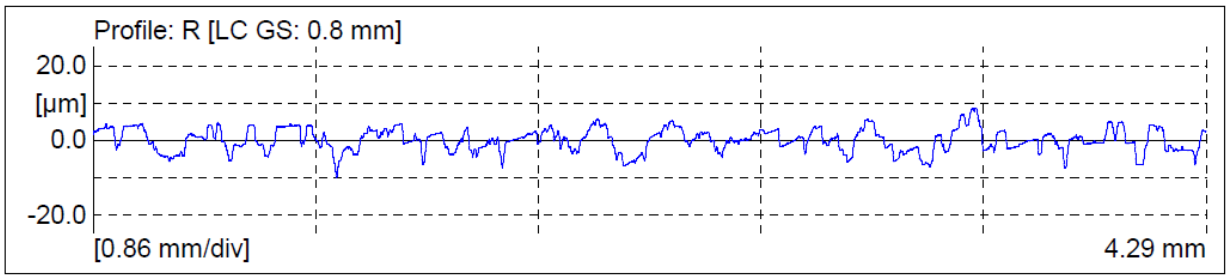

Ply number 28

Figure D.7. AWJ-32 longitudinal surface roughness along ply number 25-28

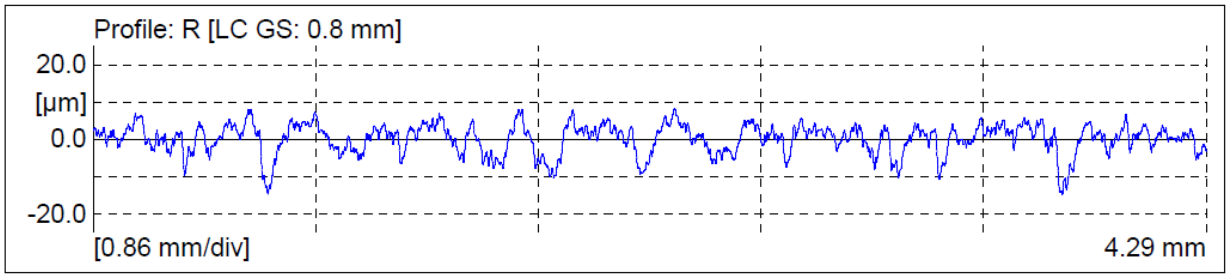

Ply number 29

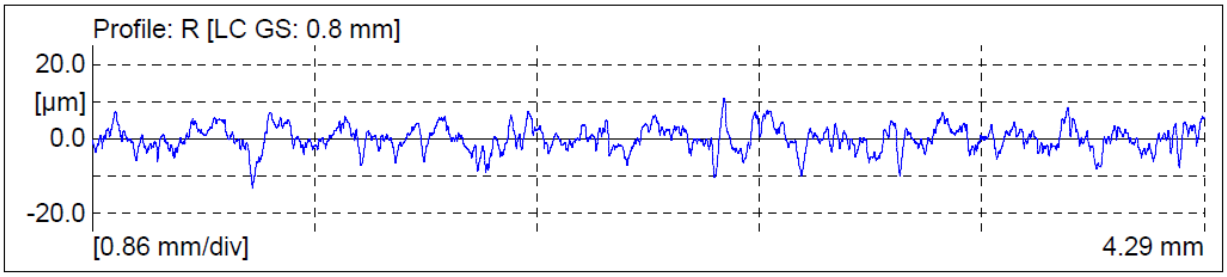

Ply number 30

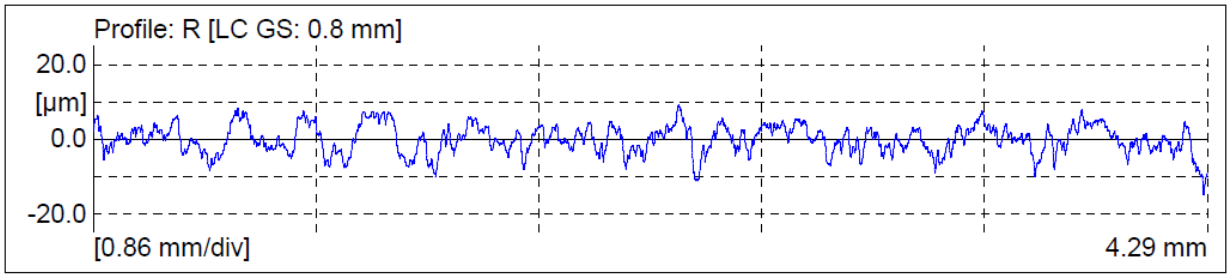

Ply number 31

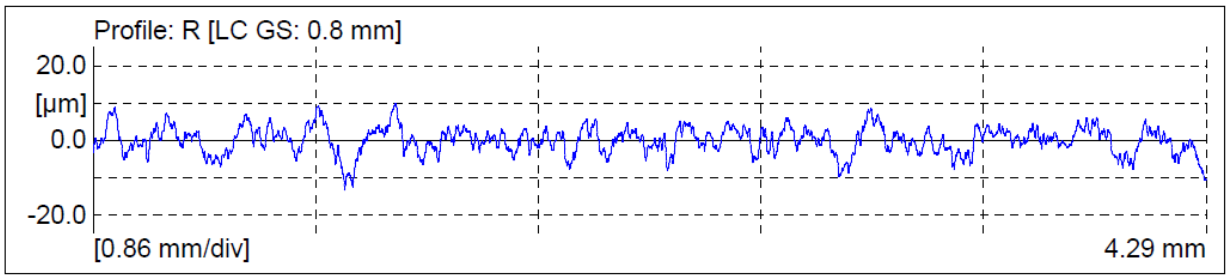

Ply number 32

Figure D.8. AWJ-32 longitudinal surface roughness along ply number 29-32

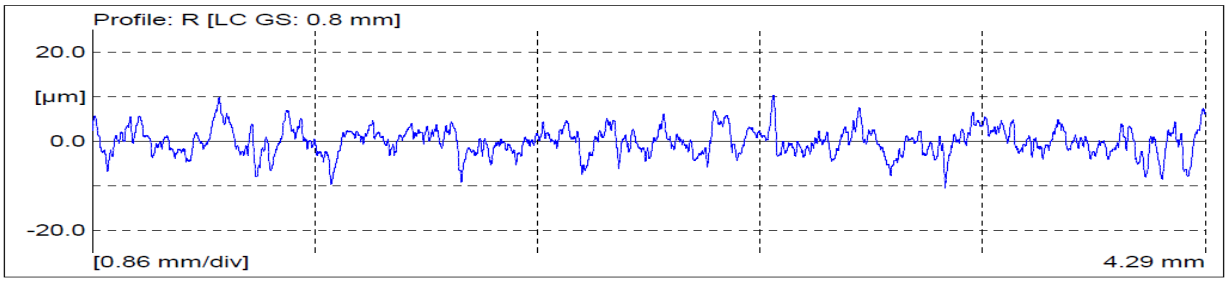

Ply number 33

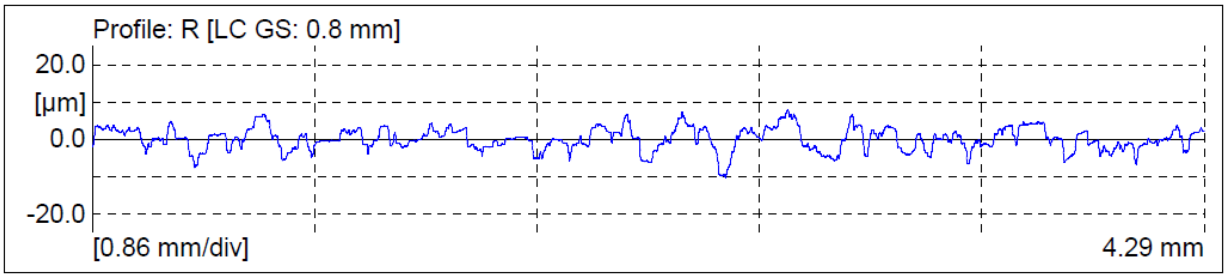

Ply number 34

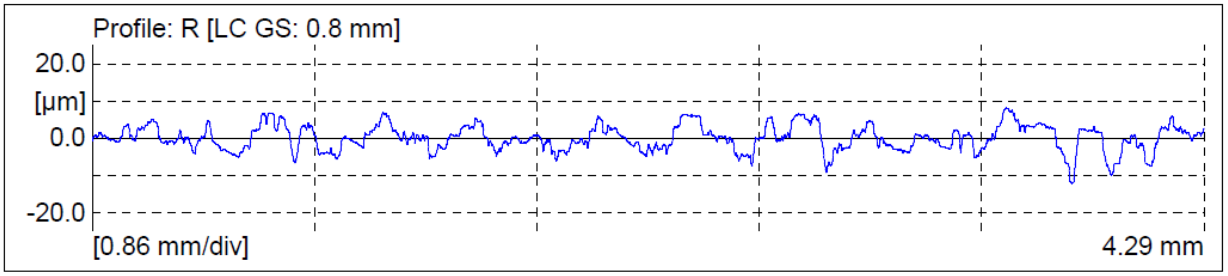

Ply number 35

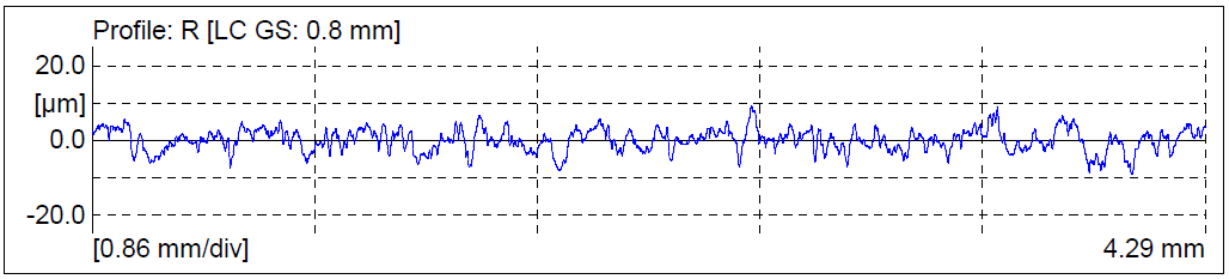

Ply number 36

Figure D.9. AWJ-32 longitudinal surface roughness along ply number 33-36

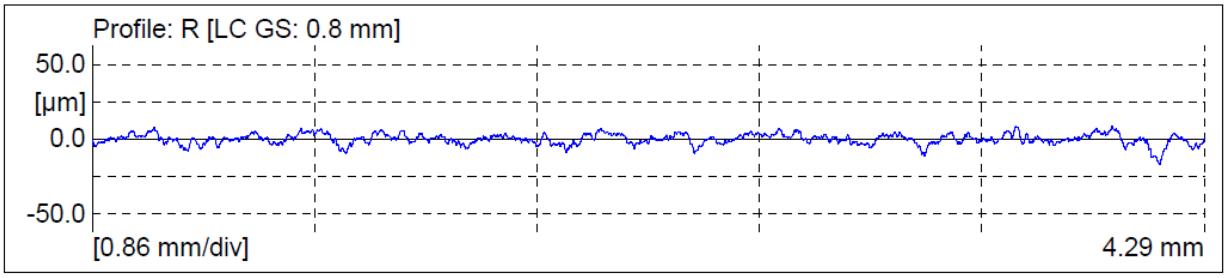

Ply number 37

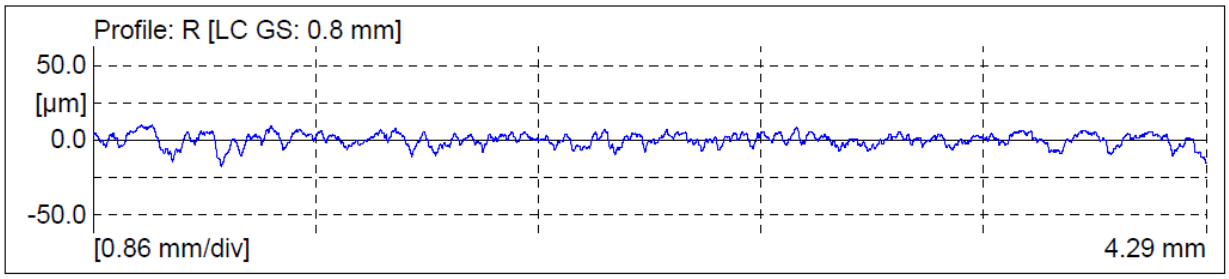

Ply number 38

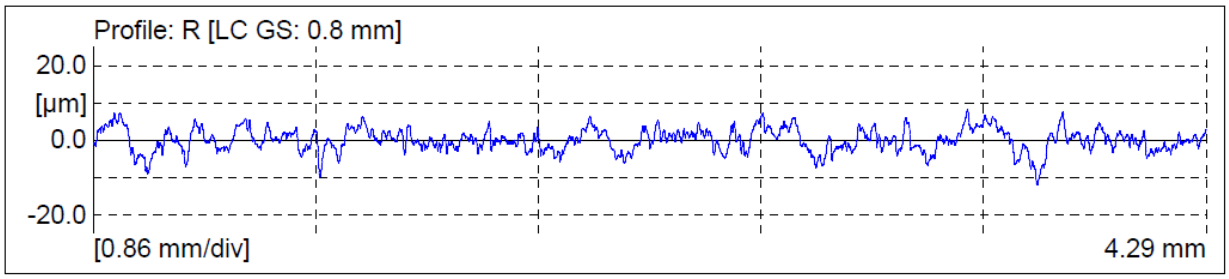

Ply number 39

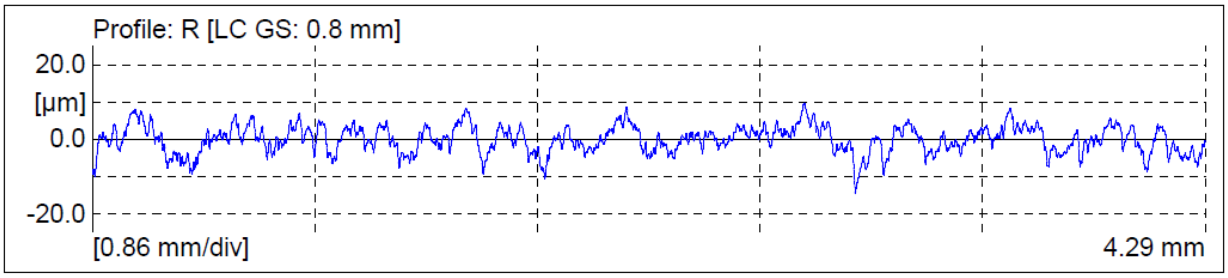

Ply number 40

Figure D.10. AWJ-32 longitudinal surface roughness along ply number 37-40

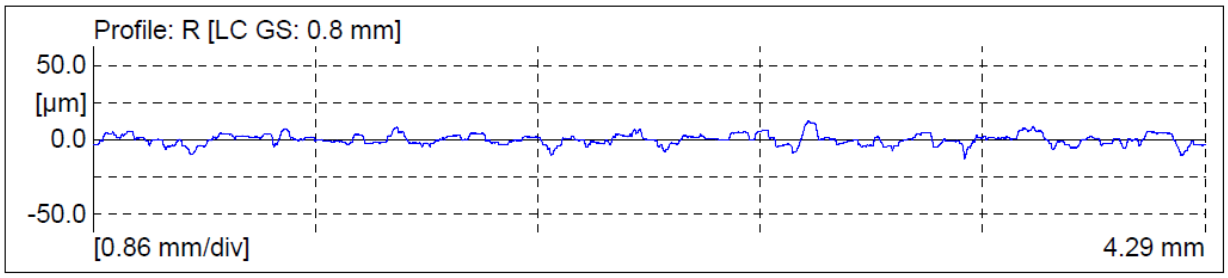

Ply number 41

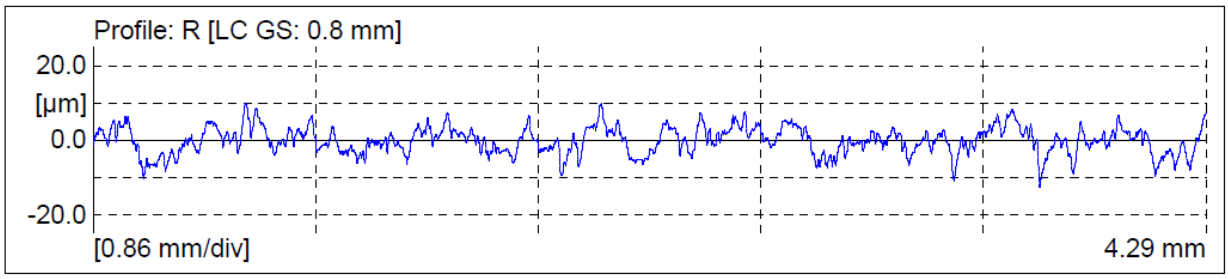

Ply number 42

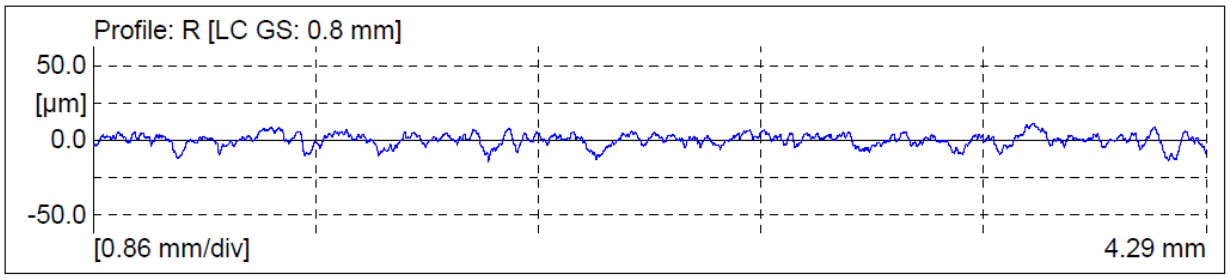

Ply number 43

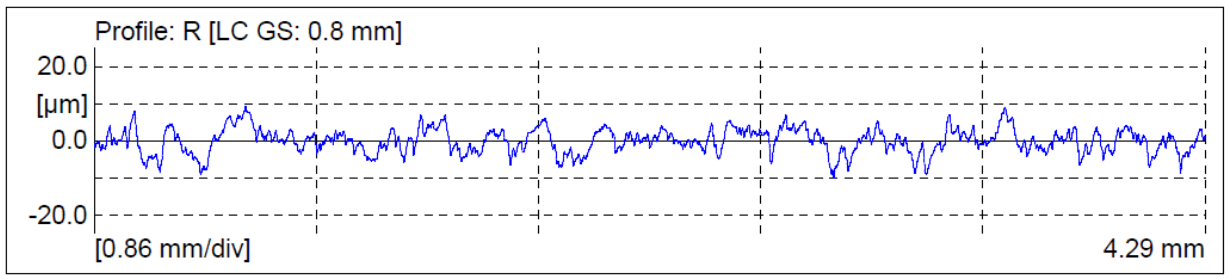

Ply number 44

Figure D.11. AWJ-32 longitudinal surface roughness along ply number 41-44

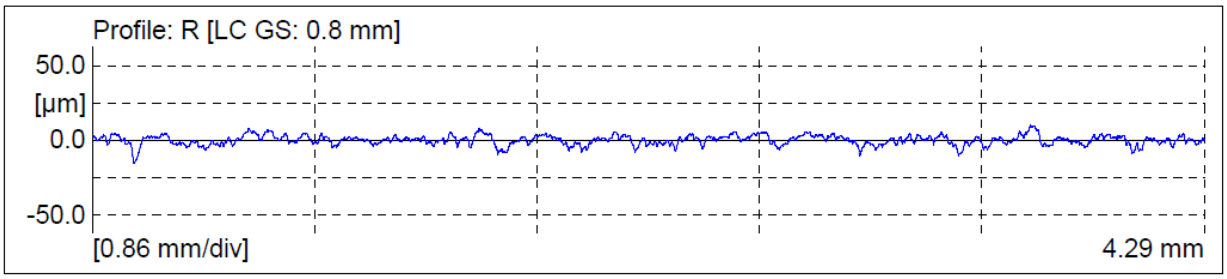

Ply number 45

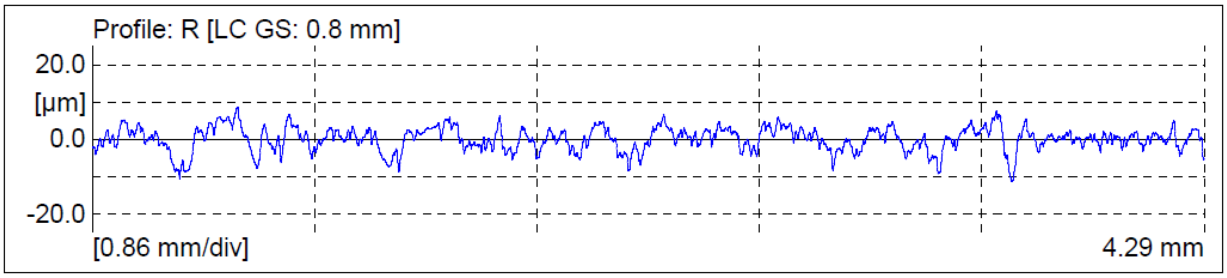

Ply number 46

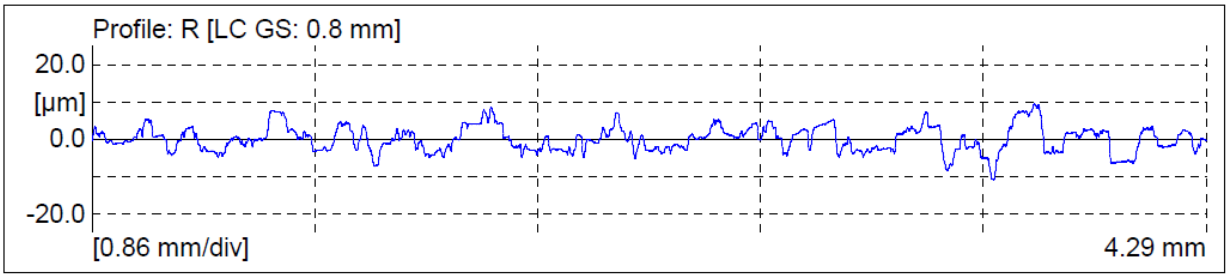

Ply number 47

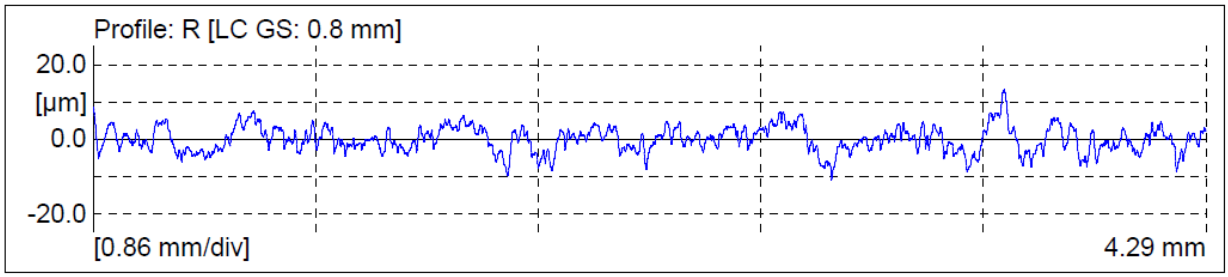

Ply number 48

Figure D.12. AWJ-32 longitudinal surface roughness along ply number 45-48

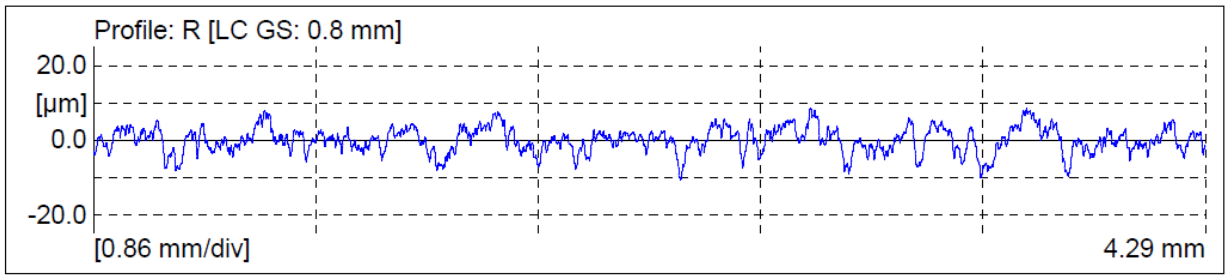

Ply number 49

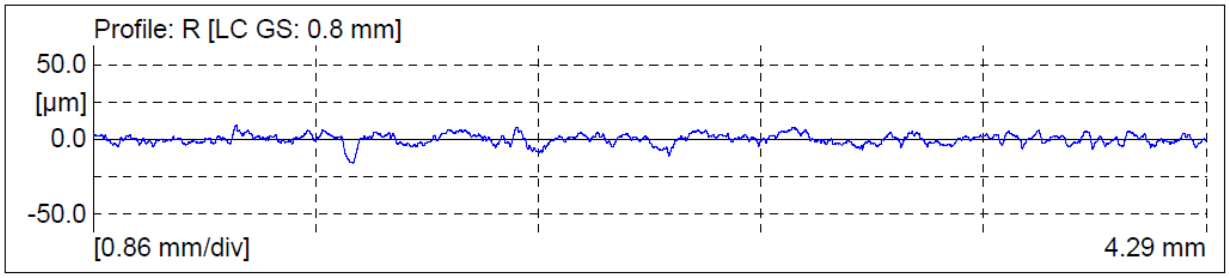

Ply number 50

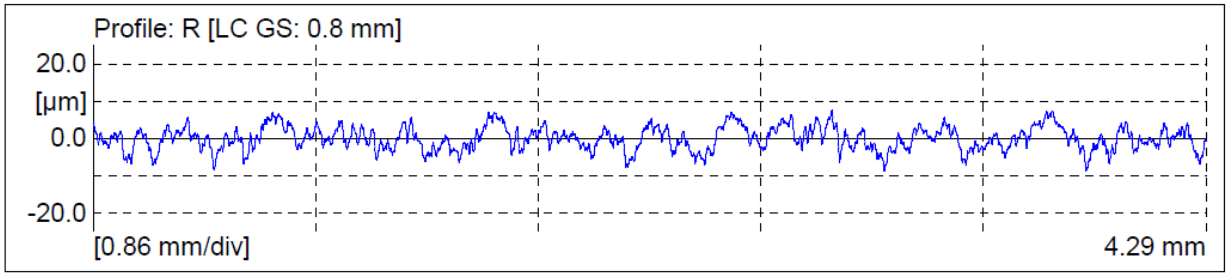

Ply number 51

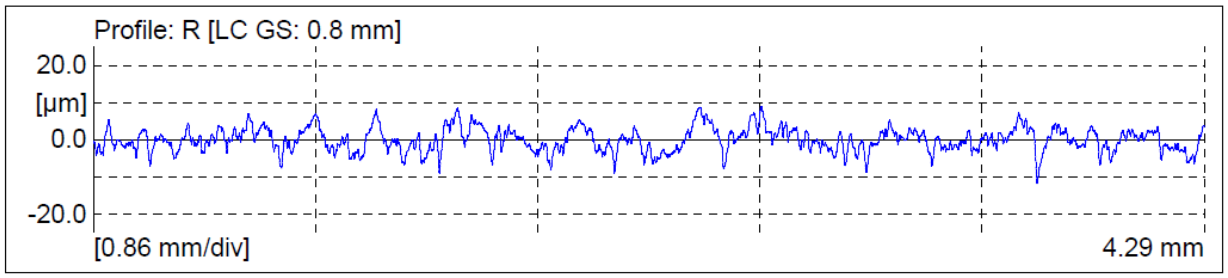

Ply number 52

Figure D.13. AWJ-32 longitudinal surface roughness along ply number 49-52

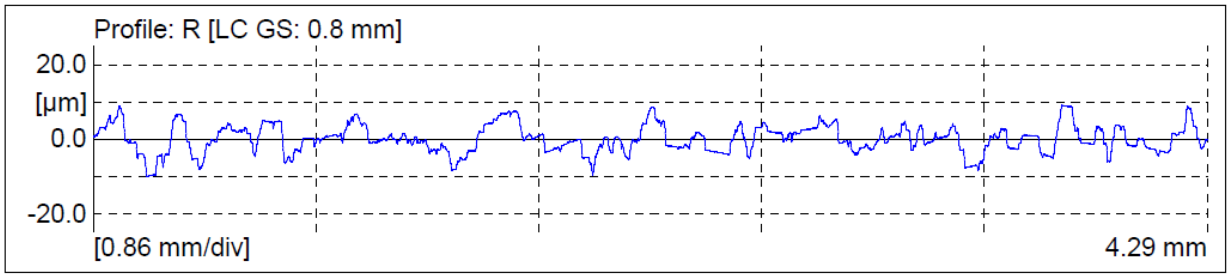

Ply number 53

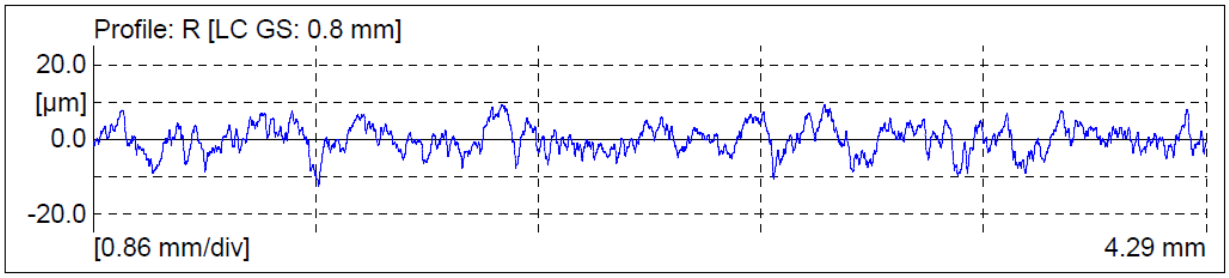

Ply number 54

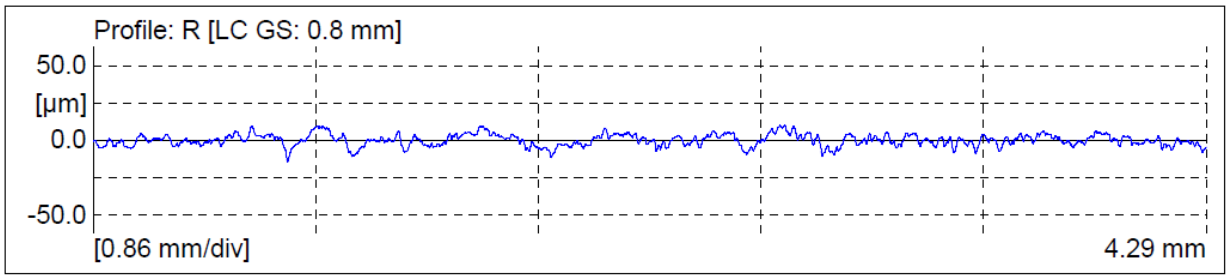

Ply number 55

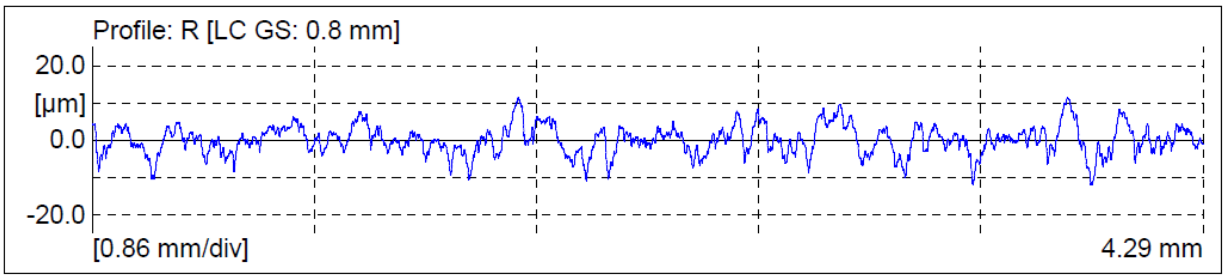

Ply number 56

Figure D.14. AWJ-32 longitudinal surface roughness along ply number 53-56

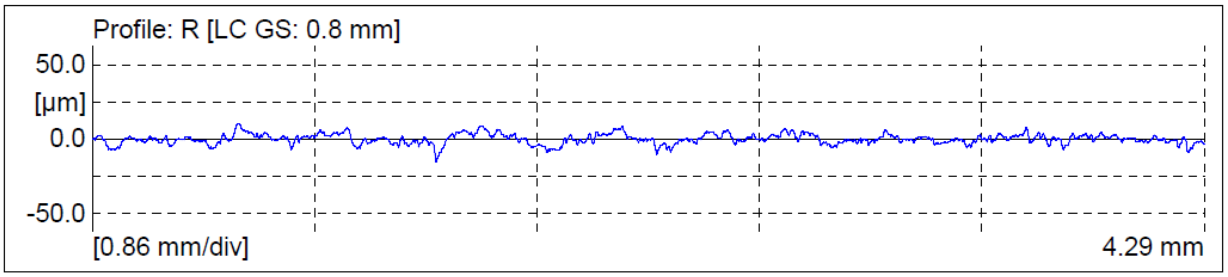

Ply number 57

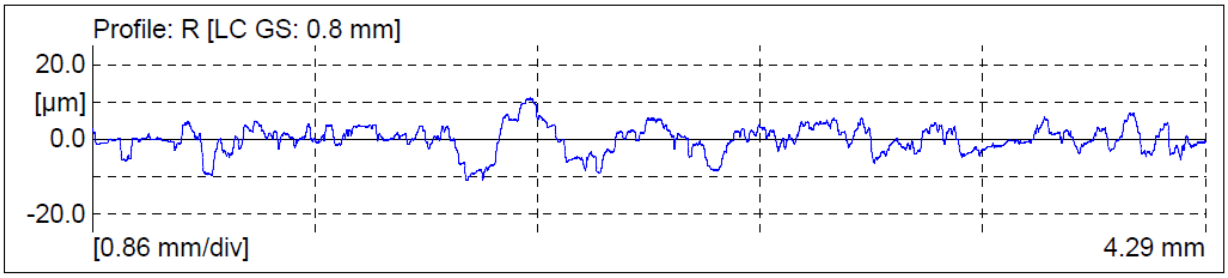

Ply number 58

Figure D.15. AWJ-32 longitudinal surface roughness along ply number 57-58